

Enhancement of spin-orbit coupling at manganite surfaces

S. Valencia,^{1,*} M. J. Calderón,^{2,†} L. López-Mir,³ Z. Konstantinovic,⁴ E. Schierle,¹
E. Weschke,¹ L. Brey,² B. Martínez,³ and Ll. Balcells³

¹*Helmholtz-Zentrum Berlin für Materialien und Energie, Albert-Einstein-Str. 15, 12489 Berlin, Germany*

²*Materials Science Factory, Instituto de Ciencia de Materiales de Madrid, ICMM-CSIC, Cantoblanco, E-28049 Madrid, Spain*

³*Institut de Ciència de Materials de Barcelona, ICMA-B-CSIC, Campus de la UAB, 08193 Bellaterra, Spain*

⁴*Center for Solid State Physics and New Materials, Institute of Physics Belgrade, University of Belgrade, Pregrevica 118, 11080 Belgrade, Serbia*



(Received 20 November 2017; revised manuscript received 28 June 2018; published 24 September 2018)

Spin-orbit coupling in magnetic systems lacking inversion symmetry can give rise to nontrivial spin textures. Magnetic thin films and heterostructures are potential candidates for the formation of skyrmions and other noncollinear spin configurations as inversion symmetry is inherently lost at their surfaces and interfaces. However, manganites, in spite of their extraordinarily rich magnetic phase diagram, have not yet been considered of interest within this context as their spin-orbit coupling is assumed to be negligible. We demonstrate here, by means of angular dependent x-ray linear dichroism experiments and theoretical calculations, the existence of a noncollinear antiferromagnetic ordering at the surface of ferromagnetic $\text{La}_{2/3}\text{Sr}_{1/3}\text{MnO}_3$ thin films whose properties can only be explained by an unexpectedly large enhancement of the spin-orbit interaction. Our results reveal that spin-orbit coupling, usually assumed to be very small in manganites, can be significantly enhanced at surfaces and interfaces adding a new twist to the possible magnetic orders that can arise in electronically reconstructed systems.

DOI: [10.1103/PhysRevB.98.115142](https://doi.org/10.1103/PhysRevB.98.115142)

I. INTRODUCTION

Broken inversion symmetry and strong spin-orbit coupling (SOC) are necessary (although not sufficient) conditions for the formation of noncollinear spin textures [1–7], such as skyrmions, magnetic bubbles or spirals. These nontrivial spin configurations, when topological, hold promise for future spin-based information technologies due to their long lifetimes, stability, and the possibility to be created, controlled and/or detected at room temperature by means of electrical currents or electric fields [8–10]. While helical and skyrmion states have been observed in several different systems [7,11–18], their stability has been found to be enhanced in 2D ones [4,15,19] such as thin films or heterostructures, as space inversion symmetry is inherently broken at surfaces and interfaces.

Manganese perovskites with formula $L_{1-x}A_x\text{MnO}_3$ (L and A being trivalent lanthanides and divalent alkaline ions, respectively), such as, for example, $\text{La}_{2/3}\text{Sr}_{1/3}\text{MnO}_3$ (LSMO) have not yet been considered as plausible hosts for nontrivial spin configurations. Although the interplay between spin, lattice, and orbital degrees of freedom leads to a rich phase diagram with a large variety of electronic reconstructions at surfaces and interfaces [20–27], the atomic spin-orbit coupling in these systems is considered to be negligible. Indeed, it is assumed that the spin-orbit interaction on Mn atoms is rather small $\lambda \sim 0.04$ eV (Ref. [28]) compared to the typical energy scale on manganites given by the

hopping parameter $t \sim 0.2\text{--}0.5$ eV. Moreover, the e_g orbitals of Mn ($x^2 - y^2$ and $3z^2 - r^2$), that host the conduction electrons in manganites, are not directly spin-orbit coupled by symmetry [29]. The coupling arises only through the t_{2g} orbitals (xy , yz , zx) as a second order process [30]. Hence the SOC between the e_g orbitals is given by $g = \lambda^2/\Delta$, being $\Delta \sim 1.5$ eV the crystal field splitting between the e_g and t_{2g} levels, being one order of magnitude smaller than λ . Such small SOC is consistent with accordingly small anisotropic responses observed in bulk [30–32].

Here we show that a non-negligible SOC, as such required for the appearance of noncollinear spin textures, arises on the surface of manganite thin films. We make use of x-ray linear dichroism (XLD) to characterize an optimally doped ($x = 1/3$) LSMO thin film. Our results confirm previous ones reporting the existence of a surface antiferromagnetic (AFM) layer [33–35] on an otherwise ferromagnetic (FM) compound. However, in contradiction with previous conjectures, we demonstrate that the AFM axis of the surface in the presence of a magnetic field is not necessarily parallel or perpendicular to the surface. By means of angular dependent XLD measurements we show that the relative orientation of the AFM axis with respect to the bulk FM ordering axis does depend on the angle at which the magnetic field is applied with respect to the film plane. We demonstrate that this result can only be explained by the enhancement of the SOC on the surface by at least one order of magnitude. Such enhancement, together with the inherent breaking of the spatial inversion symmetry at the surface of the films, makes manganites a plausible candidate for the creation and control of nontrivial spin configurations.

*sergio.valencia@helmholtz-berlin.de

†calderon@icmm.csic.es

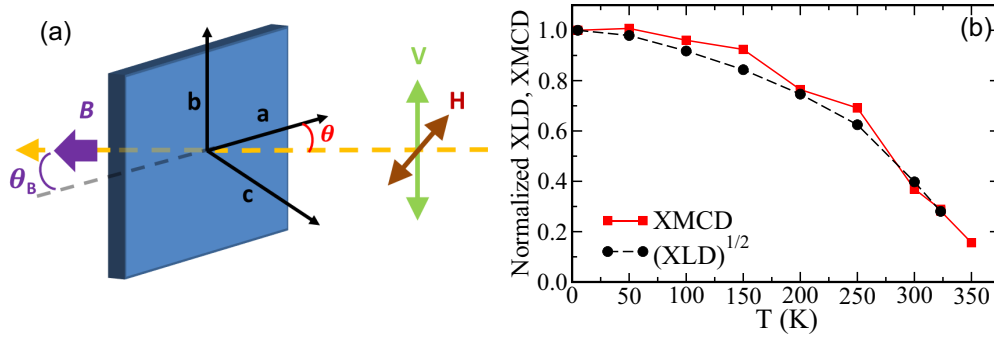


FIG. 1. (a) Sketch of the experimental setup and geometry used for the XLD measurements. (b) Comparison of the temperature dependence of the normalized XMCD and XLD measured at the Mn L_3 and L_2 edges, respectively (see Appendix A). The XLD data is square rooted to account for its square dependence on magnetization as opposed to the XMCD linear dependence. Both curves show the same T dependence confirming the AFM origin of the XLD signal (see text for discussion).

II. RESULTS

A. LSMO thin films

High-quality LSMO thin films with thickness ranging between 1.5 and 45 nm were deposited on (001)-oriented SrTiO₃ (STO) substrates by means of magnetron sputtering [36]. The experimental characterization of these samples (Refs. [34,37] and Appendix A) shows thickness dependent results in agreement with previous reports in terms of magnetic and electric properties as well as in terms of preferential orbital occupation [33–35,38–40]. In particular, the 9.4-nm-thick LSMO film under study exhibits FM and metallic behavior with magnetic transition temperature T_C and magnetization values very close to those of the bulk [37] and a preferential $x^2 - y^2$ orbital occupation that corresponds to the tensile strain conditions imposed by the STO substrate [38–41].

B. X-ray linear dichroism: Temperature dependence

The characterization of surface layers, in terms of oxidation states, orbital occupancy and magnetic properties, is possible thanks to element-selective synchrotron-related techniques [33,42,43]. In particular, XLD, calculated from the difference between two absorption spectra (I^V and I^H) taken for incoming vertical (V) and horizontal (H) linearly polarized radiation [Fig. 1(a)], probes the anisotropies around the element under investigation. Such anisotropies can arise due to a preferential orbital occupancy (XLD_{OO}) and/or by the existence of ferromagnetic (XLD_{FM}) and antiferromagnetic (XLD_{AFM}) orderings along specific crystallographic directions.

In XLD measurements, the electric field vector \mathbf{E} of the incoming radiation probes different sample directions, see Fig. 1(a). Axis parallel to (100)_{LSMO}, (010)_{LSMO}, and (001)_{LSMO} crystallographic directions have been labeled a , b , and c , respectively. Within our experimental geometry, a vertically polarized incoming beam corresponds to \mathbf{E} parallel to b independently of the angle of incidence θ , i.e., $I_\theta^V = I_b$. On the other hand, the electric field vector for incoming horizontally polarized photons has components along a and c directions, with their relative weights depending on θ .

In order to obtain accurate details of the surface magnetic configuration and, more concretely, about the relative

orientation of the FM-bulk and AFM-surface axis, we have performed XLD measurements at different angles of incidence on a 9.4-nm-thick LSMO thin film. A magnetic field of 3 T aligns the LSMO magnetization along the beam propagation direction for all θ . Within these conditions, the FM axis is always orthogonal to the electric field vector of both V and H polarized beams such that the FM order does not contribute to the XLD measurement (Ref. [33] and Appendix A). The in-plane symmetry of LSMO implies that $I_a = I_b = I_{ab}$ such that $XLD_\theta = I_\theta^V - I_\theta^H = I_{ab} - I_\theta^H$.

Figure 1(b) shows the temperature dependence of XLD_{30° . Given that XLD_{FM} is suppressed and $XLD_{OO} \ll XLD_{AFM}$ (see Appendix A) the temperature dependence of the XLD reflects that of the surface related [33–35] AFM phase. We also depict in Fig. 1(b) the temperature dependence of the x-ray magnetic circular dichroism (XMCD), see Appendix A. XMCD, being linearly dependent on the magnetization, is only sensitive to the FM bulk component of the film [44]. The close resemblance between both curves corroborates the antiferromagnetic origin of the obtained XLD signal.

C. X-ray linear dichroism: Angular dependence

Angular dependent XLD experiments have been done at the lowest possible temperature (4 K) in order to enhance the AFM contribution to the dichroic signal. As in the temperature dependence case, a magnetic field of 3 T has been applied along the beam propagation direction in order to suppress the FM component. Under these conditions it can be shown [42] that $XLD_\theta \propto \cos^2 \phi$ where ϕ is the angle between \mathbf{E} and the AFM axis.

Based on XLD measurements restricted to one or two values of θ , the existence of an AFM surface layer with magnetization axis orthogonal to the sample surface on LSMO has been previously reported [33–35]. If this were the case, XLD_θ would be a 180° periodic curve as that depicted in Fig. 2 (blue dot-dashed line) with maximum XLD at $\theta = 0^\circ$. Likewise, an in-plane AFM orientation would show identical periodicity but shifted by 90° (black dashed line). An intermediate case where the AFM axis is tilted by an angle γ with respect to the sample's normal would lead to a curve shifted by γ . The experimentally measured angular dependence of the XLD shows none of these angular dependences (red dots on Fig. 2).

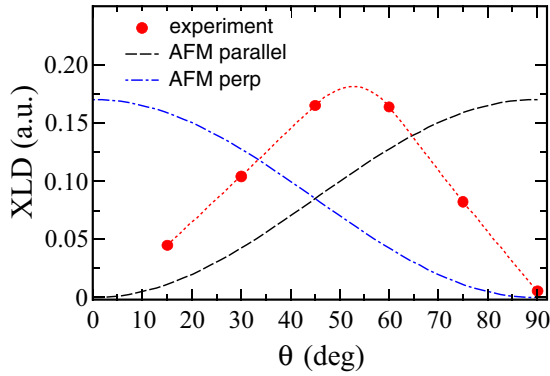


FIG. 2. Experimentally measured angular dependence of the XLD (red dots) at the Mn L_2 edge for a thin (9.4 nm) LSMO thin film. The dotted line is a guide to the eye. For comparison, we show the expected XLD angular dependent behavior for the case of AFM order with magnetic axis oriented parallel (dashed black) or orthogonal (dashed-dotted blue) to the surface plane of the sample.

Indeed, we find that XLD_{AFM} increases from $XLD \sim 0$ at gracing incidence ($\theta = 0^\circ$) towards a maximum at $45^\circ < \theta < 60^\circ$ followed by a decrease back towards $XLD \sim 0$ for ($\theta = 90^\circ$). This behavior also excludes a scenario where the angle defined by the AFM and FM axis is the same for all θ as in that case we would expect XLD_θ to be constant. Hence we conclude that the relative orientations between (i) the AFM and the FM axis and (ii) the AFM axis and the surface plane of the sample depend on the angle at which the magnetic field is applied. Namely, the AFM axis is collinear to the FM one ($XLD \sim 0$) only for $\theta = 0^\circ$ (FM and AFM in-plane) and for $\theta = 90^\circ$ (FM and AFM fully out-of-plane). For intermediate angles, the FM and AFM axis are not collinear ($XLD \neq 0$), have an out-of-plane component, and their relative orientation depends on θ .

D. Model and calculations

The experimental data in Fig. 2 cannot be explained within the standard model for manganites involving FM double exchange, AFM superexchange interactions and Jahn-Teller dis-

tortions as within this model the AFM ordering axis is always collinear with the bulk FM one, i.e., XLD_θ would be constant. A canting of the AFM axis due to the Dzyaloshinskii-Moriya interaction (DMI) [45,46] derived as a relativistic correction to superexchange [46] $\mathbf{D}_{ij} \cdot (\mathbf{S}_i \times \mathbf{S}_j)$ is not plausible either. Note that the inversion symmetry breaking with respect to the x - y surface would involve a vector coupling $(0, 0, D_z)$, which cannot give rise to a canting of the magnetic order axis in the z direction, as observed in the experiment.

To find the physical origin that explains the observed angular dependence of the XLD, we consider a model that incorporates (i) the kinetic energy through the double exchange interaction [47] which includes the two e_g orbitals [20] with hoppings given by the Slater-Koster parametrization, [48] (ii) the long-range Coulomb interaction between charges in the system, which affects the redistribution of charge close to the surface [22], and (iii) the SOC between the e_g orbitals (Ref. [30] and Appendix B). We checked that Jahn-Teller coupling, which is expected not to be important in $La_{2/3}Sr_{1/3}MnO_3$, cannot explain the observations and was therefore disregarded. We also neglected the lattice buckling on the surface [49] as its effect on the hoppings [48,50] is estimated to be much smaller than the effect of the broken inversion symmetry. In the model we use a one-atomic-plane thick surface, with a total of twelve atomic layers and periodic boundary conditions. All energies are given in units of t , the hopping parameter. The hopping processes are orbital dependent and anisotropic, with $x^2 - y^2$ producing a 2D band in the ab plane and $3z^2 - r^2$ having a larger hopping along the c direction. The SOC between the e_g orbitals occurs as a second-order process which involves the t_{2g} orbitals [30]

$$H_{SOC} = g \begin{pmatrix} 3 \cos^2(\theta_{mag}) & \sqrt{3} \cos^2(\theta_{mag}) \\ \sqrt{3} \cos^2(\theta_{mag}) & \cos^2(\theta_{mag}) + 4 \sin^2(\theta_{mag}) \end{pmatrix} \quad (1)$$

with θ_{mag} being the magnetic moment angle with respect to the surface plane and g the second order spin-orbit coupling. We only consider H_{SOC} at the surface. By itself, H_{SOC} adds a small shift ($\propto g$) to the onsite energies in such a way that, at the surface, the $3z^2 - r^2$ orbital is shifted down for $\theta_{mag} = 0$, while $x^2 - y^2$ is shifted down for $\theta_{mag} = \pi/2$. The bulk FM

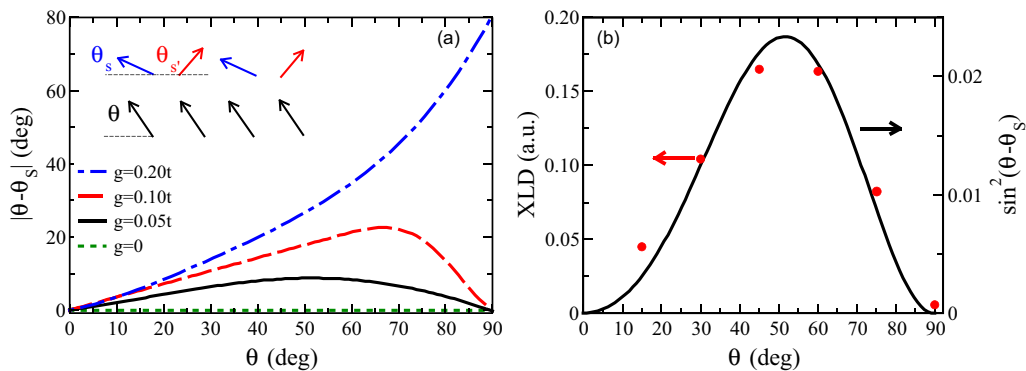


FIG. 3. (a) Predicted misalignment between the FM and AFM axis $|\theta - \theta_s|$ vs θ for different values of the interfacial SOC g . (Inset) Sketch of the spins showing the angle between the bulk FM (θ) and surface AFM (θ_s, θ'_s) axis with respect to the sample's surface. The ground state for the surface gives $\theta'_s = \theta_s + \pi$. (b) Comparison of the experimentally measured (red dots) and the predicted (solid line) XLD angular dependence for $g = 0.05t$.

ordering axis θ_{mag} is fixed by a large magnetic field (3 T in the experiment) applied along the beam propagation direction θ [see Fig. 1(a)] such that $\theta_{\text{mag}} = \theta$. For modeling the film surface, its spins are considered to be in two interpenetrating sublattices, such that all first nearest neighbors of one sublattice are on the complementary one, and allow the spins to rotate with angles θ_s and θ'_s , respectively, see inset of Fig. 3(a). The spin configuration with the lowest energy corresponds to $\theta'_s = \theta_s + \pi$, i.e., an AFM surface. The AFM order at the surface comes about because the boundary conditions on the surface [22,51,52], suppressing the FM interaction generated by the double exchange mechanism [20]. Moreover, in a (001) surface, the $x^2 - y^2$ orbital is not connected to the bulk (the hopping in the c direction is zero) and hence the $3z^2 - r^2$ orbital is preferentially occupied.

We calculate the energy of the system as a function of the orientations of the FM bulk θ and the AFM surface for different values of the SOC g . The resulting noncollinearity or misalignment between both angles $|\theta - \theta_s|$ is plotted as a function of θ in Fig. 3(a).

III. DISCUSSION

Our theoretical results show that for $g = 0$, the bulk FM ordering and the surface induced AFM ordering are collinear, namely, $\theta = \theta_s$, for all values of θ . For $0.05t \leq g \leq 0.1t$, $|\theta - \theta_s|$ varies continuously as a function of θ with a maximum at an intermediate angle between 0° and 90° which depends on g . Hence, for $0.05t \leq g \leq 0.1t$, the spins on the surface still rotate but the AFM ordering axis is not collinear with the bulk FM one and the relative angle is a function of θ . This relative tilting of the AFM ordering axis occurs due to the subtle competition between the collinear axis favored by the double exchange plus Coulomb terms and the small relative angle favored by the enhanced SOC. For even larger g , the AFM ordering axis on the surface is stuck to a small angle (θ_s) with respect to the surface plane in order to keep on favoring the occupation of the $3z^2 - r^2$ orbital.

An AFM ordering axis tilted by θ_s with respect to the sample surface leads to a linear dichroic signal $\text{XLD}_\theta = I_{ab} - I_\theta^H \propto \cos^2 \phi = \sin^2(\theta - \theta_s)$. Figure 3(b) shows the predicted $\sin^2(\theta - \theta_s)$ versus θ dependence for the $g = 0.05t$ case (solid curve) together with the experimentally measured angular dependence of XLD (dots) showing an excellent qualitative agreement. The values of g required to reproduce the experimental results amount (considering $t \sim 0.2\text{--}0.5$ eV) to $\sim 0.01\text{--}0.025$ eV. These values are significantly larger than the estimate $g = \lambda^2/\Delta = 0.001$ eV. An increase of g by at least one order of magnitude can not be solely explained by the decrease of the $t_{2g} - e_g$ splitting Δ that may take place at the interface [53]. The SOC effective enhancement is likely due to a Rashba spin-orbit contribution produced by the electric field caused by the redistribution of charge near the interface (electronic reconstruction) [22,51,52].

Spin-orbit coupling is behind many of the effects observed in manganites like the anomalous Hall effect [31] or anisotropic magnetoresistance [30,32]. However, in those cases, the observations could be explained with the usually assumed small value for SOC. Our observation of an unusually large SOC implies that a Rashba-like DMI [4,54] could

be present giving rise to complex spin textures like skyrmions and spirals on manganite surfaces. The large SOC could also explain the large tunneling anisotropic magnetoresistance measured in a related device [55]. Similar ideas have been proposed for the magnetic metallic gas formed at interfaces in $\text{LaAlO}_3/\text{SrTiO}_3$ heterostructures, a system in which Rashba spin-orbit coupling can be tuned [56], and the magnetic order has been argued to be a long wave-length spiral [3]. The case of manganite heterostructures is potentially more interesting due to the variability of magnetic orders they can sustain.

IV. CONCLUSION

In summary, we have performed x-ray linear dichroism measurements as a function of the incidence angle that reveal an antiferromagnetic order at the surface of a ferromagnetic and metallic $\text{La}_{2/3}\text{Sr}_{1/3}\text{MnO}_3$ thin film. The antiferromagnetic order axis is noncollinear to the ferromagnetic bulk one. This result can only be explained by introducing a significant spin-orbit coupling, much larger than previously assumed for manganites. This large spin-orbit coupling implies that manganite surfaces or interfaces, where the inversion symmetry is broken, might constitute a new scenario for the appearance of nontrivial spin textures, opening, in this way, a new avenue for exploration and applications of manganite heterostructures.

ACKNOWLEDGMENTS

The experimental research leading to these results has received funding from the European Community's Seventh Framework Programme (FP7/2007-2013) under Grant Agreement No. 312284. M.J.C. and L.I.B. acknowledge funding from Ministerio de Economía, Industria y Competitividad MEIC (Spain) via Grant No. FIS2015-64654-P. Z.K. thanks Project III45018 from the Ministry of Education and Science of Republic of Serbia. L.L.-M., B.M. and L.I.B. thanks MEIC through the Severo Ochoa Programme for Centres of Excellence in R&D (SEV-2015-0496) and MAT2015-71664-R.

S.V. and M.J.C. have contributed equally to this work.

APPENDIX A: SAMPLE CHARACTERIZATION

High-quality $\text{La}_{2/3}\text{Sr}_{1/3}\text{MnO}_3$ thin films with thickness ranging between 1.5 and 45 nm have been deposited on top of (001)-oriented SrTiO_3 (STO) substrates by means of magnetron sputtering [36]. The spectroscopic characterization of these samples (below) shows results in agreement with previous reports; (i) depressed magnetic properties as film thickness is reduced [37], (ii) a progressive change from a preferential $3z^2 - r^2$ orbital occupation for thinner ($t_{\text{LSMO}} \leq 2.3$ nm) to a $x^2 - y^2$ one for thicker ($t_{\text{LSMO}} \geq 3.5$ nm) films [38–40], (iii) vanishingly small orbital contribution to the XLD at temperatures below the magnetic transition temperature (i.e., $\text{XLD} \simeq \text{XLD}_{\text{AFM}}$) [33], and (iv) robust XLD_{AFM} component not depending on deviations of the nominal $\text{Mn}^{3+}/\text{Mn}^{4+}$ composition [34,35,39,57]. In this manuscript, we focus on the 9.4-nm-thick sample, with magnetic and electric properties very similar to the bulk ones.

X-ray spectroscopic measurements. XAS (x-ray absorption spectroscopy), XMCD (x-ray magnetic circular dichroism), and XLD (x-ray linear dichroism) have been measured across

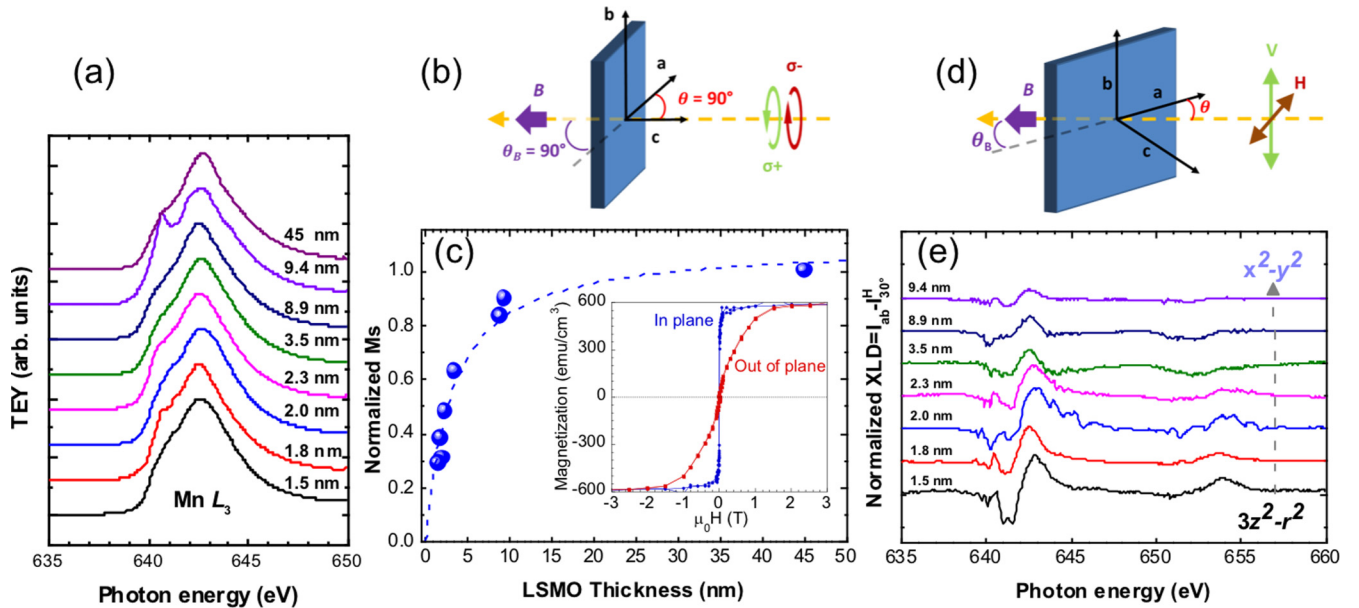


FIG. 4. (a) Mn L_3 -edge XAS vs LSMO thin film thickness. The 45-nm sample shows bulk like spectral shape. Decreasing the film thickness leads to an enhancement of the spectral weight at the low-energy side of the L_3 spectral feature related to the increase of a Mn^{3+} component. The 9.4-nm sample shows a clear peak at approximately 641 eV related to the presence of Mn^{2+} . (b) Sketch of the experimental setup used for the XMCD measurements. (c) (Main panel) Normalized spin contribution to the magnetic moment “(Ms)” of Mn vs thickness as deduced from the application of the sum rules to the XMCD spectra obtained at normal incidence at 5 K and $H = 3$ T. Data have been normalized to the magnetization obtained for the thicker bulklike film. (Inset) Magnetic hysteresis loops obtained at $T = 10$ K for magnetic fields applied parallel and orthogonal to the sample plane. (d) Sketch of the experimental setup used for the XLD measurements. (e) Orbital contribution to the XLD obtained at 350 K. At low thicknesses, the sign and shape of the XLD at the Mn L_2 -edge indicates a preferential $3z^2 - r^2$ orbital occupancy. Increasing the thickness leads to the observation of an XLD compatible with a preferential $x^2 - y^2$ orbital occupation.

the Mn $L_{2,3}$ edges. Surface sensitivity is gained when the data are acquired by using the total electron yield (TEY) mode. The XMCD, proportional to the projection of the magnetization along the beam propagation direction, is obtained by calculating the difference between the spectrum measured with incoming right (σ^+) and left (σ^-) helicity circularly polarized beams and is defined as $XMCD = \sigma^+ - \sigma^-$, see Fig. 4(b). The data have been acquired at normal incidence ($\theta = 90^\circ$) and with a 3-T magnetic field applied along the beam propagation direction. The XAS spectra have been computed from $XAS = \sigma^+ + \sigma^-$.

XLD spectra is defined as the difference in absorption between vertical (V) and horizontal (H) polarized radiation at a grazing incidence angle θ , i.e., $XLD_\theta = I_\theta^V - I_\theta^H$, see Fig. 4(d). The angle of incidence of the beam with respect to the sample surface has been changed by rotating the sample along its b axis [see Fig. 4(b)]. The relative weight of the orbital (XLD_{OO}), ferromagnetic (XLD_{FM}), and antiferromagnetic (XLD_{AFM}) contributions to the total XLD signal depends on temperature and on the applied magnetic field. At temperatures above the Curie one (T_C) the only contribution to the XLD, as long as the AFM ordering has a critical temperature below T_C , is due to the orbital occupancy, i.e., $XLD = XLD_{OO}$. At temperatures below T_C , both FM and AFM contributions are also present, i.e., $XLD = XLD_{OO} + XLD_{FM} + XLD_{AFM}$. A magnetic field of 3 T, strong enough to saturate the magnetization of the sample along the beam propagation direction, has been applied during XLD acquisition so that the XLD_{FM} component can be canceled. This

cancellation takes place because within these conditions the FM axis is forced to be along the beam propagation direction independently of θ , hence being orthogonal to the electric field vector of both V and H polarized beams. In that case, $XLD = XLD_{OO} + XLD_{AFM}$.

Spectroscopic results. Mn valence. Compared to the other thin films studied by our group, the XAS measurement for the 9.4-nm-thick sample presents a shoulder at approximately 641 eV, see Fig. 4(a), which is most likely due to the presence of Mn^{2+} (Refs. [34,58–60]). Previous results have shown that Mn^{2+} can originate as resulting of a deoxygenation process related to preexisting structural defects [57–60], which might lead to a time-dependent formation of divalent Mn [59]. Indeed, the 9.4-nm sample is the oldest of the whole set. Importantly, previous resonant photoemission experiments have shown the strong localization of Mn^{2+} and have excluded its interaction with the major Mn mixed valence Mn^{3+}/Mn^{4+} phase [58]. Moreover, recent results have shown that the spectral shape of the XLD, both at $T > T_C$ and $T < T_C$, is not affected by the presence of Mn^{2+} [35]. Indeed, our XLD spectra for 45-, 9.4-, and 8.9-nm-thick films have the same overall shape, see Fig. 5.

Ferromagnetic properties. The ferromagnetic properties of the films have been characterized by means of XMCD experiments at 4 K, i.e., well within the FM phase of LSMO. As shown in the inset of Fig. 4(c), a field of 3 T is more than enough to magnetically saturate the sample, both in and out of plane. Application of the so-called sum rules [44,61] should allow for a precise quantitative determination of both

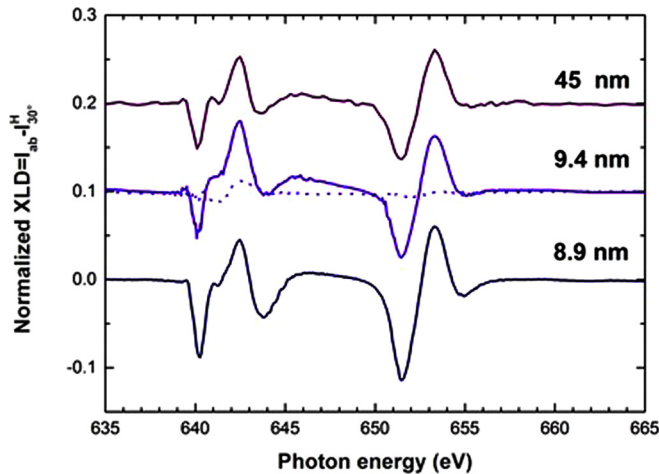


FIG. 5. XLD spectra obtained at 4 K with a magnetic field applied perpendicularly to the propagation direction of the incoming beam for samples with thickness 8.9, 9.4, and 45 nm (continuous lines). For comparison, we show the orbital contribution for the 9.4-nm sample (dotted line). The low-temperature XLD is similar in all cases and does not depend on the presence of other Mn oxidation states besides that of the mixed $\text{Mn}^{3+}/\text{Mn}^{4+}$ valence one.

spin (m_s) and orbital moments (m_l) of the element under investigation as long as the intermixing of the L_3 and L_2 parts of the spectrum is negligible [44]. Although this is not the case of Mn [62] a relative comparison is possible. Figure 4(c) shows the calculated spin magnetic moment as function of thickness normalized to that of the thicker sample. As expected, and due to the presence of non-FM layers at the interfaces of LSMO there is a strong reduction of the magnetization as the film is decreased with a thickness dependency akin to that measured by macroscopic magnetometry methods [37]. We note that the 9.4-nm sample, in spite of the presence of a minor Mn^{2+} phase, shows a normalized ms close to that of the thicker 45-nm film.

Orbital occupation. X-ray linear dichroism experiments at $\theta = 30^\circ$ and $T = 350$ K have been used to characterize the preferential orbital occupation as function of thickness, i.e., $\text{XLD}_{\text{OO}} = I^V - I^H = I_{ab} - I_{30^\circ}^H$, see Fig. 4(d). A magnetic field of 3 T has been applied along the beam propagation direction to suppress any spurious FM contribution to the XLD as the magnetization is saturated and aligned orthogonally to the electric field vector of the incoming radiation [see Fig. 4(d)]. Similarly to previous reports, we observe a change in the sign of the L_2 spectral weight as film thickness is reduced thus, highlighting a change from a preferential $3z^2 - r^2$ orbital occupation for thinner ($t_{\text{LSMO}} \leq 2.3$ nm) to a $x^2 - y^2$ one for thicker ($t_{\text{LSMO}} \geq 3.5$ nm) films, see Fig. 4(e).

Low temperature XLD data were obtained at 4 K. As in the case of the high-temperature data, a magnetic field of 3 T was applied along the propagation direction in order to remove the FM contribution to the XLD, hence $\text{XLD} = \text{XLD}_{\text{OO}} + \text{XLD}_{\text{AFM}}$. Only films with $t_{\text{LSMO}} \geq 3.5$ nm show an XLD strongly differing from that measured at 350 K (not shown), likely related to depressed magnetic properties for thinner films [37]. Selected XLD spectra, normalized to the maximum of the XAS L_3 spectral feature for the 8.9-, 9.4-, and 45-nm

samples are depicted in Fig. 5. As a comparison we also plot the XLD obtained at 350 K for the 9.4-nm sample originating from the orbital occupation (XLD_{OO}). The AFM contribution clearly dominates, i.e., at temperatures below the magnetic ordering temperature $\text{XLD} \approx \text{XLD}_{\text{AFM}}$. This is further supported by the similar temperature dependence of both XLD and XMCD for that sample, see Fig. 1(b) in the main text.

Experimental angular dependence of the XLD. The angular dependence of the XLD has been measured for $15^\circ \leq \theta \leq 90^\circ$. As in previous studies [33–35,39], the XLD analysis has focused on the L_2 spectral region where saturation effects [63] and possible off-stoichiometry effects [35] are minimized. Saturation effects, accounting for artificial changes in the absorption due to the angular dependence of the x-ray probing depth, has nonetheless been corrected [40] by using an electron probing depth for TEY of 2.7 nm for LSMO [64]. Figure 2 in the main text shows the angular dependency of XLD at a given energy across the Mn L_2 edge (653.3 eV). In agreement with other studies previously published [35,39] selecting another energy and/or integrating the XLD signal leads to similar results.

APPENDIX B: THEORETICAL MODELING

The double exchange model H_{DE} is the kinetic energy of a system in which an infinite Hund's coupling between the localized and itinerant carriers forces their spins to be parallel. This model explains the correlation between half-metallic behavior and ferromagnetic order in the optimal doped ($x = 1/3$) manganites. It can be written

$$H_{\text{DE}} = \sum_{i,j,\alpha,\beta} t_{i,j}^{\alpha,\beta} d_{i\alpha}^\dagger d_{j\beta} \quad (\text{B1})$$

with t the hopping parameter, i and j neighboring Mn sites, and orbital indices representing either $3z^2 - r^2$ or $x^2 - y^2$, and d the construction/destruction operators. This is a spinless term as the spin of the carriers has been projected on the local spin ($S = 3/2$), which corresponds to the three electrons that occupy the t_{2g} orbitals. The hoppings depend on the relative orientation of the neighboring spins as $\cos(\theta_{ij})$ and on the orbitals involved [52],

$$\begin{aligned} t_{x(y)}^{x^2-y^2, x^2-y^2} &= \pm \sqrt{3} t_{x(y)}^{x^2-y^2, 3z^2-r^2} = 3 t_{x(y)}^{3z^2-r^2, 3z^2-r^2} \\ &= \frac{3}{4} t_z^{3z^2-r^2, 3z^2-r^2} = t, \\ t_z^{x^2-y^2, x^2-y^2} &= 0, \end{aligned} \quad (\text{B2})$$

where the subindices x , y , and z refer to the directions in the lattice. In order to model the surface, it is important to include the long-range Coulomb interaction H_{Coul} between the charges in the system as we expect the charge to redistribute close to the surface. This term is included at the Hartree level [22]

$$\begin{aligned} H_{\text{Coul}} &= \frac{e^2}{\epsilon} \sum_{i \neq j} \left(\frac{1}{2} \frac{\langle n_i \rangle \langle n_j \rangle}{|\mathbf{R}_i - \mathbf{R}_j|} + \frac{1}{2} \frac{Z_i Z_j}{|\mathbf{R}_i^A - \mathbf{R}_j^A|} \right. \\ &\quad \left. - \frac{Z_i \langle n_j \rangle}{|\mathbf{R}_i^A - \mathbf{R}_j|} \right) \end{aligned} \quad (\text{B3})$$

with R_i the position of the Mn ions, n_i the occupation number on the Mn i site, eZ_i the charge of the A cation located at R_i^A , and ϵ the dielectric constant of the material. The relative strength of the Coulomb interaction is given by the parameter

$\alpha = e^2/at$, with a the lattice parameter. Here we use $\alpha = 1$. We also consider the spin-orbit interaction H_{SOC} between the e_g orbitals [30] [see Eq. (1)], which takes place through the t_{2g} orbitals.

-
- [1] U. K. Roszler, A. N. Bogdanov, and C. Pfleiderer, *Nature (London)* **442**, 797 (2006).
- [2] M. Bode, M. Heide, K. von Bergmann, P. Ferriani, S. Heinze, G. Bihlmayer, A. Kubetzka, O. Pietzsch, S. Blügel, and R. Wiesendanger, *Nature (London)* **447**, 190 (2007).
- [3] S. Banerjee, O. Erten, and M. Randeria, *Nat. Phys.* **9**, 625 (2013).
- [4] S. Banerjee, J. Rowland, O. Erten, and M. Randeria, *Phys. Rev. X* **4**, 031045 (2014).
- [5] X. Li, W. V. Liu, and L. Balents, *Phys. Rev. Lett.* **112**, 067202 (2014).
- [6] A. Soumyanarayanan, N. Reyren, A. Fert, and C. Panagopoulos, *Nature (London)* **539**, 509 (2016).
- [7] A. Fert, N. Reyren, and V. Cros, *Nat. Rev. Mater.* **2**, 17031 (2017).
- [8] S. Woo, K. Litzius, B. Krüger, M.-Y. Im, L. Caretta, K. Richter, M. Mann, A. Krone, R. M. Reeve, M. Weigand *et al.*, *Nat. Mater.* **15**, 501 (2016).
- [9] D. Maccariello, W. Legrand, N. Reyren, K. Garcia, K. Bouzouhane, S. Collin, V. Cros, and A. Fert, *Nat. Nanotechnol.* **13**, 233 (2018).
- [10] I. Gross, W. Akhtar, V. Garcia, L. J. Martínez, S. Chouaieb, K. Garcia, C. Carrétéro, A. Barthélémy, P. Appel, P. Maletinsky *et al.*, *Nature (London)* **549**, 252 (2017).
- [11] S. Mühlbauer, B. Binz, F. Jonietz, C. Pfleiderer, A. Rosch, A. Neubauer, R. Georgii, and P. Böni, *Science* **323**, 915 (2009).
- [12] W. Münzer, A. Neubauer, T. Adams, S. Mühlbauer, C. Franz, F. Jonietz, R. Georgii, P. Böni, B. Pedersen, M. Schmidt *et al.*, *Phys. Rev. B* **81**, 041203 (2010).
- [13] X. Z. Yu, Y. Onose, N. Kanazawa, J. H. Park, J. H. Han, Y. Matsui, N. Nagaosa, and Y. Tokura, *Nature (London)* **465**, 901 (2010).
- [14] S. Heinze, K. von Bergmann, M. Menzel, J. Brede, A. Kubetzka, R. Wiesendanger, G. Bihlmayer, and S. Blügel, *Nat. Phys.* **7**, 713 (2011).
- [15] X. Z. Yu, N. Kanazawa, Y. Onose, K. Kimoto, W. Z. Zhang, S. Ishiwata, Y. Matsui, and Y. Tokura, *Nat. Mater.* **10**, 106 (2011).
- [16] T. Adams, A. Chacon, M. Wagner, A. Bauer, G. Brandl, B. Pedersen, H. Berger, P. Lemmens, and C. Pfleiderer, *Phys. Rev. Lett.* **108**, 237204 (2012).
- [17] S. Seki, X. Z. Yu, S. Ishiwata, and Y. Tokura, *Science* **336**, 198 (2012).
- [18] N. Romming, C. Hanneken, M. Menzel, J. E. Bickel, B. Wolter, K. von Bergmann, A. Kubetzka, and R. Wiesendanger, *Science* **341**, 636 (2013).
- [19] A. B. Butenko, A. A. Leonov, U. K. Rößler, and A. N. Bogdanov, *Phys. Rev. B* **82**, 052403 (2010).
- [20] M. Calderón, L. Brey, and F. Guinea, *Phys. Rev. B* **60**, 6698 (1999).
- [21] J. Chakhalian, J. W. Freeland, G. Srajer, J. Stempffer, G. Khaliullin, J. C. Cezar, T. Charlton, R. Dalgliesh, C. Bernhard, G. Cristiani *et al.*, *Nat. Phys.* **2**, 244 (2006).
- [22] L. Brey, *Phys. Rev. B* **75**, 104423 (2007).
- [23] Z. Sefrioui, C. Visani, M. J. Calderón, K. March, C. Carrétéro, M. Walls, A. Rivera-Calzada, C. León, R. López Antón, T. Charlton *et al.*, *Adv. Mater.* **22**, 5029 (2010).
- [24] P. Zubko, S. Gariglio, M. Gabay, P. Ghosez, and J.-M. Triscone, *Annu. Rev. Condens. Matter Phys.* **2**, 141 (2011).
- [25] H. Y. Hwang, Y. Iwasa, M. Kawasaki, B. Keimer, N. Nagaosa, and Y. Tokura, *Nat. Mater.* **11**, 103 (2012).
- [26] J. H. Ngai, F. Walker, and C. Ahn, *Annu. Rev. Mater. Res.* **44**, 1 (2014).
- [27] Z. Liao, M. Huijben, Z. Zhong, N. Gauquelin, S. Macke, R. J. Green, S. V. Aert, J. Verbeeck, G. V. Tendeloo, K. Held *et al.*, *Nat. Mater.* **14**, 425 (2016).
- [28] O. Jaoul, I. Campbell, and A. Fert, *J. Magn. Magn. Mater.* **5**, 23 (1977).
- [29] A. P. Malozemoff, *Phys. Rev. B* **34**, 1853 (1986).
- [30] J. D. Fuhr, M. Granada, L. B. Steren, and B. Alascio, *J. Phys.: Condens. Matter* **22**, 146001 (2010).
- [31] M. J. Calderón and L. Brey, *Phys. Rev. B* **63**, 054421 (2001).
- [32] N. M. Nemes, M. J. Calderón, J. I. Beltrán, F. Y. Bruno, J. García-Barriocanal, Z. Sefrioui, C. León, M. García-Hernández, M. C. M. Muñoz, L. Brey *et al.*, *Adv. Mater.* **26**, 7516 (2014).
- [33] C. Aruta, G. Ghiringhelli, V. Bisogni, L. Braicovich, N. B. Brookes, A. Tebano, and G. Balestrino, *Phys. Rev. B* **80**, 014431 (2009).
- [34] S. Valencia, L. Peña, Z. Konstantinovic, Ll. Balcells, R. Galceran, D. Schmitz, F. Sandiumenge, M. Casanove, and B. Martínez, *J. Phys.: Condens. Matter* **26**, 166001 (2014).
- [35] D. Pesquera, A. Barla, M. Wojcik, E. Jedryka, F. Bondino, E. Magnano, S. Nappini, D. Gutiérrez, G. Radaelli, G. Herranz *et al.*, *Phys. Rev. Appl.* **6**, 034004 (2016).
- [36] Z. Konstantinovic, J. Santiso, D. Colson, A. Forget, Ll. Balcells, and B. Martinez, *J. Appl. Phys.* **105**, 063919 (1999).
- [37] F. Sandiumenge, J. Santiso, Ll. Balcells, Z. Konstantinovic, J. Roqueta, A. Pomar, J. P. Espinós, and B. Martínez, *Phys. Rev. Lett.* **110**, 107206 (2013).
- [38] A. Tebano, C. Aruta, S. Sanna, P. G. Medaglia, G. Balestrino, A. A. Sidorenko, R. De Renzi, G. Ghiringhelli, L. Braicovich, V. Bisogni *et al.*, *Phys. Rev. Lett.* **100**, 137401 (2008).
- [39] D. Pesquera, G. Herranz, A. Barla, E. Pellegrin, F. Bondino, E. Magnano, F. Sanchez, and J. Fontcuberta, *Nat. Commun.* **3**, 1189 (2012).
- [40] B. Cui, C. Song, F. Li, G. Y. Wang, H. J. Mao, J. J. Peng, F. Zeng, and F. Pan, *Sci. Rep.* **4**, 4206 (2014).
- [41] A. Baena, L. Brey, and M. J. Calderón, *Phys. Rev. B* **83**, 064424 (2011).
- [42] J. Lüning, F. Nolting, A. Scholl, H. Ohldag, J. W. Seo, J. Pompeyrine, J.-P. Locquet, and J. Stöhr, *Phys. Rev. B* **67**, 214433 (2003).

- [43] Y. Liu and X. Ke, *J. Phys.: Condens. Matter* **27**, 373003 (2015).
- [44] P. Carra, B. T. Thole, M. Altarelli, and X. Wang, *Phys. Rev. Lett.* **70**, 694 (1993).
- [45] I. Dzyaloshinsky, *J. Phys. Chem. Solids* **4**, 241 (1958).
- [46] T. Moriya, *Phys. Rev.* **120**, 91 (1960).
- [47] C. Zener, *Phys. Rev.* **82**, 403 (1951).
- [48] J. C. Slater and G. F. Koster, *Phys. Rev.* **94**, 1498 (1954).
- [49] J. M. Pruneda, V. Ferrari, R. Rurali, P. B. Littlewood, N. A. Spaldin, and E. Artacho, *Phys. Rev. Lett.* **99**, 226101 (2007).
- [50] I. A. Sergienko, C. Şen, and E. Dagotto, *Phys. Rev. Lett.* **97**, 227204 (2006).
- [51] J. Salafranca, M. J. Calderón, and L. Brey, *Phys. Rev. B* **77**, 014441 (2008).
- [52] M. J. Calderón, J. Salafranca, and L. Brey, *Phys. Rev. B* **78**, 024415 (2008).
- [53] J. D. Burton and E. Y. Tsybal, *Phys. Rev. B* **93**, 024419 (2016).
- [54] A. Kundu and S. Zhang, *Phys. Rev. B* **92**, 094434 (2015).
- [55] R. Galceran, Ll. Balcells, A. Pomar, Z. Konstantinović, N. Bagués, F. Sandiumenge, and B. Martínez, *AIP Adv.* **6**, 045305 (2016).
- [56] A. D. Caviglia, M. Gabay, S. Gariglio, N. Reyren, C. Cancellieri, and J.-M. Triscone, *Phys. Rev. Lett.* **104**, 126803 (2010).
- [57] M. P. de Jong, I. Bergenti, W. Osikowicz, R. Friedlein, V. A. Dediu, C. Taliani, and W. R. Salaneck, *Phys. Rev. B* **73**, 052403 (2006).
- [58] M. P. de Jong, I. Bergenti, V. A. Dediu, M. Fahlman, M. Marsi, and C. Taliani, *Phys. Rev. B* **71**, 014434 (2005).
- [59] S. Valencia, A. Gaupp, W. Gudat, Ll. Abad, Ll. Balcells, A. Cavallaro, B. Martinez, and F. J. Palomares, *Phys. Rev. B* **73**, 104402 (2008).
- [60] S. Valencia, A. Gaupp, W. Gudat, Ll. Abad, Ll. Balcells, and B. Martinez, *Phys. Rev. B* **75**, 184431 (2007).
- [61] B. T. Thole, P. Carra, F. Sette, and G. van der Laan, *Phys. Rev. Lett.* **68**, 1943 (1992).
- [62] P. Crocombette, B. T. Thole, and F. Jolet, *J. Phys.: Condens. Matter* **8**, 4095 (1996).
- [63] R. Nakajima, J. Stöhr, and Y. U. Idzerda, *Phys. Rev. B* **59**, 6421 (1999).
- [64] A. Ruosi, C. Raisch, A. Verna, R. Werner, B. A. Davidson, J. Fujii, R. Kleiner, and D. Koelle, *Phys. Rev. B* **90**, 125120 (2014).

The Misfit Dislocation Core Phase in Complex Oxide Heteroepitaxy

Núria Bagués, José Santiso, Bryan D. Esser, Robert E. A. Williams, Dave W. McComb, Zorica Konstantinovic, Lluís Balcells, and Felip Sandiumenge*

Misfit dislocations form self-organized nanoscale linear defects exhibiting their own distinct structural, chemical, and physical properties which, particularly in complex oxides, hold a strong potential for the development of nanodevices. However, the transformation of such defects from passive into potentially active functional elements necessitates a deep understanding of the particular mechanisms governing their formation. Here, different atomic resolution imaging and spectroscopic techniques are combined to determine the complex structure of misfit dislocations in the perovskite type $\text{La}_{0.67}\text{Sr}_{0.33}\text{MnO}_3/\text{LaAlO}_3$ heteroepitaxial system. It is found that while the position of the film–substrate interface is blurred by cation intermixing, oxygen vacancies selectively accumulate at the tensile region of the dislocation strain field. Such accumulation of vacancies is accompanied by the reduction of manganese cations in the same area, inducing chemical expansion effects, which partly accommodate the dislocation strain. The formation of oxygen vacancies is only partially electrically compensated and results in a positive net charge $q \approx +0.3 \pm 0.1$ localized in the tensile region of the dislocation, while the compressive region remains neutral. The results highlight a prototypical core model for perovskite-based heteroepitaxial systems and offer insights for predictive manipulation of misfit dislocation properties.

1. Introduction

Dislocation cores can be considered as distinct filamentary-like nanophases^[1,2] ubiquitous in crystalline solids and as such may severely impact their functional properties. Dislocations were conceptually conceived eight decades ago,^[3] even before they were observed in the transmission electron microscope.^[4] Knowledge of their chemical and structural properties has attained a high level of maturity in metals;^[5–7] however, their behavior in oxides still pose fundamental issues. The main differences between dislocations in metals and in oxides stem from the strong ionic character of the latter, making electrostatic interactions between their constituents crucial in determining the core structure and the distribution of dopants in the associated strain field, while in metals such effects are negligible.^[8,9] Particularly in the case of oxides, oxygen vacancies play an important role in the development of electrostatic interactions

and their formation has been recently the subject of several investigations. On the one hand, atomistic simulations show that oxygen vacancies accumulate at the undercoordinated structure of the dislocation core.^[10–13] Similar studies also indicate a significant decrease/increase of the vacancy formation energy at the tensile/compressive strained zones neighboring the sub-nanometer core,^[11,12] or a decrease in both zones.^[14] The coupling between strain and point defect formation is favored by volume changes that typically accompany the latter, and may lead to nonlinear effects deviating from the elastic behavior of the bulk equilibrium phase.^[15,16] In contrast with the formation of Cottrell atmospheres in metals, which can be modeled by the elastic interaction between a “misfitting” solute atom and a dislocation,^[17] dopant segregation around dislocation cores in oxides is determined by a complex interplay between elastic and electrostatic effects.^[12]


To date, the effect of dislocations on the performance of a variety of functional oxides has been documented, including high-temperature superconductors,^[18] catalysts,^[19] photovoltaics,^[20] thermoelectrics,^[21] ferroelectrics,^[22] and multiferroics.^[23] The recognition of this impact has motivated in recent years a strong interest on their complex core structures^[10,24,25] and particularly their ionic and electronic transport properties

Dr. N. Bagués, Dr. L. Balcells, Dr. F. Sandiumenge
Institut de Ciència de Materials de Barcelona
ICMAB-CSIC
Campus de la UAB
08193 Bellaterra, Catalonia, Spain
E-mail: felip@icmab.cat

Dr. N. Bagués, Dr. J. Santiso
Catalan Institute of Nanoscience and Nanotechnology (ICN2)
CSIC and BIST
Campus UAB
Bellaterra, 08193 Barcelona, Catalonia, Spain

B. D. Esser, Dr. R. E. A. Williams, Prof. D. W. McComb
Center for Electron Microscopy and Analysis
The Ohio State University
Columbus, OH 43212, USA

Dr. Z. Konstantinovic
Center for Solid State Physics and New Materials
Institute of Physics Belgrade
University of Belgrade
Pregrevica 118, 11080 Belgrade, Serbia

 The ORCID identification number(s) for the author(s) of this article can be found under <https://doi.org/10.1002/adfm.201704437>.

DOI: 10.1002/adfm.201704437

at the atomic level.^[10,12,26] The amazing complexity of the structural and functional behavior that dislocations can exhibit in complex oxides is exemplified by the $\mathbf{b} = [010]$ edge dislocation in SrTiO₃ (STO), which has been the object of renewed interest since redox-based resistive switching behavior associated to its core was reported.^[27] According to high resolution transmission electron microscopy (HRTEM), high angle annular dark field scanning TEM (HAADF-STEM) imaging, and electron energy loss spectroscopy (EELS) studies, its core is dissociated and deficient in strontium and oxygen.^[28–31] Moreover, a deficit in Sr has been shown to eventually induce a local transition to an face centered cubic (fcc) edge-sharing TiO₆ octahedral structure with a larger unit cell accommodating the tensile strain of the dislocation.^[29–31] Atomistic simulations, on the other hand, show that the experimentally observed dissociated core structure is only reproduced after removing an entire oxygen column from the undissociated core.^[10,32] This suggests that the transition between both configurations is primarily governed by oxygen stoichiometry and that the dissociated core corresponds to the thermodynamically stable oxygen deficient structure. Remarkably, the accumulation of oxygen vacancies at the sub-nanometer core also affects the defect chemistry of the neighboring material on length scales ranging from several tens to hundreds of nanometers through the formation of oxygen vacancy depleted space charge zones.^[10,11,32,33] Analogously to the behavior displayed by ferroelastic or ferroelectric domain walls, in which the localized strain may produce a variety of states not observed in the bulk phase,^[34] or even catalyze the formation of new phases with distinct physical and chemical properties,^[35] dislocation cores hold strong promise as potential discrete functional elements in perovskite oxides. However, unlike domain walls, which commonly form highly periodic patterns,^[36,37] the topological arrangement of dislocations is more difficult to control. One strategy to promote dislocation self-organization is to confine them onto the same crystallographic plane, where lateral order results from elastic interactions between neighboring lines, as it occurs at mismatched epitaxial heterointerfaces.^[38] Such misfit dislocations (MDs) are located at the interface bridging two different compounds and therefore their structure and chemical composition is expected to combine both of them. Despite the fact that the chemical and structural properties of MDs are even less understood than those of dislocations occurring in bulk crystals, recent reports highlight the strong potential of buried, laterally ordered MD networks in creating a variety of periodic strain-induced functional patterns in oxide thin films.^[39–41] For instance, the periodic strain field associated with MD networks has been proposed to induce interfacial modulations of charge density,^[39] and more recently reported to induce the formation ordered topographic nanostructures^[40,41] and electrical conduction patterns^[41] at free surfaces. These recent findings highlight the strong impact of MDs in a range of length scales, and motivate the analysis of the distinct chemical and structural states confined in their cores, here referred to as MD phase, in view of the development of dislocation-based nanostructures.

Prompted by the strong interest of MDs as spontaneously organized functional elements, in this work we investigate the MD phase in the La_{0.7}Sr_{0.3}MnO₃/LaAlO₃ (LSMO/LAO) epitaxial system to unveil the complex interplay between strain, chemical

composition, and electronic structure that governs its formation. We choose the compressive LAO substrate to induce the formation of MDs, because under a tensile strain (on STO substrates) the LSMO film relaxes by an octahedral tilting mechanism without dislocation formation.^[42] On the other hand, in the LSMO/LAO system, MD networks exhibit a high degree of order at relatively small thicknesses.^[43] Although chemical information from individual atomic columns in defect structures is commonly accessed by EELS,^[44,45] here we demonstrate the advantages of combining EELS, for electronic structure analysis, with energy dispersive X-ray (EDX) spectroscopy for elemental quantification, all at atomic resolution. On the one hand, since electronic delocalization scales inversely to the ionization energy, the much better efficiency of EDX in collecting X-ray signals from deep innershell ionizations in the incoherent imaging mode, makes EDX images more readily interpretable;^[46,47] on the other hand, the range of accessible elements by EDX is less restricted than in EELS as it allows elemental mapping over a wide range of ionization energies, making this technique particularly suited to the present work. However, recent work by Craven et al. suggests that EELS on edges up to 10 keV loss may be possible with improved microscope–spectrometer alignments.^[48] Our results indicate that the cationic distribution around the MD core is not solely dictated by elastic interactions, as reported for low aliovalent dopant concentrations in other oxides such as CeO₂^[12] or YBa₂Cu₃O₇,^[49] where larger cations are stabilized in the tensile regions of the dislocation strain field. The present results provide key elements for understanding the mechanisms governing the chemistry and electronic structure of MDs in complex oxides as a first step toward the design of laterally modulated functional heterointerfaces over a ≈20 nm length scale.

2. Results and Discussion

Figure 1a shows a cross-section high resolution HAADF image, viewed along the [100] zone axis, revealing dislocations at the interface between the LSMO film and the LAO substrate. The bottom panel is a (010)-Fourier filtered image pointing out the positions of the MDs. The extra half-plane resides in the substrate side to accommodate the −2.3% biaxial compressive mismatch. In the LSMO/LAO system, both crystal structures are polar, being described by the stacking of charged atomic layers along the [001] direction: Mn^{3.3+}O^{2−}₂ (−2/3e)/La³⁺_{0.7}Sr²⁺_{0.3}O^{2−}₂ (+2/3e) and Al³⁺O^{2−}₂ (−1e)/La³⁺O^{2−} (+1e), where the net charge per unit area in the atomic planes is given in parenthesis and e is the electron charge. The (001) surface of the LAO substrate is known to be reconstructed to screen the diverging electrostatic potential arising from the stacking of dipole moments perpendicular to the surface.^[50–52] Regardless of which type of (001) surface reconstruction is adopted by the LAO substrate, the LSMO/LAO interface introduces a polar discontinuity that can be screened either by moving electronic charges or ions.^[53] Elemental concentration profiles determined by EDX (see Figure S1, Supporting Information), obtained along the growth direction at positions in between MDs, indicate cation intermixing between the film and the substrate, and therefore interfacial charges are very likely avoided by chemical grading.^[53]

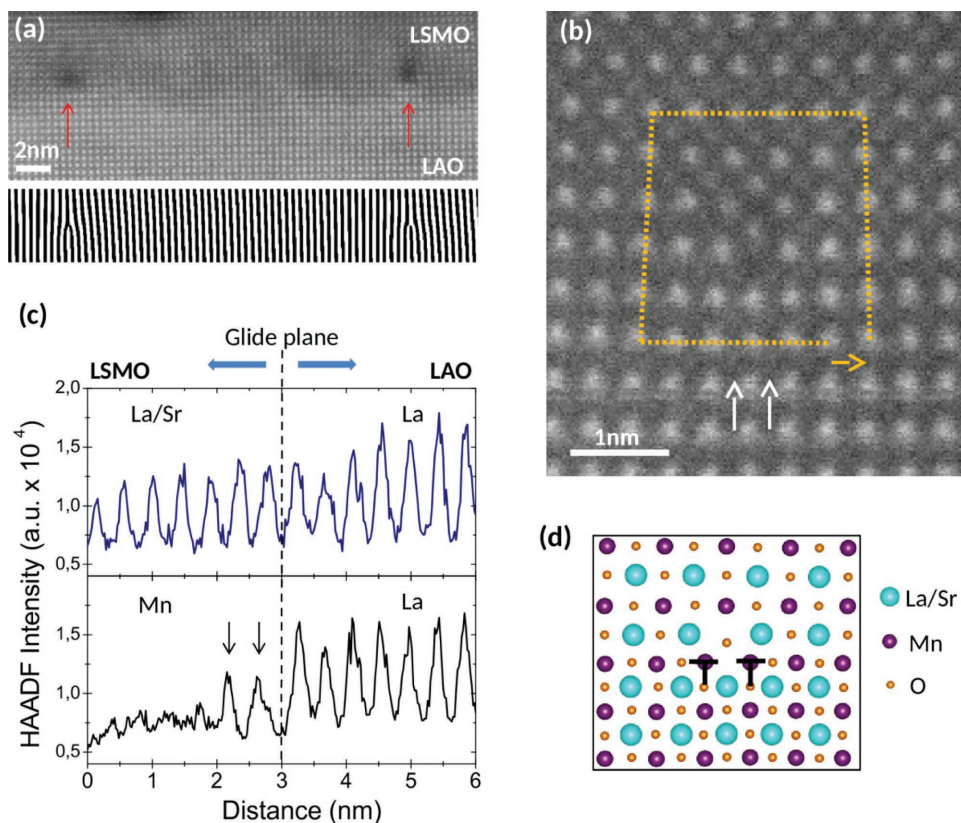


Figure 1. Misfit dislocations in partially relaxed LSMO/LAO thin films. a) Atomic resolution cross-sectional HAADF image, viewed along the [100] zone axis, of a 6 nm thick LSMO/LAO film. Vertical arrows indicate the position of misfit dislocations, seen as dark contrast. Bottom panel: Fourier filtered image using the (010) frequency to reveal the dislocations. b) Atomic resolution cross-sectional HAADF image, viewed along the [100] zone axis, of a misfit dislocation. The two arrows indicate the position of the two extra B-site/O (nominally Al/O) half-planes of the dissociated core. These planes are hardly visible in the HAADF image due to their lower atomic number. Dotted lines draw a Burgers circuit, with the yellow arrow signifying the Burgers vector $\mathbf{b} = a[010]$. c) Vertical intensity profiles taken along the axial plane containing the antiphase boundary (black) and an adjacent A-site (blue) atomic plane running through the dislocation core. The vertical line marks the position of the glide plane. The two arrows indicate the two positions next to the antiphase contact with enhanced intensity due to the replacement of Mn by heavier La atoms. d) Atomic model of the dislocation core.

Figure S1 of the Supporting Information clearly shows that for B-site cations in the ABO_3 perovskite (Mn, Al) the diffusion length extends up to 3.6 nm across the glide plane, whereas it is shorter, 2.1 nm, for A-site cations (La, Sr). A similar asymmetry between the extent of A- and B-site intermixing has been reported for other perovskite epitaxial films.^[54] Since this chemical disorder precludes a precise identification of the interface plane, we use hereafter the position of the glide plane of the MDs as a reference. In addition, the oxygen concentration profile shows a slight constant depression, ≈ 3 at%, on the film side, indicating a background level of oxygen vacancies, V_O (expressed using the Kröger–Vink notation),^[55] throughout the film volume.

An atomic column resolution HAADF image of a dislocation core is presented in Figure 1b. Since this is an incoherent image in which the brightness of atomic columns is proportional to the atomic number, Z , brighter columns correspond to the La/Sr (film) or La (substrate) atom columns. A Burgers circuit is drawn in the image, yielding a Burgers vector $\mathbf{b} = a[010]$ parallel to the interface. Therefore, the glide plane of the MDs, i.e., the plane containing the dislocation line and its Burgers vector, coincides with the interface plane. Note that in the perfect

$\mathbf{b} = a[010]$ dislocation, the extra half-plane is composed by an A-site plane plus a B-site/O plane. Since B-site/O columns are hardly visible owing to their lower atomic number, at first sight the image suggests an unrealistic perfect dislocation with a single extra half-plane of A-site columns in the substrate side. However, careful analysis of the image reveals that the core is dissociated in two partials corresponding to the two (hardly visible) extra half-planes of B-site/O columns running along the two vertical arrows shown in the image. Further confidence for this core structure comes from the analysis of HRTEM images, as discussed in the next paragraph (Figure 2a). Thus, the MD is dissociated according to $\mathbf{b} = a/2[010] + a/2[010]$ (here a is the LAO lattice parameter), and the extended core contains an antiphase boundary on the glide plane between A-site columns (below the glide plane) and B-site columns (above the glide plane). The vertical plane containing the antiphase boundary, passing between the two partials, will be hereafter referred to as axial plane. Interestingly, inspection of Figure 1b reveals that the two B-site atomic columns in the axial plane next to the antiphase contact, on the film side, exhibit higher brightness than the adjacent Mn/O columns. These two positions are clearly identified in the vertical contrast profile shown in

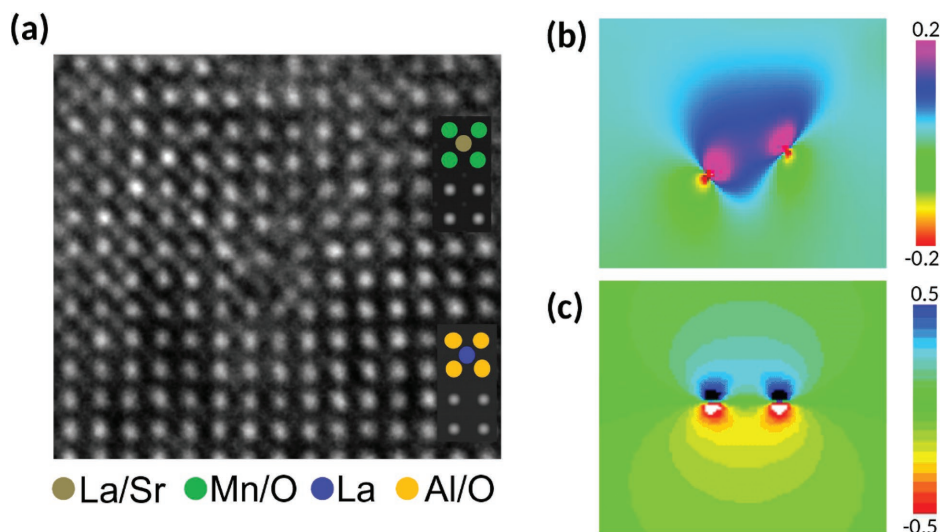


Figure 2. Structure and strain field of misfit dislocations in LSMO/LAO thin films. a) HRTEM image of a misfit dislocation core viewed along the [100] zone axis. Insets are image simulations obtained for a defocus value of 75 nm. The two arrows mark the two extra half-planes of the dissociated core, nominally Al/O. b) Dilatation map obtained from (a) by geometrical phase analysis. c) Theoretical dilatation map of an identical configuration.

Figure 1c. The increased intensity at those two B-site columns points to their partial occupancy by heavier La^{3+} or Sr^{2+} cations, forming La_{Mn}^x or Sr_{Mn}^y antisite defects, where Mn^{3+} is taken as the manganese reference state. Comparing the ionic radii of La^{3+} and Sr^{2+} in octahedral coordination, 1.032 and 1.18 Å, respectively, with that of Mn^{3+} , 0.645 Å,^[56] the driving force for the formation of such defects is considered to be the accommodation of the tensile strain above the glide plane. Similar antisite defects have been observed in an analogous misfit dislocation core in BiFeO_3 .^[57] An atomic core model derived from the present analysis is shown in Figure 1d. The composition of the glide plane is identified as B-site/O. The reverse structure, in which the two extra half-planes are built by A-site columns, has also been identified in the course of this work. This configuration is thus similar to that previously identified in STO bicrystals,^[10,28,29] and according to those studies, its occurrence can be tentatively considered as a fingerprint of oxygen stoichiometry localized at the dislocation core.

Figure 2a is an HRTEM image corresponding to a dislocation core similar to that shown in Figure 1b. According to the multislice image simulations (defocus value 75 nm, foil thickness 14.9 nm) included as insets, the bright positions correspond to B-site/O columns, and therefore the image is complementary with the HAADF image shown in Figure 1b. The corresponding dilatation map, defined as $D_{xz} = \Delta V/V = \epsilon_{xx} + \epsilon_{zz}$, where V is the volume, and ϵ_{xx} and ϵ_{zz} are the normal in-plane and perpendicular strain components, respectively, is depicted in Figure 2b. D_{xz} represents the fractional change in volume that can be correlated with the size of cations redistributed around the MD core to accommodate the dislocation strain field. The map was obtained from Figure 2a by geometrical phase analysis,^[58] using the LAO substrate as a reference; therefore D_{xz} values are somewhat exaggerated at the film side though it is difficult to quantify this effect due to the effect of cation intermixing on the lattice parameters. Figure 2c shows

the corresponding theoretical strain field obtained by adding the strain components of two $1/2[010]$ partial dislocations reproducing the configuration shown in Figure 1d. As a rough approximation, the calculation was performed using classical isotropic linear elasticity and therefore ignores the effects of the defect chemistry on the elastic behavior. The calculation also ignores the interface between the film and the substrate, and a Poisson's ratio of 0.35 was used.^[41] Note that owing to the observed cationic intermixing, a more realistic description should consider a compositional gradient instead of a sharp interface. Comparison between the experimental and theoretical maps reveals that while the latter exhibits a sharp boundary between the tensile and the compressive regions at the glide plane, in the experimental map

a positive dilatation region extends between the two partials toward the substrate. This anomaly will be addressed below.

The chemical composition around the dislocation core was investigated by atomic resolution EDX mapping. Figure 3 shows the HAADF image of a dislocation core (a) along with its corresponding La- L_{α} (b), Al- K_{α} (c), Mn- K_{α} (d), Sr- K_{α} (e), and O- K_{α} (f) net count maps. The maps show some fingerprints of the MD core on the elemental distribution, particularly visible for Sr, Mn, and to a lower extent for Al and O. There is a depletion of Sr, Al, and O ions around the core region, while there is a slight enrichment in Mn ions below the dislocation core.

Elemental concentrations were obtained by integrating net counts over two unit cell thick windows located above and below the glide plane, as indicated in Figure 3a. The integration generated a horizontal profile that was fit to a collection of Gaussian peaks centered at equidistant positions at the corresponding ion sites, all with equal width and free intensities. The integrated areas of each Gaussian were then normalized to a reference value taken at a position sufficiently apart from the MD core to be considered as the bulk LSMO and LAO values. The conversion of X-ray net counts to atomic concentrations was performed by the Cliff-Lorimer method assuming the thin foil criterion.^[59] The k-factors were obtained from a reference zone, considering a supercell $(\text{La}_{0.7}\text{Sr}_{0.3}\text{MnO}_3)_x(\text{LaAlO}_3)_y$ ($x = 7$ and $y = 7$). The error bars in the concentration profiles were estimated from the scatter of results obtained by varying x and y (further details on the procedure are given in the Supporting Information). Concentration profiles corresponding to above and below the glide plane are presented in Figure 3g,h, respectively. The position of the axial plane is indicated by arrows. The elemental concentration profiles are not strictly symmetric with respect to the axial plane very likely due to inhomogeneities in the strain field and some inaccuracies in the integration reflected by the error bars. It can be clearly seen that the distribution of elements differs markedly above and below the glide

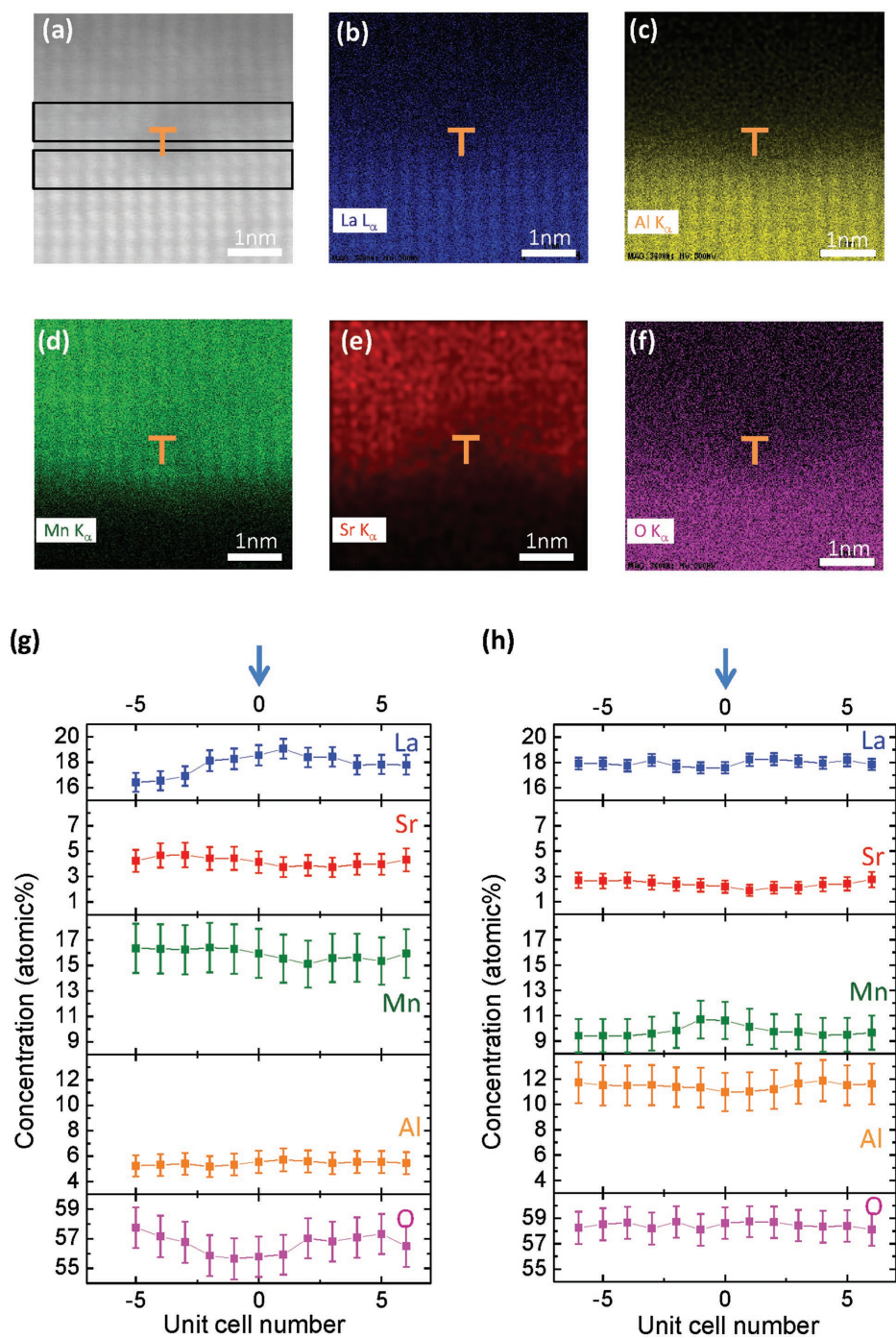


Figure 3. Elemental distribution around the misfit dislocation core. a) Atomic resolution HAADF image of a misfit dislocation core, and associated EDX net count maps corresponding to b) La-L, c) Al-K, d) Mn-K, e) Sr-K, and f) O-K ionization edges. g) Elemental concentration horizontal profiles computed from (b) to (f) using the integration window above the glide plane as indicated in (a). h) Elemental concentration horizontal profiles computed from (b) to (f) using the integration window below the glide plane as indicated in (a). Arrows mark the position of the axial plane of the misfit dislocation.

plane, in the tensile and compressive regions of the MD core, respectively. In the tensile region (Figure 3g), there is a clear enrichment in La accompanied by a depletion of Sr, although the maximum ≈ 2.5 at% La enrichment is not fully compensated by the decrease in Sr. This enrichment indicates that the increased

brightness already observed at B-site positions in Figure 1b, is very likely due to the formation of $\text{La}_{\text{Mn}}^{\text{x}}$ antisite defects localized on the axial plane. On the other hand, the imbalance between La enrichment and Sr depletion extends laterally a few unit cells at each side of the MD and therefore cannot be explained by the formation of $\text{La}_{\text{Mn}}^{\text{x}}$ antisite defects. We note, however, that a perfect balance (and site stoichiometry) is kept within the error bars. It is also worth noting that, taking into account the ionic radii of La^{3+} in cuboctahedral coordination, 1.36 Å, and Sr^{2+} , 1.44 Å,^[56] the depletion of larger Sr atoms goes against the accommodation of the tensile strain above the glide plane. Figure 3h, on the other hand, shows that below the glide plane (compressive region), the La profile is ≈ 18 at% and remains unperturbed by the presence of the MD, while the Sr concentration still shows a slight depression below the core. The behavior of B-site cations shows different trends. Comparing Figure 3g and Figure 3h, one observes that above the glide plane they do not exhibit significant variations, while below it, the Mn concentration shows an increase below the position of the MD core, accompanied by a complementary depletion of Al. The preferential substitution of Al^{3+} (ionic radius, 0.535 Å) by larger Mn^{3+} (0.645 Å)^[56] in the compressive region is again counterintuitive. However, this localized segregation of Mn nicely correlates with the anomalous dilatation observed in a similar dislocation, as shown in Figure 2b, suggesting that it might be favored by the specific core structure.

Comparing the oxygen concentration profiles obtained from the tensile and compressive regions of the MD, it becomes apparent that the glide plane marks the boundary between two well differentiated ionic landscapes. As commented

above, vertical elemental concentration profiles obtained from an integration area located between MDs indicate that there is a background V_{O}^{\cdot} concentration of about 3 at%. Comparing Figure 3g and Figure 3h, this background V_{O}^{\cdot} level is preserved in the first two unit cells above and below the glide plane, but

is selectively increased in the tensile region around the MD core. This behavior strongly suggests that the vacancy formation energy is further reduced under tensile strain, in agreement with atomistic simulations of dislocations in CeO_2 ^[12] and STO ,^[11] and biaxially strained thin films of CaMnO_3 .^[60,61]

The electronic structure of the dislocation core and its vicinity was investigated by analyzing the O-K and Mn-L energy-loss near-edge structure (ELNES). Since the strong strain field of the MD can affect the ELNES and these effects are not well understood, we paid special attention to the determination of the Mn oxidation state. Computer simulations of the Mn^{3+} - $L_{2,3}$ edge under compressive and tensile strain indicated a negligible effect on those spectral features sensitive to the oxidation state (see Figure S12, Supporting Information). Here we report results obtained using the two most widely used techniques to determine the Mn oxidation state in manganites, namely measuring the red shift of the Mn-L_3 maximum and the ratio between L_3 and L_2 intensities.^[62] **Figure 4** examines the evolution of the corresponding spectra along the interface normal, across the dislocation core. The spectra were extracted from unit cell areas, DF3 to DS3, as indicated in Figure 4a. In Figure 4b, the dashed spectrum, F, corresponds to a location in the film far away from the dislocations and is included here for reference. Spectrum S corresponds to a position below the glide plane beyond which the Mn signal vanishes and is used as a reference for the LAO substrate. The glide plane is located between spectra DF1 and DS1.

The O-K edge is interpreted in terms of the transition from O 1s core levels to O 2p states hybridized with transition metal states.^[63] It typically features three peaks, labeled a, b, and c in Figure 4b. Peak a, commonly referred to as prepeak, appears around 531 eV, and is attributed to manganese 3d states. This peak is sensitive to the Mn 3d band occupancy; thus, in the expected high-spin state, it is weakest for Mn^{3+} with its 3d t_{2g} spin-up levels fully occupied and one electron in the e_g level, and becomes stronger as the concentration of Mn^{4+} increases. The second peak, b, found around 536 eV, is attributed to the hybridization with the A-site La 5d or Sr 4d bands. A noticeable broadening of peak b is observed as the A-site, occupied only by La cations in the substrate, becomes progressively shared with Sr cations in the film. The third peak, c, found around 543 eV, is related to the projected unoccupied oxygen p states mixed with the B-site 4sp band. As the glide plane is approached from the film side,

the intensity of peak c vanishes and recovers again below the glide plane, which can be tentatively attributed to the severe distortion of the BO_6 octahedra near the MD core. Figure 4b shows that in all the spectra above the glide plane, along with that obtained from one unit cell just below it, the prepeak is hardly visible, much weaker than in the reference spectrum, F, pointing to a preferential reduction of the Mn cations along the axial plane of the MD.

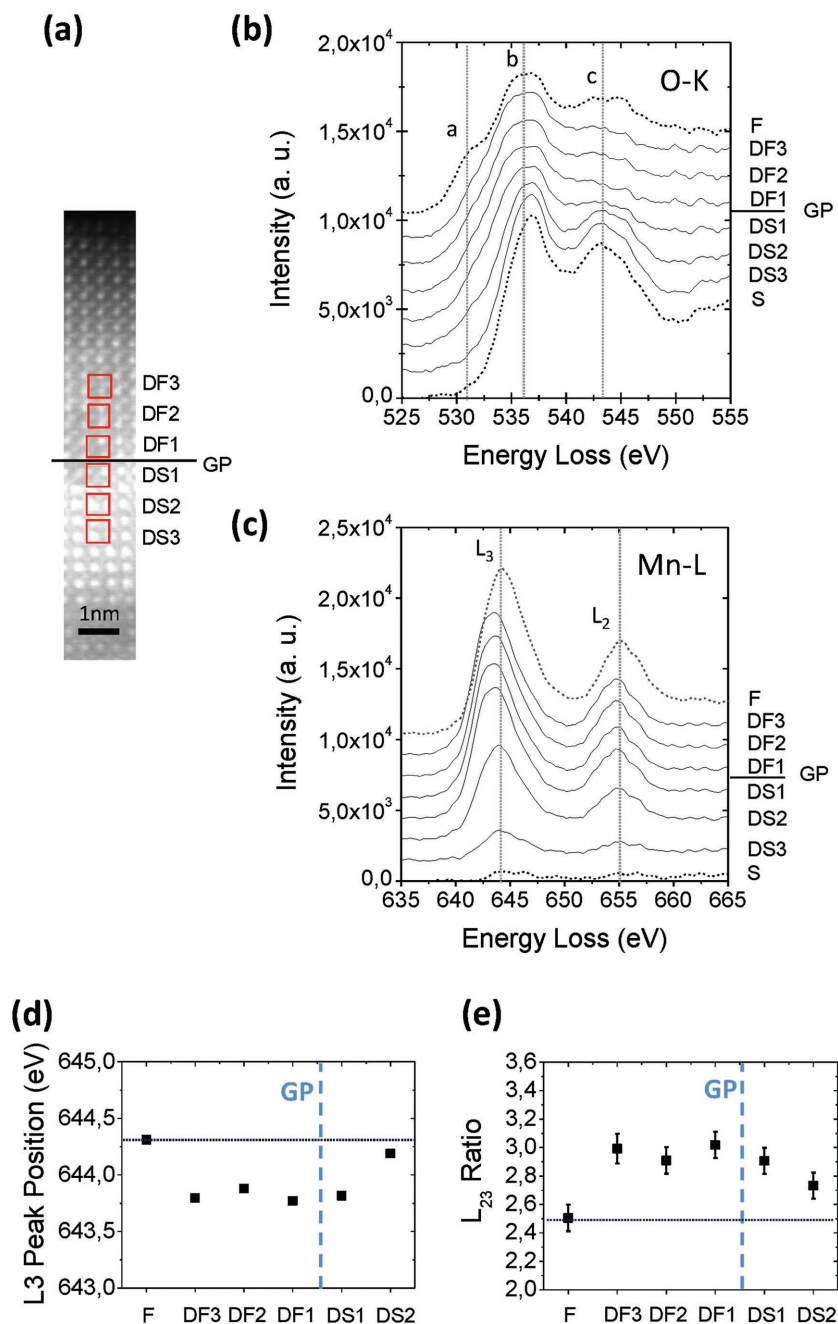


Figure 4. Vertical evolution of the EEL spectra across the misfit dislocation core. a) Atomic resolution HAADF image, and simultaneously acquired b) O-K and c) Mn- $L_{2,3}$ EEL spectra from unit cells marked in (a) with red boxes. The glide plane (GP) is located between DF1 and DS1 as indicated in (a). d,e) Variation of the L_3 peak position and the $L_{2,3}$ intensity ratio, respectively. The glide plane is marked by a vertical dashed line.

The simultaneously acquired Mn-L_{2,3} edges, depicted in Figure 4c, on the other hand, show concomitant modifications of their near edge structures. This edge consists of two white lines, L₂ and L₃, attributed to the transition from the spin-orbit split 2p_{3/2} and 2p_{1/2} levels to available states in the 3d unoccupied band.^[63] Variations in the L₂/L₃ intensity ratio or chemical shifts, are typical fingerprints of changes in the oxidation state.^[62] In particular, Figure 4c shows a red shift and an increase of the L₃/L₂ ratio relative to the F spectrum in all the spectra taken above the glide plane and one unit cell below it. The variation of L₃ peak energy with the vertical position across the dislocation core is shown in Figure 4d. A red shift value of -0.45 eV is kept almost constant from DF3 to DS1, which assuming the nominal oxidation state $+3.33$ for the unperturbed LSMO film, indicates an oxidation state of $+3.03 \pm 0.03$ in the dislocation core. Two unit cells below the glide plane the Mn oxidation state increases until its concentration vanishes. The increase of the L₃/L₂ ratio observed in Figure 4e supports a similar trend.^[63–65] Taking the value obtained from spectrum F as a reference for the nominal $+3.33$ value, we obtain an oxidation state of $+2.7 \pm 0.2$ for unit cell areas DF3 down to DS1, slightly smaller than that obtained by the chemical shift method. We therefore adopt an oxidation state of $+3$ for Mn cations located in the neighborhood of the MD core, as a compromise between the values obtained by both methods.

Figure 5 shows the lateral variation of the EEL O-K (a) and Mn-L_{2,3} (b) spectra along the glide plane, as well as an HAADF image indicating the positions from which the spectra were extracted. The prepeak intensity in the O-K edge spectrum is weakest at the MD core (position GP0 in Figure 5c). The intensity of peak c also decreases at this position in agreement with the behavior observed in the vertical profiles shown in Figure 4. As observed in Figure 5b, the trend observed in the Mn-L_{2,3} spectra is consistent with the behavior of the O-K edge prepeak intensity. The L₃ peak is shifted toward lower energies at the

MD core, indicating that the fluctuation in the Mn oxidation state caused by the dislocation is confined within a narrow region of about 5 unit cells. Beyond this distance, the Mn oxidation state adopts the value determined at the glide plane in regions far from the MDs, $+3.20 \pm 0.03$.

According to these results, the electrical charge per unit cell at the MD core was estimated assuming an Mn oxidation state of $+3$ and the cation stoichiometry derived from EDX analyses. Results obtained below and above the glide plane are shown in Figure 6a,b, respectively. Notably, it can be observed that the behavior is drastically different under tensile (b) and compressive (a) scenarios. In the former case, a positive charge of $q \approx +0.3 \pm 0.1$ decorates the MD core within a lateral range of 4 unit cells and decays with distance from the dislocation, while in the latter, charge neutrality is kept through the position of the MD. Therefore, the charge enrichment appears to be spatially correlated with the V_O concentration. This positive charge on the tensile side will have a compensating charge in the surrounding material, but unfortunately our work does not provide sufficient evidence to determine the mechanism of charge compensation. The observation of positively charged MDs draws a scenario opposed to that reported for MDs in a similar manganese-based heteroepitaxial system, Nd_{0.35}Sr_{0.65}MnO₃/STO.^[39] The mechanism proposed by those authors considers the reorganization of 2D pristine interfacial charges, present prior to the formation of MDs, into 1D chains along the dislocation strain fields when MDs are introduced. In that case, however, no experimental attempt to determine the oxygen concentration was performed and unit cell charges were estimated neglecting any possible effect of oxygen vacancies.

An attempt to describe the basic mechanisms involved in the distribution of cations and oxygen vacancies around the MD core is schematically summarized in Figure 7. As indicated on the schematic, contrary to what would be expected considering only atomic size effects, Sr cations, larger than La,

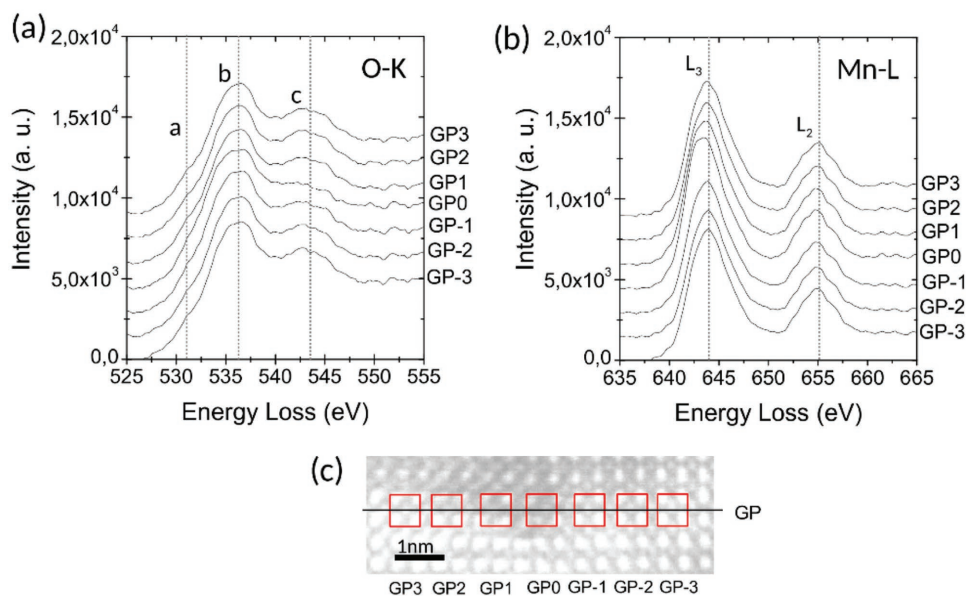


Figure 5. Lateral evolution of EEL spectra across the misfit dislocation core. a) O-K edge and b) L_{2,3} edge EEL spectra obtained from unit cells marked in the atomic resolution HAADF image shown in (c). GP0 corresponds to the locus of the misfit dislocation core.

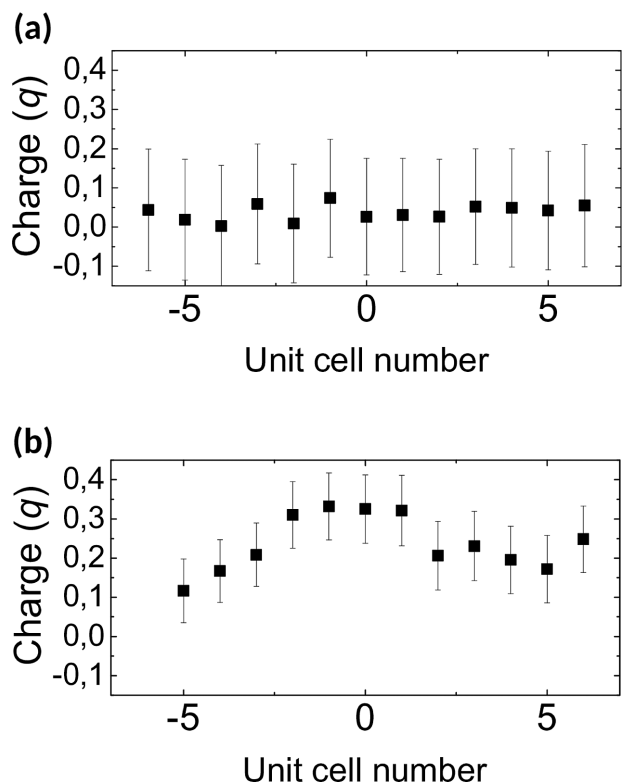


Figure 6. Unit cell charge characteristics computed from the ionic distributions a) below the glide (compressive zone), and b) above the glide plane (tensile zone).

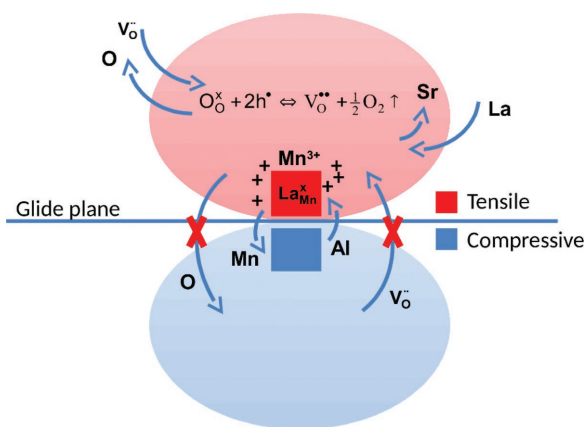
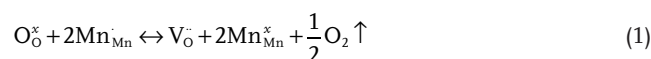


Figure 7. Schematic illustration of the basic mechanisms operating in the MD core. Red and blue represent tensile and compressive regions, respectively. The redox reaction indicated in the tensile region is displaced to the right, favoring the formation of electron donor oxygen vacancies, V_{O} . Each vacancy nominally releases two electrons which can reduce two neighboring Mn^{4+} cations according to Equation (1). The imbalance between the rate of Sr diffusion out of the core region and the concentration of V_{O} results in a positive charge in the tensile region. The glide plane acts as a barrier for the redistribution of vacancies as indicated by crossed-out pathways. $\text{La}_{\text{Mn}}^{\text{x}}$ antisite defects form at the axial plane, on the tensile region, to accommodate the tensile strain.

exhibit a slight depletion while the La/Sr ratio increases in the tensile zone. This suggests a counterbalancing volume effect of the formation of $\text{La}_{\text{Mn}}^{\text{x}}$ antisite defects, which according to the Shannon ionic radius of La^{3+} and Mn^{3+} in octahedral coordination, 1.032 and 0.645 Å, respectively,^[56] yield a huge localized positive dilatational strain of 60%. However, the strain field associated with a point strain source is known to induce a shear without dilatation in the neighboring matrix as well as to decay as $1/r^3$ with distance, r , from it.^[66] Therefore, the strain accommodating effect of point defects is very local. In this sense, the observed oxygen depletion over the tensile zone suggests a dilatational effect of oxygen vacancies.

The radius of an oxygen vacancy in the perovskite structure can be considered similar or slightly smaller than the radius of an oxide ion^[67] and therefore the accumulation of V_{O} is expected to have only a small or negligible effect on the accommodation of the MD strain. Nevertheless, the spatial correlation between the concentration of V_{O} and Mn^{3+} suggests a strain compensating effect associated with the reduction of Mn cations. The redox reaction can be expressed as



where Mn^{3+} is used as the reference state for the host B-site. According to Equation (1), each V_{O} leaves two free carriers^[68] that are transferred to the Mn d band (though at high vacancy concentrations this number can be less),^[69] thus in principle reducing two neighboring Mn^{4+} cations. Comparing the ionic radius of the average $\text{Mn}^{3+}_{0.7}\text{Mn}^{4+}_{0.3}$ cation, 0.610 Å, with that of Mn^{3+} , 0.645 Å, a chemical expansion of $\approx 6\%$ associated with the formation of oxygen vacancies can be estimated. We note, however, that considering the observed substitution level of Mn^{3+} by Al^{3+} (octahedral radius, 0.535 Å)^[56] of 1/4, see Figure 3g, the radius of the average B-site cation becomes 0.617 Å, close to the bulk value 0.610 Å. Hence, within experimental errors, there are no significant differences between the ionic radii of the average B-site cations located in the tensile region and those located in the bulk film far from the influence of the MDs. This suggests that despite the observed cation intermixing, most of the MD strain is accommodated by elastic distortion of interatomic bonds. Strikingly, the slight depletion of Sr, leading to a decrease in size of the average A-site cations in the tensile zone, is not compensated by any significant dilatation of the B-sites. Therefore, we can conclude that the unique significant chemical expansion effect contributing to the relaxation of the tensile strain above the glide plane of the MD, comes from the formation of $\text{La}_{\text{Mn}}^{\text{x}}$ antisite defects on the axial plane, which as commented above, have a very local compensation effect.

Interestingly, the results of the present study are in contrast to atomistic simulations of the distribution of trivalent dopants around an edge dislocation in ceria.^[12] In that case, the driving force governing the distribution of dopants is the minimization of the elastic energy, i.e., larger dopants accumulate in the tensile zone whilst smaller ones replace Ce^{4+} in the compressive zone. Those authors also conclude that the spatial distribution of V_{O} is controlled by electrostatic interactions: positively charged oxygen vacancies are attracted by negatively charged trivalent

dopants regardless of whether they are located in the tensile or compressive regions of the dislocation. Following a similar mechanism, in our case one would expect the association of positively charged oxygen vacancies, V_{O}^{\bullet} , accumulated in the tensile zone, with negatively charged Sr'_{La} species, in contrast with the decrease of the Sr concentration observed in Figure 3g,h. In the present case, however, the doping level of divalent Sr cations, 33%, is much higher and the chemical behavior of the system very likely cannot be properly described by individual point defect interactions. Taking into account the LSMO stoichiometry, $\text{La}^{3+}_{1-x}\text{Sr}^{2+}_x\text{Mn}^{3+}_{1-y}\text{Mn}^{4+}_y\text{O}_{3-\delta}$, and neglecting Al interdiffusion, charge neutrality imposes $\delta = (x - y)/2$. Since, on the basis of the present EELS analysis, both, Mn cations located in the neighborhood of the MD core and Al, are in an oxidation state of +3, the charge neutrality condition becomes $\delta = x/2$, which in Kröger–Vink notation reads as $[\text{Sr}'_{\text{La}}] = 2[V_{\text{O}}^{\bullet}]$. According to this relation, the electrostatic energy arising from the charge unbalance induced by the formation of oxygen vacancies could be canceled by enrichment in Sr over the tensile zone, contrary to the observed depletion (see Figure 7). Moreover, recalling that Sr cations are larger than La ones, such enrichment would simultaneously accommodate the tensile strain above the glide plane. On the other hand, charge compensation could be also favored by the formation of negatively charged cationic vacancies. Nevertheless, the cationic concentrations shown in Figure 3g,h, do not provide conclusive evidences for the occurrence of significant amounts of vacancies neither in the A nor the B sites. The observed behavior in fact points to a complex energy balance between elastic and electrostatic effects that cannot be completely captured from the present analysis.

3. Conclusion

The present work demonstrates that the detailed atomic and chemical structure of misfit dislocations in the complex oxide heterostructure LSMO/LAO can be quantitatively accessed by a combination of transmission electron microscopy imaging (HRTEM, HR-HAADF) and spectroscopic (EDX, EELS) techniques. The atomic structure shows a dissociation scheme similar to that found in oxygen deficient dislocation cores in STO,^[10,28,29] suggesting that it may be considered as a model scheme for other perovskite on perovskite epitaxial systems. Here we provide experimental evidence of the selective formation of oxygen vacancies in the tensile zone of the dislocation, on the film side. As a result, a positive charge enrichment occurs at the tensile zone while the compressive one remains neutral. The dislocation glide plane thus defines a selective boundary regarding the distribution of oxygen vacancies, while allowing intermixing between the film and the substrate within a few unit cells. Oxygen vacancies, in turn, induce the reduction of neighboring Mn cations to Mn^{3+} and generate electrostatic interactions that ultimately govern the cationic distribution around the dislocation core. Notably, on the basis of averaged ionic radii, the resulting compositional modification does not directly correlate with the dislocation strain field, thus pointing to a complex balance between point defect formation, electrostatic and elastic energies. The present results provide essential insights into the complex chemical behavior of misfit

dislocations formed at the interface between two multinary oxides.

4. Experimental Section

Films: High quality films with (100) orientation and thicknesses of 3.5 and 6 nm, were epitaxially grown under a biaxial compressive strain of -2.3% on LAO substrates by magnetron sputtering as reported elsewhere.^[70]

Transmission Electron Microscopy: Thin foil specimens were prepared by conventional cutting–gluing–grinding procedures, followed by Ar milling at a grazing incidence down to perforation. Cross-section atomic resolution images (HRTEM) were obtained at 200 kV using the field-emission gun FEI Tecnai F20 S/TEM. STEM combined with EEL spectrum imaging (SI) and EDX spectral mapping of cross-section samples, were performed in the image-corrected FEI Titan3 G2 60–300 operating at 300 kV, equipped with a Super-X four quadrant detector and a Gatan Quantum dual EELS spectrometer. STEM images were acquired with a convergence angle of 10 mrad and an annular detector inner radius of 138 mrad. The detailed procedure employed for EDX data analysis is explained in the Supporting Information. The dual EELS-SI data were acquired using a 22 mrad collection angle. The EELS spectrometer was vertically binned by 130 \times to improve the readout speed. The zero-loss and core-loss, from 500 to 900 eV, were acquired for every pixel compensating for the intensity difference between them. The core-loss acquisition time per pixel was 0.5 s and the low-loss spectrum was 0.001 s. A dispersion of 0.25 eV per channel was used. Spatial drift corrections were applied in order to minimize drift. The energy resolution measured as the full width at half-maximum of the zero-loss peak was ≈ 1.75 eV. The zero-loss was used to correct the energy shift of core-loss. The principal components analysis provided by Lucas et al.^[71] for Digital Micrograph was used to remove random noise from the EEL spectrum. The power law function was used before each energy peak to remove the background, then deconvolution was performed using the Fourier Ratio method. The Mn-L_{2,3} ratio was measured following the procedure described by Varela et al.^[62] HAADF images were obtained in a probe-corrected Titan3 80–300 operating at 300 kV. The images of cross-section samples were acquired with a probe convergence angle of 10 mrad and an annular detector inner radius of 69 mrad.

Image Processing and Simulation: HRTEM images were simulated by the multislice method using the jems software package.^[72] Strain maps were computed from HRTEM images by geometrical phase analysis.^[58]

Simulation of EELS Spectra: Atomic multiplet calculations were performed to simulate the Mn-L_{2,3} edge under compressive and tensile uniaxial strain, using the CTM4XAS program.^[73] Details on the simulations are given in the Supporting Information.

Supporting Information

Supporting Information is available from the Wiley Online Library or from the author.

Acknowledgements

The authors thank Dr. Belén Ballesteros for her assistance in TEM experiments with the FEI Tecnai F20 S/TEM microscope. This research was funded by the Spanish MINECO through the “Severo Ochoa” Programme for Centres of Excellence in R&D (SEV-2015-0496) and MAT2015-71664-R, and the European Union Horizon 2020 research and innovation programme under the Marie Skłodowska-Curie Grant Agreement No. 645658. ICN2 was supported by the Severo Ochoa program from Spanish MINECO (Grant No. SEV-2013-0295) and by the CERCA Programme (Generalitat de Catalunya). The authors also acknowledge financial aid from the Generalitat de Catalunya

(2014 SGR 501 and 2014 SGR 1216). N.B. thanks the Spanish MINECO for the financial support through the FPI program. Z.K. is grateful for the support from the Ministry of Education, Science, and Technological Development of the Republic of Serbia through Project No. III45018. B.D.E. and D.W.M. acknowledge support from the Center for Emergent Materials at the Ohio State University, a National Science Foundation Materials Research Science and Engineering Center (Grant No. DMR-1420451).

Conflict of Interest

The authors declare no conflict of interest.

Keywords

complex oxides, epitaxy, misfit dislocations, oxygen vacancies, strain

Received: August 4, 2017

Revised: October 22, 2017

Published online:

- [1] M. Kuzmina, M. Herbig, D. Ponge, S. Sandlöbes, D. Raabe, *Science* **2015**, *349*, 1080.
- [2] M. E. Glicksman, C. L. Vold, *Surf. Sci.* **1972**, *31*, 50.
- [3] G. I. Taylor, *Proc. R. Soc. London, Ser. A* **1934**, *145*, 362.
- [4] P. B. Hirsch, R. W. Horne, M. J. Whelan, *Philos. Mag.* **1956**, *1*, 677.
- [5] J. Huang, M. Meyer, V. Pontiki, *Phys. Rev. Lett.* **1989**, *63*, 628.
- [6] L. Y. Chen, M.-R. He, J. Shin, G. Richter, D. S. Gianola, *Nat. Mater.* **2015**, *14*, 707.
- [7] M. Legros, G. Dehm, E. Arzt, T. J. Balk, *Science* **2008**, *319*, 1646.
- [8] R. Smoluchowski, *J. Phys., Colloq.* **1966**, *27*, C3-3-C3-11.
- [9] D. Hull, D. J. Bacon, *Introduction to Dislocations*, Elsevier, Oxford, UK **2001**.
- [10] V. Metlenko, A. H. H. Ramadan, F. Gunkel, H. Du, H. Schraknepper, S. Hoffmann-Eifert, R. Dittmann, R. Waser, R. A. De Souza, *Nanoscale* **2014**, *6*, 12864.
- [11] D. Marrocchelli, L. Sun, B. Yildiz, *J. Am. Chem. Soc.* **2015**, *137*, 4735.
- [12] L. Sun, D. Marrocchelli, B. Yildiz, *Nat. Commun.* **2015**, *6*, 6294.
- [13] A. H. H. Ramadan, R. A. De Souza, *Acta Mater.* **2016**, *118*, 286.
- [14] S.-Y. Choi, S.-D. Kim, M. Choi, H.-S. Lee, J. Ryu, N. Shibata, T. Mizoguchi, E. Tochigi, T. Yamamoto, S.-J. Kang, Y. Ikuhara, *Nano Lett.* **2015**, *15*, 4129.
- [15] M. Greenberg, E. Wachtel, I. Lubomirsky, J. Fleig, J. Maier, *Adv. Funct. Mater.* **2006**, *16*, 48.
- [16] A. Kossoy, Y. Feldman, E. Wachtel, I. Lubomirsky, J. Maier, *Adv. Funct. Mater.* **2006**, *17*, 2393.
- [17] a) A. H. Cottrell, B. A. Bilby, *Proc. Phys. Soc., London, Sect. A* **1949**, *62*, 49; b) L. V. Meisel, *J. Appl. Phys.* **1967**, *38*, 4780.
- [18] F. Sandiumenge, T. Puig, J. Rabier, J. Plain, X. Obradors, *Adv. Mater.* **2000**, *12*, 375.
- [19] A. Trovarelli, P. Fornasiero, *Catalysis by Ceria and Related Materials*, 2nd ed., Imperial College Press, London **2012**.
- [20] H. J. J. Snaith, *Phys. Chem. Lett.* **2013**, *4*, 3623.
- [21] S. B. Riffat, X. Ma, *Appl. Therm. Eng.* **2003**, *23*, 913.
- [22] M.-W. Chu, I. Szafraniak, R. Scholz, C. Harnagea, D. Hesse, M. Alexe, U. Gösele, *Nat. Mater.* **2004**, *3*, 87.
- [23] R. Ramesh, N. A. Spaldin, *Nat. Mater.* **2007**, *6*, 21.
- [24] Z. Wang, M. Saito, K. P. McKenna, Y. Ikuhara, *Nat. Commun.* **2014**, *5*, 3239.
- [25] P. P. Dholabhai, G. Pilania, J. A. Aguiar, A. Misra, B. P. Uberuaga, *Nat. Commun.* **2014**, *5*, 5043.
- [26] K. P. McKenna, *J. Am. Chem. Soc.* **2013**, *135*, 18859.
- [27] K. Szot, W. Speier, G. Bihlmayer, R. Waser, *Nat. Mater.* **2006**, *5*, 312.
- [28] Z. Zhang, W. Sigle, M. Rühle, *Phys. Rev. B* **2002**, *66*, 094108.
- [29] H. Du, C.-L. Jia, L. Houben, V. Metlenko, R. A. De Souza, R. Waser, J. Mayer, *Acta Mater.* **2015**, *89*, 344.
- [30] J. P. Buban, M. Chi, D. J. Masiel, J. P. Bradley, B. Jiang, H. Stahlberg, N. D. Browning, *J. Mater. Res.* **2009**, *24*, 2191.
- [31] K. Takehara, Y. Sato, T. Tohei, N. Shibata, Y. Ikuhara, *J. Mater. Sci.* **2014**, *49*, 3962.
- [32] S. P. Waldow, R. A. De Souza, *ACS Appl. Mater. Interfaces* **2016**, *8*, 12246.
- [33] K. K. Adepalli, J. Yang, J. Maier, H. L. Tuller, B. Yildiz, *Adv. Funct. Mater.* **2017**, *27*, 1700243.
- [34] G. Catalan, J. Seidel, R. Ramesh, J. F. Scott, *Rev. Mod. Phys.* **2012**, *84*, 119.
- [35] S. Farokhipoor, C. Magén, S. Venkatesan, J. Íñiguez, C. J. M. Daumont, D. Rubí, E. Snoeck, M. Mostovoy, C. de Graaf, A. Müller, M. Döblinger, C. Scheu, B. Noheda, *Nature* **2014**, *515*, 379.
- [36] N. Farag, M. Bobeth, W. Pompe, A. E. Romanov, J. S. Speck, *J. Appl. Phys.* **2005**, *97*, 113516.
- [37] J. Santiso, Ll. Balcells, Z. Konstantinovic, J. Roqueta, P. Ferrer, A. Pomar, B. Martínez, F. Sandiumenge, *CrystEngComm* **2013**, *15*, 3908.
- [38] S. C. Jain, A. H. Harker, R. A. Cowley, *Philos. Mag. A* **1997**, *6*, 1461.
- [39] C.-P. Chang, M.-W. Chu, H. T. Jeng, S.-L. Cheng, J. G. Lin, J.-R. Yang, C. H. Chen, *Nat. Commun.* **2014**, *5*, 3522.
- [40] S. Pandya, A. R. Damodaran, R. Xu, S.-L. Hsu, J. C. Agar, L. W. Martin, *Sci. Rep.* **2016**, *6*, 26075.
- [41] F. Sandiumenge, N. Bagués, J. Santiso, M. Paradinas, A. Pomar, Z. Konstantinovic, C. Ocal, Ll. Balcells, M.-J. Casanove, B. Martínez, *Adv. Mater. Interfaces* **2016**, *3*, 1600106.
- [42] F. Sandiumenge, J. Santiso, Ll. Balcells, Z. Konstantinovic, J. Roqueta, A. Pomar, J. P. Espinós, B. Martínez, *Phys. Rev. Lett.* **2013**, *110*, 107206.
- [43] J. Santiso, J. Roqueta, N. Bagués, C. Frontera, Z. Konstantinovic, Q. Lu, B. Yildiz, B. Martínez, A. Pomar, Ll. Balcells, F. Sandiumenge, *ACS Appl. Mater. Interfaces* **2016**, *8*, 16823.
- [44] G. A. Botton, *MRS Bull.* **2012**, *37*, 21.
- [45] M. Varela, J. Gazquez, S. J. Pennycook, *MRS Bull.* **2012**, *37*, 29.
- [46] M.-W. Chu, S. C. Liou, C.-P. Chang, F.-S. Choa, C. H. Chen, *Phys. Rev. Lett.* **2010**, *104*, 196101.
- [47] A. J. D'Alfonso, B. Freitag, D. Klenov, L. J. Allen, *Phys. Rev. B* **2010**, *81*, 100101.
- [48] A. J. Craven, H. Sawada, S. McFadzean, I. MacLaren, *Ultramicroscopy* **2017**, *180*, 66.
- [49] R. F. Klie, J. P. Buban, M. Varela, A. Franceschetti, C. Jooss, Y. Zhu, N. D. Browning, S. T. Pantelides, S. J. Pennycook, *Nature* **2005**, *435*, 475.
- [50] A. J. H. van der Torren, S. J. van der Molen, J. Aarts, *Phys. Rev. B* **2015**, *91*, 245426.
- [51] C. H. Lanier, J. M. Rondinelli, B. Deng, R. Kilaas, K. R. Poepelmeier, L. D. Marks, *Phys. Rev. Lett.* **2007**, *98*, 086102.
- [52] H. Seo, A. A. Demkov, *Phys. Rev. B* **2011**, *84*, 045440.
- [53] N. Nakagawa, H. Y. Hwang, D. A. Muller, *Nat. Mater.* **2006**, *5*, 204.
- [54] C.-P. Chang, J. G. Lin, H. T. Jeng, S.-L. Cheng, W. F. Pong, Y. C. Shao, Y. Y. Chin, H.-J. Lin, C. W. Chen, J.-R. Yang, C. H. Chen, M.-W. Chu, *Phys. Rev. B* **2013**, *87*, 075129.
- [55] A. Kröger, H. J. Vink, in *Solid State Physics* Vol. 3, (Eds: F. Seitz, D. Turnbull), Academic Press, New York **1956**, p. 307.
- [56] R. D. Shannon, *Acta Crystallogr., Sect. A: Found. Adv.* **1976**, *32*, 751.
- [57] A. Lubk, M. D. Rossell, J. Seidel, Y. H. Chu, R. Ramesh, M. J. Hytch, E. Snoeck, *Nano Lett.* **2013**, *13*, 1410.

- [58] M. J. Hytch, *Microsc. Microanal. Microstruct.* **1997**, *8*, 41.
- [59] G. Cliff, G. W. Lorimer, *J. Microsc.* **1975**, *103*, 203.
- [60] U. Aschauer, N. A. Spaldin, *Appl. Phys. Lett.* **2016**, *109*, 031901.
- [61] U. Aschauer, R. Pfenninger, S. M. Selbach, T. Grande, N. A. Spaldin, *Phys. Rev. B* **2013**, *88*, 054111.
- [62] M. Varela, M. P. Oxley, W. Luo, J. Tao, M. Watanabe, A. R. Lupini, S. T. Pantelides, S. J. Pennycook, *Phys. Rev. B* **2009**, *79*, 085117.
- [63] H. Kurata, C. Colliex, *Phys. Rev. B* **1993**, *48*, 2102.
- [64] T. Sparrow, B. Williams, C. Rao, J. Thomas, *Chem. Phys. Lett.* **1984**, *108*, 547.
- [65] W. G. Waddington, P. Rez, I. P. Grant, C. J. Humphreys, *Phys. Rev. B* **1986**, *34*, 1467.
- [66] N. F. Mott, F. R. N. Nabarro, *Proc. Phys. Soc.* **1940**, *52*, 86.
- [67] D. Marrocchelli, N. H. Perry, S. R. Bishop, *Phys. Chem. Chem. Phys.* **2015**, *17*, 10028.
- [68] H. Yamada, G. R. Miller, *J. Solid State Chem.* **1973**, *6*, 169.
- [69] W. Gong, H. Yun, Y. B. Ning, J. E. Greedan, W. R. Datars, C. V. Stager, *J. Solid State Chem.* **1991**, *90*, 320.
- [70] Z. Konstantinovic, J. Santiso, D. Colson, A. Forget, Ll. Balcells, B. Martínez, *J. Appl. Phys.* **2009**, *105*, 063919.
- [71] G. Lucas, P. Burdet, M. Cantoni, C. Hebert, *Micron* **2013**, *52–53*, 49.
- [72] P. Stadelmann, *Ultramicroscopy* **1987**, *21*, 131.
- [73] E. Stavitski, F. M. F. de Groot, *Micron* **2010**, *41*, 687.

Shaped Co^{2+} doped TiO_2 nanocrystals synthesized from nanotubular precursor: Structure and ferromagnetic behavior

M. VRANJEŠ^a, J. KULJANIN JAKOVLJEVIĆ^a, Z. KONSTANTINOVIC^b,
A. POMAR^c, M. STOILJKOVIĆ^a, M. MITRIĆ^a, T. RADETIĆ^d, Z. ŠAPONJIĆ^{a,*}

^aVinča Institute of Nuclear Sciences, University of Belgrade, P.O. Box 522, 11001 Belgrade, Serbia

^bCenter for Solid State Physics and New Materials, Institute of Physics Belgrade, University of Belgrade, Pregrevica 118, 11080 Belgrade, Serbia

^cInstitut de Ciència de Materials de Barcelona, CSIC, Campus UAB, 08193 Bellaterra, Spain

^dFaculty of Technology and Metallurgy, University of Belgrade, Karnegijeva 4, 11120 Belgrade, Serbia

Received: January 02, 2017; Revised: April 24, 2017; Accepted: May 31, 2017

© The Author(s) 2017. This article is published with open access at Springerlink.com

Abstract: Co^{2+} doped TiO_2 nanocrystals were synthesized by a hydrothermal treatment procedure applied to precursor dispersion of titania nanotubes and Co^{2+} ions. Mixture of polygonal and prolate spheroid-like nanocrystals was obtained. The results of X-ray diffraction (XRD) analysis showed that resulted nanocrystals retain anatase crystal phase for both dopant concentrations (1.69 and 2.5 at%), but the crystal lattice parameters were affected. Reflection spectra revealed altered optical properties compared to bare TiO_2 . Room temperature ferromagnetic ordering with saturation magnetic moment in the range of 0.001–0.002 μ_{B}/Co was observed for both measured films made of Co^{2+} doped TiO_2 nanocrystals.

Keywords: hydrothermal synthesis; X-ray diffraction (XRD); transmission electron microscopy (TEM); doped TiO_2 ; magnetic properties

1 Introduction

The ability to control the spin of electrons in addition to their charge in materials such as nanoscale diluted magnetic semiconductors (DMSs) would expand their applications from conventional to spin-based electronic devices. Traditionally, the DMSs refer to a non-magnetic semiconductor material, as a host, in which a few atomic percents of its cations are replaced with transition metal ions. DMSs are mostly based on III–V (GaN, GaP, etc.) or II–VI (ZnS, CdTe) compounds because, among other things, valence of

host cations (+3 or +2) matches well that of common magnetic ions. Generally, in these materials, ferromagnetism has been achievable far below room temperature. Typically, they have Curie temperatures below 100 K making them unattractive for practical applications in future devices characterized by simultaneous control of spin and charge of electrons [1]. Recently, oxide (ZnO , TiO_2 , SnO_2 , In_2O_3)-based DMS materials have attracted considerable attention due to the reports of ferromagnetism at room temperature which open the possibility of their application in emerging field of thin-film magneto-optic and spin-electronic devices [2–12].

The origin of ferromagnetism in oxide DMSs is still subject of controversy and the debate spans from

* Corresponding author.
E-mail: saponjic@vinca.rs

intrinsic ferromagnetism over possible precipitation of magnetic clusters to the formation of secondary magnetic phases [13]. Generally, conventional exchange mechanisms (direct or superexchange interactions) used for explanation of ferromagnetic behavior cannot be applied on oxide DMSs. The reason is the absence of long-range magnetic ordering at applied concentrations of 3d dopants that are far below the percolation threshold associated with nearest-neighbor cation coupling [14]. Numerous studies, experimental and theoretical, suggest that oxygen vacancies, acting as donors who introduce n-type doping in the material, play an important role in the magnetic ordering of oxide DMSs [15–17]. Electrons associated with oxygen vacancy defects tend to form bound magnetic polarons (BMP model), coupling the 3d moments of the dopant ions within their orbits [14].

The differences between the mechanisms of dopant ion incorporations in bulk material and nanocrystals should be taken into account in order to overcome the problems in nanodoping process [18]. More precisely, the problem of so called “self-purifications”, according to which the dopant ions are expelled from the nanoparticle core during the crystal growth when synthesis starts from the molecular precursors [19], should be prevailed. We developed hydrothermal synthetic procedure for incorporation of various dopant ions (transition metal ions and rare earth ions) in TiO₂ nanocrystals of various shapes (faceted nanoparticles, prolate nanospheroids) using dispersions of titania nanotubes and dopant ions, as precursors [20–23]. In our previous work, we reported ferromagnetic ordering in faceted Co²⁺ doped TiO₂ nanoparticles synthesized hydrothermally in acidic conditions (pH=3), by shape transformation of titania nanotubes in the presence of Co²⁺ ions [24]. According to Erwin *et al.* [18], the underlying mechanism that generally controls doping is an initial adsorption of dopant ions on the nanocrystal surface during the growth which is on the other hand controlled by surface morphology and nanocrystal shape. Having that in mind, we exploited the presence of an undercoordinated defect site on the surface of titania nanotubes for an initial adsorption of dopant anions enabling formation of the highly stable central core of the resulting particle, without influence of further growth on doping efficiency. In theory of transformation of nanotubes, it was suggested that the existing TiO₆ octahedra layers served as a seed layer for the epitaxial anatase crystals nucleating and

growing along specific directions on the nanotube surface [25,26].

The aim of this work was to hydrothermally synthesize Co²⁺ doped TiO₂ nanocrystals of different shape, and to examine their shape dependent magnetic, structural, and optical properties. The study of shape dependent magnetic properties of prolate spheroid-like and polygonal (faceted) Co²⁺ doped TiO₂ nanocrystals, for the synthesis of which were used, as precursors, weak acidic (pH=5) dispersions of titania nanotubes and Co²⁺ ions in two different concentrations, is presented for the first time, to the best of our knowledge. Morphologies of the doped nanocrystals and their crystalline structures were studied by transmission electron microscopy (TEM) and X-ray diffraction (XRD) analysis, respectively. The inductively coupled plasma (ICP) emission spectrometry was applied for determination of the amount of Co²⁺ dopant ions incorporated within TiO₂ nanocrystals. The optical characterization of powdered samples of the Co²⁺ doped TiO₂ nanocrystals was carried out by UV–Vis spectroscopy in reflection mode. The superconducting quantum interference device (SQUID) magnetometer was used to study the magnetic properties of films made of Co²⁺ doped TiO₂ nanocrystals.

2 Experimental procedure

All chemicals were reagent grade from Aldrich and used as received. Titania nanotubes were synthesized via hydrothermal method according to Kasuga *et al.* [27], using commercial TiO₂ powder (Degussa) as precursor. The 2 g of TiO₂ powder was dispersed in 50 mL 10 M NaOH and hydrothermally treated for 48 h in a Teflon vessel (Parr acid digestion bomb, total volume 125 mL) under saturated vapor pressure of water at 120 °C. After autoclaving, the ensuing powder was washed with 1 M HCl and subsequently with distilled water. Separation of powder from the washing solution, after each washing step, was done by centrifugation. The washing procedure was repeated until pH of water achieved 7. The powder was then air dried at 70 °C.

For the synthesis of Co²⁺ doped TiO₂ nanocrystals, two precursor dispersions of titania nanotubes (125 mg/50 mL each) at pH=5 containing two different concentrations of CoCl₂ (3.11×10^{-4} and 6.23×10^{-4} M) were prepared and stirred for 3 h at room temperature after which the hydrothermal treatments at 250 °C for

90 min (Parr acid digestion bomb, total volume 125 mL) were applied. Obtained Co^{2+} doped TiO_2 nanocrystals were efficiently re-dispersed in water and dialyzed against 10 times larger volume of acidified water ($\text{pH} = 5$) at 4°C for 3 days in order to remove excess of Co^{2+} ions. Water was changed daily. Spectra/Por Dialysis Membrane, MWCO: 3500 (Spectrum Laboratories, Inc., Rancho Dominguez, CA, USA) was used for dialysis.

The percentage ratio of Co^{2+} to Ti^{4+} ions in doped nanocrystals was determined using ICP emission spectrometer (ICAP 6000 series, Thermo Electron Corporation). Prior to the ICP measurements, the powdered sample was dispersed in 3 mL of concentrated sulfuric acid and hydrothermally treated for 60 min at 250°C in Teflon vessel (Parr acid digestion bomb, total volume 25 mL). The final concentrations of Co^{2+} ions in dialyzed samples of doped TiO_2 nanocrystals were 1.69 and 2.5 at% of the amount of Ti^{4+} ions.

The shape and size of precursor titania nanotubes were characterized in Hitachi H-700 FA TEM at 125 kV, while the Co^{2+} doped TiO_2 nanocrystals were characterized by JEOL 100 CX TEM at 100 kV.

Reflectance spectra of powder of Co^{2+} doped TiO_2 nanocrystals were recorded at room temperature using Thermo Scientific Evolution 600 UV/Vis spectrophotometer.

The X-ray diffraction (XRD) patterns were obtained using a Philips PW-1050 automated diffractometer using $\text{Cu K}\alpha$ radiation (operated at 40 kV and 30 mA). Diffraction data for crystallographic analysis were collected in the 2θ range of 10° – 120° , with scanning step of 0.02° and exposure time of 12 s. Crystallographic analysis was done using the KOALARIE computing program [28], based on the Rietveld full profile refinement method [29]. Samples for XRD measurements were prepared using standard protocol [30].

The field dependence magnetic moment was measured with a superconducting quantum interference device magnetometer (Quantum Design). The magnetic field was applied parallel to the film surface. The measured magnetization at 300 K was corrected for the diamagnetic background of the glass substrate (derived from high-field dependence magnetization data). Films for magnetic characterization were prepared by drop casting of dialyzed dispersions of Co^{2+} doped TiO_2 nanoparticles onto pre-cleaned glass substrate. The films were annealed in air for 2 min at 100°C after

adding each drop. Weights of all films were measured for purposes of determining the amounts of the dopant ions required for magnetic moment calculations.

3 Results and discussion

Titania nanotubes represent a suitable starting material for the synthesis of highly crystalline doped TiO_2 nanoparticles of various sizes and shapes through structural reorganization and shape transformation in the presence of dopant ions. In this study, as precursor were used synthesized titania nanotubes with a layered structure of scrolled nanotubes (Fig. 1(a)). Their size was fairly uniform and with characteristic parameters: outer diameter was in 10 nm range, inner diameter was about 5 nm, while the interlayer spacing was quite large, approximately 0.7 nm (Fig. 1(a)).

Hydrothermal treatment of dispersion of titania nanotubes at $\text{pH} = 5$ in the presence of Co^{2+} ions resulted in formation of Co^{2+} doped TiO_2 nanoparticles (2.5 at% Co^{2+}) of mixed shapes and sizes. The mixture (Fig. 1(b)) consists of polygonal (faceted), non-spherical nanocrystals with average dimension of 14 nm and the larger, anisotropic nanocrystals with shapes like prolate spheroids and lengths up to 120 nm.

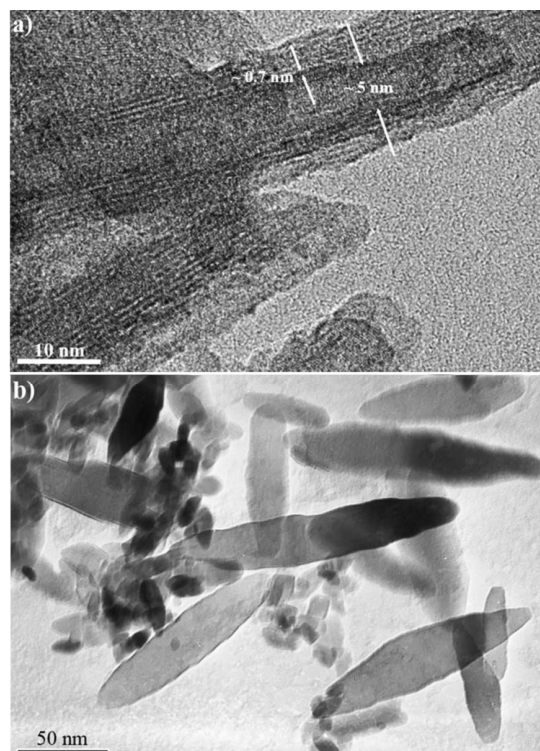


Fig. 1 TEM images of (a) precursor nanotubes and (b) 2.5 at% Co^{2+} doped TiO_2 nanocrystals.

The process of synthesis was controlled by the hydrothermal conditions such as the temperature and duration time as well as the concentration and pH value of precursor dispersions [20,31,32]. Our previous results showed that the hydrothermal treatment of titania nanotubes at pH=5 leads to formation of elongated, prolate spheroid-like nanocrystals independently of the concentration of starting dispersion of titania nanotubes and the concentration of dopant ions [20]. The appearance of Co^{2+} doped TiO_2 nanoparticles of mixed shapes in this study (Fig. 1(b)), although the synthesis conditions were similar to Ref. [20], can be explained by the modified post-synthetic rinsing procedure of precursor titania nanotubes (rinse once with 1 M HCl, followed by rinsing with H_2O until pH=7). The release of residual H^+ ions from the interlayers of nanotubes could induce the lowering of the pH during the hydrothermal treatment of nanotubes and hence the appearance of nanocrystals of mixed shapes and sizes.

Barnard and Curtiss [33] used the free energy of nanocrystals as a function of size and shape, to determine the minimum energy morphology of anatase and rutile TiO_2 nanocrystals with different surface chemistry (acid or alkaline conditions). They found that in hydrogen dominancy on the surface (acidic conditions), there is little change in the shape of the nanocrystals with respect to the (neutral) water terminated nanoparticles. However, when oxygen is dominant on the surface (alkaline conditions), the nanoparticles of both polymorphs become elongated. According to Sugimoto and Zhou [34], who studied formation of TiO_2 nanoparticles, their anisotropic growth and increase of the final size, with increasing of pH, are the consequence of the reduction of nucleation rate and increased adsorption of OH^- groups on the embryos of TiO_2 nuclei. By analogy with formation of TiO_2 nanoparticles during dissolution process of $\text{Ti}(\text{OH})_4$ gel, the rate-determining step for the growth of doped TiO_2 particles, probably is not the dissolution process of nanotubes than the deposition process of the solute onto the growing TiO_2 particles which proceeds with increasing pH [35]. Under these circumstances, the crystal growth is governed by kinetics, rather than thermodynamics, thus leading to the formation of the metastable anatase [36,37]. Presence of dopant ions can also stabilize anatase crystalline structure of TiO_2 and retard the formation of more stable rutile phase [38].

The XRD pattern of precursor nanotubes is shown in

Fig. 2. The development of anatase crystalline phase with characteristic peaks at $2\theta=25.3^\circ$, 37.9° , 48.2° , 53.9° , 55.1° , and 62.7° assigned to (101), (004), (200), (105), (211), and (204) crystal planes, respectively, was confirmed (JCPDS Card No. 21-1272). Asymmetry of peak which appears at $2\theta=25.3^\circ$ indicates the presence of monoclinic $\text{TiO}_2(\text{B})$ structure ($2\theta=24.5^\circ$) [39,40] and also hydrogentitanate, compounds which usually appear in the samples of hydrothermally synthesized titania nanotubes. These results follow the trend of observations of the crystal structure of titania nanotubes as quasi-anatase crystal phase with the presence of insignificantly small amount of monoclinic $\text{TiO}_2(\text{B})$ crystalline structure [31,41,42].

The XRD analysis of 1.69 and 2.5 at% Co^{2+} doped TiO_2 nanocrystals are presented in Fig. 3. Spectra of the both samples have peaks unambiguously indexed as the tetragonal anatase crystal form of TiO_2 . High intensity and sharpness of peaks in the XRD patterns indicate high crystallinity of the samples. No diffraction peaks related to impurities such as metallic Co clusters, CoO, or Co–Ti oxide species are detected, implying incorporation of Co^{2+} ions into TiO_2 crystal lattice. Such finding opens up possibility to correlate magnetic properties to Co^{2+} ions incorporated into anatase lattice.

The crystal parameters of anatase phases in both samples of Co^{2+} doped TiO_2 nanocrystals (1.69 and 2.5 at% Co), based on XRD analysis by Rietveld full profile refinement method, are shown in Table 1. The lattice parameters of the both samples are larger than reference values of the pure anatase (JCPDS Card No. 89-4921) (Table 1). The increase in lattice parameters is a further indication of substitution of Ti^{4+} by Co^{2+} within crystal

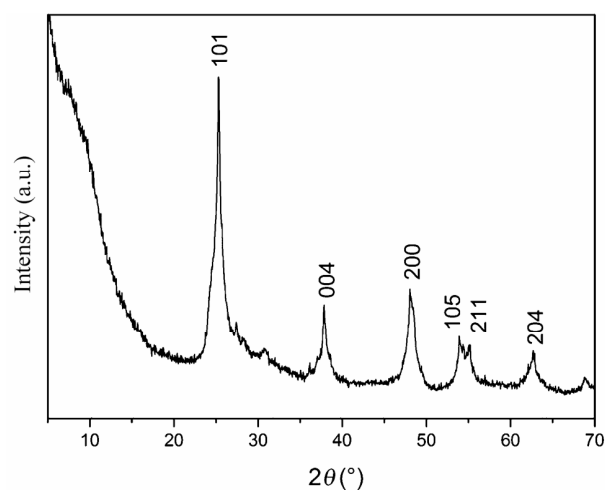


Fig. 2 XRD pattern of precursor nanotubes.

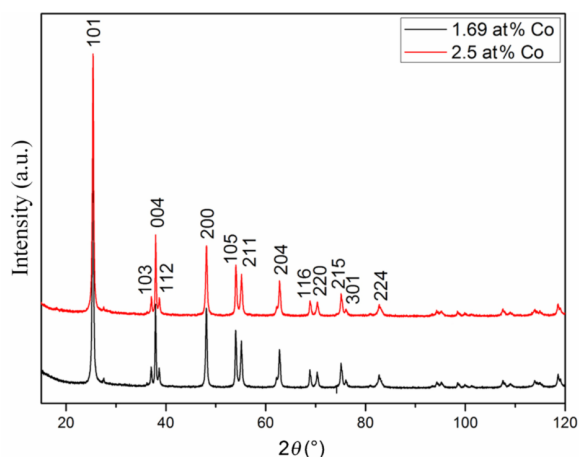


Fig. 3 XRD patterns of 1.69 and 2.5 at% Co^{2+} doped TiO_2 nanocrystals.

Table 1 Refined values of unit cell parameters of Co^{2+} doped TiO_2 nanocrystals

Sample	a (Å)	c (Å)	V (Å ³)
TiO_2	3.77700	9.50100	135.5400
1.69 at% Co	3.78850	9.50816	136.4678
2.5 at% Co	3.78924	9.50791	136.5175

structure of doped TiO_2 nanoparticles [43]. It is known that Co impurities induce local geometrical distortions in crystal lattice of TiO_2 [17]. Ionic radius of Co^{2+} ions in octahedral coordination is 0.79 or 0.885 Å when Co^{2+} is in its high spin state, which is slightly larger than ionic radius of Ti^{4+} ions in octahedral coordination (0.745 Å) [44], while bond lengths with nearest neighboring oxygen surrounding the impurity are reduced by about 0.05 Å [17]. Calculations by Weissmann and Errico [17] predicted that Co^{2+} ions in anatase crystal lattice tend to be located in rows along a -axis. Because of the charge imbalance between dopant (Co^{2+}) and host (Ti^{4+}) ions, the overall charge neutrality in the lattice of TiO_2 nanoparticles after incorporation of Co^{2+} ions is maintained by introducing oxygen interstitial defects [3,17]. Due to fact that the TiO_2 is an ionic crystal, formation of oxygen vacancies induces a large structural relaxation as a consequence of the repulsion of nearby titanium ions [3,15,17,45].

In order to further confirm incorporation of Co^{2+} ions into the crystal lattice of TiO_2 , we have investigated the optical properties of powdered samples of the 1.69 and 2.5 at% Co^{2+} doped TiO_2 nanoparticles. The reflection spectra of doped TiO_2 nanoparticles are presented in Fig. 4.

The influence of dopant on optical properties of TiO_2 matrix is evident (Fig. 4). Increase of absorbance of

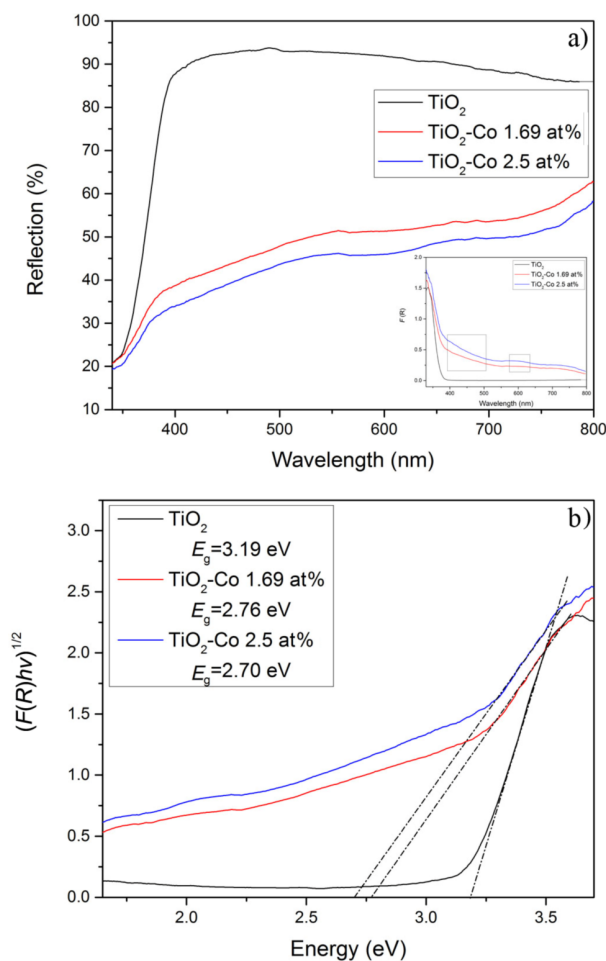


Fig. 4 (a) Reflection spectra of non-doped and 1.69 and 2.5 at% Co^{2+} doped TiO_2 nanocrystals (inset: absorption mode) and (b) band gap determinations.

Co^{2+} doped TiO_2 nanoparticles in the visible part of the spectra could be related to the narrowing of the band gap of TiO_2 . As can be seen from Fig. 4(a), there are two specific features observed in the both spectra of Co^{2+} doped TiO_2 nanoparticles: between 400 and 500 nm and around 600 nm. These features are related to the ${}^4\text{T}_{1g}$ to ${}^4\text{T}_{1g}(\text{P})$ and ${}^4\text{T}_{1g}$ to ${}^4\text{A}_{2g}$ transitions, respectively, which are the consequence of crystal field splitting of d-electronic transitions of Co^{2+} in octahedral or pseudo-octahedral coordination [46]. Upon substitution of Ti^{4+} ions by Co^{2+} , the electrons in the d orbital of Co^{2+} will undergo repulsion by the electrons of the six surrounding oxygen atoms which results in the splitting of d orbital of Co^{2+} . Appearance of these transitions in the spectra of doped TiO_2 nanoparticles is an indication of incorporation of Co^{2+} ions in TiO_2 lattice [43,47,48].

For the analysis of reflectance spectra, Kubelka–Munk relation $F(R) = (1-R)^2/2R$, which allows the

optical absorbance ($F(R)$) of the sample to be approximated from its reflectance (R in %), was applied. Using this relation semiconducting materials can be analyzed with a Tauc plot, whereby the absorption coefficient, α , in the Tauc equation is substituted with $F(R) ((F(R)h\nu)^{1/2} = f(h\nu)$, where exponent 1/2 indicates the indirect nature of band-to-band transition) [49,50]. Band gap energies of the Co^{2+} doped TiO_2 nanoparticles synthesized at $\text{pH}=5$ were estimated from the variation of the Kubelka–Munk function with photon energy (Fig. 4(b)). According to this method, determined band gap energies of 1.69 and 2.5 at% Co^{2+} doped TiO_2 nanocrystals, revealed their red shifts to 2.76 and 2.70 eV, respectively.

While certain groups of authors claimed that doping does not reduce the actual band gap of TiO_2 but instead introduces some mid-band gap states which results in red shift of band gap, other groups associated the narrowing of band gap to the sp-d exchange interactions between the host and dopant ions [51,52]. Owing to formation of oxygen vacancies in the crystal lattice of TiO_2 after substitution of Ti^{4+} with Co^{2+} ions, the defect states in the forbidden zone of the energy band gap of TiO_2 are created. The existence of these defect states is a reason for appearance of absorption bands in the visible spectral region [53]. Some theoretical calculations suggested that a high vacancy concentration could induce a vacancy band of electronic states just below the conduction band [54]. According to Zuo *et al.* [55], the band gap narrowing in Co^{2+} doped TiO_2 nanoparticles is a consequence of the presence of a mini-band just below the conduction band minimum, related to the oxygen vacancy associated with Ti^{3+} .

The magnetic responses of films in dependence of magnetic field are shown in Fig. 5. Weak ferromagnetic behavior was observed in both samples, with coercive field of $H_c \approx 100$ Oe and low saturation moments in the range of $M_s = 0.001\text{--}0.002 \mu_B/\text{Co}$. The diamagnetic contribution determined from the room temperature magnetic field dependence of magnetization at high field (for $H > 10$ kOe) was subtracted in both samples and not considered below. According to saturation magnetization values, the total number of magnetic moments in Co^{2+} doped TiO_2 nanoparticles increases with increasing amount of dopant ions (Fig. 5).

Furthermore, temperature dependence of magnetic susceptibility ($H = 1000$ Oe) in films made of 1.69 and 2.5 at% Co^{2+} doped TiO_2 nanocrystals enabled the

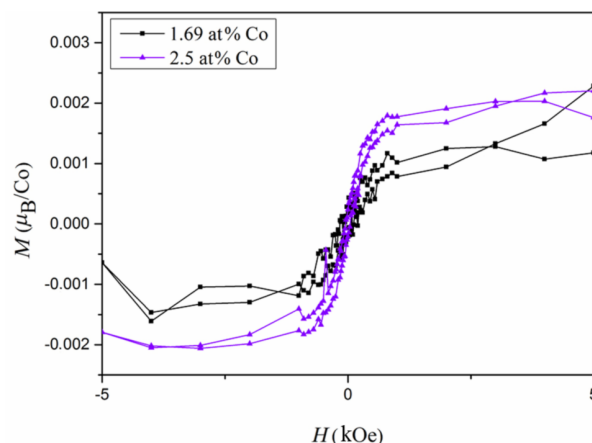


Fig. 5 Room temperature magnetizations of the films made of 1.69 and 2.5 at% Co^{2+} doped TiO_2 nanocrystals.

examination of the nature of magnetism (Fig. 6). The increase of susceptibility is observed at low temperature for both samples indicating dominant paramagnetic behavior of isolated Co^{2+} ions [56]. Zero-field-cooled (ZFC) and field-cooled (FC) magnetic susceptibility (not shown) under low field of 100 Oe completely overlap for both samples showing no change from behavior presented in Fig. 6, without signature of Co magnetic clusters. Temperature dependent susceptibility follows Curie–Weiss dependence:

$$\chi = \frac{C}{T - \theta} \tag{1}$$

where C is Curie constant and θ is Curie–Weiss temperature, indicating the straight nature of the magnetic interactions. The values of C and θ obtained from the fit of Curie–Weiss law are given in Table 2.

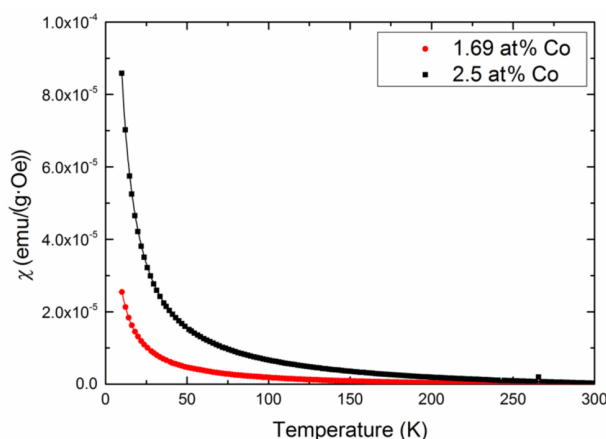


Fig. 6 Temperature variations of the magnetic susceptibility measured at $H=1000$ Oe. Solid lines represent Curie–Weiss fit.

Table 2 Values of C , θ , and μ_{eff} obtained from Curie–Weiss fit for 1.69 and 2.5 at% Co^{2+} doped TiO_2

Sample	C (emu·K/(g·Oe))	θ (K)	μ_{eff} (μ_{B}/Co)
1.69 at% Co	2.99×10^{-4}	1.2	3.4
2.5 at% Co	6.51×10^{-4}	0.2	4.1

In both samples, θ has a very small positive value indicating very weak ferromagnetic coupling. The Curie constant, C , is related to the effective magnetic moment μ_{eff} of Co^{2+} in Co^{2+} doped TiO_2 through the relation [57]:

$$C = \frac{N \mu_{\text{eff}}^2 \mu_{\text{B}}^2}{3k_{\text{B}}} \quad (2)$$

where N is the number of interaction magnetic ions per g, μ_{B} is Bohr magneton, and k_{B} is Boltzmann constant. The effective magnetic moment calculated from the experimental values of Curie constant, Table 2, are very close to the theoretical value ($\mu_{\text{eff}} = 3.87 \mu_{\text{B}}/\text{Co}$) for high-spin ($S=3/2$) Co^{2+} with the quenching of orbital angular moment under the crystal field formed by surrounding O^{2-} ions [58]. The magnitude of experimentally estimated μ_{eff} indicates that high-spin Co^{2+} ions contribute to the paramagnetic behavior of the Co^{2+} doped TiO_2 films, as well as to the ferromagnetic behavior observed at room temperature (Fig. 5). The oxygen defects/vacancies surrounding Co^{2+} ions appear to be crucial parameter leading to weak ferromagnetic behavior.

In general, ferromagnetic ordering in transition metal doped TiO_2 could be explained in terms of the non-carrier mediated bound magnetic polaron (BMP) model. According to this theory, when defect concentration exceeds the percolation threshold, oxygen vacancy defects overlap many dopant ions to yield BMPs, which results in ferromagnetic coupling between dopant ions mediating through oxygen vacancy [8,14]. The polaron percolation threshold, δ_{p} , and the dopant cation percolation threshold, x_{p} , represent two main parameters that determine the nature of the magnetic interaction. Ferromagnetic ordering occurs when $\delta > \delta_{\text{p}}$ and $x < x_{\text{p}}$, while antiferromagnetism or ferrimagnetism appears beyond x_{p} , where there are continuous paths throughout the crystal, joining nearest-neighbor magnetic cations [14]. Slight increase of the value of magnetic moment with increasing the concentration of Co^{2+} ions in studied samples (Fig. 5), indicated that the dopant concentration does not exceed the percolation threshold.

On the other hand, a significant decrease of magnetic moment per cobalt atom was observed in 1.69 and 2.5 at% Co^{2+} doped TiO_2 nanocrystals of various shapes (polygonal and prolate spheroids), compared to the magnetic moment per Co ($0.25 \mu_{\text{B}}/\text{Co}$) reported in our previous work, for 0.46 at% Co^{2+} doped TiO_2 nanocrystals (only polygonal), synthesized in the same way [24]. According to literature, there are several reasons for the observed reduction of the magnetic moment per cation. The possible existence of clusters of antiferromagnetically-coupled spins when dopant cation concentration is less than dopant cation percolation threshold ($x < x_{\text{p}}$), can reduce the average moment per cation [14]. However, obtained magnetization curves with observed saturation (Fig. 5), indicate no such paraprocess involved. Also, the existence of low-spin state of Co^{2+} is excluded if it is incorporated in anatase TiO_2 [59]. Yermakov *et al.* [60] explained observed reduction of the magnetic moment in nanocrystalline $\text{TiO}_2:\text{Co}$ samples by itinerant magnetism model due to cobalt localization and magnetic ordering on the surface which also contains oxygen defects.

It is known that the concentration of oxygen vacancies, i.e., undercoordinated defects in TiO_2 nanocrystals depends on their surface morphologies and sizes [42]. A low concentration of oxygen vacancies in 1.69 and 2.5 at% Co^{2+} doped TiO_2 nanocrystals could be the reason for the observed significantly lower magnetic moment in spite of relatively high concentrations of dopant ions (max. 2.5 at%) in comparison to 0.46 at% Co^{2+} doped TiO_2 nanoparticles [24]. Since TEM characterization (Fig. 1(b)) revealed mixture of finer polygonal and coarser prolate ellipsoid nanocrystals in 2.5 at% Co^{2+} doped TiO_2 sample, the low value of magnetic moment in this sample might be related to lower level of surface oxygen vacancy defects in prolate nanospheroids [61]. To confirm the existence of different concentration of oxygen vacancies in polygonal and prolate ellipsoid TiO_2 nanocrystals, we applied photoluminescence spectroscopy, a method sensitive to the presence of defects in the crystalline structure of semiconductor nanoparticles [21]. Photoluminescence spectrum of TiO_2 nanocrystals of different shapes (polygonal and prolate spheroids) after band gap excitation at $\lambda_{\text{exc}} = 365 \text{ nm}$ which were synthesized under the same experimental conditions but in absence of Co ions is shown in Fig. 7.

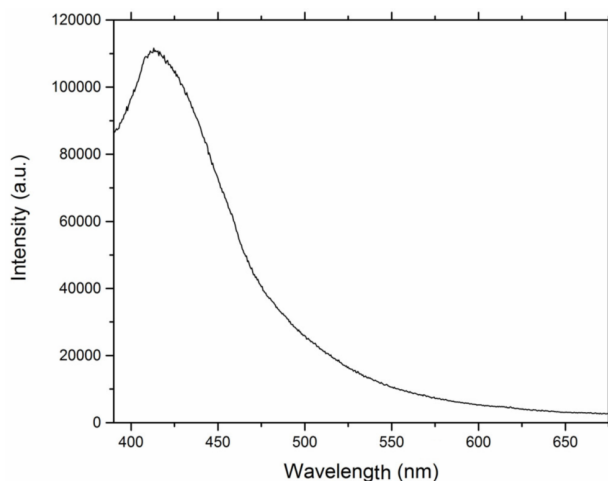


Fig. 7 PL spectrum of non-doped TiO₂ nanocrystals of mixed shapes (polygonal and prolate ellipsoid).

An intense band observed at 2.95 eV (420 nm) can be assigned to the lowest indirect transition from the center to the edge of the Brillouin zone, $\Gamma_{1b}-X_{1a}$ [62]. Absence of intense bands in the low energy region of PL spectrum was an indication of lower concentration/amount of structural defects. Namely, in our previous work we reported that appearance of the lower energy emissions in the photoluminescence spectrum of polygonal (only) TiO₂ nanocrystals, at 2.88 and 2.56 eV, which originate from the intra-gap levels transitions, was an indication of existence of lattice and/or surface structural defects (oxygen vacancies) [21]. Observed difference in PL spectrum of TiO₂ nanocrystals consisting of polygonal and prolate spheroid-like particles (Fig. 7), compared to only polygonal TiO₂ particles [21] implied to the significantly lower concentration of oxygen vacancies in prolate spheroid-like nanocrystals. Such assumption is in agreement with their larger dimension, decreased curvature, and consequently lower amount of surface defects. Finally, it can be concluded that room temperature ferromagnetism observed in our sample is directly correlated to the concentration of oxygen vacancies.

However, Santara *et al.* [63] demonstrated that concentration of oxygen vacancies by itself does not affect the magnitude of magnetic moment, but they also suggested that the defect environment and the surface morphology of the nanoparticles could be of crucial importance for achieving of measurable ferromagnetic interaction. The greater density of the oxygen vacancy helps to produce more BMP which yields a greater overall volume occupied by BMP, leading to an overlap of BMPs and enhancing ferromagnetic behavior.

4 Conclusions

In summary, Co²⁺ doped TiO₂ nanocrystals were synthesized in a two-step hydrothermal method. Dispersions of previously synthesized titania nanotubes in the presence of different concentrations of Co²⁺ ions at pH=5, were used as precursors. XRD study demonstrated the absence of impurity phases and confirmed anatase crystal structure in 1.69 and 2.5 at% Co²⁺ doped TiO₂ nanocrystals independently of the concentrations of dopant ions. TEM analysis revealed the presence of the mixture of polygonal nanocrystals, with average dimension of 14 nm, and prolate spheroid-like nanocrystals with lengths up to 120 nm. Both samples of 1.69 and 2.5 at% Co²⁺ doped TiO₂ nanocrystals exhibited weak ferromagnetic ordering with closed loop and coercivity $H_c \approx 100$ Oe, accompanied with paramagnetic behavior. The low values of magnetic moments per Co in both samples that contain polygonal and prolate spheroid-like nanocrystals, were probably the consequence of the lower total number of surface defects/oxygen vacancies. The PL spectrum of non-doped TiO₂ nanocrystals of different shapes confirmed the lower number of surface defects (oxygen vacancies) within.

Acknowledgements

The financial support for this work was provided by the Ministry of Education, Science and Technological Development of Republic of Serbia (Project Nos. OI 172056 and III 45020). This work was done under umbrella of COST Action MP1106. Z. K. thanks for the support from the project III 45018 from the Ministry of Education, Science and Technological Development of Republic of Serbia. TEM characterization of titania nanotubes was provided by Prof. P. Ahrenkiel, South Dakota School of Mines & Technology, Rapid City, SD, USA.

References

- [1] Janisch R, Gopal P, Spaldin NA. Transition metal-doped TiO₂ and ZnO—Present status of the field. *J Phys: Condens Matter* 2005, **17**: R657–R689.
- [2] Nguyen HH, Prellier W, Sakai J, *et al.* Substrate effects on the room-temperature ferromagnetism in Co-doped TiO₂ thin films grown by pulsed laser deposition. *J Appl Phys* 2004, **95**: 7378–7380.
- [3] Kim J-Y, Park J-H, Park B-G, *et al.* Ferromagnetism

- induced by clustered Co in Co-doped anatase TiO₂ thin films. *Phys Rev Lett* 2003, **90**: 017401.
- [4] Kennedy RJ, Stampe PA, Hu E, *et al.* Hopping transport in TiO₂:Co: A signature of multiphase behavior. *Appl Phys Lett* 2004, **84**: 2832–2834.
- [5] Hong NH, Sakai J, Prellier W. Distribution of dopant in Fe:TiO₂ and Ni:TiO₂ thin films. *J Magn Magn Mater* 2004, **281**: 347–352.
- [6] Sharma P, Gupta A, Rao KV, *et al.* Ferromagnetism above room temperature in bulk and transparent thin films of Mn-doped ZnO. *Nat Mater* 2003, **2**: 673–677.
- [7] Lim S-W, Jeong M-C, Ham M-H, *et al.* Hole-mediated ferromagnetic properties in Zn_{1-x}Mn_xO thin films. *Jpn J Appl Phys* 2004, **43**: L280–L283.
- [8] Patel SKS, Gajbhiye NS. Room temperature magnetic properties of Cu-doped titanate, TiO₂(B) and anatase nanorods synthesized by hydrothermal method. *Mater Chem Phys* 2012, **132**: 175–179.
- [9] Venkatesan M, Fitzgerald CB, Lunney JG, *et al.* Anisotropic ferromagnetism in substituted zinc oxide. *Phys Rev Lett* 2004, **93**: 177206.
- [10] Yan L, Ong CK, Rao XS. Magnetic order in Co-doped and (Mn,Co) codoped ZnO thin films by pulsed laser deposition. *J Appl Phys* 2004, **96**: 508–511.
- [11] Gupta A, Cao H, Parekh K, *et al.* Room temperature ferromagnetism in transition metal (V, Cr, Ti) doped In₂O₃. *J Appl Phys* 2007, **101**: 09N513.
- [12] Wang XL, Dai ZX, Zeng Z. Search for ferromagnetism in SnO₂ doped with transition metals (V, Mn, Fe, and Co). *J Phys: Condens Matter* 2008, **20**: 045214.
- [13] Ogale SB. Dilute doping, defects, and ferromagnetism in metal oxide systems. *Adv Mater* 2010, **22**: 3125–3155.
- [14] Coey JMD, Venkatesan M, Fitzgerald CB. Donor impurity band exchange in dilute ferromagnetic oxides. *Nat Mater* 2005, **4**: 173–179.
- [15] Errico LA, Renteria M, Weissman M. Theoretical study of magnetism in transition-metal-doped TiO₂ and TiO_{2-δ}. *Phys Rev B* 2005, **72**: 184425.
- [16] Choudhury B, Choudhury A. Oxygen vacancy and dopant concentration dependent magnetic properties of Mn doped TiO₂ nanoparticle. *Curr Appl Phys* 2013, **13**: 1025–1031.
- [17] Weissmann M, Errico LA. The role of vacancies, impurities and crystal structure in the magnetic properties of TiO₂. *Physica B* 2007, **398**: 179–183.
- [18] Erwin SC, Zu L, Haftel MI, *et al.* Doping semiconductor nanocrystals. *Nature* 2005, **436**: 91–94.
- [19] Bryan JD, Gamelin DR. Doped semiconductor nanocrystals: Synthesis, characterization, physical properties, and applications. *Prog Inorg Chem* 2005, **54**: 47–126.
- [20] Vranješ M, Kuljanin-Jakovljević J, Radetić T, *et al.* Structure and luminescence properties of Eu³⁺ doped TiO₂ nanocrystals and prolate nanospheroids synthesized by the hydrothermal processing. *Ceram Int* 2012, **38**: 5629–5636.
- [21] Vranješ M, Kuljanin-Jakovljević J, Ahrenkiel SP, *et al.* Sm³⁺ doped TiO₂ nanoparticles synthesized from nanotubular precursors—Luminescent and structural properties. *J Lumin* 2013, **143**: 453–458.
- [22] Vranješ M, Konstatinović Z, Pomar A, *et al.* Room-temperature ferromagnetism in Ni²⁺ doped TiO₂ nanocrystals synthesized from nanotubular precursors. *J Alloys Compd* 2014, **589**: 42–47.
- [23] Vranješ M, Kuljanin-Jakovljević J, Konstatinović Z, *et al.* Room temperature ferromagnetism in Cu²⁺ doped TiO₂ nanocrystals: The impact of their size, shape and dopant concentration. *Mater Res Bull* 2016, **76**: 100–106.
- [24] Kuljanin-Jakovljević J, Radoičić M, Radetić T, *et al.* Presence of room temperature ferromagnetism in Co²⁺ doped TiO₂ nanoparticles synthesized through shape transformation. *J Phys Chem C* 2009, **113**: 21029–21033.
- [25] Yan HG, Zeng HC. Synthetic architectures of TiO₂/H₂Ti₅O₁₁·H₂O, ZnO/H₂Ti₅O₁₁·H₂O, ZnO/TiO₂/H₂Ti₅O₁₁·H₂O, and ZnO/TiO₂ nanocomposites. *J Am Chem Soc* 2005, **127**: 270–278.
- [26] Yang X, Karthik C, Li X, *et al.* Oriented nanocrystal arrays of selectable polymorphs by chemical sculpture. *Chem Mater* 2009, **21**: 3197–3201.
- [27] Kasuga T, Hiramatsu M, Hoson A, *et al.* Titania nanotubes prepared by chemical processing. *Adv Mater* 1999, **11**: 1307–1311.
- [28] Cheary RW, Coelho A. A fundamental parameters approach to X-ray line-profile fitting. *J Appl Cryst* 1992, **25**: 109–121.
- [29] Rietveld HM. A profile refinement method for nuclear and magnetic structures. *J Appl Cryst* 1969, **2**: 65–71.
- [30] Pecharsky VK, Zavalij PY. *Fundamentals of Powder Diffraction and Structural Characterization of Materials*. New York: Springer, 2009.
- [31] Šaponjić ZV, Dimitrijević NM, Poluektov OG, *et al.* Charge separation and surface reconstruction: A Mn²⁺ doping study. *J Phys Chem B* 2006, **110**: 25441–25450.
- [32] Dimitrijević NM, Šaponjić ZV, Rabatić BM, *et al.* Effect of size and shape of nanocrystalline TiO₂ on photogenerated charges. An EPR study. *J Phys Chem C* 2007, **111**: 14597–14601.
- [33] Barnard AS, Curtiss LA. Prediction of TiO₂ nanoparticle phase and shape transitions controlled by surface chemistry. *Nano Lett* 2005, **5**: 1261–1266.
- [34] Sugimoto T, Zhou X. Synthesis of uniform anatase TiO₂ nanoparticles by the gel–sol method: 2. Adsorption of OH⁻ ions to Ti(OH)₄ gel and TiO₂ particles. *J Colloid Interface Sci* 2002, **252**: 347–353.
- [35] Sugimoto T, Zhou X, Muramatsu A. Synthesis of uniform anatase TiO₂ nanoparticles by gel–sol method: 1. Solution chemistry of Ti(OH)_n⁽⁴⁻ⁿ⁾⁺ complexes. *J Colloid Interface Sci* 2002, **252**: 339–346.
- [36] Nian J-N, Teng H. Hydrothermal synthesis of single-crystalline anatase TiO₂ nanorods with nanotubes as the precursor. *J Phys Chem B* 2006, **110**: 4193–4198.
- [37] Bischoff BL, Anderson MA. Peptization properties in the sol–gel preparation of porous anatase (TiO₂). *Chem Mater* 1995, **7**: 1772–1778.
- [38] De los Santos DM, Navas J, Sánchez-Coronilla A, *et al.* Highly Al-doped TiO₂ nanoparticles produced by ball mill method: Structural and electronic characterization. *Mater Res Bull* 2015, **70**: 704–711.

- [39] Delgado AV, González-Caballero F, Hunter RJ, *et al.* Measurement and interpretation of electrokinetic phenomena. *J Colloid Interface Sci* 2007, **309**: 194–224.
- [40] Yahia MB, Lemoigno F, Beuvier T, *et al.* Updated references for the structural, electronic, and vibrational properties of TiO₂(B) bulk using first-principles density functional theory calculations. *J Chem Phys* 2009, **130**: 204501.
- [41] Vranješ M, Šaponjić ZV, Živković LS, *et al.* Elongated titania nanostructures as efficient photocatalysts for degradation of selected herbicides. *Appl Catal B: Environ* 2014, **160–161**: 589–596.
- [42] Šaponjić ZV, Dimitrijević NM, Tiede DM, *et al.* Shaping nanometer-scale architecture through surface chemistry. *Adv Mater* 2005, **17**: 965–971.
- [43] Khurana C, Pandey OP, Chudasama B. Synthesis of visible light-responsive cobalt-doped TiO₂ nanoparticles with tunable optical band gap. *J Sol–Gel Sci Technol* 2015, **75**: 424–435.
- [44] Cobalt: Radii of atoms and ions. Available at http://www.webelements.com/cobalt/atom_sizes.html.
- [45] You M, Kim TG, Sung Y-M. Synthesis of Cu-doped TiO₂ nanorods with various aspect ratios and dopant concentration. *Cryst Growth Des* 2010, **10**: 983–987.
- [46] Lee JD. *Concise Inorganic Chemistry*. John Wiley & Sons, 2008.
- [47] Choudhury B, Choudhury A. Luminescence characteristics of cobalt doped TiO₂ nanoparticles. *J Lumin* 2012, **132**: 178–184.
- [48] Husain S, Alkhtaby LA, Giorgetti E, *et al.* Influence of cobalt doping on the structural, optical and luminescence properties of sol–gel derived TiO₂ nanoparticles. *Philos Mag A* 2017, **97**: 17–27.
- [49] Tauc J, Grigorovici R, Vancu A. Optical properties and electronic structure of amorphous germanium. *Phys Status Solidi b* 1966, **15**: 627–637.
- [50] Pal M, Pal U, Jimenez JMGY, *et al.* Effects of crystallization and dopant concentration on the emission behavior of TiO₂:Eu nanophosphors. *Nanoscale Res Lett* 2012, **7**: 1–12.
- [51] Das K, Sharma SN, Kumar M, *et al.* Morphology dependent luminescence properties of Co doped TiO₂ nanostructures. *J Phys Chem C* 2009, **113**: 14783–14792.
- [52] Archer PI, Santangelo SA, Gamelin DR. Direct observation of sp-d exchange interactions in colloidal Mn²⁺- and Co²⁺-doped CdSe quantum dots. *Nano Lett* 2007, **7**: 1037–1043.
- [53] Emeline AV, Kuznetsov VN, Rybchuk VK, *et al.* Visible-light-active titania photocatalysts: The case of N-doped TiO₂s—Properties and some fundamental issues. *International Journal of Photoenergy* 2008, **2008**: Article ID 258394.
- [54] Justicia I, Ordejon P, Canto G, *et al.* Designed self-doped titanium oxide thin films for efficient visible-light photocatalysis. *Adv Mater* 2002, **14**: 1399–1402.
- [55] Zuo F, Wang L, Wu T, *et al.* Self-doped Ti³⁺ enhanced photocatalyst for hydrogen production under visible light. *J Am Chem Soc* 2010, **132**: 11856–11857.
- [56] Anitha B, Abdul Khadar A, Banerjee A. Paramagnetic behavior of Co doped TiO₂ nanocrystals controlled by self-purification mechanism. *J Solid State Chem* 2016, **239**: 237–245.
- [57] Punnoose A, Hays J, Shutthanandan V, *et al.* Room-temperature ferromagnetism in chemically synthesized Sn_{1-x}Co_xO₂ powders. *Appl Phys Lett* 2004, **85**: 1559.
- [58] Spaldin NA. *Magnetic Materials: Fundamentals and Applications*. Cambridge University Press, 2003.
- [59] Geng WT, Kim KS. Interplay of local structure and magnetism in Co-doped TiO₂ anatase. *Solid State Commun* 2004, **129**: 741–746.
- [60] Yermakov AY, Zakharova GS, Uimin MA, *et al.* Surface magnetism of cobalt-doped anatase TiO₂ nanopowders. *J Phys Chem C* 2016, **120**: 28857–28866.
- [61] Rabatic BM, Dimitrijevic NM, Cook RE, *et al.* Spatially confined corner defects induce chemical functionality of TiO₂ nanorods. *Adv Mater* 2006, **18**: 1033–1037.
- [62] Daude N, Gout C, Jouanin C. Electronic band structure of titanium dioxide. *Phys Rev B* 1977, **15**: 3229.
- [63] Santara B, Giri PK, Imakita K, *et al.* Evidence of oxygen vacancy induced room temperature ferromagnetism in solvothermally synthesized undoped TiO₂ nanoribbons. *Nanoscale* 2013, **5**: 5476–5488.

Open Access The articles published in this journal are distributed under the terms of the Creative Commons Attribution 4.0 International License (<http://creativecommons.org/licenses/by/4.0/>), which permits unrestricted use, distribution, and reproduction in any medium, provided you give appropriate credit to the original author(s) and the source, provide a link to the Creative Commons license, and indicate if changes were made.



Room temperature ferromagnetism in Cu²⁺ doped TiO₂ nanocrystals: The impact of their size, shape and dopant concentration



M. Vranješ^a, J. Kuljanin-Jakovljević^a, Z. Konstantinović^{b,c}, A. Pomar^c, S.P Ahrenkiel^d, T. Radetić^e, M. Stoiljković^a, M. Mitrić^a, Z. Šaponjić^{a,*}

^a Vinča Institute of Nuclear Sciences, University of Belgrade, P.O. Box 522, 11001 Belgrade, Serbia

^b Center for Solid State Physics and New Materials, Institute of Physics Belgrade, University of Belgrade, Pregrevica 118, 11080 Belgrade, Serbia

^c Institut de Ciència de Materials de Barcelona, CSIC, Campus UAB, 08193 Bellaterra, Spain

^d South Dakota School of Mines & Technology, Rapid City, SD 57701, USA

^e Faculty of Technology and Metallurgy, University of Belgrade, Karnegijeva 4, 11120 Belgrade, Serbia

ARTICLE INFO

Article history:

Received 14 September 2015

Received in revised form 22 November 2015

Accepted 26 November 2015

Available online 8 December 2015

Keywords:

- A. Nanostructures
- A. Oxides
- A. Semiconductors
- B. Solvothermal
- B. Magnetic properties
- C. X-ray diffraction
- C. Transmission electron microscopy (TEM)
- D. Crystal structures
- D. Defects

ABSTRACT

Cu²⁺ doped TiO₂ nanocrystals were synthesized using dispersions of titania nanotubes in the presence of Cu²⁺ ions as a precursors. The morphologies of nanotubular titania precursors and resulted Cu²⁺ doped TiO₂ nanocrystals were characterized by TEM. Structural and optical properties were studied by XRPD analysis and UV–vis spectroscopy in reflectance mode, respectively. Their magnetic properties were investigated using SQUID magnetometer. Tetragonal anatase crystalline structure was confirmed in all synthesized samples. Polygonal ($d \sim 15$ nm) and spheroid like (length, up to 90 nm) Cu²⁺ doped TiO₂ nanocrystals in samples synthesized at different pHs were observed by TEM. Ferromagnetic ordering with almost closed loop ($H_c \sim 200$ Oe) was detected in all Cu²⁺ doped TiO₂ nanoparticle films. The saturation magnetization values varied depending on the Cu²⁺ concentration, nanoparticles shape, size and consequently different number of oxygen vacancies. This study revealed possibility to control magnetic ordering by changing the shape/aspect ratio of Cu²⁺ doped TiO₂ nanocrystals.

© 2015 Elsevier Ltd. All rights reserved.

1. Introduction

The possibility of combining magnetic and semiconductor properties in materials such as diluted magnetic semiconductors (DMSs) have provoked great interest due to the open road for fabrication of spin-based devices. These devices can be used for optical and magnetic sensors as well as for the processing, transmission and storage of digital information [1–3]. For fabrication of spin-based devices the materials such as wide band gap diluted magnetic semiconductors with significant magnetic moments and high Curie temperature are indispensable [4]. Most of the initial work was focused, in particular, on intrinsically magnetic transition metal ions doped III–V and II–VI compound semiconductors. These materials have been broadly studied because of interesting magnetic, optical, magneto-optical and magnetic transport properties [5].

Recently it was theoretically predicted that transition metal ions doped metal oxides (TiO₂, SnO₂, In₂O₃, ZnO) are suitable material for DMSs with ferromagnetic behavior at room temperature [6–13]. The origin of ferromagnetism in oxide DMSs is still controversial subject due to suggested intrinsic ferromagnetism [14] and on the other hand due to suspected precipitation of magnetic clusters or secondary magnetic phases formed [15]. Hence, with aim to escape the possible contribution of secondary phases in the material to ferromagnetism, the use of basically non-magnetic dopant ions such as Cu, motivated researchers to probe experiments on Cu doped metal oxides. Cu is potentially magnetic ion with total spin of $1/2$ by Hund's rule [16]. Secondary phases that could be formed in Cu doped metal oxides, such as CuO, Cu₂O and metallic Cu are non-ferromagnetic [8]. Duhalde et al. reported unexpected and significant room temperature ferromagnetism in Cu-doped TiO₂ films grown by pulse laser deposition [17]. They used films to enhance the role of defects due to their greater surface or interface to volume ratio comparing to single-crystal or polycrystalline ceramics. Recently, Patel et al. studied the role of dopant ions in the origin of room temperature ferromagnetism in

* Corresponding author at: Laboratory for Radiation Chemistry and Physics, "Vinča" Institute of Nuclear Sciences, University of Belgrade, P.O. Box 522, 11001 Belgrade, Serbia. Fax: +381 11 3408607.

E-mail address: saponjic@vinca.rs (Z. Šaponjić).

Cu doped titanate, monoclinic TiO_2 (B) and anatase TiO_2 nanorods synthesized by hydrothermal method [8].

In this article we reported a new approach toward hydrothermal synthesis of Cu^{2+} doped TiO_2 nanocrystals of various shapes and sizes using as a precursor dispersions of titania nanotubes at $\text{pH}=3$ and $\text{pH}=5$, in the presence of different concentrations of Cu^{2+} ions. The main focus of this study was on hysteresis loop (M–H) measurements of Cu^{2+} doped TiO_2 nanocrystals that were applied to check the particles size, shape and Cu^{2+} concentration dependent room temperature ferromagnetism. The morphologies of doped nanocrystals were characterized by TEM. Their structural and optical properties were studied by XRPD analysis and UV–vis spectroscopy in reflectance mode, respectively. The magnetic properties were studied by SQUID magnetometer.

2. Experimental

2.1. Synthesis

All chemicals were reagent-grade from Aldrich and used as received. The precursor titania nanotubes were synthesized according to modified procedure of Kasuga et al. [18]. The 2 g of Degussa TiO_2 powder was dispersed in 50 ml of 10 M NaOH solution and hydrothermally treated for 48 h in a Teflon vessel (Parr acid digestion bomb, total volume 125 ml) under saturated vapor pressure of water at 120°C . Subsequently, the ensuing powder was washed once with 1 M HCl and thereafter was rinsed by distilled water. Separation of powder from the washing solution (water) was done by centrifugation, after each washing step. The washing procedure was repeated till reached $\text{pH}=7$. The powder was then air dried at 70°C .

The Cu^{2+} doped TiO_2 nanocrystals were prepared by hydrothermal method, using the dispersions of titania nanotubes at $\text{pH}=3$ and $\text{pH}=5$, in the presence of different concentrations of Cu^{2+} ions, as precursor. The 0.29, 0.34 and 0.37 at% Cu^{2+} doped TiO_2 nanocrystals were synthesized applying hydrothermal treatment to precursor dispersions which contained titania nanotubes (125 mg/50 ml H_2O at $\text{pH}=3$), in the presence of three different concentrations of $\text{Cu}(\text{NO}_3)_2 \times 2.5\text{H}_2\text{O}$: 3.11×10^{-4} M (1%), 6.23×10^{-4} M (2%) and 1.24×10^{-3} M (4%), respectively. The precursor dispersions were stirred for 3 h followed by hydrothermal treatment at 250°C for 90 min in Teflon vessel (Parr acid digestion bomb, total volume 125 ml).

The 0.83 and 1.03 at% Cu^{2+} doped TiO_2 nanocrystals were synthesized applying hydrothermal treatment on precursor dispersions which contained titania nanotubes (125 mg/50 ml H_2O , at $\text{pH}=5$), in the presence of two different concentrations of $\text{Cu}(\text{NO}_3)_2 \times 2.5\text{H}_2\text{O}$: 3.11×10^{-4} M (1%) and 6.23×10^{-4} M (2%). The stirring and hydrothermal treatment conditions were the same as previously described for the processing at $\text{pH}=3$.

After completion of hydrothermal process the resulted doped TiO_2 nanocrystals were efficiently re-dispersed in water. The excess of unbound Cu^{2+} ions and simply adsorbed on the particles surface as well as Cu^{2+} ions weakly bound to the anatase lattice in the undercoordinated surface defect sites (first few atomic layers), in all synthesized samples were removed by dialysis against 10 times the larger volume of acidified water ($\text{pH}=3$ or $\text{pH}=5$, depending on the previous conditions of synthesis) at 4°C for 3 days. Water was changed daily. For dialysis processes were used Spectra/Por Dialysis Membranes, MWCO: 3500 (Spectrum Laboratories, Inc., Rancho Dominguez, CA). This procedure was applied in order to monitor the phenomena that are only a consequence of the incorporated dopant ions into the crystalline structure of nanoparticles.

2.2. Characterization

The percentage ratios of Cu^{2+} to Ti^{4+} ions in doped TiO_2 nanocrystals were determined using ICP Emission Spectrometer: ICAP 6000 series (Thermo Electron Corporation). Prior to the ICP measurements, to efficient dissolving of nanoparticles, the each powdered sample was dispersed in 3 ml of concentrated sulfuric acid and hydrothermally treated (60 min/ 250°C) in Teflon vessel (Parr acid digestion bomb).

The shape and size of precursor titania nanotubes were characterized using a JEOL TEM 2100 LaB₆ operated at 200 kV, while the Cu^{2+} doped TiO_2 nanoparticles were characterized by JEOL 100CX TEM operating at 100 kV.

Reflectance spectra of powders of Cu^{2+} doped TiO_2 nanoparticles were recorded at room temperature using Thermo Scientific Evolution 600 UV/Vis spectrophotometer.

The XRPD patterns were obtained on a Philips PW-1050 automated diffractometer using $\text{Cu K}\alpha$ radiation (operated at 40 kV and 30 mA). Diffraction data for structural analysis were collected in the 2θ range 10 – 120° , with scanning steps of 0.02 and exposition time of 12 s. Structure analysis was done using the KOALARIE computing program [19], based on the Rietveld full profile refinement method [20]. Samples for XRPD measurements were prepared using standard protocol [21].

The films for magnetic characterization were prepared by drop casting of dialyzed dispersions of Cu^{2+} doped TiO_2 nanocrystals onto pre-cleaned glass substrate. The films were annealed in air for 2 min at 100°C after each drop. The amount of the dopant ions for magnetic moment calculation was determined from the weight of each film.

The field dependence of the magnetic moment was measured with a super conducting quantum interference device magnetometer (Quantum Design). The magnetic field was applied parallel to the film surface. The measured magnetization at 300 K was corrected for the diamagnetic background of the glass substrate

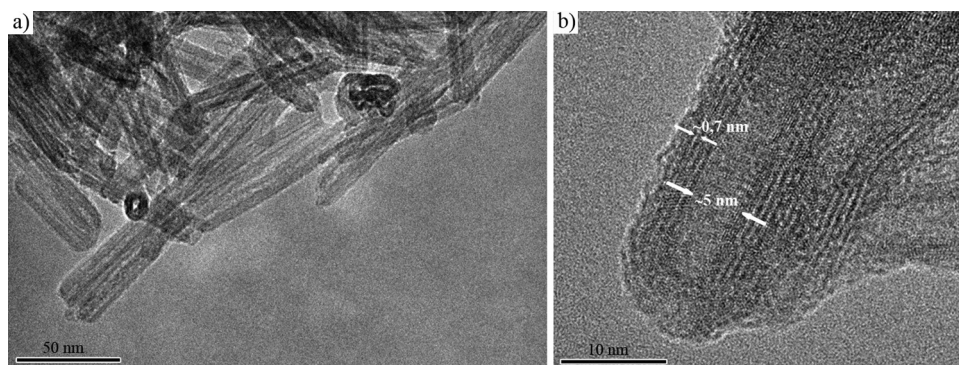


Fig. 1. TEM images of scrolled titania nanotubes at lower (a) and higher resolutions (b).

(derived from high-field dependence magnetization data). Ferromagnetism did not disappear in the next two months after synthesis keeping the sample in air.

3. Results and discussion

The Cu^{2+} doped TiO_2 nanocrystals of different shapes were obtained by a two-step synthesis process using dispersions of titania nanotubes in the presence of various concentrations of Cu^{2+} ions as precursor. Precursor titania nanotubes were synthesized according to modified Kasuga's procedure [18]. In our synthetic approach the duration of hydrothermal process extended, temperatures decreased and finally different washing procedure of synthesized nanotubes applied.

In Fig. 1, conventional TEM images at different resolutions are presented. Nanotubes of different lengths but with uniform diameter of about 10 nm were observed. Layered structure of scrolled titania nanotubes with quite large interlayer spacing, about 0.7 nm and inner diameter of 5 nm can be clearly seen in Fig. 1b.

From XRPD measurements, presented in our previous work [22], the development of the anatase crystalline phase in the presence of insignificantly small amount of monoclinic TiO_2 (B) crystalline structure in synthesized nanotubes was observed.

It is known that additional hydrothermal treatment applied on dispersions of titania nanotubes leads to their transformation in highly crystalline TiO_2 nanocrystals of different shapes and sizes [23]. We exploited this fact to manage transformation of nanotubes in the presence of Cu^{2+} ions with aim to synthesize Cu^{2+} doped TiO_2 nanocrystals of different shapes, size and surface structure.

Size and shape of Cu^{2+} doped TiO_2 nanocrystals were studied using TEM. The TEM image of 0.34 at% Cu^{2+} doped TiO_2 nanocrystals, synthesized at pH=3, is shown in Fig. 2a. Irregularly shaped polygonal nanoparticles with average dimension of $d \sim 15$ nm were observed.

In Fig. 2b, TEM micrograph of 1.03 at% Cu^{2+} doped TiO_2 nanocrystals synthesized at pH=5 is shown. The appearance of larger, ellipsoid like nanoparticles beside polygonal one can be clearly seen. The lengths of ellipsoid like particles were up to more than 100 nm, with larger size distribution. This finding is in agreement with our previous work where in the course of the hydrothermal synthesis of doped nanoparticles using, as a precursor, dispersion of titania nanotubes at higher pH, the formation of anisotropic doped TiO_2 nanoparticles also detected, independently of the type of dopant ions [24].

The reflection spectra of powdered samples of 0.26–0.37 at% Cu^{2+} doped TiO_2 nanoparticles, synthesized at pH=3, are shown in Fig. 3a. A wide range of defect related absorption in the wavelength region $\lambda \sim 400$ –600 nm, was noticed. The influence of dopant

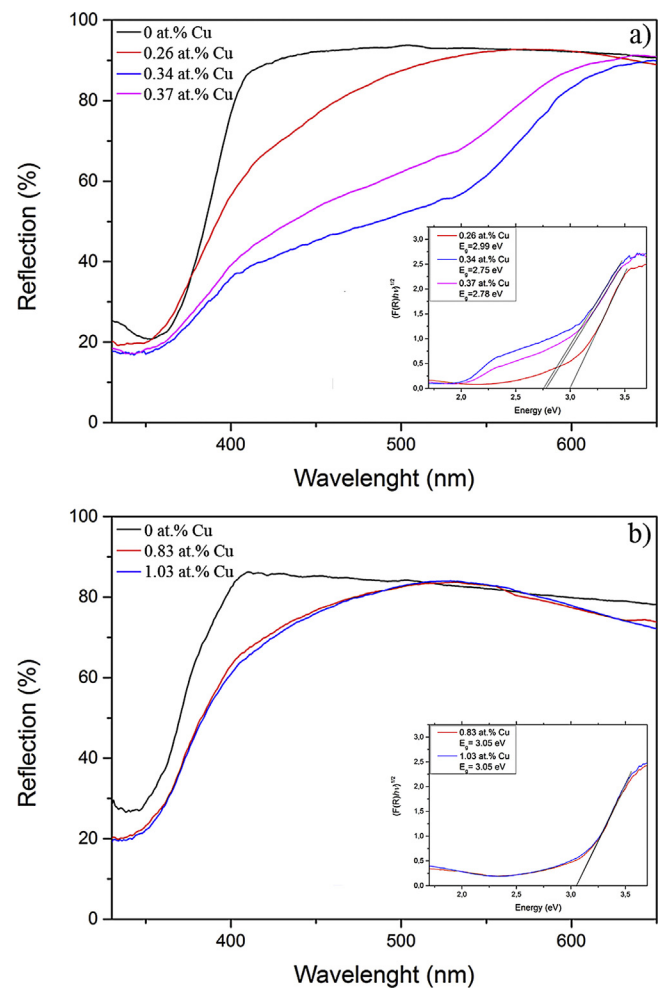


Fig. 3. Reflection spectra of powdered samples of undoped, 0.26, 0.34 and 0.37 at% Cu^{2+} doped TiO_2 nanoparticles synthesized at pH=3 (a) and undoped, 0.83 and 1.03 at% Cu^{2+} doped TiO_2 nanoparticles synthesized at pH=5 (b). Insets: Tauc plots for band gap energy estimations.

concentrations on optical properties of TiO_2 matrix is evident. Observed changes were an indication of successful incorporation of Cu^{2+} ions in anatase crystalline structure of TiO_2 nanoparticles. On the other hand, without incorporation of Cu^{2+} ions, the reflection spectra will be identical to reflection spectrum of bare TiO_2 nanoparticles which is characterized with monotonous build-up of absorption at 388 nm. Also should be mentioned that simple undesired adsorption of unincorporated Cu^{2+} ions on the surface of

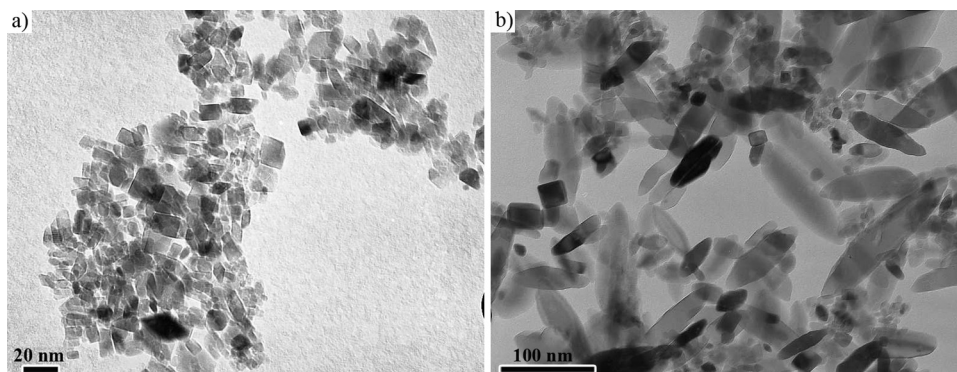


Fig. 2. TEM images of 0.34 at% Cu^{2+} doped TiO_2 nanoparticles synthesized at pH=3 (a) and 1.03 at% Cu^{2+} doped TiO_2 nanocrystals synthesized at pH=5 (b).

TiO₂ nanocrystals, cannot lead to the observed changes in reflection spectra.

For the analysis of reflectance spectra Kubelka–Munk relation was used, which allows the optical absorbance of a sample to be approximated from its reflectance (R). The function is expressed as:

$$F(R) = \frac{(1 - R)^2}{2R} \quad (1)$$

Using this equation semiconducting materials can be analyzed with a Tauc plot, whereby the absorption coefficient, α , in the Tauc equation is substituted with $F(R)$ [25,26]. Band-gap energies of the Cu²⁺ doped TiO₂ nanoparticles synthesized at pH=3 were estimated from the variation of the Kubelka–Munk function with photon energy, inset Fig. 3a. According to this method, red shifts of band gap energies, which were varied between 2.99 to 2.78 eV for Cu²⁺ doped TiO₂ nanoparticles, observed.

Resulting enhanced absorption of photon energy below the direct band gap in Cu²⁺ doped TiO₂ nanoparticles, Fig. 3a, according to one group of authors, could be the consequence of the narrowing of intrinsic band gap of TiO₂ [27]. However, others opposed to band gap narrowing claiming that the oxygen vacancies formed upon doping lead to the formation of color centers responsible for appearance of absorption bands in the visible spectral region [27]. It is known that high concentration of oxygen vacancy in doped nanocrystals could break selection rule for indirect transitions, characteristic for defect free TiO₂ crystals, therefore enhancing the absorption for photon frequencies below the direct band gap [28,29].

The intensity of absorption of Cu²⁺ doped TiO₂ nanoparticles in visible part of the spectra, Fig. 3a, increases with increasing concentration of dopant ions. This phenomenon indicates increased number of created oxygen vacancies within doped nanocrystals as a consequence of successful incorporation of Cu²⁺ into the TiO₂ lattice. Oxygen vacancies in such significant amount, as reflection spectra suggested, cannot be formed in crystalline structure of TiO₂ nanoparticles, synthesized on the same way, in the absence of dopant ions. Incorporation of Cu²⁺ ions and

formation of oxygen vacancies in crystalline structure of TiO₂ nanoparticles are interrelated phenomena that occur when applied this synthetic route.

From the *ab initio* calculations it is known that low concentration of Cu impurities reduces oxygen vacancy formation energy in the TiO₂ films [17]. Duhalde et al. predicted by calculation that the energy required to form an oxygen vacancy decreases from 10 eV in the undoped system to 4 eV in the case it is near a Cu impurity. Also, oxygen vacancies will tend to position itself close to the Cu dopant and the energy required to replace a Ti atom by a Cu atom is reduced by 5 eV when there is an oxygen vacancy [17].

The reflection spectra of 0.83 and 1.03 at% Cu²⁺ doped TiO₂ nanoparticles synthesized at pH = 5, are shown in Fig. 3b.

The synthesis of Cu²⁺ doped TiO₂ nanoparticles at pH = 5, resulted in changes of their size and shape, Fig. 2b, as well as in its optical properties, Fig. 3b. Band-gap energies, inset Fig. 3b, associated to 0.83 and 1.03 at% Cu²⁺ doped TiO₂ nanoparticles synthesized at pH=5 were the same, $E_g = 3.05$ eV. The weaker influence of greater concentration of Cu²⁺ ions embedded in crystalline structure of TiO₂ nanoparticles, on their optical properties is obvious, Fig. 3b. The lower absorption in visible part of the spectra compared to absorption of Cu²⁺ doped TiO₂ nanoparticles synthesized at pH = 3, was an indication of lower number of oxygen vacancies formed. The reason for this can be found in bigger size and consequently larger crystallinity domain, different shape and surface structure of ellipsoid like nanoparticles. It was shown in our previous paper that in the ellipsoid like TiO₂ nanoparticles, so called under-coordinated surface defect sites are confined only within five layers of the surface on their tips but without appearance on other surfaces [30]. Under-coordinated defect sites in TiO₂ are characterized by lack of oxygen in the titanium atom coordination (pentacoordinated instead octahedral) [31]. Lower number of under-coordinated defect sites in ellipsoid like nanoparticles, is in agreement with observed changes in reflectance spectra, Fig. 3b, taking into account contribution of oxygen vacancies.

The structural parameters of Cu²⁺ doped TiO₂ nanocrystals synthesized at both pH values (pH=3 and pH=5) were studied

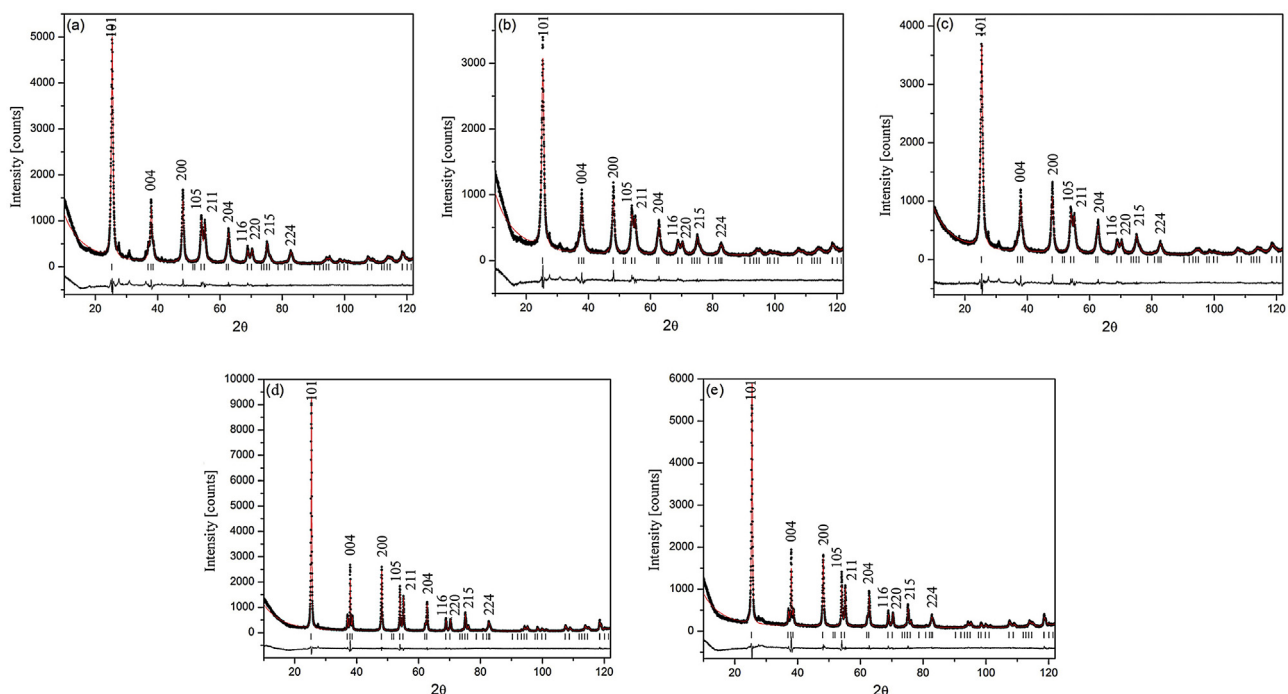


Fig. 4. Rietveld refined X-ray powder diffraction patterns of 0.26 at% (a), 0.34 at% (b), 0.37 at% (c), 0.83 at% (d) and 1.03 at% (e) Cu²⁺ doped TiO₂ nanoparticles. Bragg peak positions, Miller indices, and peak intensities for anatase TiO₂ are included for the reference.

using the X-ray powder diffraction technique. In Fig. 4a–c, the Rietveld refined X-ray powder diffraction patterns of 0.26, 0.34 and 0.37 at% Cu²⁺ doped TiO₂ nanoparticles synthesized at pH=3 were shown. In Fig. 4d–e, XRPD patterns of 0.83 and 1.03 at% Cu²⁺ doped TiO₂ nanoparticles synthesized at pH=5, were presented.

The quite sharp and intense peaks in XRPD patterns, Fig. 4, imply high crystallinity of all samples independently of size and shape of nanoparticles and concentrations of dopant ions. It is known from the literature that the presence of dopant ions also stabilize anatase crystalline structure of TiO₂ [32]. The analysis of positions of diffraction peaks in XRPD patterns has confirmed the tetragonal anatase TiO₂ crystal phase in all samples of Cu²⁺ doped TiO₂ nanoparticles. Absence of diffraction peaks characteristic for impurity phases such as clusters of metallic Cu is evident. Taking into account the applied synthetic route for the synthesis of Cu²⁺ doped TiO₂ nanocrystals, there is no doubt that the Cu (metallic) particles cannot be formed. More precisely, hydrothermal treatments (250 °C/90 min) of dispersions of titania nanotubes in the presence of various concentrations of Cu²⁺ ions, as precursors, were carried out in the dominantly oxidative atmosphere-aerated conditions. Also, there was no reducing species in the dispersion that would be able to reduce Cu²⁺ ions to metallic copper in two electron process ($E^\circ = +0.3419$ eV vs. NHE). Moreover, there was no stabilizing agent in the precursor dispersion without which it is difficult to have stable metal particles in the system. Finally, and even that there was metallic (Cu(0)) copper nanoparticles in the system during the synthesis, they can be easily oxidized under exposure to air in the dark [33]. Also, according to XRD measurements there were no impurities such as copper(I) oxide (Cu₂O), Cu (II) oxide (CuO), and titanium–copper alloy (Cu–Ti) in the final product. Thus, the recrystallization process of titania nanotubes in the presence of Cu²⁺ ions which resulted in formation of Cu²⁺ doped titania nanoparticles, was not disrupted. Also, this finding was an indication of successful integration of Cu ions within TiO₂ matrix, despite the possibility that the amounts of secondary phases formed in the samples could be too low to be detected by XRPD measurement.

The lattice cell parameters of anatase TiO₂ crystalline phase, obtained from Rietveld full profile refinement method and characteristic for all samples of Cu²⁺ doped TiO₂ nanoparticles, are shown in Table 1.

Shifts of lattice parameters *a* and *c* in anatase crystal structures of all samples independently of dopant concentration and synthetic conditions, toward higher values compared to reference values for TiO₂ (PDF 89–4921, *a*=3.777 Å; *c*=9.501 Å), were observed. Such increase of lattice parameters values could be an indication of substitution of Ti⁴⁺ by Cu²⁺ within crystal structure of doped TiO₂ nanoparticles [34]. It should be mentioned here that the ionic radius of Cu²⁺ ions in octahedral coordination (0.87 Å) is not too much larger than ionic radius of Ti⁴⁺ ions (0.745 Å) in the same coordination, to cause significant deformation of anatase crystal lattice [35]. Generally, slightly larger diameter of dopant ions, as in our case for Cu²⁺ ions and significantly different charge from Ti⁴⁺, according to literature [36–38], are not necessarily obstacles for successful incorporation into the anatase lattice. We showed in our previous work [39], in which we presented EXAFS/

XANES characterization of Mn²⁺ doped TiO₂ nanoparticles, the possibility of the bond lengths shortening that occurs in titania matrix after doping with transition metal ions. Also, we have unambiguously confirmed successful doping of subatomic concentrations (0.04–0.4 at%) of even more bigger dopant ions such as Eu³⁺ (ionic radius: 0.947 Å) and Sm³⁺ (ionic radius: 0.964 Å) in anatase TiO₂ nanocrystals, using highly sensitive photoluminescence spectroscopy [24,40]. Likewise, dispersions of titania nanotubes in the presence of rare earth ions were used as a precursors. Possibility for lattice expansion when dopant ions substituted the Ti⁴⁺ was mentioned in the literature [41–43]. According to Sundaresan et al., the increase of lattice parameters with decreasing particle size (from bulk) could be the results of oxygen vacancies formation in nanoparticles [44]. The cell parameters *a* and *c* of the Cu²⁺ doped TiO₂ nanoparticles are increased by up to 0.4% and 0.12%, respectively, as compared with the cell parameters in undoped TiO₂. The reason for such increment could be found also in the nonuniform substitution of Cu²⁺ ion into the Ti sites.

General request for overall charge neutrality in the lattice of TiO₂ nanoparticles after doping with divalent ions is fulfilled by the formation of two oxygen interstitial defects [45] and oxygen vacancies in the nearest-neighbor shell of the dopant. From *ab initio* calculation Duhalde et al. concluded that energy required to form two vacancies near Cu is larger than for formation of one vacancy in the first shell of neighbors of two different Cu impurities and discarded possibility for formation of vacancy clusters [46]. Due to fact that the TiO₂ is an ionic crystal, formation of oxygen vacancies induces a large structural relaxation as a consequence of the repulsion of nearby titanium ions [47]. From tabulated data, shifts toward lower values of lattice parameter *a* by the increase of the dopant concentration in all samples, were observed. On the other hand, value of lattice parameter *c* increased under the same conditions.

The magnetic properties of synthesized samples were investigated at room temperature using SQUID magnetometer. The measurements of magnetic field dependent magnetizations ($M=f(H)$) of the nanoparticulate films made of TiO₂ nanoparticles doped with various (0.26–0.37 at%) concentrations of Cu²⁺ ions, are shown in Fig. 5. The small but distinct evidence of ferromagnetic ordering in samples of 0.34 and 0.37 at% Cu²⁺ doped TiO₂ nanoparticles was observed, while the TiO₂ nanoparticles doped by lowest concentration of Cu²⁺ ions (0.26 at%) shows negligible saturation magnetization (M_s) and coercivity (H_c). On the other hand, the observed coercivity values (H_c) of 0.34 and 0.37 at% Cu²⁺ doped TiO₂ nanoparticles after subtracting diamagnetic moments of the substrates were ~200 Oe for both samples. These values are

Table 1
Refined values of unit cell parameters of Cu²⁺ doped TiO₂ nanoparticles.

Sample	<i>a</i> (Å)	<i>c</i> (Å)	V(Å ³)
0.26 at% Cu ²⁺	3,79245	9,50245	136,7356
0.34 at% Cu ²⁺	3,79234	9,50866	136,7523
0.37 at% Cu ²⁺	3,79179	9,50786	136,7012
0.83 at% Cu	3,78893	9,51087	136,5383
1.03 at% Cu	3,78991	9,51279	136,6362

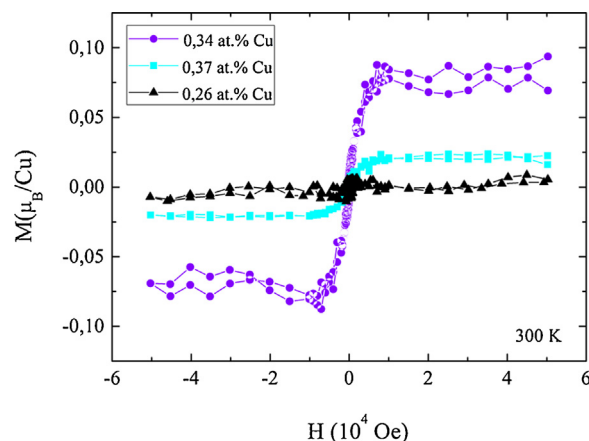


Fig. 5. Magnetization curves of 0.26, 0.34 and 0.37 at% Cu²⁺ doped TiO₂ nanoparticles.

comparable with the results reported by others [8]. Observed stable saturation magnetizations in samples 0.34 and 0.37 at% Cu²⁺ doped TiO₂ nanoparticles also indicated low paramagnetic contribution from conduction electron, as expected.

Applying *a b initio* calculations on bulk Cu-doped TiO₂, Duhalde et al. have shown that magnetic moment can be expected for super-cell containing one Cu impurity and a neighbor oxygen vacancy. On the other hand, no magnetic moment appeared if the oxygen vacancy is absent [17]. Weissmann et al. concluded from an *ab initio* study, that Cu impurities produce a magnetic moment for very small concentrations only and proposed that it depends strongly on the distance between Cu atoms [47].

The reason for observed decrease of saturation magnetization value in the sample doped with highest concentration of Cu²⁺ ions (0.37 at%) could be found in different ratio of oxygen vacancies taking into account that difference in dopant concentration was not significant.

The saturation magnetization values of samples prepared from 0.83 and 1.03 at% Cu²⁺ doped TiO₂ nanoparticles, synthesized at pH = 5, Fig. 6, were almost one order of magnitude lower compared to samples doped by lower concentration of Cu²⁺ ions (0.26–0.37 at%), Fig. 5. Considering these differences in magnetizations, appearance of doped nanoparticles of various shapes in samples synthesized at pH=5, should be taken into account for explanation. It is known that the ferromagnetism is sensitive to the shape and size of the nanostructures. Namely, according to TEM measurements, Fig. 2, beside polygonal nanoparticles, in the TEM image of 1.03 at% Cu²⁺ doped TiO₂ nanoparticles synthesized at pH = 5 also ellipsoid like nanoparticles clearly observed.

The origin of the ferromagnetism in Cu doped TiO₂ nanoparticles can be explained by non-carrier mediated bound magnetic polarons model [48,49] which implies that ferromagnetic coupling between two Cu²⁺ ions is facilitated through oxygen vacancy. Sufficient concentration of oxygen vacancy defects which exceeded the some percolation threshold, leads to their overlaps with dopant ions forming bound magnetic polarons [50].

The concentration of oxygen vacancies depends on the surface morphologies and size of the nanostructures, which can be the reason for the observed different magnetic moments. Therefore, weaker ferromagnetic ordering i.e., decrease of the total number of magnetic moments in the samples synthesized at pH = 5, could be related to lower level of surface oxygen vacancy defects in observed nanospheroids, Fig. 2. It should be mentioned here that the reflectance spectra of 0.83 and 1.03 at% Cu²⁺ doped TiO₂ nanoparticles synthesized at pH=5, Fig. 3b, also indicated the presence of fewer vacancies. Definitely, the number of Ti surface

atoms which adopt incomplete coordination (undercoordinated surface defect sites) and propagate in five surface layers within nanoparticles, is lower in nanospheroids than in the doped nanoparticles synthesized at pH=3. The large surface area and high curvature in the nanoparticles synthesized at pH = 3, results in the change of crystalline symmetry of surface and nearly surface ions, causing an increased number of oxygen vacancies which reflected in increased ferromagnetism. On the other hand, bearing in mind the bigger particles dimensions, lower magnetization in samples synthesized at pH = 5 could be an indication of the dilution of bulk oxygen vacancies i.e. decreases of overall volume occupied by the oxygen vacancies within particle. In that case the probability of coalescence of bound magnetic polarons into ferromagnetic domains rapidly declining.

4. Conclusions

In this study we presented new synthetic approach for efficient doping of TiO₂ nanoparticles with Cu²⁺ ions, through shape, size and structure transformation of tubular precursor nanomaterial. The Cu²⁺ doped TiO₂ nanocrystals of different morphology were synthesized hydrothermally using dispersion of titania nanotubes in the presence of Cu²⁺ ions as a precursor. XRD study confirmed tetragonal anatase crystal structure in all Cu²⁺ doped TiO₂ nanocrystals independently of concentration of dopant ions, synthetic conditions and size and shape of nanocrystals. Polygonal Cu²⁺ doped TiO₂ nanocrystals synthesized at pH=3 (*d* ~ 15 nm) were observed by TEM while bigger spheroid like nanocrystals (length, up to 90 nm) were appeared in samples synthesized at pH = 5. All samples of Cu²⁺ doped TiO₂ nanocrystals were exhibited ferromagnetic ordering with almost closed loop (*H*_c ~ 200 Oe). Saturation magnetization values in the Cu²⁺ doped TiO₂ nanospheroids were almost one order of magnitude lower compared to Cu²⁺ doped TiO₂ nanoparticles as effect of reducing the number of oxygen vacancies. This study confirmed that magnetic ions capable to develop ferro- or ferrimagnetic ordering are not necessary to be present to obtain ferromagnetic ordering in doped TiO₂, and revealed possibility to control magnetic ordering by changing the shape/aspect ratio of Cu²⁺ doped TiO₂ nanocrystals.

Acknowledgments

The financial support for this work was provided by the Ministry of Education, Science and Technological Development of Republic of Serbia (Projects 172056 and 45020). This work was done under umbrella of COST Action MP1106. Z. K. thanks for the support from the project III 45018 from the Ministry of Education, Science, and Technological Development of Republic of Serbia. Support for contributions from South Dakota School of Mines & Technology was received through the U.S. National Aeronautics and Space Administration South Dakota EPSCoR Space Grant Consortium.

References

- [1] J.K. Furdyna, *J. Appl. Phys.* 64 (1988) R29.
- [2] Y.H. Lee, J.M. Yoo, D.H. Park, D.H. Kim, B.K. Ju, *Appl. Phys. Lett.* 86 (2005) 033110.
- [3] S.A. Wolf, D.D. Awschalom, R.A. Buhrman, J.M. Daughton, S. Vonmolnar, M.L. Roukes, A.Y. Chtchelkanova, D.M. Treger, *Science* 294 (2001) 1488.
- [4] Y. Matsumoto, M. Murakami, T. Shono, T. Hasegawa, T. Fukumura, M. Kawasaki, P. Ahmet, T. Chikyow, S. Koshihara, H. Koinuma, *Science* 291 (2001) 854.
- [5] H. Ohno, A. Shen, F. Matsukura, A. Oiwa, A. Endo, S. Katsumoto, Y. Iye, *Appl. Phys. Lett.* 69 (1996) 363.
- [6] J.Y. Kim, J.H. Park, B.G. Park, H.J. Noh, S.J. Oh, J.S. Yang, D.H. Kim, S.D. Bu, T.W. Noh, H.J. Lin, H.H. Hsieh, C.T. Chen, *Phys. Rev. Lett.* 90 (2003) 017401.
- [7] R. Kennedy, P. Stampe, E. Hu, P. Xion, S. von Molár, Y. Xin, *Appl. Phys. Lett.* 84 (2004) 2832.
- [8] S.K.S. Patel, N.S. Gajbhiye, *Mat. Chem. Phys.* 132 (2012) 175.

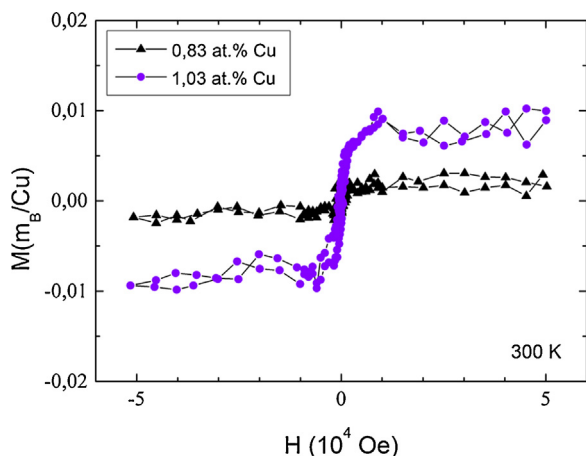


Fig. 6. Magnetization curves of 0.83 and 1.03 at% Cu²⁺ doped TiO₂ nanoparticles.

- [9] N.H. Hong, J. Sakai, W. Prellier, J. Magn. Mater. 281 (2004) 347.
- [10] M. Venkatesan, C.B. Fitzgerald, J.G. Lunney, J.M.D. Coey, Phys. Rev. Lett. 93 (2004) 177206.
- [11] L. Yan, C.K. Ong, X.S. Rao, J. App. Phys. 96 (2004) 508.
- [12] A. Gupta, H. Cao, K. Parekh, K.V. Rao, A.R. Raju, U.V. Waghmare, J. Appl. Phys. 101 (2007) 09N513.
- [13] X.L. Wang, Z.X. Dai, Z. Zeng, J. Phys.: Condens. Matter 20 (2008) 045214.
- [14] K.A. Griffin, A.B. Pakhomov, C.M. Wang, S.M. Heald, K.M. Krishnan, Phys. Rev. Lett. 94 (2005) 157204.
- [15] D.H. Kim, J.S. Yang, K.W. Lee, S.D. Bu, T.W. Noh, S.J. Oh, Y.W. Kim, J.S. Chung, H. Tanaka, H.Y. Lee, T. Kawai, Appl. Phys. Lett. 81 (2002) 2421.
- [16] T.S. Heng, S.P. Lau, S.F. Yu, H.Y. Yang, X.H. Ji, J.S. Chen, N. Yasui, H. Inaba, J. Appl. Phys. Lett. 99 (2006) 086101.
- [17] S. Duhalde, M.F. Vignolo, F. Golmar, C. Chilotte, C.E. Rodriguez Torres, L.A. Errico, A.F. Cabrera, M. Renteria, F.H. Sanchez, M. Weissmann, Phys. Rev. B 72 (2005) 161313R.
- [18] T. Kasuga, M. Hiramatsu, A. Hoson, T. Sekino, K. Niihara, Adv. Mater. 11 (1999) 1307–1311.
- [19] R.W. Cheary, A.A.J. Coelho, Appl. Cryst. 25 (1992) 109.
- [20] H.J. Rietveld, Appl. Cryst. 2 (1969) 65.
- [21] V.K. Pecharsky, P.Y. Zavalij, Fundamentals of Powder Diffraction and Structural Characterization of Materials, 11, Springer, 2005, pp. pp 292 (Chapter 3).
- [22] M. Vranješ, Z.V. Šaponjić, S. Lj. Živković, V.N. Despotović, B.F. Šojić, I. Čomor, App. Cat. B Environmental 160–161 (2014) 589.
- [23] N.M. Dimitrijević, Z.V. Šaponjić, B.M. Rabatić, O.G. Poluektov, T. Rajh, J. Phys. Chem. C 111 (2007) 14597.
- [24] M. Vranješ, J.K. Jakovljević, T. Radetić, M. Stoiljković, M. Mitrić, Z.V. Šaponjić, J. Nedeljković, Cer. Int. 38 (2012) 5629.
- [25] J. Tauc, R. Grigorovici, A. Vanco, Phys. Status Solidi 15 (1966) 627.
- [26] M. Pal, U. Pal, J.M.G.Y. Jimenez, F. Perez-Rodriguez, Nanoscale Res. Lett. 7 (2012) 1.
- [27] A. Emeline, V.N. Kuznetsov, V.K. Rybchuk, N. Serpone, Int. J. Photoenergy 2008 (2008) Article ID 258394.
- [28] L.F. Zuo, T. Wang, Z. Wu, D. Borchardt Zhang, J. Am. Chem. Soc. 132 (2010) 11856.
- [29] I. Justicia, P. Ordejon, G. Canto, J.L. Mozos, J. Fraxedes, G.A. Battiston, R. Gerbasi, A. Figueras, Adv. Mater. 14 (2002) 1399.
- [30] B. Rabatić, N.M. Dimitrijević, R.E. Cook, Z.V. Šaponjić, T. Rajh, Adv. Mater. 18 (2006) 1033.
- [31] L.X. Chen, T. Rajh, Z. Wang, M.C. Thurnauer, J. Phys. Chem. B 101 (1997) 10688.
- [32] D.M. de los Santos, J. Navas, A. Sanchez-Coronilla, R. Alcantara, C. Fernandez-Lorenzo, J. Martin-Calleja, Mat. Res. Bull. 70 (2015) 704.
- [33] K. Sunada, T. Watanabe, K. Hashimoto, Environ. Sci. Technol. 37 (2003) 4785 Technol.
- [34] J.Y. Zheng, S.H. Bao, Y.H. Lv, P. Jin, ACS Appl. Mater. Interfaces 6 (24) (2014) 22243.
- [35] http://www.webelements.com/copper/atom_sizes.html
- [36] C. Huang, X. Liu, Y. Liu, Y. Wang, Chem. Phys. Lett. 432 (2006) 468.
- [37] M.L. Cui, J. Zhu, X.Y. Zhong, Y.G. Zhao, X.F. Duan, Appl. Phys. Lett. 85 (2004) 1698.
- [38] A. Manivannan, M.S. Seehra, S.B. Majumder, R.S. Katiyar, Appl. Phys. Lett. 83 (2003) 111.
- [39] Z.V. Šaponjić, N.M. Dimitrijević, O.G. Poluektov, L.X. Chen, E. Wasinger, U. Welp, D.M. Tiede, X. Yuo, T. Rajh, J. Phys. Chem. B 110 (2006) 25441.
- [40] M. Vranješ, J. Kuljanin-Jakovljević, S.P. Arhenkiel, I. Zeković, M. Mitrić, Z. Šaponjić, J.M. Nedeljković, J. Lumin. 143 (2013) 453.
- [41] R.D. Shannon, Acta. Cryst. A 32 (1976) 751.
- [42] W. Li, A.I. Frenkel, J.C. Woicik, C. Ni, S.I. Shah, Phys. Rev. B 72 (2005) 155315.
- [43] J.C. Sczancoski, L.S. Cavalcante, T. Badapanda, S. Rout, V.R. Mastelaro, J.A. Varela, M. Siu Li, E. Longo, Solid State Sci. 12 (2010) 1160.
- [44] A. Sundaresan, R. Bhargavi, N. Rangarajan, U. Siddesh, C.N. Rao, Phys. Rev. B 74 (2006) 161306(R).
- [45] M. Vranješ, Z. Konstantinović, A. Pomar, J. Kuljanin Jakovljević, M. Stoiljković, J. M. Nedeljković, Z. Šaponjić, J. Alloy Comp. 589 (2014) 42.
- [46] C.E. Rodriguez Torres, F. Golmar, A.F. Cabrera, L. Errico, A.M. Mudarra Navarro, M. Renteria, F.H. Sanchez, S. Duhalde, App. Surf. Sci. 254 (2007) 365.
- [47] M. Weissmann, L.A. Errico, Physica B 398 (2007) 179.
- [48] A. Kaminski, S.D. Sarma, Phys. Rev. Lett. 88 (2002) 247202.
- [49] J.M.D. Coey, M. Venkatesan, C.B. Fitzgerald, Nat. Mater. 4 (2005) 173.
- [50] S.K.S. Patel, S. Kurian, N.S. Gajbhiye, Mater. Res. Bull. 48 (2013) 655.

Self-Arranged Misfit Dislocation Network Formation upon Strain Release in $\text{La}_{0.7}\text{Sr}_{0.3}\text{MnO}_3/\text{LaAlO}_3(100)$ Epitaxial Films under Compressive Strain

José Santiso,^{*,†} Jaume Roqueta,[†] Núria Bagués,^{†,‡} Carlos Frontera,[‡] Zorica Konstantinovic,[⊥] Qiyang Lu,[§] Bilge Yildiz,[§] Benjamín Martínez,[‡] Alberto Pomar,[‡] Lluís Balcells,[‡] and Felip Sandiumenge[‡]

[†]Catalan Institute of Nanoscience and Nanotechnology (ICN2), CSIC, and the Barcelona Institute of Science and Technology (BIST), Campus UAB, Bellaterra, Barcelona 08193, Spain

[‡]Materials Science Institute of Barcelona (ICMAB), CSIC, Campus UAB, Bellaterra, Barcelona 08193, Spain

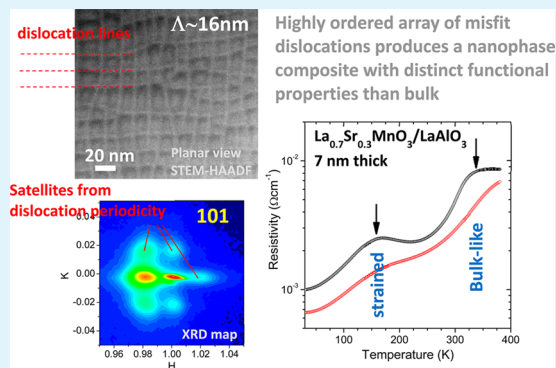
[§]Massachusetts Institute of Technology (MIT), Cambridge, Massachusetts 02139, United States

[⊥]Center for Solid State Physics and New Materials, Institute of Physics Belgrade, University of Belgrade, Pregrevica 118, 11080 Belgrade, Serbia

Supporting Information

ABSTRACT: Lattice-mismatched epitaxial films of $\text{La}_{0.7}\text{Sr}_{0.3}\text{MnO}_3$ (LSMO) on LaAlO_3 (001) substrates develop a crossed pattern of misfit dislocations above a critical thickness of 2.5 nm. Upon film thickness increases, the dislocation density progressively increases, and the dislocation spacing distribution becomes narrower. At a film thickness of 7.0 nm, the misfit dislocation density is close to the saturation for full relaxation. The misfit dislocation arrangement produces a 2D lateral periodic structure modulation ($\Lambda \approx 16$ nm) alternating two differentiated phases: one phase fully coherent with the substrate and a fully relaxed phase. This modulation is confined to the interface region between film and substrate. This phase separation is clearly identified by X-ray diffraction and further proven in the macroscopic resistivity measurements as a combination of two transition temperatures (with low and high T_c). Films thicker than 7.0 nm show progressive relaxation, and their macroscopic resistivity becomes similar than that of the bulk material. Therefore, this study identifies the growth conditions and thickness ranges that facilitate the formation of laterally modulated nanocomposites with functional properties notably different from those of fully coherent or fully relaxed material.

KEYWORDS: strain relaxation, misfit dislocation arrangement, nanophase modulation, nanotemplate



1. INTRODUCTION

Strain engineering in thin epitaxial films of transition metal oxides with perovskite structure has become an important field of study in the past decade because of the strong correlations between the subtle structure variations induced by the epitaxial growth on mismatched substrates and the electronic properties of oxide films, which have proven to render the film material very different functional properties to those of the equilibrium material.^{1–4}

Lattice-mismatched heterostructures of perovskite oxides are also of interest because the regions surrounding the defects generated during the strain relief, typically misfit dislocations (MDs) or walls between crystal domains with different orientation, very often show a different structure and symmetry than the rest of the film material at the nanoscale.^{5–7} This may offer a basis for fabrication of a variety of low-dimensional and mesoscopic systems in solid-state physics.^{8–11}

In epitaxial growth on substrates with lattice mismatch, the film structure is submitted to an in-plane biaxial strain, either compressive or tensile depending on the mismatch with the substrate. The out-of-plane cell parameter is therefore expanded or compressed, as a result of the elastic response of the material. According to the classical model by Frank and van der Merwe¹² and Matthews-Blakeslee,¹³ the films grow pseudomorphically with the substrate below a certain critical thickness. Above this thickness, the film usually releases the accumulated strain energy via plastic deformation, thus generating MDs, which progressively accommodate the strain toward the equilibrium bulk structure.¹⁴

At a local scale, the strain accommodation by a pure edge dislocation is uniaxial and was early described by the Peierls–

Received: March 8, 2016

Accepted: June 9, 2016

Published: June 9, 2016

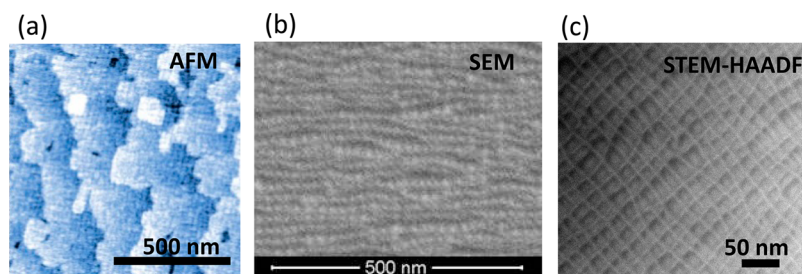


Figure 1. Planar view images of a 7 nm thick LSMO/LAO thin film with a well-developed MD pattern as observed by (a) AFM topography, (b) orientation contrast SEM, and (c) STEM taken at HAADF mode. In all cases, the image contrast defines parallel lines that correspond to the position of the MD cores parallel to $[100]$ and $[010]$ directions.

Nabarro model.¹⁵ It follows the in-plane projection of the corresponding Burgers vector perpendicular to the dislocation line. Therefore, the biaxial strain in the films is necessarily accommodated by the formation of an array of MDs, as early observed by the concomitant formation of a cross-hatched surface morphology pattern in lattice-mismatched heterostructures of III–V semiconductors like GaAsP/GaAs,¹⁶ which was further theoretically described by Speck and Pompe.¹⁴ This is typically observed in thick films by means of optical or atomic force microscopy (AFM) but is difficult to trace in very thin films. The observation of MDs arrays has been more recently reported also in some perovskite oxide heterostructures such as in SrRuO₃/SrTiO₃(100),¹⁷ in buried (Ca_{1-x}Sr_x)(Zr_{1-x}Ru_x)O₃/SrRuO₃/SrTiO₃(100),¹⁸ in La_{0.5}Ca_{0.5}MnO₃/SrTiO₃(100),¹⁹ or in BaTiO₃/SrTiO₃(100).²⁰

In heterostructures that undergo strain relief by the formation of a high density of dislocations, they often arrange into highly ordered periodic patterns. This self-arrangement is induced by the repulsive forces generated in the interaction between MDs as well as their mobility along the interfaces, which depends on the elastic properties of the material and the deposition conditions. In an ideal case of a perfect periodical arrangement, it may provide a route to obtain the size uniformity needed for electronic applications such as in quantum dot arrays.²¹ The dislocation pattern may also serve as a nanotemplate for the guided growth of 2D nanostructured materials, such as demonstrated in the preferential nucleation of Fe and Cu metal particles on strain-relieved Pt(111),²² the growth of ZnSe nanowires and nanorod structures on GaAs,²³ as well as the growth of exotic nanomaterials seeded by screw dislocations.²⁴

Understanding the formation and self-organization mechanism of such MD arrays in oxide perovskite materials is important for the fabrication of low-dimensional structures, thus providing an opportunity for the finding of novel physical phenomena. One perfect example is the recently reported condensation of two-dimensional oxide-interfacial charges into one-dimensional electron chains induced by the misfit-dislocation strain field in (Nd_{0.35}Sr_{0.65})MnO₃/SrTiO₃.¹¹

This paper aims to investigate the progressive self-organization of the MD network occurring during the epitaxial growth of a heterostructure of complex oxide materials with perovskite structure submitted to a large biaxial compressive stress, exemplified by La_{0.7}Sr_{0.3}MnO₃ (LSMO) grown on LaAlO₃ (100) substrates (LAO). The strain modulation observed in ultrathin nanostructured films of LSMO material is correlated with the measured magnetotransport behavior.

2. EXPERIMENTAL METHODS

La_{0.7}Sr_{0.3}MnO₃ films with different thicknesses from 2.0–14.0 nm were deposited by magnetron sputtering under the same conditions and experimental setup as described in previous works.^{25,26} LaAlO₃(100) crystals (Crystec, GmbH) were used as substrates. The surface morphology along with the formation of MDs was examined by AFM (PicoSPM, Molecular Imaging, in tapping mode) and scanning electron microscopy (SEM; Quanta 200 FEG-ESEM, FEI). Detailed observations of the strain fields induced by the presence of the MDs were obtained by transmission electron microscopy (TEM) in HAADF (high angle annular dark field) mode as well as high-resolution TEM planar images (field emission gun Tecnai F20 S/TEM, FEI at 200 kV). High-resolution TEM images of film cross-section were obtained in a Cs-corrected microscope (F20 Tecnai, FEI). The overall film structure and the features induced by the arrangement of the MD network were analyzed by X-ray diffraction (XRD) making use of laboratory diffractometers (Panalytical X'Pert MRD, Rigaku SmartLab) for standard and in-plane diffraction geometry. The 2D X-ray reciprocal space mapping experiments were performed on beamline BM25 at the European Synchrotron Radiation Facility (ESRF), Grenoble, France. The 3D XRD reciprocal space maps were carried out by using synchrotron radiation at the KMC-2 beamline at Helmholtz-Zentrum Berlin (Bessy II). Resistivity of the films was measured as a function of temperature, from 10–380 K, in absence of magnetic field ($H = 0$ T) and in the presence of a magnetic field of $H = 9$ T by using a physical properties measurement system (PPMS) from Quantum Design.

3. RESULTS AND DISCUSSION

All deposited films are continuous and show essentially flat morphology with single unit cell step terraces, as revealed by topography images obtained by AFM as depicted in Figure 1a, for the LSMO/LAO film of 7 nm thickness. A closer observation of the morphology of this film reveals the presence of a dense cross-hatched pattern following two perpendicular directions (corresponding to $[100]$ / $[010]$ main crystallographic directions), which form subtle ridges of less than one unit cell height. Figure 1b, shows the orientation contrast SEM image of the same 7 nm thick film. As in the previous AFM image, it shows a clear contrast forming a crossed pattern of parallel lines following $[100]$ / $[010]$ crystallographic directions. Because of the low film roughness and the absence of secondary phases, the corresponding SEM image shows only contrast related to crystallographic defects or strain fields. These lines presumably correspond to the presence of buried MDs at the interface between film and substrate generated because of the partial release of the misfit strain. A planar view scanning TEM (STEM) image of that film in HAADF is presented in Figure 1c. Again it shows a clear contrast forming lines running parallel to $[100]$ and $[010]$ main directions of the cubic primitive perovskite cell, in agreement with AFM and

SEM observations. The bright lines in the HAADF image coincide with the position of the MDs core lines. The distance between dislocations is quite regular in the depicted area and spans from 20–30 nm.

High-resolution TEM observations of planar view and cross-section of the 7 nm LSMO/LAO film are shown in Figure 2a,b,

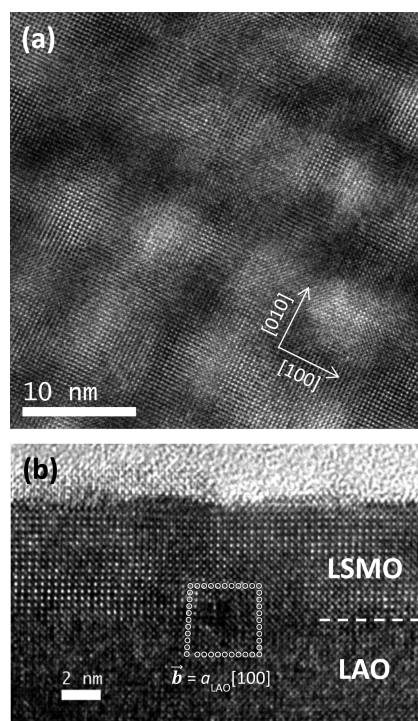


Figure 2. High-resolution TEM images of a (a) planar view and (b) cross-section of a 7 nm thick LSMO/LAO film. The cross-section shows a Burgers circuit around a MD core at the film–substrate interface with a Burgers vector $\mathbf{b} = a_{\text{LAO}}[100]$.

respectively. The planar view shows a high crystal quality with atomic column resolution. The dark and white contrast is related to the strain field caused by the MDs and shows a complex pattern already observed in the lower magnification image in Figure 1c. The cross-section image shows the presence of one MD core at the interface between film and substrate. The Burgers circuit around the MD core indicates a Burgers vector $\mathbf{b} = a_{\text{LAO}}[100]$ parallel to the interface with magnitude equal to one primitive unit cell of the LAO substrate, which is typical in perovskite oxides and was previously reported in LSMO/LAO.²⁷

3.1. Evolution of MD Distribution with Film Thickness.

For a comparison of the MDs density evolution Figure 3a shows orientation-contrast SEM images of the LSMO films deposited on LAO substrates with different thicknesses from 2–14 nm. Orientation-contrast-SEM (OC-SEM) images offer a direct method to reveal the presence of MDs pattern clearer than AFM and much simpler to prepare than TEM planar view specimens.

The thinnest film of 2 nm does not show any evidence of MD formation. However, the film with 3.5 nm thickness already shows a pattern of lines corresponding to MDs with different spacing. Films with larger thickness of 7 and 14 nm show a dense distribution of crossed MDs forming a regular grid. Therefore, from these images, it can be estimated that the critical thickness for the formation of MDs lies roughly between

2.0 and 3.5 nm, and the films progressively show a higher MD density with thickness.

To quantify the MDs distribution, Figure 4a shows histograms of their spacing obtained from a large number (about 190) of linear scans across the SEM images. They consist of a single mode Poisson distribution with different mean and standard deviation values as opposed to the bimodal distributions often observed in semiconductors (in the diluted MD dislocation regime) and related to the interaction between 60° dislocations with opposite in-plane component to form pure edge dislocations.²⁸ The film with 3.5 nm thickness shows a mean dislocation separation around 38 nm, which corresponds to a dislocation linear density of $2.6 \times 10^5 \text{ cm}^{-1}$, while for the 7 and 14 nm thick samples, the mean separations were 25 and 16 nm, respectively (linear dislocation densities around $4.0 \times 10^5 \text{ cm}^{-1}$ and $6.2 \times 10^5 \text{ cm}^{-1}$). For thicker films, the image of the dislocation gets blurred because of the limited penetration depth of the electrons, and it is difficult to accurately measure their separation by SEM. In a fully relaxed LSMO film (with cell parameter $a_{\text{LSMO}} = 3.885 \text{ \AA}$, and pseudocubic cell parameter $a_{\text{LAO}} = 3.790 \text{ \AA}$ for the LAO substrate), a simple calculation gives a saturation MD density of $6.45 \times 10^5 \text{ cm}^{-1}$, assuming a Burgers vector equal to one unit cell in the direction parallel to [100], $\mathbf{b} = a_{\text{LAO}}[100]$. This corresponds to one MD every 40 u.c. of the LSMO structure, that is, an average MD separation of 15.5 nm. The mean values of the experimental linear dislocation density progressively increase with thickness reaching almost full relaxation for the 14 nm thick sample. Figure 4b depicts that density as a function of the reciprocal film thickness. The dependence is roughly linear following the expression

$$\rho_{\text{MD}} = \rho_{\text{relaxed}}(1 - h_c/h) \quad (1)$$

above a critical thickness h_c before it reaches saturation at the maximum dislocation density for the fully relaxed films, consistent with Matthews and Blakeslee model.¹³ The critical thickness value can be extrapolated from the $\rho_{\text{MD}} = 0$ intercept to be roughly 2.5 nm.

From thermodynamic equilibrium considerations, Matthews and Blakeslee derived a self-contained expression for the critical thickness, h_c :²⁹

$$h_c = \frac{b}{4\pi f} \frac{(1 - \nu \cos^2 \theta)}{(1 + \nu) \sin \theta \cos \phi} \ln \left(\frac{\alpha h_c}{b} \right) \quad (2)$$

where b is the modulus of the Burgers vector, f is the magnitude of the strain, ν is the Poisson ratio, and θ and ϕ are the angles between the Burgers vector and the dislocation line and the interface plane, respectively. The value of the dislocation core parameter, α , may vary between $\alpha = 1$ and $\alpha = 4$, and in practical cases, it is obtained from experimental data. As an estimate, in this case, we assume the value of $\alpha = 2.72$ first derived in the Matthews and Blakeslee theory.²⁹ The values of $b = 3.885 \text{ \AA}$ (1 u.c.), mismatch $|f| = 0.024$, $\theta = 90^\circ$, $\phi = 0^\circ$, were taken for the present case of LSMO/LAO. The Poisson ratio was calculated from the experimental LSMO cell parameters of the fully strained 2.0 nm film measured by high-resolution XRD $2\theta/\omega$ scans (out-of-plane $c = 3.985 \text{ \AA}$; in-plane $a = 3.790 \text{ \AA}$). Assuming an equilibrium cell structure $a = 3.885 \text{ \AA}$, the corresponding strains are $\varepsilon_{//} = -0.0244$; $\varepsilon_{\perp} = +0.0257$, and the Poisson ratio calculated from the expression for biaxial strain $\varepsilon_{\parallel} = -(2\nu/1 - \nu)\varepsilon_{\perp}$ ³⁰ was $\nu = 0.32$. Therefore, a critical thickness

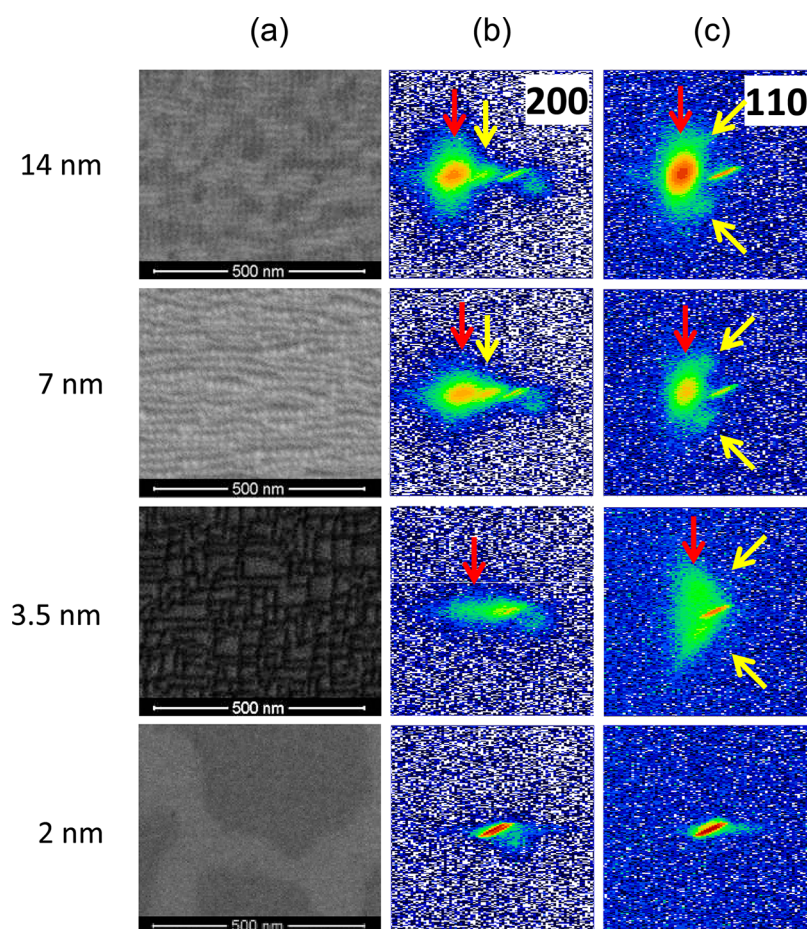


Figure 3. Chart shows details of LSMO films with different thicknesses from 2, 3.5, 7, and 14 nm. In columns (from left to right): (a) OC-SEM images of the same samples. The observed horizontal and vertical lines correspond to MDs running parallel to $[100]$ and $[010]$ crystallographic directions; in-plane XRD 2θ - ϕ area of (b) 200 and (c) 110 reflections of LSMO film and LAO substrate (obtained with $\text{CuK}\alpha$ radiation in laboratory diffractometer, at 0.5° incidence angle). The horizontal axis corresponds to 2θ angle and vertical axis to ϕ angle. These axes are approximately following the $[100]/[010]$ directions for 200 reflection, and $[110]/[-110]$ for 110. The angular range for both 2θ and ϕ scans was 4° .

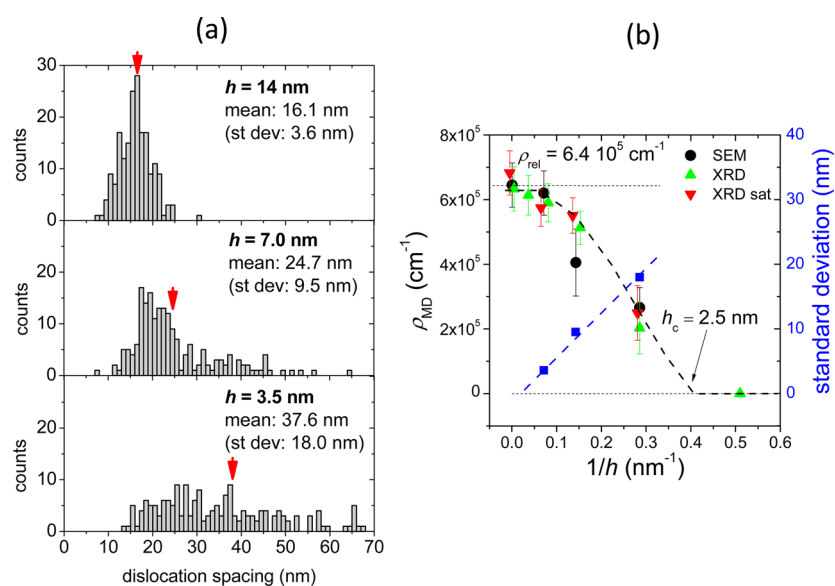


Figure 4. (a) Distribution histograms of the separation between consecutive MDs measured from the SEM images of the films of different thicknesses; (b) dependence of the linear dislocation density versus the reciprocal film thickness (as measured by SEM (black symbols) and XRD as estimated from the LSMO cell parameter value (green symbols) and from the satellite peak position (red symbols), along with the standard deviation of the distribution by SEM (blue symbols).

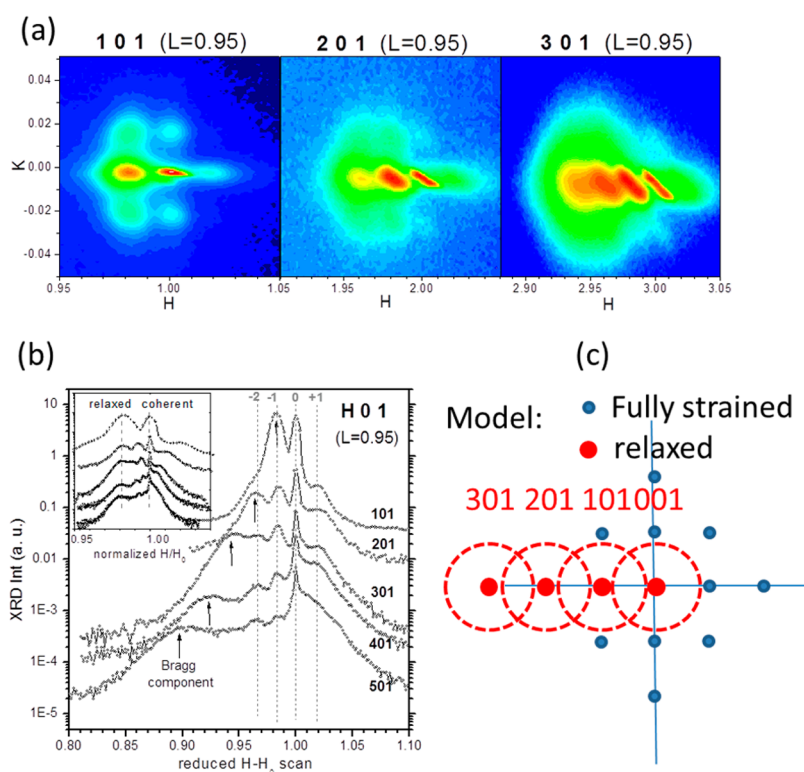


Figure 5. (a) HK reciprocal space maps of $H\ 0\ 1$ ($H = 1, 2,$ and 3) reflections of the LSMO film with $7\ \text{nm}$ thickness; (b) linear H scans of the different reflections $H\ 0\ 1$, from $H = 1-5$, the scans are shifted to coincide in the H position of the LAO substrate at $H = 1$ (the inset shows the same scans reduced dividing by H_0 along with (c) the corresponding model showing the overlap in the reciprocal space of fully strained and partially relaxed LSMO structures.

of $h_c = 1.7\ \text{nm}$ is obtained from eq 2, which is slightly below the experimental observation.

The standard deviation of the distribution of MD separation depicted in Figure 4a also varies with film thickness, being very wide for the $3.5\ \text{nm}$ thick sample, which is about $18\ \text{nm}$. The standard deviation distribution becomes gradually reduced to about 9.5 and $3.6\ \text{nm}$ for the 7 and $14\ \text{nm}$ thick samples, respectively. The same graph in Figure 4b shows an almost linear dependence of the distribution standard deviations with the reciprocal thickness approaching to a zero value for the thicker films, which indicates the trend toward a perfect arrangement of the MD network. At the critical thickness, the distribution deviation extrapolates to very large values, which essentially indicate that at the very onset of the MD formation their distribution is flat with random separation distance between them. Upon the MD density increases, their strain fields interact, which progressively narrows their distribution until they self-arrange forming a highly ordered crossed network already at a film thickness of $7\ \text{nm}$.

It is also interesting to notice that in the $3.5\ \text{nm}$ thick film, where the MD density is low and the self-arrangement is far from being complete, the MDs show also a wide distribution in length from long segments of several hundreds of nm to short dislocations of only a few tenths of nm, as evidenced in Figure 3a. Some MDs end within the film, although most of the MDs end when they meet another orthogonal MD line. This observation is consistent with the finding previously reported in SiGe and III-V semiconductors where the ends of the MDs turn into threading dislocations half loops emerging at the film surface.³¹ In a regime with low density of MDs, the threading dislocations loops do not get annihilated and they persist in the

film, their lateral diffusion being blocked by the strain field of some other crossing MD. Upon increasing the MD dislocation density, the threading dislocations have larger probability to overcome those barriers, eventually meeting another threading dislocations and annihilate each other, turning into longer sections of MD lines. In the $7\ \text{nm}$ film, short length MDs are rare, and most of them extend for hundreds of nm, as observed in the SEM and TEM images in Figure 1b,c.

3.2. Structure Lateral Modulation. It is difficult to accurately measure the in-plane cell parameter for ultrathin films of only a few nm thickness by reciprocal space mapping because of their very weak signal and the overlap with the intense substrate peaks. Instead, the in-plane diffraction geometry (with grazing incidence and exit angles) allows for a qualitative insight into the in-plane cell parameter relaxation. This provides an alternative way to indirectly measure the MD density. Figure 3b,c show in-plane $2\theta-\phi$ area scans of 200 and 110 in-plane reflections, respectively. Any variation in the Bragg peak position along the horizontal 2θ -axis corresponds to a change in the in-plane cell parameter, while a variation in the vertical ϕ -axis most likely corresponds to some tilt in the structure. The 200 area scans of the $2.0\ \text{nm}$ thick film show one single peak at around $2\theta = 48^\circ$ that corresponds to the same position expected for the LAO substrate. The slight elongation of the spot along $[110]$ corresponds to an instrumental origin coming from the X-ray optics. The presence of one single peak indicates that the film in-plane cell parameters are coherent with those of the substrate, and therefore, the film is fully strained. Although this grazing angle geometry is intended to enhance the diffracted signal from the topmost part of the film, the penetration of the X-rays still gives a non-negligible overlap

with the peak from the substrate for very thin films of a few nm. The same occurs for the corresponding 110 area scan where only one peak is observed. However, the 200 and 110 area scans of the 3.5 nm thick film show a considerable diffuse scattering at lower 2θ angles from the substrate peak, which point to an incipient relaxation of its in-plane cell parameter (red arrows). Interestingly, the diffuse scattering in the 110 area scan shows two different branches following [100] and [010] orthogonal directions (yellow arrows). This is an indication of the uniaxial relaxation character due to the presence of the crossed MDs.

The 200 and 110 area scans of the 7.0 and 14 nm thick films show a very sharp reflection corresponding to the LAO position (at larger 2θ angle, on the right of the scan) and a broader intense reflection (at lower 2θ angle, on the left) corresponding to the partially relaxed LSMO structure (red arrows). This peak position in the maps indicates that in-plane LSMO cell parameters relax equally along [100] and [010] directions, thus keeping a square basal a/b plane. The corresponding cell parameters were measured to be 3.865 and 3.877 Å for the 7.0 and 14 nm thick films, respectively. By taking these values, the numbers of unit cells between dislocations are calculated as $N = 50$ and 44, which correspond to distances of 19.5 and 17.0 nm, respectively. These values are in good agreement with those calculated from the SEM observations previously shown in Figure 3a and included in Figure 4b.

Along with the main Bragg peaks, these area scans show additional features, as indicated by yellow arrows. In the 200 area scans, between the substrate and film peak positions, there is a clear peak. This peak does not correspond to a Bragg peak. Instead, it corresponds to a first-order satellite peak coming from a lateral structure modulation within the film plane induced by the presence of the dislocation network. Those satellites are also observed in the in-plane XRD maps of the 110 reflection. They deviate from the [110] directions and split in phi angle (vertical axis in the scans) following the [100] and [010] directions, as in the thinner 3.5 nm film. This splitting corresponds to the previously mentioned modulation along the plane of the sample, along both [100] and [010] directions. The distance in the reciprocal space between the first satellite position and the zero order position (on the LAO position) was an indication of the modulation periodicity. For the 3.5, 7, and 14 nm thick LSMO films, the modulation period was calculated to be 40(\pm 13), 18(\pm 2), and 17(\pm 2) nm, respectively, in good agreement with the separation between MDs. The corresponding MD linear densities for these data were also incorporated in Figure 4b.

A clearer view of the satellite pattern induced by the modulated structure is observed in the HK reciprocal space maps of the H01 reflections of the 7 nm thick film shown in Figure 5a for $H = 1, 2,$ and 3. $H, K,$ and L axes correspond to the [100], [010], and [001] directions, respectively ($H, K,$ and L are expressed in reciprocal lattice units of the LAO substrate). These measurements were performed by using synchrotron radiation and were taken at the $L = 0.95$ position optimized for the LSMO film, slightly lower than the substrate position at $L = 1$ because in the relaxed LSMO structure, the c -axis parameter is larger than that for LAO. The sharp reflections at the ($H = 1, K = 0$) position along with ($H = 2, K = 0$) and ($H = 3, K = 0$) for in the 101, 201, and 301 maps, respectively, correspond to the LAO substrate overlapped with the fully strained LSMO component. The intense reflections at ($H = 0.98, K = 0$), ($H = 1.96, K = 0$), and ($H = 2.94, K = 0$) for the 101, 201, and 301

maps, respectively, correspond to the LSMO partially relaxed Bragg component. The rest of the peaks correspond to satellite reflections in positions ($H = H_0 \pm nd, K = 0 \pm md$) centered at the H_0 position of the fully coherent LSMO structure, being (n, m) the order of the satellite reflections along H and K directions in the map, respectively. The distance d between satellites along H and K shows a constant value of about 0.019 (in reciprocal space units) for all H 0 1 reflections, which is consistent with a square-shape in-plane modulation with periodicity $\Lambda \approx 20$ nm along both [100] and [010]. This is consistent with the presence of the crossed pattern of perfectly parallel MDs network. First-order satellites are clearly visible, while second- or third-order satellites are only visible in the proximity of the LSMO partially relaxed reflection.

Figure 5b shows the intensity profiles along linear H scans at $K = 0$ for the different H01 reflections ($H = 1, 2, 3, 4,$ and 5). The scans have been translated so the position of the corresponding H01 LAO reflection coincides for all them at $H - H_0 = 1.0$. It is clear that satellite reflections (up to second order on the left part of the scan, indicated by the dashed vertical lines) keep the same separation in reciprocal space with respect to the central zero order ($H - H_0 = 1$) reflection, which is consistent with the in-plane modulation. The curves also show a broad component (indicated with arrows in the graph) progressively shifted to lower H values, from 101 to 501 reflections that corresponds to the Bragg component of the LSMO partially relaxed structure. The inset shows the same scans reduced by dividing by the corresponding H_0 value of the reflection. As expected, all the Bragg components show the same value at around $H/H_0 = 0.98$ corresponding to an average in-plane cell parameter of 3.864 Å.

It is not surprising to notice that the partially relaxed LSMO component at the 101 and 201 reflections coincides with the position of $n = -1$ and $n = -2$ ($m = 0$) satellite reflections, respectively. In fact, for a fully relaxed LSMO structure, we might expect a dislocation distance Λ equal to $\Lambda = Na_{\text{LSMO}} = (N + 1)a_{\text{LAO}}$, where N is the number of unit cells of LSMO to exactly match $N + 1$ cells of LAO. Therefore, in the reciprocal space, the position of the n th order satellite will correspond to $Q_x^\Lambda = n(N + 1)^{-1} a_{\text{LAO}}^{-1}$. For a couple of HKL reflections of LSMO film and LAO substrate, their corresponding positions along [100]* direction in the reciprocal space are $Q_x^{\text{LAO}} = H a_{\text{LAO}}^{-1}$ and $Q_x^{\text{LSMO}} = H a_{\text{LSMO}}^{-1}$. If we calculate their separation in the reciprocal space, $\Delta Q_x^{\text{LAO,LSMO}} = (Q_x^{\text{LAO}} - Q_x^{\text{LSMO}}) = H(N + 1)^{-1} a_{\text{LAO}}^{-1}$. In this way, for a fully relaxed film, we should expect a perfect coincidence of the modulated structure when $H = n$. Since the 7 nm thick film is close to full relaxation, we observe such coincidence at $n = 1$ for the $H = 1$ (101) reflection, and $n = 2$ for the $H = 2$ (201) reflections.

The overlap of these reflections enhances the intensity of the satellites, along with those at $m = \pm 1$ (along [010]* direction). This is an indication of some degree of constructive interference between the scattered waveforms of both fully strained and fully relaxed LSMO components. As depicted in the sketch in Figure 5c, the pattern may be described as the overlap between (i) a fully strained LSMO contribution coherent with the LAO substrate, with the corresponding square shape satellite pattern generated by the MD periodicity (in blue), (ii) plus the partially relaxed LSMO component moving along H , depending on the H01 reflection (in red color). Since part of the partially relaxed structure is also modulated with the same periodicity, it is not surprising that it

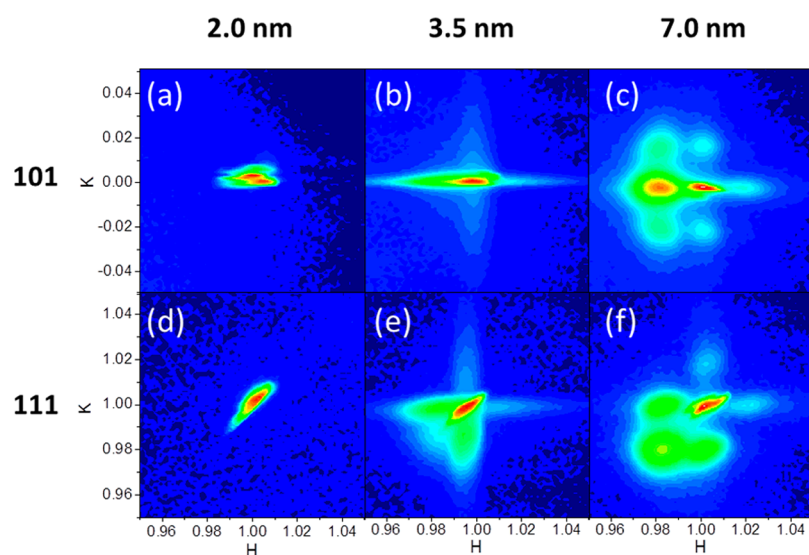


Figure 6. *HK* reciprocal space maps of the 101 and 111 reflections for the LSMO films with thickness (a, d) 2.1 nm, (b, e) 3.5 nm, and (c, f) 7.0 nm. Maps were positioned at $L = 0.95$ corresponding to the maximum of the LSMO contribution (HKL in LAO reciprocal lattice units).

reproduces the same satellite square pattern but centered in the LSMO reflection, with a certain coincidence in some satellite positions. In this way, the region around this last component (indicated as the dashed circle) enhances the intensity of the close satellite reflections.

To follow in more detail the progression of the MD generation and the degree of order of the strain pattern upon film thickness increase, reciprocal space *HK* maps of the 101 and 111 reflections were collected by using synchrotron radiation (at constant $L = 0.95$, as optimized for the LSMO signal), on the samples with 2.0, 3.5, and 7.0 nm thickness, as shown in Figure 6. Similarly to the in-plane 200 and 110 maps depicted in Figure 3b,c the 101 and 111 *HK* maps of the film with 2.0 nm, in Figure 6a,d show one single peak at ($H = 1, K = 0$) and ($H = 1, K = 1$), respectively, with no evidence of relaxation. These 101 and 111 reflections were optimized at $L = 0.95$ where film signal is maximum, thus minimizing the overlap with the very narrow LAO rod whose maximum, is at $L = 1$. The *HK* maps of the 3.5 nm thick film, shown in Figure 6b,e present diffuse scattering around the central position following $[100]$ and $[010]$ directions. Since the periodical arrangement of the dislocations is not yet established, the diffuse scattering associated with the linear defects shows broad branches. The substantial asymmetry of the map showing larger intensity tails at $H = 0.98, K = 0$, for the 101 map (left branch in Figure 6b), and $H = 0.98, K = 1$ and $H = 1, K = 0.98$ values, along the corresponding crossed branches in the 111 map (in bottom and left quadrant of Figure 6e), points to the uniaxial relaxation of the structure around each set of MDs. Still, there is a weak contribution to the biaxial relaxation visible in the 111 map along the $[110]$ bisect direction at $H = 0.98, K = 0.98$. The very weak intensity of the branches at larger H and K values is the reason why they were not previously observed in the in-plane maps measured in the lab diffractometer with a conventional $\text{CuK}\alpha$ tube source. The film with 7.0 nm thickness, in Figure 6c,f shows already a clear biaxially relaxed peak at $H = 0.98, K = 0$ for the 101 map, and $H = 0.98, K = 0.98$ for the 111 map. As in previous observations, the periodical arrangement of the crossed MDs defines clear first-order satellites around the central position. Again, the asymmetry between the intensities of the satellites is related to the degree of coherence between

relaxed and strained LSMO structures, as explained in the model in Figure 5c. This makes particularly intense first-order satellites at ($H = 0.98, K = 1$) and ($1, 0.98$) positions for the 111 map as well as particularly intense second-order satellites in the 101 map at ($H = 0.98, K = \pm 0.02$) positions.

It is important to point out that the representation of the different *HK* maps at constant L value has some difficulties given the fact that the optimal value of L for maximizing the intensity of the reflection corresponding to the relaxed part of the LSMO structure is not exactly the same as for the LSMO structure coherent with the substrate. Since these structures are submitted to a different in-plane biaxial strain, they show different out-of-plane c -axis parameters. Similarly, the satellite reflections show a maximum intensity at different L positions. Therefore, it is more adequate to represent them in 3D. A collection of these 3D representations is shown in the Supporting Information.

3.3. Depth Distribution. Up to this point, we have described the LSMO/LAO films as a combination of a LSMO relaxed structure and a largely strained structure modulated by the presence of the MD network. It is very likely to expect that the modulated structure is in close proximity to the MD lines, and therefore close to the film–substrate interface, while the relaxed LSMO part may be at a certain distance from the dislocations close to the film surface. This difference along the depth of the sample was explored by grazing incidence in-plane diffraction by varying the incidence angle, and therefore the penetration depth of the X-rays. Figure 7a shows linear $2\theta - \chi$ scans around the 200 in-plane reflection of the 7 nm thick LSMO/LAO film for different ω incidence angles from 0.1 – 0.5° . The scans show the three components: relaxed LSMO at $2\theta - \chi = 47.0^\circ$, fully strained LSMO with a possible overlap with LAO substrate at $2\theta - \chi = 48.0^\circ$, and the intense first-order satellite of the modulated structure at $2\theta - \chi = 47.5^\circ$. The overall intensity of the scan increases with the penetration depth. However, the relative intensities of the peaks vary with the incidence angle. Figure 7b depicts the relative intensity of the integrated area of the first order satellite peak compared to the relaxed LSMO reflection. The increase of this ratio with the incidence angle indicates that the relaxed LSMO part is closer to the film surface, while the modulated part is found deeper in

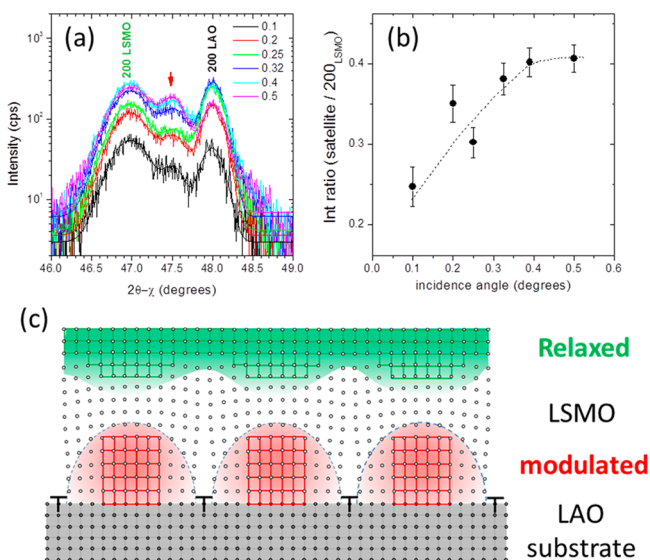


Figure 7. (a) In-plane diffraction $2\theta - \chi$ scans of the 200 reflection of the 7 nm thick LSMO/LAO film using different incidence ω angles from 0.1–0.5°. (b) Integrated intensity ratio of the satellite component versus the 200 LSMO Bragg reflection. (c) Model of the depth distribution of the outer relaxed LSMO and buried strained-modulated LSMO structure.

the film. The sketch in Figure 7c schematically represents the distribution of the two different phases. It is very likely that there is not a clear separation between these phases and there is a gradual change in strain between the top surface and the bottom interface of the film. The real situation may be even more complex if taken into account the strong strain field in the proximity of the MD cores. These may induce sudden changes in the sign of the linear strain but also in the shear strain, probably giving rise to more complex microstructure involving some local monoclinic distortions.

3.4. Influence on Film Functionality. The macroscopic observation of the planar resistivity in the films also evidences the formation of a distribution of two different phases. Figure 8 shows the resistivity of the films with different thicknesses from 2–14 nm at $H = 0\text{ T}$ (black) and $H = 9\text{ T}$ (red). The application of a magnetic field strongly enhances ferromagnetic correla-

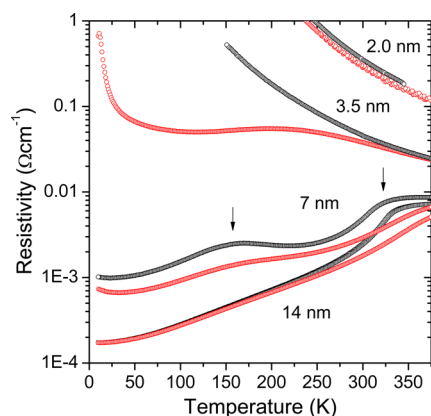


Figure 8. Resistivity versus temperature measured in thin LSMO/LAO films with different thickness at 0T (black) and 9T (red) applied magnetic field. The arrows indicate for the 7 nm thick film the maximum of magnetoresistance corresponding to the coexistence of low and high T_c phases.

tions, and the associated decrease of resistance gives rise to the so-called Colossal magnetoresistance (CMR) effect. This response achieves its maximum close to the ferromagnetic (metallic) to paramagnetic (insulating) phase transition, that is, to the corresponding ferromagnetic transition temperature T_c . We observe from Figure 8 that there is a clear evolution of transport properties when film thickness is increased from an insulating-like behavior for ultrathin films to a ferromagnetic-metallic behavior typical of LSMO bulk for thicker films. Films with intermediate thickness, namely 3.5 and 7 nm films, exhibit more complex magnetotransport properties that, nevertheless, can be easily understood in terms of the distorted structure (average measured c/a cell parameter ratio), as reported in ref 27 and the presence of the dislocations network in these films. The thinnest film of 2.0 nm exhibits a highly resistive (insulating) behavior with no sign of ferromagnetic correlations in the range of temperatures available, thus suggesting a nonmagnetic character. In the absence of MDs, this film is in a coherently strained state with a very large c/a ratio of ~ 1.06 . In this situation, the extremely distorted octahedral environment is expected to promote selective orbital occupancy and electronic localization, thus leading to an antiferromagnetic-insulating behavior.³² When thickness increases up to 3.5 and 7 nm, conductivity is enhanced, and magnetoresistive response appears as magnetic field promotes ferromagnetic correlations and electronic delocalization. Thus, it is reasonable to ascribe this behavior to the appearance of the dislocation network and the coexistence of a poor conducting phase in the distorted region between dislocations and a progressively increasing phase with reduced distortion and improved conductivity. In this way, the alternate arrangement of the dislocations leads to a complex conducting behavior of two competing phases with different resistances. At 3.5 nm, the relative extent of the insulating phase is large enough to block current paths at zero field (see Figure 8), but this blocking is overcome with the application of magnetic field. At 7 nm, both phases are of similar volume, which is manifested by the two distinct maxima in the resistance (around 150 and 320 K), each of them reflecting their corresponding transition temperature. For the thicker film (14 nm), bulk-like metallic behavior is recovered, and a single transition temperature is observed close to 330 K. In this case, the dominant undistorted phase governs the magnetotransport probably percolating through the whole sample since remnant distorted areas are confined to the interface region between film and substrate, as described in the sketch in Figure 7c. Therefore, in terms of their transport properties, there is a limited range of film thickness for the macroscopic manifestation of the nanophase mixture of phases.

3.5. Mechanism for MD Formation. Another striking observation of the LSMO films grown on LAO is that no twin formation was present in the whole range of thicknesses analyzed. This is clearly in contrast with previous observations of homogeneously twinned LSMO films with total absence of MDs when deposited on SrTiO_3 (STO) substrates at the same deposition conditions.^{25,26} This different film microstructure on LAO substrates is explained in terms of the competition between the MDs and twin domain formation mechanisms.

MDs are generated during film growth at elevated temperatures depending on the film–substrate mismatch and film thickness. Little variations are expected to occur beyond that step once an equilibrium MD pattern is achieved. At 900 °C, close to the LSMO rhombohedral-to-cubic transformation, shear distortion is less than 0.05° as measured in LSMO/STO

films in air.²⁶ Under these conditions, no twin domains are expected to form. Subsequently, the twin domains nucleate during the cooling step upon release of the progressively increasing shear stress of the LSMO rhombohedral film structure. The distorted structure nuclei grow until they meet another transformed domain. In LSMO films with no MDs when grown on STO, the rhombohedral domains compete with each other and arrange forming a homogeneous distribution of striped twin domains, thus achieving a long-range order depending on the crystal quality of the original crystal matrix. In LSMO/STO, striped twin domains were observed from early stages of the growth (above 2.0 nm thickness). However, in the LSMO films on LAO, since a high density of MDs is already formed at high temperature, the growth front of the transformed nuclei is most likely confined by the strain field originated by the buried MDs, particularly in ultrathin films. Therefore, it is blocking the long-range order of the twin domains and no striped microstructure is achieved. Only sufficiently thick films may transform generating a distribution of twin domains once the influence of the buried MDs is minimized.

There are several competing mechanisms that cause LSMO films on STO to not show any evidence of MD formation, even at film thicknesses as large as several hundreds of nanometres (despite of the critical thickness value $h_c \approx 5$ nm calculated from eq 2 assuming a + 0.7% tensile strain of LSMO on STO). This is evidently in contrast with the early formation of MDs on LAO. In a previous work, it was described that in LSMO/STO, the tensile strain is accommodated by an enrichment of the Mn³⁺ oxidation state at the interface, thus enlarging the equilibrium cell volume.²⁵ In the absence of a La/Sr composition segregation, the charge is compensated by the generation of oxygen vacancies. This reduces the film–substrate mismatch, which avoids the formation of MDs. However, this mechanism is precluded for the –2.4% compressive strain on LAO because the necessary cell volume reduction, which could be induced by the enhancement of Mn⁴⁺ oxidation state, cannot be compensated with an oxygen excess. Moreover, it cannot be ruled out that the absence of MDs in the LSMO films under tensile strain may be also related to an enhancement in the energy barrier for their nucleation and diffusion in comparison to films under compressive biaxial stress. This is not surprising and was already described in early studies. Generally, in semiconducting materials, and to a lower extent in metal heterostructures, there were observed some discrepancies on the critical thickness between the standard models and the experimental density of dislocations, which were attributed to non-negligible energies for the MD nucleation at the free surface of the film, as well as for their propagation toward the film–substrate interface.²⁹ The dislocation nucleation energy depends largely in the sign of the stress, and the critical thickness for MD nucleation is generally smaller for compression than under tension.³³ The fact that the experimental critical thickness obtained in these series of LSMO/LAO samples, $h_c = 2.5$ nm, does not deviate too much from that calculated from a thermodynamic equilibrium model of 1.7 nm is an indication that under compression there are not substantial barriers for MD nucleation and propagation, as opposed to the growth LSMO under tension.

4. CONCLUSIONS

In summary, we have observed that LSMO/LAO under large compressive strain of –2.4% starts relaxing forming MDs from

a critical thickness of about 2.5 nm. Progressively, the MDs density increases, which follows the expected linear dependence with the reciprocal thickness. At high enough linear densities, above 5×10^5 cm⁻¹, they self-arrange to form a periodic crossed network of edge dislocations with a very narrow distribution of distances. The highly ordered defect structure produces a lateral superperiodicity in the films that can be readily analyzed by XRD in perfect correlation with the direct observation of the MD lines by SEM and TEM. The presence of such high density of MDs blocks the formation of long striped twin domains. It is very likely that at a local scale the material transforms to the rhombohedral equilibrium structure. However, for the very thin films analyzed in this work, the domains are constrained within the nanoscale square regions flanked by crossed MDs, and twin walls were not observed. Within these small regions, the concurrence of domains with uniaxial relaxation in perpendicular directions very likely induces a complex pattern of cell distortions as exemplified in the strain contrast pattern of the planar view images in Figures 1c and 2a. The accurate description of this pattern falls beyond the scope of this study and is intended for further work, in correlation with high resolution planar view TEM images. The highly ordered distribution of nanophases with a different cell distortion results in the simultaneous appearance of low and high T_c transition temperatures in the resistivity curves, but only in a limited range of film thickness. The achievement of a control over the defect arrangement along with the confinement of the rhombohedral-cubic transformation at the nanoscale may produce a combination of metastable phases with unique physical properties as well as serve as a template for subsequent growth of heterostructures with lateral periodicity.

■ ASSOCIATED CONTENT

Supporting Information

The Supporting Information is available free of charge on the ACS Publications website at DOI: 10.1021/acsami.6b02896.

3D representation of reciprocal space maps of 002 symmetric, as well as 301 and 113 asymmetric reflections for different film thickness measured at KMC-2 beamline at HZB (Bessy II) (PDF)

Video of 3D representation of reciprocal space map of the 113 reflection (AVI)

■ AUTHOR INFORMATION

Corresponding Author

*E-mail: jose.santiso@icn2.cat. Phone: +34 93 7373634.

Author Contributions

The manuscript was written through contributions of all authors. All authors have given approval to the final version of the manuscript.

Notes

The authors declare no competing financial interest.

■ ACKNOWLEDGMENTS

This research was funded by the Spanish MINECO (projects: MAT2011-29081-C02, MAT2012-33207, and MAT2013-47869-C4-1-P, Consolider-Ingenio CSD2008-00023) and the European Union Horizon 2020 research and innovation programme under the Marie Skłodowska-Curie Grant Agreement No. 645658. We also acknowledge financial aid from the Generalitat de Catalunya (2014 SGR 501 and 2014 SGR 1216).

J.S. thanks the support of Ministry of Education and Science through program “Salvador de Madariaga” for a grant (ref: PRX14/00297) to perform a stay at MIT. Z.K. is grateful for the support from the Ministry of Education, Science, and Technological Development of the Republic of Serbia through Project No. III45018. Q.L. and B.Y. thank the National Science Foundation for support through the MIT Center of Materials Science and Engineering MRSEC under Grant No. DMR-1419807. This work made use of the Shared Experimental Facilities supported in part by the MRSEC Program of the National Science Foundation under Award No. DMR-1419807. We thank Dr. Belén Ballesteros (ICN2, Barcelona) and Prof. Marie-Jo Casanova (CEMES, Toulouse) for their assistance with TEM experiments. We are grateful to J. Rubio-Zuazo and the ESRF for providing assistance in using beamline BM25. We also thank HZB for the allocation of synchrotron radiation beamtime at Bessy.

REFERENCES

- (1) Schlom, D. G.; Chen, L. Q.; Eom, C. B.; Rabe, K. M.; Streiffer, S. K.; Triscone, J. M. Strain Tuning of Ferroelectric Thin Films. *Annu. Rev. Mater. Res.* **2007**, *37*, 589–626.
- (2) Jang, H. W.; Baek, S. H.; Ortiz, D.; Folkman, C. M.; Das, R. R.; Chu, Y. H.; Shafer, P.; Zhang, J. X.; Choudhury, S.; Vaithyanathan, V.; Chen, Y. B.; Felker, D. A.; Biegalski, M. D.; Rzchowski, M. S.; Pan, X. Q.; Schlom, D. G.; Chen, L. Q.; Ramesh, R.; Eom, C. B. Strain-Induced Polarization Rotation in Epitaxial (001) BiFeO₃ Thin Films. *Phys. Rev. Lett.* **2008**, *101*, 107602.
- (3) Bozovic, I.; Logvenov, G.; Belca, I.; Narimbetov, B.; Sveklo, I. Epitaxial Strain and Superconductivity in La_{2-x}Sr_xCuO₄ Thin Films. *Phys. Rev. Lett.* **2002**, *89*, 107001.
- (4) Schlom, D. G.; Chen, L. Q.; Pan, X.; Schmehl, A.; Zurbuchen, M. A. (2008). A Thin Film Approach to Engineering Functionality into Oxides. *J. Am. Ceram. Soc.* **2008**, *91*, 2429–2454.
- (5) Catalan, G.; Seidel, J.; Ramesh, R.; Scott, J. F. (2012). Domain Wall Nanoelectronics. *Rev. Mod. Phys.* **2012**, *84*, 119.
- (6) Farokhipoor, S.; Magén, C.; Venkatesan, S.; Íñiguez, J.; Daumont, C. J.; Rubi, D.; Snoeck, E.; Mostovoy, M.; de Graaf, C.; Müller, A.; Döblinger, M.; Scheu, C.; Noheda, B. Artificial Chemical and Magnetic Structure at the Domain Walls of an Epitaxial Oxide. *Nature* **2014**, *515*, 379–383.
- (7) Arredondo, M.; Ramasse, Q. M.; Weyland, M.; Mahjoub, R.; Vrejoiu, I.; Hesse, D.; Browning, N. D.; Alexe, M.; Munroe, P.; Nagarajan, V. Direct Evidence for Cation Non-Stoichiometry and Cottrell Atmospheres Around Dislocation Cores in Functional Oxide Interfaces. *Adv. Mater.* **2010**, *22*, 2430–2434.
- (8) Chu, M. W.; Szafraniak, I.; Scholz, R.; Harnagea, C.; Hesse, D.; Alexe, M.; Gösele, U. Impact of Misfit Dislocations on the Polarization Instability of Epitaxial Nanostructured Ferroelectric Perovskites. *Nat. Mater.* **2004**, *3*, 87–90.
- (9) Nagarajan, V.; Jia, C. L.; Kohlstedt, H.; Waser, R.; Misirliglu, I. B.; Alpay, S. P.; Ramesh, R. Misfit Dislocations in Nanoscale Ferroelectric Heterostructures. *Appl. Phys. Lett.* **2005**, *86*, 192910.
- (10) Lubk, A.; Rossell, M. D.; Seidel, J.; Chu, Y. H.; Ramesh, R.; Hÿtch, M. J.; Snoeck, E. Electromechanical Coupling among Edge Dislocations, Domain Walls, and Nanodomains in BiFeO₃ Revealed by Unit-Cell-Wise Strain and Polarization Maps. *Nano Lett.* **2013**, *13*, 1410–1415.
- (11) Chang, C. P.; Chu, M. W.; Jeng, H. T.; Cheng, S. L.; Lin, J. G.; Yang, J. R.; Chen, C. H. Condensation of Two-Dimensional Oxide-Interfacial Charges into One-Dimensional Electron Chains by the Misfit-Dislocation Strain Field. *Nat. Commun.* **2014**, *5*, 3522.
- (12) Frank, F. C.; Van der Merwe, J. H. One-Dimensional Dislocations. II. Misfitting Monolayers and Oriented Overgrowth. *Proc. R. Soc. London, Ser. A* **1949**, *198*, 216–225.
- (13) Matthews, J. W.; Blakeslee, A. E. Defects in epitaxial multilayers: II. Dislocation Pile-ups, Threading Dislocations, Slip Lines and Cracks. *J. Cryst. Growth* **1975**, *29*, 273–280.
- (14) Speck, J. S.; Pompe, W. Domain Configurations Due to Multiple Misfit Relaxation Mechanisms in Epitaxial Ferroelectric Thin Films. I. Theory. *J. Appl. Phys.* **1994**, *76*, 466–476.
- (15) Nabarro, F. R. N. Dislocations in a Simple Cubic Lattice. *Proc. Phys. Soc.* **1947**, *59*, 256.
- (16) Kishinû, S.; Ogirima, M.; Kurata, K. A Cross-Hatch Pattern in GaAs_{1-x}P_x Epitaxially Grown on GaAs Substrate. *J. Electrochem. Soc.* **1972**, *119*, 617–622.
- (17) Sánchez, F.; García-Cuenca, M. V.; Ferrater, C.; Varela, M.; Herranz, G.; Martínez, B.; Fontcuberta, J. Transition from Three- to Two-Dimensional Growth in Strained SrRuO₃ Films on SrTiO₃ (001). *Appl. Phys. Lett.* **2003**, *83*, 902.
- (18) Kim, S. G.; Wang, Y.; Chen, I.-W. Strain Relaxation in Buried SrRuO₃ Layer in (Ca_{1-x}Sr_x)(Zr_{1-x}Ru_x)O₃/SrRuO₃/SrTiO₃. *Appl. Phys. Lett.* **2006**, *89*, 031905.
- (19) Wang, Z. H.; Lebedev, O. I.; Van Tendeloo, G.; Cristiani, G.; Habermeyer, H. U. Crosshatching on La_{0.5}Ca_{0.5}MnO₃ Ultrathin Films Epitaxially Grown on SrTiO₃(100). *Phys. Rev. B: Condens. Matter Phys.* **2008**, *77*, 115330.
- (20) Sun, H. P.; Tian, W.; Pan, X. Q.; Haeni, J. H.; Schlom, D. G. Evolution of Dislocation Arrays in Epitaxial BaTiO₃ Thin Films Grown on (100)SrTiO₃. *Appl. Phys. Lett.* **2004**, *84*, 3298–3300.
- (21) Tersoff, J.; Teichert, C.; Lagally, M. G. Self-Organization in Growth of Quantum Dot Superlattices. *Phys. Rev. Lett.* **1996**, *76*, 1675.
- (22) Kern, K.; Brune, H.; Giovannini, M.; Bromann, K. Self-Organized Growth of Nanostructure Arrays on Strain-Relief Patterns. *Nature* **1998**, *394*, 451–453.
- (23) Zhang, X.; Liu, Z.; Li, Q.; Leung, Y.; Ip, K.; Hark, S. Routes to Grow Well-Aligned Arrays of ZnSe Nanowires and Nanorods. *Adv. Mater.* **2005**, *17*, 1405–1410.
- (24) Meng, F.; Morin, S. A.; Forticaux, A.; Jin, S. Screw Dislocation Driven Growth of Nanomaterials. *Acc. Chem. Res.* **2013**, *46*, 1616–1626.
- (25) Sandiumenge, F.; Santiso, J.; Balcells, L.; Konstantinovic, Z.; Roqueta, J.; Pomar, A.; Espinós, J. P.; Martínez, B. Competing Misfit Relaxation Mechanisms in Epitaxial Correlated Oxides. *Phys. Rev. Lett.* **2013**, *110*, 107206.
- (26) Santiso, J.; Balcells, L.; Konstantinovic, Z.; Roqueta, J.; Ferrer, P.; Pomar, A.; Martínez, B.; Sandiumenge, F. Thickness Evolution of the Twin Structure and Shear Strain in LSMO films. *CrystEngComm* **2013**, *15*, 3908–3918.
- (27) Sandiumenge, F.; Bagués, N.; Santiso, J.; Paradinas, M.; Pomar, A.; Konstantinovic, Z.; Ocal, C.; Balcells, L.; Casanove, M.-J.; Martínez, B. Misfit Dislocation Guided Topographic and Conduction Patterning in Complex Oxide Epitaxial Thin Films. *Adv. Mater. Interfaces* **2016**, DOI: 10.1002/admi.201600106.
- (28) MacPherson, G.; Goodhew, P. J.; Beanland, R. A Model for the Distribution of Misfit Dislocations Near Epitaxial Layer Interfaces. *Philos. Mag. A* **1995**, *72*, 1531–1545.
- (29) Matthews, J. W.; Blakeslee, A. E. Defects in Epitaxial Multilayers: I. Misfit Dislocations. *J. Cryst. Growth* **1974**, *27*, 118–125.
- (30) Ohring, M. *Materials Science of Thin Films*, 2nd ed.; Academic Press: New York, 2002.
- (31) Freund, L. B. Dislocation Mechanisms of Relaxation in Strained Epitaxial Films. *MRS Bull.* **1992**, *17*, 52–60.
- (32) Fang, Z.; Solovyev, I. V.; Terakura, K. Phase Diagram of Tetragonal Manganites. *Phys. Rev. Lett.* **2000**, *84*, 3169.
- (33) Dong, L.; Schnitker, J.; Smith, R. W.; Srolovitz, D. J. Stress Relaxation and Misfit Dislocation Nucleation in the Growth of Misfitting Films: A Molecular Dynamics Simulation Study. *J. Appl. Phys.* **1998**, *83*, 217.

Tunneling anisotropic magnetoresistance in $\text{La}_{2/3}\text{Sr}_{1/3}\text{MnO}_3/\text{LaAlO}_3/\text{Pt}$ tunnel junctions

R. Galceran,¹ L. Balcells,¹ A. Pomar,¹ Z. Konstantinović,² N. Bagués,^{1,3} F. Sandiumenge,¹ and B. Martínez¹

¹*Instituto de Ciencia de Materiales de Barcelona - CSIC, Campus UAB, Bellaterra- 08193, Spain*

²*Center for Solid State Physics and New Materials, Institute of Physics Belgrade, University of Belgrade, Pregrevica 118, 11080 Belgrade, Serbia*

³*Institut Català de Nanociència i Nanotecnologia, ICN2-CSIC, Campus UAB, E-08193 Bellaterra, Spain*

(Received 13 November 2015; accepted 31 March 2016; published online 11 April 2016)

The magnetotransport properties of $\text{La}_{2/3}\text{Sr}_{1/3}\text{MnO}_3$ (LSMO)/ LaAlO_3 (LAO)/Pt tunneling junctions have been analyzed as a function of temperature and magnetic field. The junctions exhibit magnetoresistance (MR) values of about 37%, at $H=90$ kOe at low temperature. However, the temperature dependence of MR indicates a clear distinct origin than that of conventional colossal MR. In addition, tunneling anisotropic MR (TAMR) values around 4% are found at low temperature and its angular dependence reflects the expected uniaxial anisotropy. The use of TAMR response could be an alternative of much easier technological implementation than conventional MTJs since only one magnetic electrode is required, thus opening the door to the implementation of more versatile devices. However, further studies are required in order to improve the strong temperature dependence at the present stage. © 2016 Author(s). All article content, except where otherwise noted, is licensed under a Creative Commons Attribution (CC BY) license (<http://creativecommons.org/licenses/by/4.0/>). [<http://dx.doi.org/10.1063/1.4946851>]

INTRODUCTION

Magnetic tunneling junctions (MTJ) have been a subject of intense research during the last decade due to their potential interest for the implementation of high-density magnetic random access memories (MRAM).¹ Their response relies on the strong dependence of the magnetoresistance on the relative orientation of the magnetization directions in each magnetic electrode and their spin polarizations. However, the requirement of two independently controlled ferromagnetic electrodes and spin-coherent tunneling imposes some technical challenges, such as the uniformity of the magnetic properties of the electrodes, the insulating barrier uniformity or the thermal stability, for the implementation of MTJ-based devices that, in spite of the work already done, are not fully resolved yet.² Different attempts have been made to overcome these problems such as, for instance, increasing the magnitude of the tunneling magnetoresistance (TMR) response by using half-metallic materials as electrodes.^{3,4} Even though TMR values of several hundred percent have been achieved in some cases⁵⁻⁸ by using those materials, they become vanishing small well below room temperature,^{5,6,9,10} therefore severely hampering technological applications. To overcome these challenges requires exploring new possibilities. An alternative to conventional TMR could be tunneling anisotropic magnetoresistance (TAMR) phenomena, i.e. the dependence of the magnetoresistance on the orientation of the magnetization of the electrodes with respect to the crystallographic axes or the current flow direction.^{11,12} This angular-dependent contribution is due to the coupling of orbital and electronic spin degrees of freedom and its origins may be diverse including: (a) spin-orbit induced changes of the density of states of the ferromagnetic electrode, (b) the interference between Bychkov-Rashba and Dresselhaus spin-orbit couplings at junctions interfaces and in the tunneling region, (c) resonant states whose coupling to the scattering channels

depends on magnetization direction. It is worth mentioning that TAMR is present even in the case of only one ferromagnetic electrode when conventional TMR is absent.^{13,14} Since TAMR-based devices can operate with only one magnetic electrode they could be an alternative of much easier technological application than conventional MTJs, thus opening the door to the implementation of more versatile devices, avoiding the need for two independently controlled ferromagnetic electrodes and spin-coherent tunneling. Even though TAMR was initially found in magnetic semiconductors, it has also been found in TJs with ferromagnetic metal electrodes.^{14,15} Studies in ferromagnetic metal systems were initially conducted in most of the cases in spin valve-like systems with two magnetic electrodes and a complex stacking sequence.¹⁶ However, TAMR reports in system with only one magnetic electrode are much more recent and scarce.^{17,18} In these cases values of TAMR around 5-10 % at low temperature and with a strong dependence of the bias voltage are reported. In this context, the introduction of manganite electrodes could be of interest for combining different functionalities and hopefully enhancing the TAMR response while reducing the complex stacking sequence typically used in metallic MTJs. Among manganites $\text{La}_{2/3}\text{Sr}_{1/3}\text{MnO}_3$ (LSMO), with the highest Curie temperature ($T_C \sim 370$ K) of this family of materials, is the most interesting one for the implementation of devices.

In this work we report on the tunneling magnetotransport properties of the $\text{La}_{2/3}\text{Sr}_{1/3}\text{MnO}_3$ (LSMO)/ LaAlO_3 (LAO) bilayer system as a function of temperature and applied magnetic field with the aim to analyze their TAMR response and its potential for technological applications. A Pt metallic electrode has been used because of its good adhesion properties. The conduction across the LSMO/LAO/Pt heterostructure exhibits typical features expected for a tunneling conduction process. However, the temperature dependence of the junction resistance exhibits a peak at about 170 K whose origin is not well understood yet. A clear TAMR response that amounts about 4% at low temperature is observed when a magnetic field higher than the anisotropy field, ($H_a \cong 10$ kOe) is applied parallel or perpendicular to the current flow direction.

RESULTS AND DISCUSSION

LSMO/LAO bilayers used in this work have been prepared by RF-magnetron sputtering on top of (001)-oriented SrTiO_3 (STO) substrates treated before deposition to select a unique atomic termination, likely to be TiO_2 .¹⁹ Bilayers are highly crystalline with a $\text{STO}(001)/\text{LSMO}(001)/\text{LAO}(001)$ epitaxial relationship and sharp clean interfaces (see Fig. 1). LAO was chosen as insulating barrier because it has demonstrated to be less harmful for the magnetic and electronic properties of LSMO than other oxides such as SrTiO_3 or MgO .²⁰⁻²² LSMO layer thickness was about 40 nm while the thickness of the LAO layer was about 1.5 nm, as corroborated from TEM images (see Fig. 1), and in good agreement with the estimation from growth rate.²³

For the fabrication of metallic contacts samples were covered with a layer of polymethyl methacrylate (PMMA) resist by spin coating, then electron beam lithography was used to define square holes in the PMMA resist. After developing, Pt was deposited by evaporation through a shadow mask defining the upper metallic electrode precisely on top of the openings of PMMA resist engraved by lithography. Further details about sample preparation can be found elsewhere.²³

Electronic transport properties were measured in a commercial physical properties measurement system (PPMS) by Quantum Design using a 3-point configuration between a large area macro-contact and top contacts, this configuration was adopted to avoid contributions from the bottom electrode. The current was applied perpendicular to the film plane while the magnetic field was rotated from out of plane, i.e., parallel to the current direction, [001] direction, to in plane parallel to [100] direction. The dependencies on temperature, magnetic field and angle orientation between magnetization and current directions were proved.

The conduction across the LSMO/LAO/Pt heterostructure exhibits typical features expected for a tunneling conduction process (see inset in Fig. 2). However, due to the slimness of the LAO barrier and the procedure to prepare it, the existence of microstructural defects and randomly distributed pinholes through the barrier cannot be fully excluded. The temperature dependence of the junction resistance, $R(T)$, of a $12 \mu\text{m}^2$ LSMO/LAO/Pt junction is shown in Fig. 2. The $R(T)$ curve exhibits a smooth increase of the resistance on lowering temperature compatible with direct

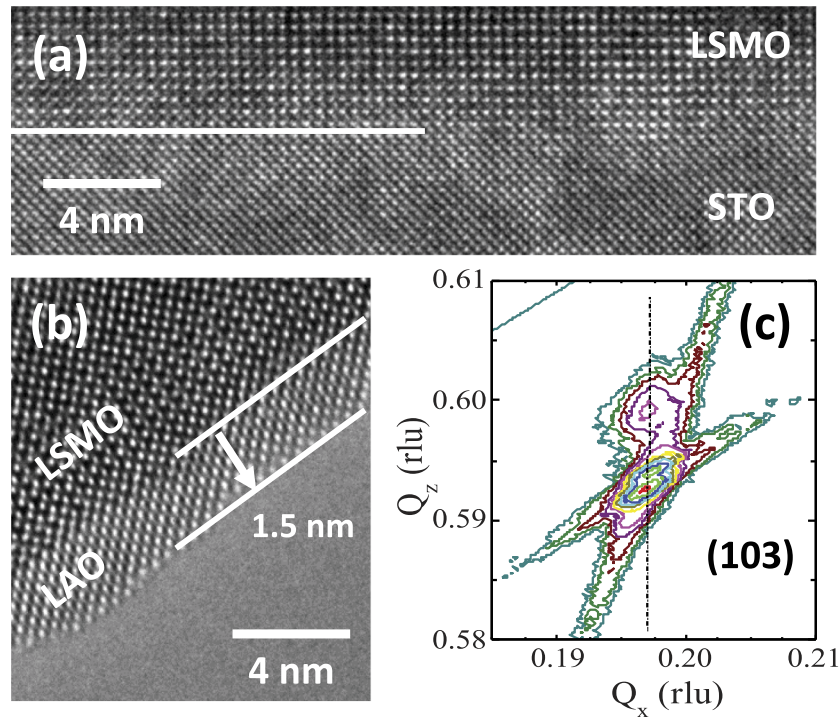


FIG. 1. HRTEM picture of the STO/LSMO (a) and LSMO/LAO (b) interfaces. (c) Reciprocal space map around the STO (103) reflection for a STO/LSMO/LAO heterostructure.

tunneling transport.²⁴ However, $R(T)$ exhibits a peak with a maximum at about 170 K that seems to be a common feature in MTJs containing manganite electrodes and whose origin is not well established yet.^{7,25,26} As shown by the figure the application of a magnetic field (regardless of its orientation) results in an important reduction of the junction's resistance. Interestingly, in contrast

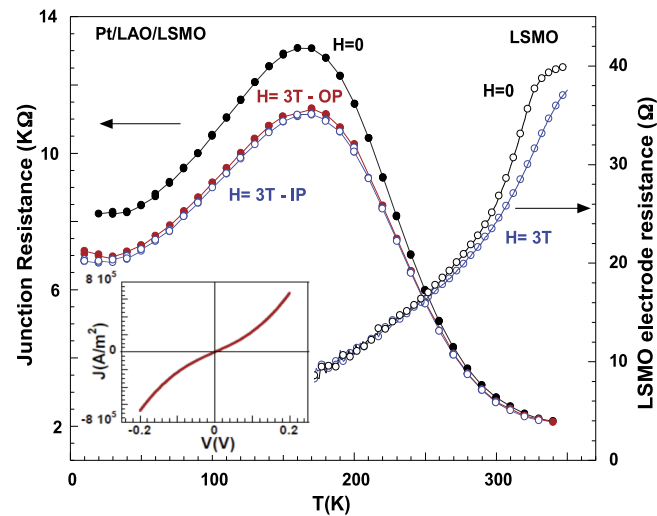


FIG. 2. Temperature dependence of the Pt/LAO/LSMO junction resistance measured in 3-terminal configuration in a $12 \mu\text{m}^2$ junction for applied bias voltage of 100 mV. Two different values of the magnetic field are shown ($H=0$ (black dots) and $H=3$ T. The latter has been applied parallel to the junction's plane (IP, blue open dots) and perpendicular to it (OP, red dots). The temperature dependence of the $R(T)$ of the LSMO bottom electrode is also shown for comparison purposes (the field ($H=3$ T) was applied perpendicular to the film plane). Measurements were done after a zero field cooling process. The inset shows a typical I-V characteristic curve of the junction at $T=10$ K.

with the typical behavior of CMR materials, no shift in the temperature of the peak of the junction resistance is observed. This key observation indicates that the measured MR has nothing to do with the typical behavior of double-exchange mediated CMR materials thus, strongly suggesting that the origin of the peak in $R(T)$ is not related to an oxygen-deficient layer at the LSMO/LAO interface as reported previously.^{26,27} The temperature dependence of the resistance of the LSMO electrode is also shown in Fig. 2. It exhibits the typical behavior of a good quality LSMO film with T_C slightly above 350 K, large CMR values close to T_C , small residual resistance at low temperature and saturation magnetization slightly below bulk saturation values. Thus, excluding a major role of effects related to phase segregation and magnetic frustration that could be important for very thin LSMO films. Worth to mention that the resistance of the LSMO electrode is almost three orders of magnitude smaller than the resistance of the TJ, thus the contribution of the LSMO electrode to the resistance of the junction is almost negligible.

The MR of the junction is better appreciated in the $R(H)$ curves depicted in Fig. 3. A negative MR of about 37% at 90 kOe is measured at low temperature, and then it smoothly decreases when increasing temperature below 5% at room temperature (see Fig. 4) as the ferromagnetic transition temperature of the LSMO electrode ($T_C \sim 350$ K) is approached. This MR response is observed independently of the orientation of the magnetic field. The fact that this high-field MR is larger at low temperatures (10 K) than at the peak temperature of the junction $R(T)$ (~ 170 K, Fig. 2 left) or the LSMO transition temperature ($T_C \sim 350$ K) further corroborates that this MR contribution cannot be ascribed to conventional CMR. However, the curve exhibits a clear signature of the $R(T)$ peak at 170 K. The origin of this high-field MR contribution is not clear and it may well be related to magnetic disorder at the interface, which would give a MR contribution similar to that observed in LSMO granular systems.

Additionally, a MR response is also observed when the orientation of the magnetic field is changed from parallel to perpendicular to the sample surface, i.e., parallel to the current (see Figures 2 and 3). This MR response, unexpected, in principle, because the junction has only one magnetic electrode, (LSMO), corresponds to the so-called TAMR and it amounts about 4% at low temperatures. As temperature is increased, TAMR slowly decreases and vanishes close to room temperature (see Fig. 4). As mentioned in the introduction, MR in magnetic tunneling junctions may depend on the orientation of the magnetization with respect to the crystallographic axis or the direction of the current flow.^{13,14} The geometry of the present LSMO/LAO/Pt stack is shown in the

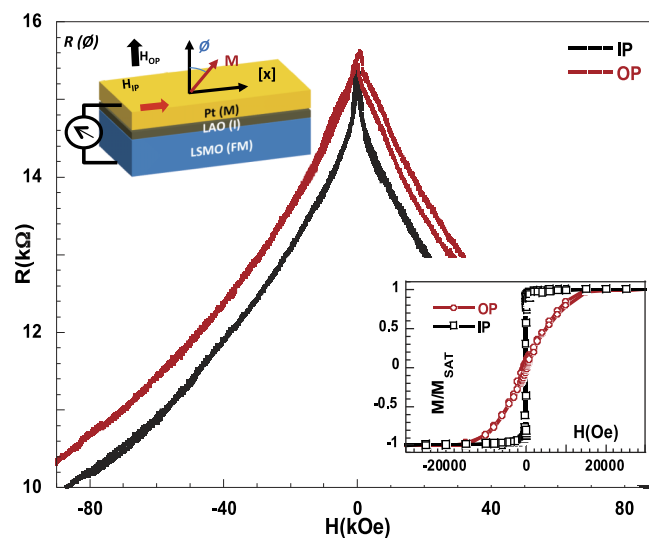


FIG. 3. $R(H)$ curves measured at 10 K, and voltage bias of 10 mV, with the applied magnetic field in-plane (IP) and out-of-plane (OP) configurations for a $12 \mu\text{m}^2$ Pt/LAO/LSMO junction. The corresponding hysteresis loops are shown in the lower inset. Upper inset: Sketch of the measurement configuration for the corresponding in-plane (IP) and out-of-plane (OP) applied magnetic field.

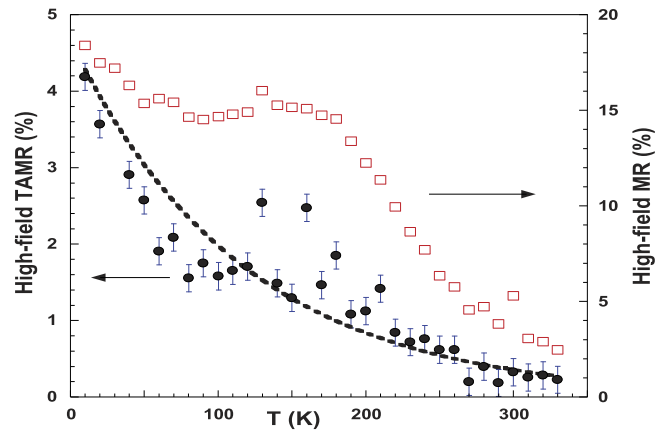


FIG. 4. Temperature dependence of the different high-field MR contributions for a $12 \mu\text{m}^2$ Pt/LAO/LSMO junction measured at 100 mV. Red squares, referred to the right axis, depict the difference between the resistance at $H=0$ and 30 kOe applied in-plane (IP). Black dots, referred to the left axis, represent the difference in resistance for a fixed magnetic field of 30 kOe applied in-plane (IP) and out-of-plane (OP).

upper inset of Fig. 3 and corresponds to the so-called out-of-plane TAMR with a single magnetic electrode.²⁸ In these circumstances TAMR reflects the change in the tunneling magnetoresistance when the magnetization is rotated from parallel to the plane of the junction ($\phi = 90^\circ$) to perpendicular to it ($\phi = 0^\circ$) and is given by: $\text{TAMR}(\phi) = (R(\phi) - R(0))/R(0)$, being ϕ the angle between the normal to the junction plane and the direction of the magnetization. Since the LSMO/LAO/Pt stack exhibits in-plane easy magnetization direction, a field H applied perpendicular to the stacking plane progressively drags the magnetization M out from the film plane until it is saturated in the field direction, (i.e. parallel to the current direction) once the anisotropy field is surpassed (see lower inset of Fig. 3). Thus, above the anisotropy field TAMR should be constant as evidenced in Fig. 3 where in-plane and out-of-plane branches of the $R(H)$ curves are shown to be parallel in the high field regime. The angular dependence of TAMR is better appreciated in Fig. 5 where the

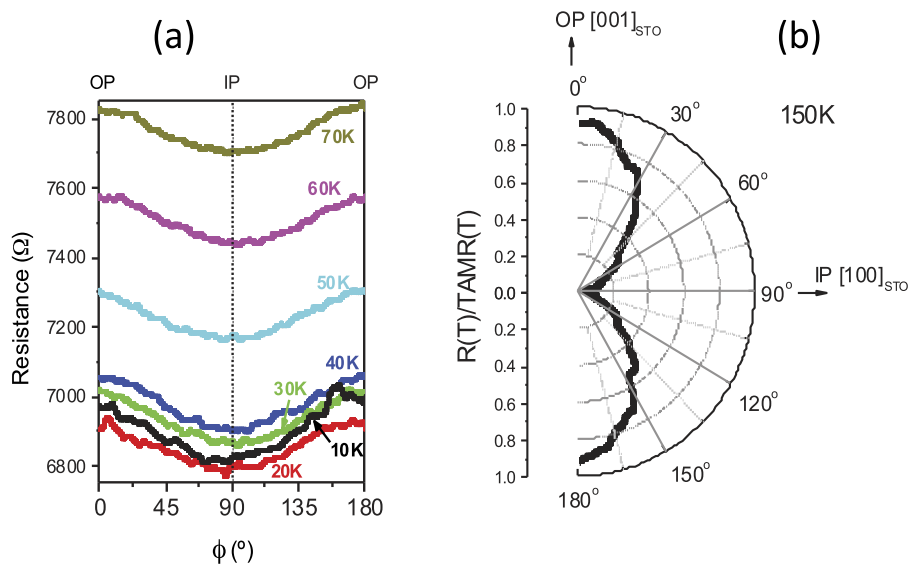


FIG. 5. TAMR at high magnetic fields of a $12 \mu\text{m}^2$ Pt/LAO/LSMO junction. (a) Resistance as a function of the angle between the current (normal to the sample surface) and the applied magnetic field, ϕ , for several temperatures. Different colors represent measurements taken at different temperatures, from 10 K to 70 K; (b) Polar plot of the normalized $R(\phi)/\text{TAMR}(T)$ at 150 K. IP and OP correspond to the configurations where magnetization is aligned in-plane and out-of-plane, respectively.

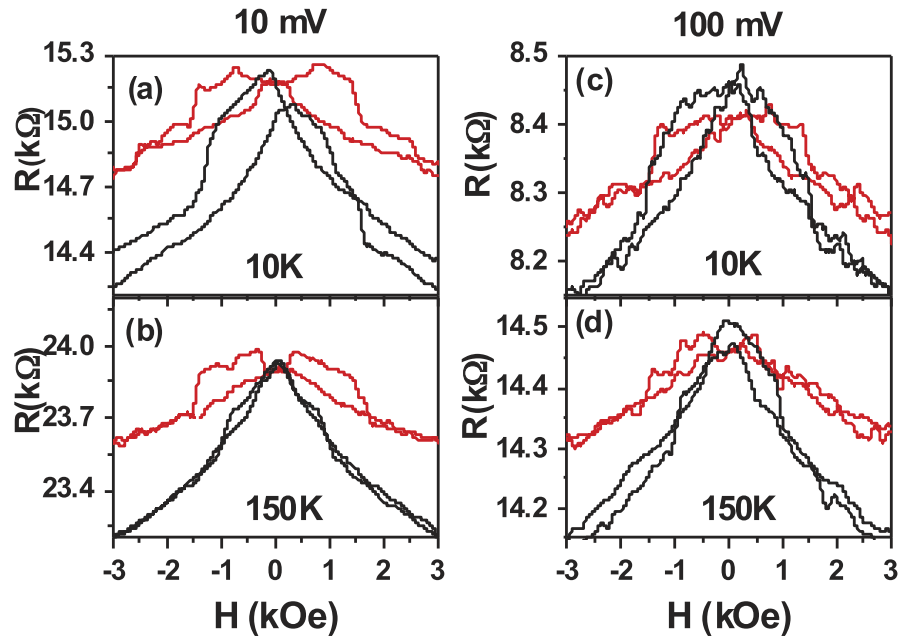


FIG. 6. TAMR at low magnetic fields of a $12 \mu\text{m}^2$ Pt/LAO/LSMO junction: $R(H)$ curves taken for the in-plane (IP) (black lines) and out-of-plane (OP) (red lines) configurations, at different bias voltage values (10 mV (a and b) and 100 mV (c and d)), for different temperatures ($T=10$ K (a and c) and $T=150$ K (b and d)).

junction resistance is depicted as a function of the angle between the magnetization and current directions, $R(\phi)$, for several temperatures when the magnetic field is rotated from the [001] to the [100]. A polar plot of the normalized $R(\phi)/\text{TAMR}$ at 150 K is also shown in the figure making evident the expected uniaxial anisotropy character. Similar values of TAMR are obtained when the magnetic field is rotated from the [001] direction to the [010]. On the other hand, TAMR values are substantially reduced when increasing bias voltages as already observed in metallic MTJs.¹⁶ As mentioned in the introduction, this angular-dependent contribution is due to the coupling of orbital and electronic spin degrees of freedom however; our macroscopic measurements do not allow determining the microscopic origin.

In the low field regime, i.e. below the anisotropy field, M and H may not be fully aligned and $R(H)$ curves exhibit switching between distinct resistance states in a spin-valve-like fashion (see Fig. 6). As our system has a single ferromagnetic electrode, TAMR must be at the origin of such behavior through a magnetization reversal that takes place in a multi-step process, so that the jumps in resistance correspond to the rotation of different magnetic domains.^{14,29} As shown in Fig. 6 the effect is stronger for smaller bias voltages and lower temperatures; TAMR is hardly distinguishable from the noise for the measurement taken at 150 K and 100 mV. This could be attributed to the fact that providing more energy to the system (via thermal energy or via electric field) leads to a faster magnetization reversal, with no intermediate magnetization steps.

In summary, the magnetotransport properties of LSMO/LAO/Pt tunneling junctions have been analyzed as a function of temperature and magnetic field demonstrating the existence of TAMR response. The temperature dependence of the junction resistance, $R(T)$, exhibits a peak at about 170 K, as in the case of other tunneling junctions with manganite electrodes, whose origin is not well understood yet. Our system exhibits MR values of about 37%, at $H=90$ kOe and low temperature, and its temperature dependence, which cannot be explained through conventional CMR mechanisms, strongly suggests that the previously reported scenario of an interfacial layer of under-doped manganite with reduced ordering temperature is very unlikely. This MR response may well be related to magnetic disorder at the interface. In addition, the system exhibits TAMR values of around 4% at low temperature, despite the weak spin-orbit coupling in this system, and its angular dependence reflects the expected uniaxial anisotropy. These values are very similar to

that reported for ferromagnetic metal MTJ but with a much more simple stacking sequence which would be of major interest for the implementation of TAMR-based devices. The use of TAMR response could be an alternative of much easier technological implementation than conventional MTJs opening the door to the implementation of more versatile devices avoiding the need for two independently controlled ferromagnetic electrodes and spin-coherent tunneling. However, further studies are required in order to improve the strong temperature dependence that severely restricts potential technological applications in the present stage.

ACKNOWLEDGEMENTS

We acknowledge financial support from the Spanish Ministry of Economy and Competitiveness, through the “Severo Ochoa” Programme for Centres of Excellence in R&D (SEV- 2015-0496)”, MAT2015-71664-R, and FEDER program. R.G. thanks the Spanish MINECO for the financial support through the FPI program. ZK thanks Project III45018 from the Ministry of Education, Science, and Technological Development of Republic of Serbia.

- ¹ S. Maekawa, S. Takahashi, and H. Imamura, in *Spin Dependent Transport in Magnetic Nanostructures*, edited by S. Maekawa and T. Shinjo (Taylor and Francis, New York, 2002), pp. 143–236.
- ² E. Y. Tsymlal, O. N. Mryasov, and P. R. LeClair, *J. Phys.: Condens. Matter* **15**, R109–R142 (2003).
- ³ P. Seneor, A. Fert, J.L. Maurice, F. Montaigne, F. Petroff, and A. Vaures, *Appl. Phys. Lett.* **74**, 4017 (1999).
- ⁴ G. Hu and Y. Suzuki, *Phys. Rev. Lett.* **89**, 276601 (2002).
- ⁵ M. Bowen, M. Bibes, A. Barthélémy, J.P. Contour, A. Anane, Y. Lemaître, and A. Fert, *Appl. Phys. Lett.* **82**, 233 (2003).
- ⁶ M.H. Jo, N.D. Mathur, N.K. Todd, and M.G. Blamire, *Phys. Rev. B* **61**, R14901 (2000).
- ⁷ Y. Ishii, H. Yamada, H. Sato, H. Akoh, Y. Ogawa, M. Kawasaki, and Y. Tokura, *Appl. Phys. Lett.* **89**, 042509 (2006).
- ⁸ E. T. Wertz and Q. Li, *Appl. Phys. Lett.* **90**, 142506 (2007).
- ⁹ J. O’Donnell, A. E. Andrus, S. Oh, E. V. Colla, and J. N. Eckstein, *Appl. Phys. Lett.* **76**, 1914 (2000).
- ¹⁰ J. S. Noh, T. K. Nath, C. B. Eom, J. Z. Sun, W. Tian, and X. Q. Pan, *Appl. Phys. Lett.* **79**, 233 (2001).
- ¹¹ M. Tanaka and Y. Higo, *Phys. Rev. Lett.* **87**, 026602 (2001).
- ¹² L. Brey, C. Tejedor, and J. Fernandez-Rosier, *Appl. Phys. Lett.* **85**, 1996 (2004).
- ¹³ A. D. Giddings, M. N. Khalid, T. Jungwirth, J. Wunderlich, S. Yasin, R. P. Campion, K. W. Edmonds, J. Sinova, K. Ito, K.-Y. Wang, D. Williams, B. L. Gallagher, and C. T. Foxon, *Phys. Rev. Lett.* **94**, 127202 (2005).
- ¹⁴ J. Moser, A. Matos-Abiague, D. Schuh, W. Wegscheider, J. Fabian, and D. Weiss, *Phys. Rev. Lett.* **99**, 056601 (2007).
- ¹⁵ B.G. Park, J. Wunderlich, D.A. Williams, S.J. Joo, K.Y. Jung, K.H. Shin, K. Olejnik, A.B. Shick, and T. Jungwirth, *Phys. Rev. Lett.* **100**, 087204 (2008).
- ¹⁶ Li Gao, X. Jiang, S.-H. Yang, J.D. Burton, E.Y. Tsymlal, and S.S.P. Parkin, *Phys. Rev. Lett.* **99**, 226602 (2007).
- ¹⁷ S. Hatanaka, S. Miwa, K. Matsuda, K. Nawaoka, K. Tanaka, H. Morishita, M. Goto, N. Mizouchi, T. Shinjo, and Y. Suzuki, *Appl. Phys. Lett.* **107**, 082407 (2015).
- ¹⁸ K. Wang, T.L.A. Tran, P. Brinks, J.G.M. Sanderink, T. Bolhuis, W.G. van der Wiel, and M.P. de Jong, *Phys. Rev. B* **88**, 054407 (2013).
- ¹⁹ T. Nakamura, H. Inada, and M. Iiyama, *Appl. Surf. Sci.* **130-132**, 576 (1998).
- ²⁰ H. Yamada, Y. Ogawa, Y. Ishii, H. Sato, M. Kawasaki, H. Akoh, and Y. Tokura, *Science* **305**, 646 (2004).
- ²¹ S. Valencia, Z. Konstantinovic, D. Schmitz, A. Gaupp, Ll. Balcells, and B. Martinez, *Phys. Rev. B* **84**, 024413 (2011).
- ²² S. Valencia, L. Peña, Z. Konstantinovic, Ll. Balcells, R. Galceran, D. Schmitz, F. Sandiumenge, M. Casanove, and B. Martinez, *J. Phys.: Condens. Matter* **26**, 166001 (2014).
- ²³ R. Galceran, Ll. Balcells, A. Pomar, Z. Konstantinović, F. Sandiumenge, and B. Martínez, *J. of Appl. Phys.* **117**, 103909 (2015).
- ²⁴ B.J. Jonsson-Akerman, R. Escudero, C. Leighton, S. Kim, and I.K. Schuller, *Appl. Phys. Lett.* **77**, 1870 (2000).
- ²⁵ J. Z. Sun, K. P. Roche, and S. S. P. Parkin, *Phys. Rev. B* **61**, 11244 (2000); J. Z. Sun, D. W. Abraham, K. P. Roche, and S. S. P. Parkin, *Appl. Phys. Lett.* **73**, 1008 (1998).
- ²⁶ M. Viret, M. Drouet, J. Nassar, J. P. Contour, C. Fermon, and A. Fert, *Europhys. Lett.* **39**, 545 (1997).
- ²⁷ J. Z. Sun, L. Krusin-Elbaum, P. R. Ducombe, A. Gupta, and R. B. Laibowitz, *Appl. Phys. Lett.* **70**, 1769 (1997).
- ²⁸ A. Matos-Abiague and J. Fabian, *Phys. Rev. B* **79**, 155303 (2009).
- ²⁹ M. Ciorga, M. Schlapps, A. Einwanger, S. Geißler, J. Sadowski, W. Wegscheider *et al.*, *New J. Phys.* **9**, 351 (2007).

Misfit Dislocation Guided Topographic and Conduction Patterning in Complex Oxide Epitaxial Thin Films

Felip Sandiumenge,* Núria Bagués, José Santiso, Markos Paradinas, Alberto Pomar, Zorica Konstantinovic, Carmen Ocal, Lluís Balcells, Marie-Jo Casanove, and Benjamín Martínez

Interfacial dissimilarity has emerged in recent years as the cornerstone of emergent interfacial phenomena, while enabling the control of electrical transport and magnetic behavior of complex oxide epitaxial films. As a step further toward the lateral miniaturization of functional nanostructures, this work uncovers the role of misfit dislocations in creating periodic surface strain patterns that can be efficiently used to control the spatial modulation of mass transport phenomena and bandwidth-dependent properties on a ≈ 20 nm length scale. The spontaneous formation of surface strain-relief patterns in $\text{La}_{0.7}\text{Sr}_{0.3}\text{MnO}_3/\text{LaAlO}_3$ films results in lateral periodic modulations of the surface chemical potential and tetragonal distortion, controlling the spatial distribution of preferential nucleation sites and the bandwidth of the epilayer, respectively. These results provide insights into the spontaneous formation of strain-driven ordered surface patterns, topographic and functional, during the growth of complex oxide heterostructures on lengths scales far below the limits achievable through top-down approaches.

1. Introduction

Thin film heteroepitaxy of complex oxides has evolved in recent years to a fascinating platform for the manipulation

Dr. F. Sandiumenge, N. Bagués, Dr. M. Paradinas,
Dr. A. Pomar, Prof. C. Ocal, Dr. Ll. Balcells,
Prof. B. Martínez
ICMAB-CSIC

Campus de la UAB
08193 Bellaterra, Spain
E-mail: felip@icmab.es

N. Bagués, Dr. J. Santiso, Dr. M. Paradinas
CIN2 (CSIC-ICN)
Campus de la UAB
08193 Bellaterra, Spain

Dr. Z. Konstantinovic
Center for Solid State Physics and New Materials
Institute of Physics Belgrade
University of Belgrade
Pregrevica 118, 11080 Belgrade, Serbia

Prof. M.-J. Casanove
CNRS
CEMES
Universite de Toulouse UPS
29 Rue J. Marvig, Toulouse 31055, France



DOI: 10.1002/admi.201600106

of materials properties by altering the subtle energy landscape of competing interactions through epitaxial strain and dissimilarity.^[1,2] Notably, this strategy has led to the discovery of exotic interfacial phenomena,^[3,4] while opening the possibility to tune the bulk transport, magnetic, ferroelectric, and multiferroic properties of thin films.^[5–9] However, next generation nanodevices demand a further step toward miniaturization, facing challenging strategies to controllably manipulate the lateral modulation of atomic length scales. In semiconductor epitaxy, this goal can be achieved through the Stranski–Krastanov growth mode, leading to the formation of self-assembled quantum dots on a wetting layer^[10] driven by lateral gradients in the surface chemical potential.^[11] This strategy, however, typically leads to nanostructures exhibiting broad size distributions and

poor positional order. Strained films, on the other hand, usually relax by misfit dislocations (MDs) above a critical thickness at which their elastic energy exceeds the energy of the interfacial dislocation network.^[12] The overlapping of strain fields emanating from individual dislocations causes lateral modulations of lattice distortions which may extend up to the free surface. Therefore, highly organized MD networks buried at the substrate–film interface not only modulate the physical properties of thin films, but in addition can promote the growth of ordered nanostructures on their surfaces. In this sense, MDs have been used to produce strain guided patterned surfaces in semiconductor^[13,14] and metal^[15,16] systems, and more recently to tune Dirac surface states in topological insulators.^[17] However, to date, the extension of this concept to oxide epitaxy remains elusive.

A unique property of dislocations, that make them highly appealing for creating new functional nanostructures, is their multiscale character. While being essentially linear defects, they store their elastic energy at comparatively large distances (several nanometers) from their sub-nanometer core. As a consequence, they can modify the properties of the host material in two different length scales. On the one hand, dislocation lines can be considered as a separate phase exhibiting its own physical behavior.^[18] A clear manifestation of their singularity, for instance, comes from the observation that oxygen deficient dislocations in SrTiO_3 ^[19–22] exhibit bistable resistive switching,^[23]

or that their nonsuperconducting cores induce pinning of the magnetic flux lines in type-II superconductors.^[24,25] On the other hand, owing to the strong sensitivity of the electronic structure to strain, MD long range strain fields are key for the realization of periodic functional (magnetic, electronic or catalytic)^[26] bulk and surface patterns. Particularly, in manganite thin films, theoretical studies show that the sign of the misfit strain profoundly alters their magnetotransport response.^[6] A compressive/tensile biaxial strain promotes a stronger/weaker Mn 3*d*-O 2*p* orbital overlapping leading to a broader/narrower bandwidth, allowing a local control on the electrical conduction by imposing spatial strain modulations. As MDs typically form square networks, they provide positional order along two mutually perpendicular directions for the creation of self-organized surface templates,^[13–17] in contrast with substrate steps which only induce unidirectional ordering.^[27] Notably, dislocation spacings within the 10–20 nm range are commonly obtained, which is far below the miniaturization limits achievable in oxides by top-down approaches,^[28] and can be manipulated through an appropriate choice of the substrate and the thickness of the film.

Despite the strong potential of MDs in oxide heterostructures to create ordered functional patterns, their associated long range strains remain poorly understood. In particular, previous studies have been mainly focused on ferroelectric films, where MD strains have been shown to induce piezoelectric couplings at different length scales,^[29] alter the chemical composition around dislocation cores,^[30] and cause a local decrease of the spontaneous polarization,^[31] leading to the formation of interfacial dead layers,^[32,33] or to the suppression of ferroelectricity in lattice-mismatched nanoislands.^[34] On the other hand, theoretical analysis shows that threading segments of the MDs induce a smearing of the ferroelectric phase transformation over a range of temperatures.^[35] Exploiting the profound impact of these defects on the material's properties in a deterministic way, however, is challenged by the difficulty to predict the misfit relaxation behavior of the framework structure building these materials, as well as to the requirement of correlating local surface properties with localized buried strain sources.

In this work we address these issues using thin films of the highly spin-polarized room temperature ($T_C \approx 370$ K) half-metal ferromagnet, $\text{La}_{0.7}\text{Sr}_{0.3}\text{MnO}_3$ (LSMO),^[36] as a model system. The interest on strategies to functionalize their surfaces stems from its strong potential in technological applications such as tunneling junctions and spin filters,^[37] high-density data storage media,^[38] nanosensors or catalysts.^[39] It is shown that strain modulated thin films constitute an

ideal scenario to investigate the complex interplay between strain and functionality at a local level, while providing a clue for the realization of spontaneous functional nanostructures in the ≈ 20 nm range.

2. Results and Discussion

2.1. Dislocation Structure and Strain Evolution

Figure 1a shows a cross-section high resolution electron transmission microscopy (HRTEM) image of the 2 nm thick film, exhibiting coherent, dislocation free, interfaces and flat surfaces. The out-of-plane lattice parameter determined by high-resolution X-ray diffraction (HR-XRD) is 3.98(1) Å, which for a fully strained film yields a Poisson's ratio $\nu = \epsilon_{zz}/(\epsilon_{zz} - 2\epsilon_{xx}) = 0.35$, very

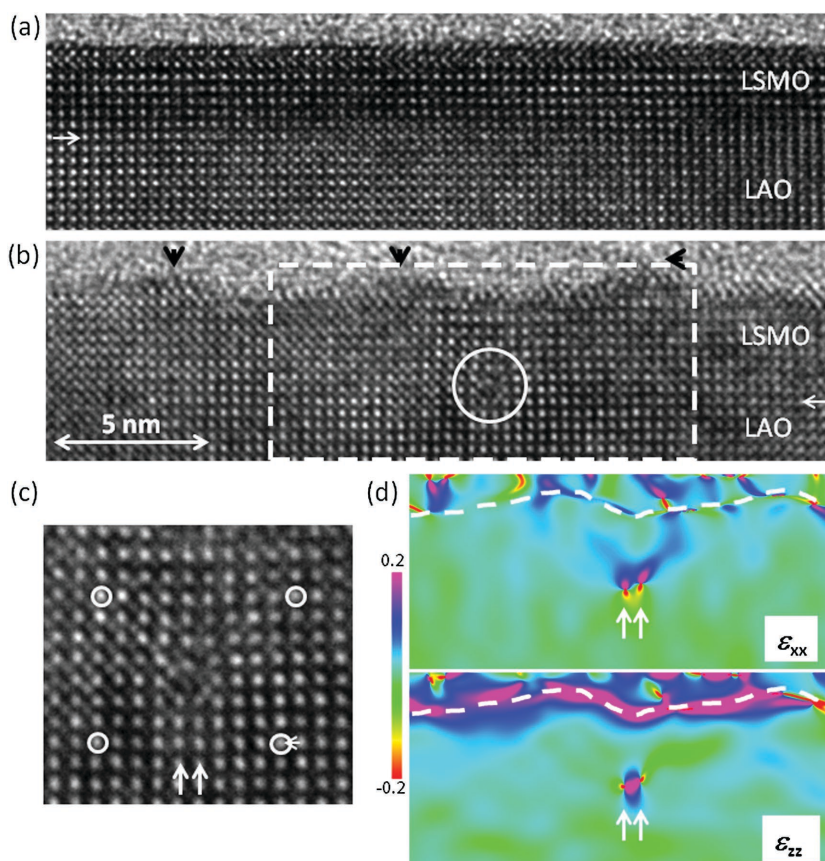


Figure 1. a) Cross-section HRTEM image of a 2 nm thick LSMO/LAO film, exhibiting a coherent, fully strained, interface (indicated by a horizontal arrow), and a flat surface. b) Cross-section HRTEM image corresponding to a 3.5 nm thick film, exhibiting a dislocated interface (an MD is shown inside the white circle) and an undulated surface (outgrowths are indicated by black arrowheads); the boxed area corresponds to the strain maps shown in panel (d). c) Magnified view of the dislocation core encircled in panel (b); white circles mark the corners of a Burgers circuit yielding Burgers vector, $\mathbf{b}_x = a_{\text{LAO}}[100]$; the two vertical arrows indicate two extra half-planes consistent with a split core consisting of two $1/2[100]$ partials; careful inspection of the image reveals a downward bending of atomic rows above the core. d) In-plane (ϵ_{xx}) and out-of-plane (ϵ_{zz}) strain maps, corresponding to the rectangular dashed window shown in panel (b), as determined from GPA analysis; the two vertical arrows indicate the positions of the two partials building the split core; the surface of the film is indicated by a dashed line; the color scale bar corresponds to a full strain range of ± 0.2 (negative and positive being compressive and tensile, respectively).

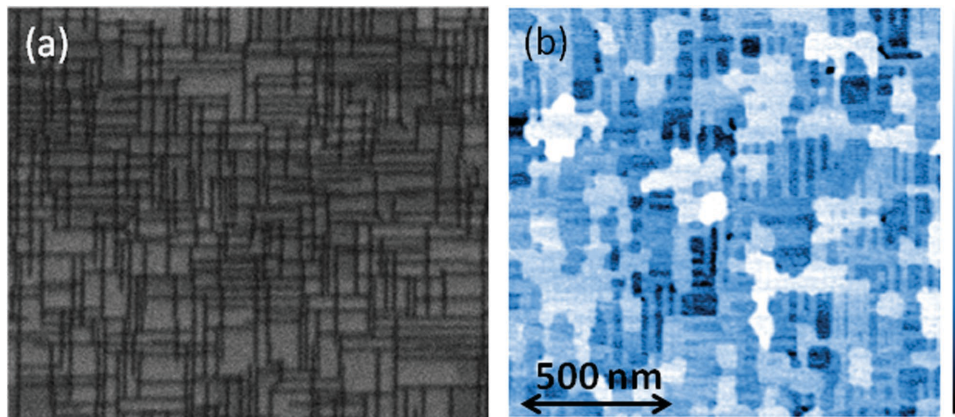


Figure 2. a) AFM image showing the topography of a 3.5 nm thick film, consisting of ridges aligned with the [100] and [010] directions, and terraces; the color scale bar corresponds to a full range of 1.5 nm. b) Orientation contrast SEM images revealing the MD network of the same film. The scale bar is the same for both images. It can be observed that the ridge pattern mimics the underlying buried dislocation network.

close to that derived for tensile strained LSMO/STO films in their elastic regime, $\nu = 0.33$.^[7] As shown in Figure 1b, the 3.5 nm thick film, on the other hand, exhibits an undulated surface and a dislocated interface (see the encircled MD). Careful inspection of this image shows that the surface undulations are due to both, a downward bending of the horizontal atomic rows above the dislocation core (see also Figure 1c), and outgrowths, as indicated by arrowheads, that as a general trend form on the surface at each side of the projected line of the buried MDs, ≈ 4 nm away from them (see Figure 1b). In thicker films, the outgrowths are no longer present, while the bending of atomic planes prevails independently of film thickness, Figure S1 (Supporting Information).

An enlarged view of the core structure of the encircled MD is presented in Figure 1c. The Burgers circuit yields a Burgers vector $\mathbf{b}_x = [100]$, parallel to the interface, as indicated in the figure. The two arrowed vertical atomic rows terminating at the slip plane bear witness of a split core: $[100] \rightarrow 1/2[100] + 1/2[100]$ ($\mathbf{b}_x = \mathbf{b}_1 + \mathbf{b}_2$). It is worthy to mention that similarly dissociated cores have been theoretically predicted for oxygen deficient $\mathbf{b}_x = [100]$ edge dislocations in SrTiO_3 ,^[22] and also identified as a polymorphic form of $\mathbf{b}_x = [100]$ dislocations in MgO .^[40] In fact, analysis of several MD cores indicated that this core splitting is a general trend among the observed MDs. The two adjacent \mathbf{b}_1 and \mathbf{b}_2 partial dislocations build a rather compact core structure. The displacement field above the core is clearly manifested as a downward bending of the atomic rows, with a maximum amplitude of ≈ 1.25 Å at the horizontal locus of the buried dislocation. Figure 1d shows maps of the in-plane, $\epsilon_{xx}(x,z)$, and out-of-plane, $\epsilon_{zz}(x,z)$, strain components around the MD, computed from the experimental image shown in panel (c) using Geometrical Phase Analysis.^[41] The positions of the two partials in the composite core are clearly discerned, along with the compressive (red, yellow) and tensile regions (magenta, blue) extending into the substrate and the film, respectively. It can be observed that the misfit relieving tensile strains, ϵ_{xx} , draw two arms propagating up to the film surface, whilst normal strains, ϵ_{zz} , rapidly vanish as a result of the boundary condition of a free (001) surface, $\sigma_{zz} = \sigma_{zx} = \sigma_{yx} = 0$ (σ_{ij} are components of the stress tensor).

A projection of the MD network on the interface plane obtained by orientation contrast scanning electron microscopy (SEM) is shown Figure 2a. The MD network is formed by irregularly spaced short (≈ 100 nm) dislocation segments along the [100] and [010] directions, with average spacing $\langle S \rangle = 25 \pm 10$ nm (see Figure S1, Supporting Information). These lines correspond to the projection of half-loops onto the interfacial plane, where they leave a MD segment which increases in length as the threading segments move apart. With increasing film thickness to 6 nm, $\langle S \rangle$ reduces to 19 ± 6 nm, while most of dislocations run across the limits of the imaged $1000 \text{ nm} \times 1000 \text{ nm}$ areas (see Figure S1, Supporting Information). The theoretical dislocation spacing for full relaxation, $b_x/\epsilon = 16.5$ nm, is achieved for the 14 nm thick film, with $\langle S \rangle = 16 \pm 3$ nm. According to equilibrium theory, the energy barrier needed for a half-loop of critical radius to survive increases with decreasing misfit strain.^[42] Therefore, as the misfit is relieved by expansion of existing half-loops, the nucleation of new ones becomes kinetically suppressed. As a consequence, the average dislocation length increases whilst their lateral spacing narrows as the films thicken, in excellent agreement with experimental observations (see Figure S1, Supporting Information). Since the glide plane coincides with the interface plane, the MDs can easily rearrange their positions on that plane to minimize their elastic interactions, resulting in increasingly ordered patterns. According to this evolution, the density of threading arms of MDs rapidly decreases as the films thicken, while the strain state of the films becomes determined by the increasingly ordered interfacial MD network.

In order to analyze the morphological transition occurring between 2 and 3.5 nm, Figure 2 compares the MD network shown in panel (a) with a topographic atomic force microscopy (AFM) image of the same film panel (b). In agreement with the cross-section HRTEM image shown in Figure 1b, it is clearly seen that the surface topography consists of a network of ridges and terraces mimicking the underlying dislocation network. Hence, the outgrowths shown in Figure 1b correspond to a section of the ridges observed in the AFM image. To visualize the bulk strain state of the dislocated films, we obtained planar view strain sensitive low-angle annular dark field (LAADF)

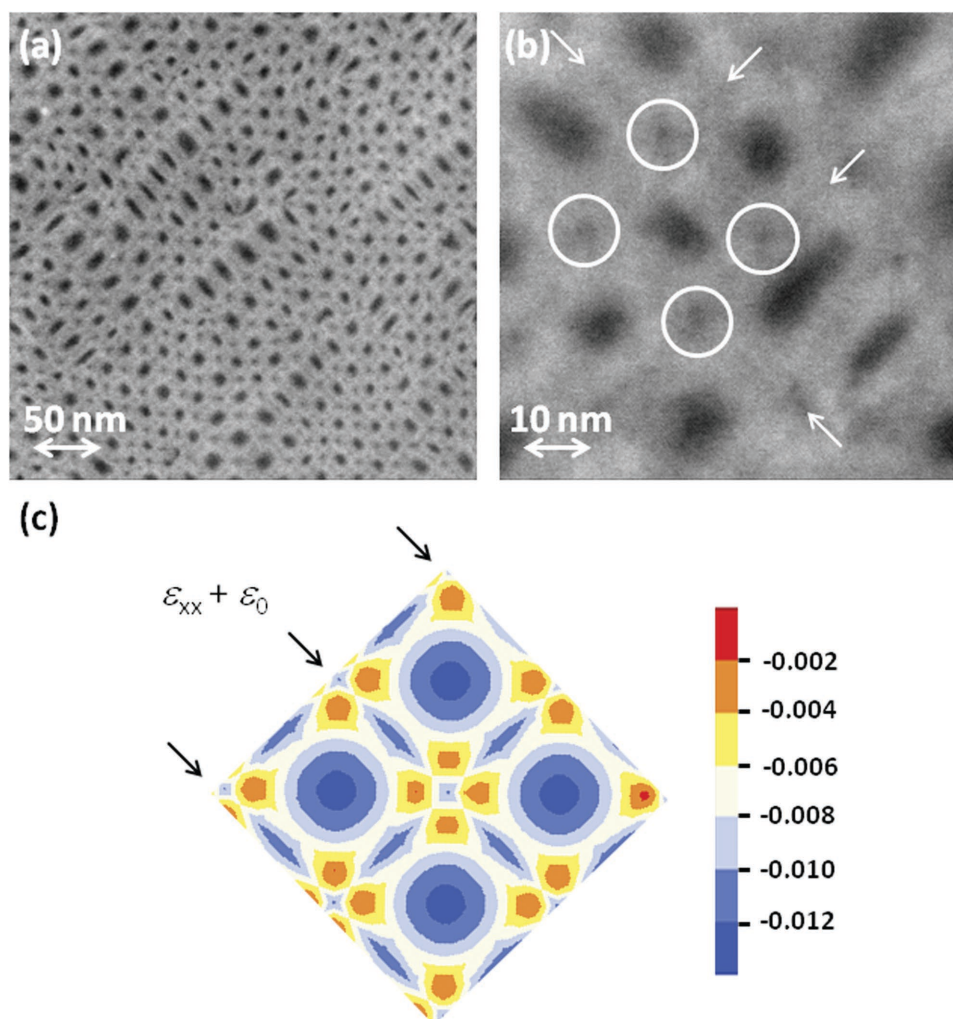


Figure 3. a) Planar view strain sensitive LAADF image corresponding to a 6 nm thick film. b) Enlarged view of panel (a) showing in detail the strain contrast associated with the buried MD network; arrows indicate dislocation lines running along the [100] and [010] directions, and circles mark their intersections. c) Calculated distribution of residual strains $(\epsilon_{xx} + \epsilon_0)(x,y)$ in a similar film; arrows indicate dislocation lines, and colors correspond to different strain levels, as indicated in the color scale bar.

images from the 6 nm thick film (see **Figure 3a,b**) and compared them with the spatial distribution of the residual in-plane strain $\epsilon_{xx}(x,y) + \epsilon_0$, ($\epsilon_0 = -2.3\%$ is the background misfit strain), arising from a square network of $\mathbf{b}_x = [100]$ and $\mathbf{b}_y = [010]$ dislocations, using continuum isotropic elasticity (see **Figure 3c**). We employed the isotropic-average shear modulus of LSMO derived from the Voigt–Reuss–Hill averaging,^[43] using the cubic elastic stiffness coefficients reported by Darling et al.^[44] $G = 50.98$ GPa. Note that the LSMO is softer than the LAO substrate ($G = 133.10$ GPa).^[45] In this situation, the core of the dislocation is predicted to lie in the film very close to the interface,^[46] in agreement with the present observations. The calculated strain map shows good match with the LAADF experimental image, in which darker areas correspond to a lower degree of misfit relaxation between dislocations. Minimum relaxation levels are also attained along the locus of dislocation lines and, to a lower extent, at the crossing points, as also resolved in the experimental image (see **Figure 3b**). This suggests that the observed topography results from

preferential growth at surface sites with a minimum level of residual strain.

Since here we are interested on the effect of strains on surface phenomena, to confirm this hypothesis, here we estimate the strain state of the free film surface using displacement fields derived from the image dislocation approach.^[43] The vertical and horizontal atomic displacements, u_z and u_x , at the free surface of a film with thickness d , induced by an interfacial dislocation with Burgers vector b_x , are given by^[47]

$$u_z(x) = \frac{b_x}{\pi} \left(\frac{d^2}{x^2 + d^2} \right) \quad (1a)$$

$$u_x(x) = \frac{b_x}{\pi} \left[\frac{-dx}{x^2 + d^2} + \tan^{-1} \left(\frac{x}{d} \right) \right] \quad (1b)$$

From Equation (1), the amplitude of the downward atomic displacement at the dislocation coordinate $x = 0$ is $b_x/\pi \approx 1.20$ Å

($b_x = a_{\text{LSMO}} = 3.79 \text{ \AA}$), in excellent agreement with the displacement field determined from Figure 1c. The modulation of the surface strain is then obtained by differentiation of Equation (1b), $\epsilon_{xx}(x) = \partial u_x(x)/\partial x$

$$\epsilon_{xx}(x) = \frac{b_x d}{\pi(x^2 + d^2)} \left(\frac{x^2 - d^2}{x^2 + d^2} + 1 \right) \quad (2)$$

The tensile strain given by Equation (2) is superimposed over the background compressive misfit strain due to the substrate, ϵ_0 , yielding a residual surface strain, $\epsilon_{xx}(x) + \epsilon_0$, as plotted in Figure 4a for the 3.5 and 6 nm thick films, respectively. The figure includes three dislocations, the central one at $x = 0$. For the 3.5 nm thick film, assuming a dislocation spacing of 25 nm, almost total relaxation ($\epsilon_{xx}(x) + \epsilon_0 \approx 0$) occurs at each side of the dislocation line at a distance of about 4 nm. For the 6 nm thick one, assuming a dislocation spacing of 19 nm, the overlapping of strain fields erases the fluctuation between adjacent MDs. In this case complete relaxation is achieved within a region of size similar to the thickness of the film located between adjacent dislocations. However, for those two thicknesses, specially for the thinner film, the dispersion of S values is still high enough

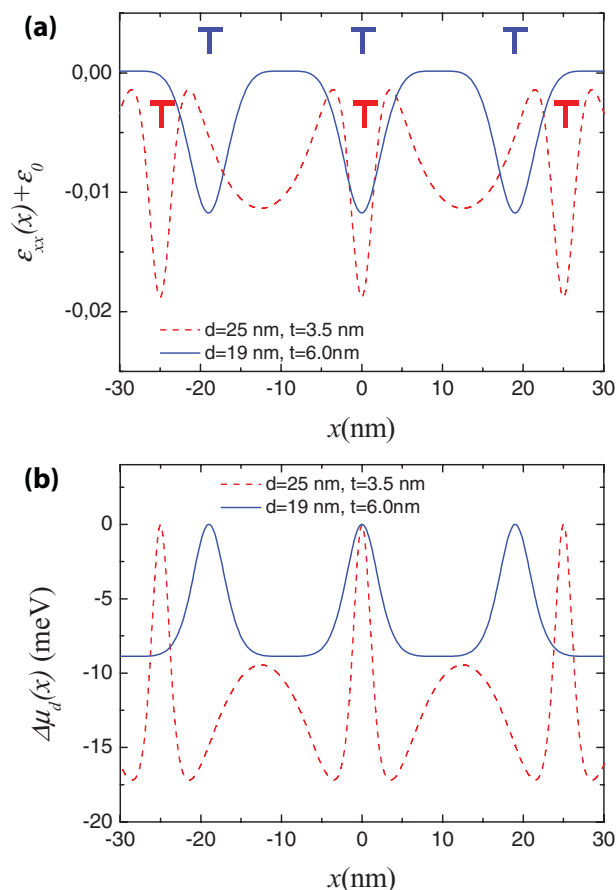


Figure 4. a) Calculated modulation of in-plane strain at the surface of 3.5 and 6 nm thick films, originated from buried MDs; the spacing between MDs is the average spacing determined experimentally for each thickness. b) Corresponding modulation of the surface chemical potential. The location of dislocations for each thickness is indicated in a).

to expect the coexistence of both types of modulation in the same sample.

2.2. Evolution of Film Topography

The link between the morphological evolution of a free surface and its strain state is given by the surface chemical potential $\mu(x) = \mu_0 + \gamma\Omega\kappa(x) + \Omega w(x)$,^[11] where μ_0 is the chemical potential of the unstressed flat surface, γ is the surface free energy per unit area, Ω is the volume of a growth unit, $\kappa(x)$ is the surface curvature, and $w(x)$ is the local surface strain energy density.^[48] Assuming a flat surface, $\kappa \approx 0$, the modulation of the driving force for strain induced surface mass transport due to an underlying *pure edge* MD located at $x = 0$, $\Delta\mu_0(x) = \mu(x) - \mu_0 = \Omega w(x)$, can be expressed as

$$\Delta\mu_0(x) = \Omega M \left(\epsilon_0^2 + \epsilon_0 \epsilon_{xx}(x) + \frac{\epsilon_{xx}^2(x)}{2 + 2\nu} \right) \quad (3)$$

where $M = 2G(1 + \nu)/(1 - \nu)$. According to Equation (3), growth units will migrate from highly strained regions to find stable positions at locations exhibiting minimum $\Delta\mu_0(x)$ values at each side of the dislocation. To illustrate this, Figure 4b depicts the chemical potential reduction relative to the position of the MD, as a function of distance, x : $\Delta\mu_d(x) = \mu(x) - \mu_d$ (μ_d is the surface chemical potential at the position of the MD) for the 3.5 and 6 nm thick films, with $\langle S \rangle = 25$ and 19 nm, respectively. For the 3.5 nm thick film, the fluctuation draws two minima at each side, ≈ 4 nm away from the MDs, where the chemical potential is reduced by 17 meV. This abrupt gradient in $\Delta\mu_d(x)$ should induce the preferential nucleation of LSMO at each side of the MDs, leading to the formation of the observed topographic pattern. It should be noted, however, that since in this case the glide plane is parallel to the interface plane, MDs can easily move to rearrange their positions and, therefore, those surface features do not necessarily appear associated with them. It is to be noted that there exists a kinetic limitation for the vertical growth of the ridges: Once a ridge is formed, the rapid increase in surface curvature at that point causes the competition between the surface energy, $\gamma\kappa(x)$, and strain energy, $w(x)$, terms of the chemical potential, eventually hindering its vertical growth. This scenario drastically changes as the film surface moves further apart from the dislocation strain sources (and those ones get closer), as exemplified by the 6 nm thick film (see Figure 4b). The plot clearly shows that a thickness increase of 2.5 nm results in nearly a 50% decrease in the amplitude of the fluctuation in $\Delta\mu_d(x)$. This effect contributes to homogenize the chemical potential throughout the surface, resulting in flatter films, in agreement with experimental observations (see Figure S1, Supporting Information). Therefore, the formation of terraces in the 3.5 nm thick film, exhibiting a wider dispersion in S values, can be attributed to the overlapping of the strain field in regions with locally enhanced MD densities.

2.3. Strain Effects on Surface Currents

Before considering the local effect of buried MDs on surface currents, we will take into consideration the bulk transport

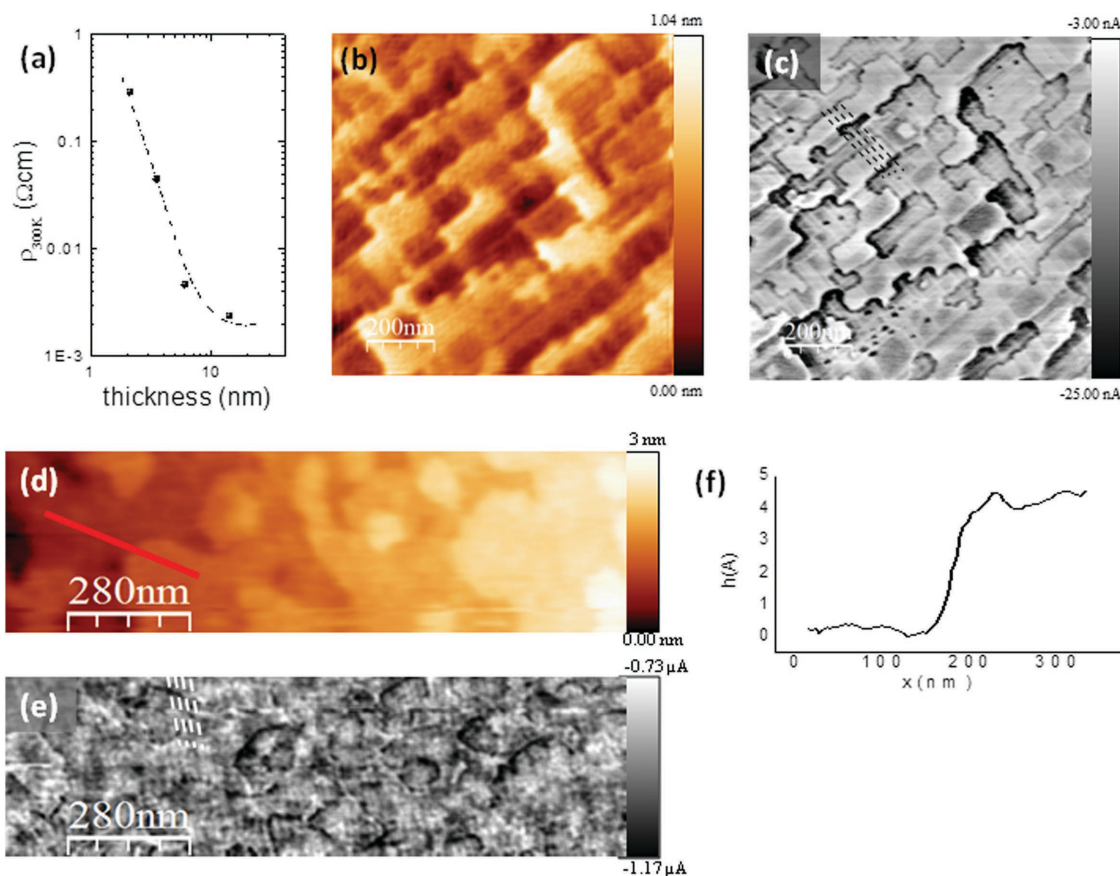


Figure 5. a) Room temperature thickness dependence of the resistivity of the LSMO/LAO films. b, d) Topography and c, e) simultaneous current maps for 3.5 and 6 nm thick films, respectively. f) Line profile along the segment indicated in panel (d), the step height corresponds to one unit cell (≈ 4 Å). Dashed lines, black (c)/white (e), in the current maps serve as a guide to the eye to highlight the dislocation network on the film surface.

behavior of the films. **Figure 5a** depicts standard four-point electrical resistivity measurements as a function of the thickness of the films. As seen in the figure, room temperature resistivity values decrease as the film thickness, thereof the relaxation level as manifested by the variation in the c/a lattice parameter ratio, increases. The temperature dependence of the resistivity of the different films, on the other hand, indicates bulk-like insulating behavior for the 2 nm and 3.5 nm thick films, and metallic behavior for larger thicknesses (6 and 14 nm), see Figure S2 (Supporting Information). As far as the surface electrical properties of the films are concerned, however, current maps indicate local resistivity fluctuations that appear associated with the formation of MDs. Starting with the 3.5 nm thick film, Figure 5b shows an AFM image corresponding to the $I(x, z)$ current map shown in Figure 5c. Despite its bulk insulating behavior, this film exhibits surface metallic behavior. Current enhancements are clearly seen as dark contrasts decorating surface steps, which are attributed to the extended tip-surface contact area along their ledges. Within the terraces, brighter lines of depressed current are also observed along the in-plane $\langle 100 \rangle$ directions. Both, topographic and conduction images are correlated with the underlying MD network. For the 6 nm thick films, the topographic ridge/terrace pattern is no longer present (Figure 5d and Figure S1, Supporting Information) and exhibits unit cell height steps (Figure 5f), the

corresponding current map still exhibits current depressions along lines parallel to the in-plane $\langle 100 \rangle$ directions, as clearly seen in Figure 5e.

The influence of strain on the magnetotransport properties ABO_3 perovskite compounds is intimately correlated to tilt and distortion processes of the MnO_6 octahedral framework. Strain affects magnetotransport properties by acting on different mechanisms at a microscopic level. First strain affects both $\langle Mn-O-Mn \rangle$ bond angle and the $Mn-O$ bond length, thus modifying the strength of the double exchange ferromagnetic (DEF) interactions. For the same reasons strain also affects antiferromagnetic (AF) superexchange interactions. In addition, strain may introduce an orbital bias since in-plane compressive or tensile strains may promote selective $d_{3z^2-r^2}$ or $d_{x^2-y^2}$ orbital occupancy, respectively. Therefore, as a first approximation, an elongation of the $Mn-O$ distances or a decrease of the $\langle Mn-O-Mn \rangle$ bond angle would promote a reduction of the strength of DEF interactions and therefore, a reduction of the ferromagnetic Curie temperature, T_C , and an increase of electrical resistivity. On the contrary, the reduction of $Mn-O$ distances or the straightening of the $\langle Mn-O-Mn \rangle$ bond angle promotes the strengthening of DEF interactions and a reduction of resistivity. The observation of enhanced conductivity at (100)-type twin walls in LSMO/STO thin films, which are submitted to a severe compressive strain, indeed

supports these arguments.^[49] Nevertheless, this scenario may be strongly affected by selective orbital occupancy and AF superexchange interactions. The balance between these competing effects is controlled by the ratio between perpendicular and in-plane lattice parameters c/a , reflecting the degree of tetragonal distortion of the structure.^[50] In such scenario, increasing $c/a > 1.0$ works against the metallic ferromagnetic behavior and would promote an increment of the resistivity. Since according to our analysis above, the behavior of the present films is well described by the continuum isotropic elasticity theory, the influence of rigid octahedral tilting mechanisms can be safely neglected, which otherwise would manifest as noticeable anomalies in the behavior of lattice parameters.^[7] Accordingly, the image contrast in the AFM current maps may be analyzed in terms of local c/a values, directly governed by the residual misfit strain, $(\epsilon_{xx} + \epsilon_0)(x)$ shown in Figure 4a. The lateral modulation of the c/a ratio at the film surface is given by $c/a(x) = (\epsilon_{zz}(x)+1)/[(\epsilon_{xx} + \epsilon_0)(x)+1]$, where ϵ_{xx} is given by Equation (2), and ϵ_{zz} is solely determined by the outward relaxation determined by the Poisson's effect, $\epsilon_{zz} = 2\nu\epsilon_{xx}/(\nu-1)$. In the case of the 6 nm thick film, using the Poisson's ratio derived for the 2 nm thick film, $\nu = 0.35$ (see above), a c/a ratio of ≈ 1.03 can be estimated at the locus of the dislocation ($\epsilon_{xx} \approx -0.013$) while $c/a \approx 1.0$ in a large area between dislocations ($\epsilon_{xx} \approx 0$). As a result, the metallic character is expected to be depressed at the dislocations that would exhibit a higher resistivity. Thus, the pattern observed in current maps is a close mimic of the dislocations pattern. The very same reasoning may be applied to explain the low conducting paths observed on the surface of the 3.5 nm thick film. In this case we find $c/a = 1.05$ ($\epsilon_{xx} \approx -0.020$) above the dislocation lines. Experimental determinations of the c/a ratio from the GPA derived strain maps indeed support the above behavior. **Figure 6a** shows the $c/a(x)$ dependence at two different levels above the dislocation analyzed in Figure 1c,d, corresponding to the 3.5 nm thick film. The blue and red curves are taken close to the film surface and at half way from the buried dislocation core, as indicated in Figure 6b. It can be clearly observed that the c/a ratio locally increases above the dislocation, reaching values closely similar to those derived from linear elasticity. It can be also observed that the average c/a level increases toward the film surface, which can be attributed to an elastic relaxation perpendicular to the film surface.

Identifying the strained regions as less conducting is also in agreement with the insulating behavior observed in the 2 nm thick film, prior to the appearance of dislocations. In those films, $c/a \approx 1.06$ ($\epsilon_{xx} \approx -0.023$), i.e., they are expected to lie well within an antiferromagnetic insulating phase.^[6] Above the onset of plastic relaxation, this analysis yields a view of partly relaxed LSMO/LAO thin films as a conducting compressed matrix, decorated with nanometric paths of higher resistance material aligned with the in-plane $\langle 100 \rangle$ directions coinciding with the positions of the buried MDs, in agreement with experimental $I(x,y)$ maps. As shown above, the topological distribution of strained, high-resistivity regions, throughout the volume of the films varies with the film thickness. Just after the onset of plastic relaxation, the MD density is low, but their associated strains occupy a significant fraction of the film volume owing to its reduced thickness. Thus, in the 3.5 nm thick film, the average bulk insulating behavior can be understood

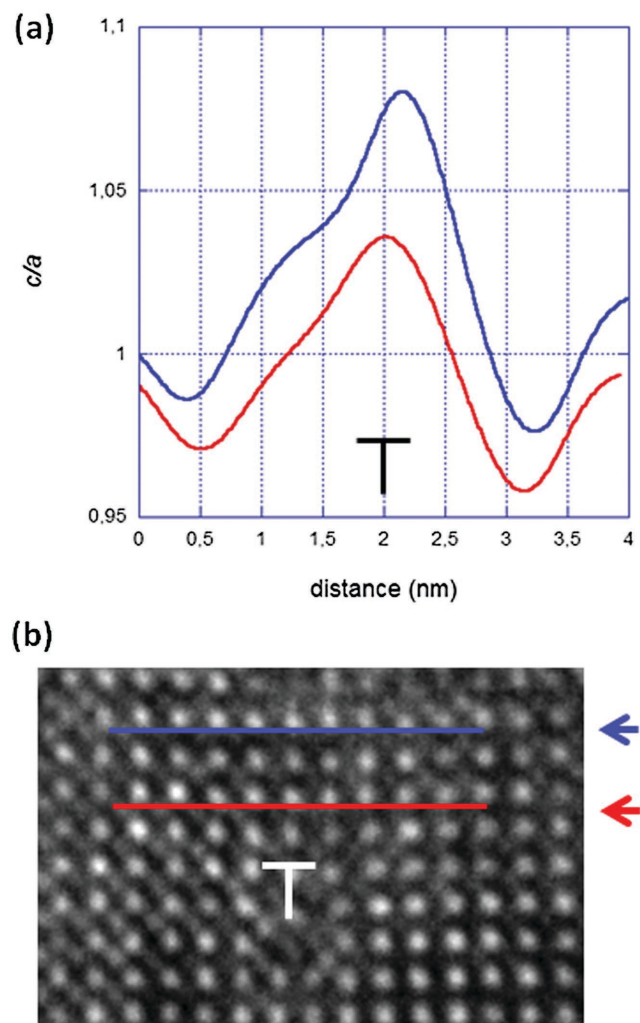


Figure 6. a) Variation of the c/a ratio across the position of a buried MD as determined from the experimental ϵ_{xx} and ϵ_{zz} strain maps shown in Figure 1d. b) Selected area of the HRTEM image shown in Figure 1d, showing the positions of the profiles shown in panel (a); the red and blue lines correspond to the red and blue curves, respectively.

by considering that the connectivity between metallic regions is below the percolating threshold. At larger thicknesses, the increased dislocation density promotes a higher average level of relaxation consistent with the metallic behavior observed in the 6 nm thick film.

3. Conclusion

To conclude, the strain field of MDs in a complex oxide heterostructure introduces a lateral modulation of the chemical potential and the bandwidth-dependent properties at the free surface of the film. In particular, the present experiments shed light on the structural mechanisms underpinning the topographic and electrical conduction patterning of the surface of LSMO/LAO thin films. It is shown that, even if perovskite thin films may relax misfit strains by combining octahedral distortions and octahedral tilting which may eventually elude the formation of

MDs, the strain state of dislocated films is well described by continuum elasticity. This allows straightforward modeling of the strain state of the films and their free surfaces, and the interpretation of their effect on local surface properties like the chemical potential and the bandwidth controlling the transport properties of these materials. These properties exhibit different dependencies on the amplitude of surface strain fluctuations, which in turn depend on film thickness and MD density. Chemical potential fluctuations are rapidly smeared out, limiting the thickness range useful for topographic patterning. On the other hand, surface current patterning is shown to persist up to larger thicknesses. Interestingly, our analysis indicates that current depressions along the projection of dislocation lines on the film surface are well described by the lateral modulation of the c/a axial ratio, controlling the balance between selective Mn d orbital occupation, in-plane Mn $3d$ -O $2p$ orbital overlapping, and AF interactions.^[50] These results demonstrate the feasibility of using MDs in a controlled way to produce spontaneous, highly ordered, surface topographic and conduction patterns on a ≈ 20 nm length scale. Further optimization of each of the surface properties investigated in this work can be achieved through the magnitude of the misfit strain and the strength of the Burgers vector of the MDs.

4. Experimental Section

Films: High-quality films with (100) orientation and thicknesses of 2, 3.5, 6, and 14 nm were epitaxially grown under a biaxial compressive strain of $\epsilon_0 = -2.3\%$ on LAO substrates by magnetron sputtering as reported elsewhere.^[51]

Electrical Resistivity: The in-plane electrical resistivity was measured using the standard four-point geometry with a constant applied current of 5 nA.

Conducting Atomic Force Microscopy: Local electrical conductivity maps were measured by conducting AFM under an N_2 environment, using commercial conductive CrPt-coated Si tips mounted on cantilevers with $k = 40 \text{ Nm}^{-1}$ (BudgetSensors). The lateral resolution of the technique is, in principle, limited by the tip radius of ≈ 10 – 20 nm. In the employed setup, the sample was grounded and the voltage was applied to the tip. An external I - V converter (Stanford Research Systems) was used to provide access to a wide range of compliance currents (1 pA to 1 mA).

High-Resolution X-Ray Diffraction: The lattice parameters of the films were determined from HR-XRD using a four-angle goniometer and primary optics consisting of a parabolic mirror and a $4 \times \text{Ge}(220)$ asymmetric monochromator (X'Pert Pro MRD-Panalytical). The in-plane lattice parameters were determined in the same equipment with a parabolic mirror in the incidence beam optics, fixed grazing angle of 0.5° on the sample, and parallel plate collimator in the diffracted optics.

Transmission Electron Microscopy: Thin foil specimens were prepared by conventional cutting–gluing–grinding procedures, followed by Ar milling at a grazing incidence down to perforation. Cross-section atomic resolution images (HRTEM) were obtained at 200 kV using the field-emission gun FEI Tecnai F20 S/TEM and the Cs-corrected Tecnai F20 electron microscopes. The projected strain distribution on the plane of the film was directly imaged by LAADF microscopy,^[52] using a field emission gun Tecnai F20 S/TEM electron microscope.

Orientation Contrast Scanning Electron Microscopy: Orientation contrast SEM images^[53] were obtained in a QUANTA FEI 200 FEG-ESEM electron microscope in order to determine dislocation densities over large areas.

Supporting Information

Supporting Information is available from the Wiley Online Library or from the author.

Acknowledgements

The authors thank Dr. Belén Ballesteros for her assistance with electron microscopy experiments. This research was sponsored by the Spanish MINECO (“Severo Ochoa” Programme for Centres of Excellence in R&D: SEV- 2015-0496, MAT2015-71664-R, FEDER program, MAT2012-33207, and MAT2013-47869-C4-1-P), and the European Union Horizon 2020 research and innovation program under the Marie Skłodowska–Curie grant agreement No. 645658. The authors also acknowledge financial aid from the Generalitat de Catalunya (2014 SGR 501). N.B. and F.S. also acknowledge funding from the European Union Seventh Framework Programme under Grant Agreement 312483-ESTEEM2 (Integrated Infrastructure Initiative I3) for providing access to aberration corrected electron microscope at CEMES (Toulouse). N.B. thanks the Spanish MINECO for financial support through the FPI program. F.S. acknowledges support from the Labex (Excellence Laboratory) NEXT for a visiting scientist fellowship at CEMES (Toulouse, France). Z.K. is grateful for the support from the Ministry of Education, Science, and Technological Development of the Republic of Serbia through Project III45018.

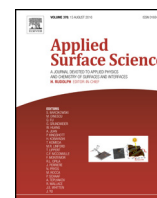
Received: February 5, 2016

Revised: March 17, 2016

Published online:

- [1] H. Y. Hwang, Y. Iwasa, M. Kawasaki, B. Keimer, N. Nagaosa, Y. Tokura, *Nat. Mater.* **2012**, *11*, 103.
- [2] P. Zubko, S. Gariglio, M. Gabay, Ph. Ghosez, J. J.-M. Triscone, *Annu. Rev. Condens. Matter Phys.* **2011**, *2*, 141.
- [3] C. W. Bark, D. A. Felker, Y. Wang, Y. Zhang, H. W. Jang, C. M. Folkman, J. W. Park, S. H. Baek, H. Zhou, D. D. Fong, X. Q. Pan, E. Y. Tsymlal, M. S. Rzchowski, C. B. Eom, *Proc. Natl. Acad. Sci. USA* **2011**, *108*, 4720.
- [4] H. W. Jang, D. A. Felker, C. W. Bark, Y. Wang, M. K. Niranjani, C. T. Nelson, Y. Zhang, D. Su, C. M. Folkman, S. H. Baek, S. Lee, K. Janicka, Y. Zhu, X. Q. Pan, D. D. Fong, E. Y. Tsymlal, M. S. Rzchowski, C. B. Eom, *Science* **2011**, *331*, 886.
- [5] A. J. Millis, T. Darling, A. Miglioni, *J. Appl. Phys.* **1998**, *83*, 1588.
- [6] A. Mukherjee, W. S. Cole, P. Woodward, M. Randeria, N. Trivedi, *Phys. Rev. Lett.* **2013**, *110*, 157201.
- [7] F. Sandiumenge, J. Santiso, Ll. Balcells, Z. Konstantinovic, J. Roqueta, A. Pomar, J. P. Espinós, B. Martínez, *Phys. Rev. Lett.* **2013**, *110*, 107206.
- [8] R. Ramesh, N. A. Spaldin, *Nat. Mater.* **2007**, *6*, 21.
- [9] J. H. Haeni, P. Irvin, W. Chang, R. Uecker, P. Reiche, Y. L. Li, S. Choudhury, W. Tian, M. E. Hawley, B. Craigo, A. K. Tagantsev, X. Q. Pan, S. K. Streiffer, L. Q. Chen, S. W. Kirchoefer, J. Levy, D. G. Schlom, *Nature* **2004**, *430*, 758.
- [10] V. A. Shchukin, D. Bimberg, *Rev. Mod. Phys.* **1999**, *71*, 1125.
- [11] D. J. Srolovitz, *Acta Metall.* **1989**, *37*, 621.
- [12] S. C. Jain, A. H. Harker, R. A. Cowley, *Philos. Mag. A* **1997**, *75*, 1461.
- [13] S. Y. Shiryayev, F. Jensen, J. L. Hansen, J. W. Petersen, A. N. Larsen, *Phys. Rev. Lett.* **1997**, *78*, 503.
- [14] K. Häusler, K. Eberl, F. Noll, A. Trampert, *Phys. Rev. B* **1996**, *54*, 4913.
- [15] Y.-W. Lee, B. M. Clemens, *Phys. Rev. B* **2005**, *71*, 245416.
- [16] H. Brune, M. Giovannini, K. Bromann, K. Kern, *Nature* **1998**, *394*, 451.
- [17] I. Zeljkovic, D. Walkup, B. A. Assaf, K. L. Scipioni, R. Sankar, F. Chou, V. Madhavan, *Nat. Nanotechnol.* **2015**, *10*, 849.
- [18] M. Kuzmina, M. Herbig, D. Ponge, S. Sandlöbes, D. Raabe, *Science* **2015**, *349*, 1080.
- [19] D. Marrocchelli, L. Sun, B. Yildiz, *J. Am. Chem. Soc.* **2015**, *137*, 4735.

- [20] C. L. Jia, A. Thust, K. Urban, *Phys. Rev. Lett.* **2005**, *95*, 225506.
- [21] M. Kim, G. Duscher, N. D. Browning, K. Sohlberg, S. T. Pantelides, S. J. Pennycook, *Phys. Rev. Lett.* **2001**, *86*, 4056.
- [22] V. Metlenko, A. H. H. Ramadan, F. Gunkel, H. Du, H. Schraknepper, S. Hoffmann-Eifert, R. Dittmann, R. Waser, Roger A. De Souza, *Nanoscale* **2014**, *6*, 12864.
- [23] K. Szot, W. Speier, G. Bihlmayer, R. Wasser, *Nat. Mater.* **2006**, *5*, 312.
- [24] B. Dam, J. M. Huijbregtse, F. C. Klaassen, R. C. F. van der Geest, G. Doornbos, J. H. Rector, A. M. Testa, S. Freisem, J. C. Martinez, B. Stäuble-Pümpin, R. Griessen, *Nature* **1999**, *399*, 439.
- [25] F. Sandiumenge, T. Puig, J. Rabier, J. Plain, X. Obradors, *Adv. Mater.* **2000**, *12*, 375.
- [26] J. Suntivich, K. J. May, H. A. Gasteiger, J. B. Goodenough, Y. A. Shao-Horn, *Science* **2011**, *334*, 1383.
- [27] a) Z. Konstantinović, J. Santiso, Ll. Balcells, B. Martínez, *Small* **2009**, *5*, 265; b) Z. Konstantinovic, F. Sandiumenge, J. Santiso, Ll. Balcells, B. Martinez, *Nanoscale* **2013**, *5*, 1001.
- [28] D. Ruzmetov, Y. Seo, L. J. Belenky, D.-M. Kim, X. Ke, H. Sun, V. Chandrasekhar, C.-B. Eom, M. S. Rzechowski, X. Pan, *Adv. Mater.* **2005**, *17*, 2869.
- [29] A. Lubk, M. D. Rossell, J. Seidel, Y. H. Chu, R. Ramesh, M. J. Hytch, E. Snoeck, *Nano Lett.* **2013**, *13*, 1410.
- [30] M. Arredondo, Q. M. Ramasse, M. Weyland, R. Mahjoub, I. Vrejoiu, D. Hesse, N. D. Browning, M. Alexe, P. Munroe, V. Nagarajan, *Adv. Mater.* **2010**, *22*, 2430.
- [31] C. L. Jia, S. B. Mi, K. Urban, I. Vrejoiu, M. Alexe, D. Hesse, *Phys. Rev. Lett.* **2009**, *102*, 117601.
- [32] V. Nagarajan, C. L. Jia, H. Kohlstedt, R. Waser, I. B. Misirlioglu, S. P. Alpay, R. Ramesh, *Appl. Phys. Lett.* **2005**, *86*, 192910.
- [33] S. P. Alpay, I. B. Misirlioglu, V. Nagarajan, R. Ramesh, *Appl. Phys. Lett.* **2004**, *85*, 2044.
- [34] M.-W. Chu, I. Szafraniak, R. Scholz, C. Harnagea, D. Hesse, M. Alexe, U. Gösele, *Nat. Mater.* **2004**, *3*, 87.
- [35] I. B. Misirlioglu, S. P. Alpay, M. Aindow, V. Nagarajan, *Appl. Phys. Lett.* **2006**, *88*, 102906.
- [36] A. Urushibara, Y. Morimoto, T. Arima, A. Asamitsu, G. Kido, Y. Tokura, *Phys. Rev. B* **1995**, *51*, 14103.
- [37] A. Bernand-Mantel, P. Seneor, K. Bouzouhane, S. Fusil, C. Deranlot, F. Petroff, A. Fert, *Nat. Phys.* **2009**, *5*, 920.
- [38] B. D. Terris, T. Thomson, *J. Phys. D: Appl. Phys.* **2005**, *38*, R199.
- [39] M.-C. Daniel, D. Astruc, *Chem. Rev.* **2003**, *104*, 293.
- [40] Z. Wang, M. Saito, K. P. McKenna, Y. Ikuhara, *Nat. Commun.* **2014**, *5*, 3239.
- [41] M. J. Hytch, *Microsc., Microanal., Microstruct.* **1997**, *8*, 41.
- [42] R. Hull, J. C. Bean, *Crit. Rev. Solid State Mater. Sci.* **1992**, *17*, 507.
- [43] J. P. Hirth, J. Lothe, *Theory of Dislocations*, McGraw-Hill, New York, USA.
- [44] T. W. Darling, A. Migliori, E. G. Moshopoulou, S. A. Trugman, J. J. Neumeier, J. L. Sarrao, A. R. Bishop, D. J. Thompson, *Phys. Rev. B* **1998**, *57*, 5093.
- [45] X. Luo, B. Wang, *J. Appl. Phys.* **2008**, *104*, 073518.
- [46] X. Wu, G. C. Weatherly, *Semicond. Sci. Technol.* **2003**, *18*, 307.
- [47] G. Springholz, *Appl. Surf. Sci.* **1997**, *112*, 12.
- [48] G. Springholz, G. Bauer, V. Holy, *Phys. Rev. B* **1996**, *54*, 4500.
- [49] Ll. Balcells, M. Paradinas, N. Bagués, N. Domingo, R. Moreno, R. Galceran, M. Walls, J. Santiso, Z. Konstantinovic, A. Pomar, M.-J. Casanove, C. Ocal, B. Martínez, F. Sandiumenge, *Phys. Rev. B* **2015**, *92*, 075111.
- [50] Z. Fang, I. V. Solovyev, K. Terakura, *Phys. Rev. Lett.* **2000**, *84*, 3169.
- [51] Z. Konstantinovic, J. Santiso, D. Colson, A. Forget, Ll. Balcells, B. Martínez, *J. Appl. Phys.* **2009**, *105*, 063919.
- [52] L. Fitting, S. Thiel, A. Schmehl, J. Mannhart, D. A. Muller, *Ultra-microscopy* **2006**, *106*, 1053.
- [53] D. J. Prior, A. P. Boyle, F. Brenker, M. C. Cheadle, A. Day, G. Lopez, L. Peruzzo, G. J. Potts, S. Reddy, R. Spiess, N. E. Timms, P. Trimby, J. Wheeler, L. Zetterström, *Am. Mineral.* **1999**, *84*, 1741.



Morphology and magnetic properties of the ethylene-co-vinyl acetate/iron nanocomposite films prepared by implantation with Fe⁶⁺ ions



Dušan K. Božanić^{a,1}, Ilija Draganić^{b,2}, Nataša Bibić^a, Adriaan S. Luyt^b, Zorica Konstantinović^{c,d}, Vladimir Djoković^{a,*}

^a Vinča Institute of Nuclear Sciences, University of Belgrade, P.O. Box 522, 11001 Belgrade, Serbia

^b Center for Advanced Materials, Qatar University, P.O. Box 2713, Doha, Qatar

^c Instituto de Ciencia de Materiales de Barcelona—CSIC, Campus UAB, Bellaterra, 08193, Spain

^d Center for Solid State Physics and New Materials, Institute of Physics, University of Belgrade, Pregrevica 118, 11080 Belgrade, Serbia

ARTICLE INFO

Article history:

Received 18 January 2016

Received in revised form 8 March 2016

Accepted 4 April 2016

Available online 6 April 2016

Keywords:

Ion implantation

Nanocomposite

Iron

Multiple charged ions

Magnetic properties

Ion beam mixing

ABSTRACT

Ethylene-co-vinyl acetate/iron nanocomposite films were fabricated by implantation with multiple charged ions at different fluencies. The films obtained with ion fluency of $1 \times 10^{17} \text{ cm}^{-2}$ were used for specific studies. It was found that spherical $\sim 1.5 \text{ nm}$ diameter nanoparticles were formed upon implantation. They were clustered into a single 80 nm wide strip about 40 nm beneath the film surface. The magnetic measurements of the film showed that the particles exhibit superparamagnetic behavior with a blocking temperature below 5 K . A second type of the samples was also prepared with ion fluency of $1 \times 10^{17} \text{ cm}^{-2}$, but prior to implantation, the iron was evaporated onto the co-polymer surface. A nanocomposite film of different morphology was obtained upon the implantation and the particles were much smaller ($\sim 0.8 \text{ nm}$). The magnetic behavior of both the films was that of isolated nanoparticles, despite the high ion fluency of $1 \times 10^{17} \text{ cm}^{-2}$.

© 2016 Elsevier B.V. All rights reserved.

1. Introduction

Ion implantation is a well-established technique for modification of the surface regions of a material. It is used in different areas, particularly in the production of microelectronics through a non-thermal selective doping of semiconductor substrates. Recently, ion implantation proved to be a good method for fabrication of nanostructured materials such as metal-polymer nanocomposites [1–3]. A strong demand for new functional materials in nanoscience and nanotechnology reflected also in the field of polymer nanocomposites, where a huge number of physical and chemical synthetic methods were developed. The advantage of the ion implantation is that it provides a controllable synthesis of metallic nanoparticles at various depths under the surface [1–3]. At the same time, it allows

reaching of a high metal filling factor in a polymer substrate that sometimes goes beyond the equilibrium limit of metal solubility. Typical ion beam energies in the fabrication of the nanocomposites are $100\text{--}150 \text{ eV}$, while the irradiation doses go up to $10^{17} \text{ ions/cm}^2$. So far, the metal-polymer nanocomposites with plasmonic nanoparticles (Ag [3–7], Au [5,8,9], Cu [5,10], Pt [8]) as well as with magnetic nanoparticles (Fe [1,7,11–13], Co [1,14,15]) are the most studied hybrid systems. Polymers implanted with some other metallic ions such as W [16], Ti [16], Sn [17] and Mn [18] are also mentioned in the literature. In the present paper, we investigate the morphology and magnetic properties of the nanocomposites prepared by implantation of ethylene (vinyl acetate) (EVA) copolymer films with Fe⁶⁺ ions.

Magnetic polymer nanocomposites are typically prepared by using single charge metallic ions during the implantation. Here, we wanted to establish whether using Fe⁶⁺ ions can induce changes in the morphology of the obtained nanocomposites. By using an electron cyclotron resonance ion source and the metal-ions-from-volatile-compounds (MIVOC) method, we were able to produce different types of iron ions with charges ranging from Fe³⁺ to Fe¹²⁺ [19]. Since the morphology and size of the particles strongly depend on the viscosity of the substrate [7], it was decided to use EVA

* Corresponding author.

E-mail addresses: djokovic@vinca.rs, vladimirdjokovic@hotmail.com

(V. Djoković).

¹ Present address: Synchrotron SOLEIL, L'Orme des Merisiers, St. Aubin BP 48, 91192 Gif sur Yvette, France.

² Present address: Los Alamos National Laboratory, Los Alamos, NM 87544, United States.

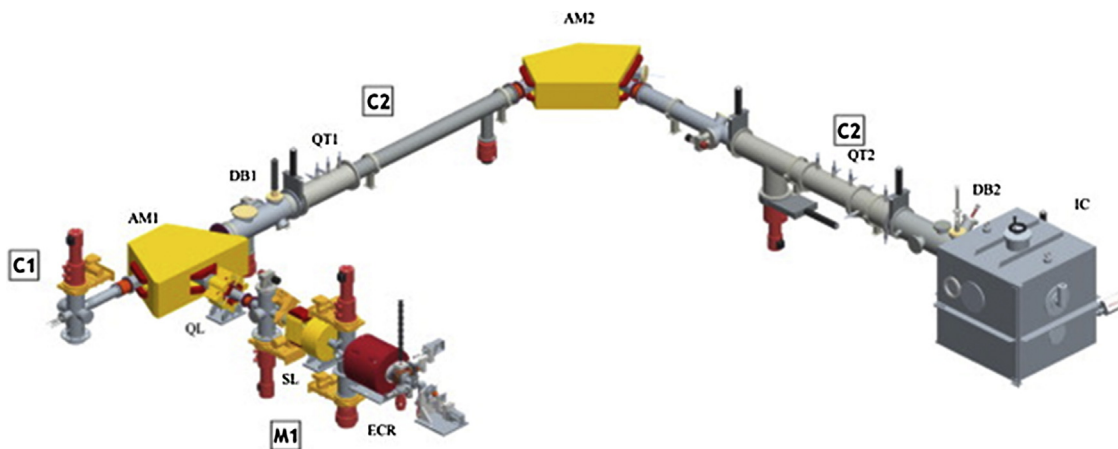


Fig. 1. The scheme of the experimental setup for ion implantation.

copolymer films as targets. This is an inherently flexible, tough, and transparent material, slightly softer than pure polyethylene. Finally, the nanocomposites were also prepared by an ion beam mixing approach [20]. EVA films with surface evaporated iron layers were irradiated by Fe^{6+} ions. As it will be seen, the size of the iron nanoparticles formed and their distribution within the surface layer of the polymer films strongly depend on the fabrication method employed.

2. Experimental

2.1. Preparation of copolymer substrates

Ethylene(vinyl acetate) copolymer was supplied by Plastamid, South Africa. It contained 9% vinyl acetate (VA) co-monomers and has a density of $\rho = 0.93 \text{ g cm}^{-3}$. The $200 \mu\text{m}$ thick isotropic EVA sheets were prepared by compression moulding. The EVA pellets were kept at 120°C for 10 min. After that, 1.75 MPa pressure was applied for another 5 min and the sheets were then quenched in water at 0°C .

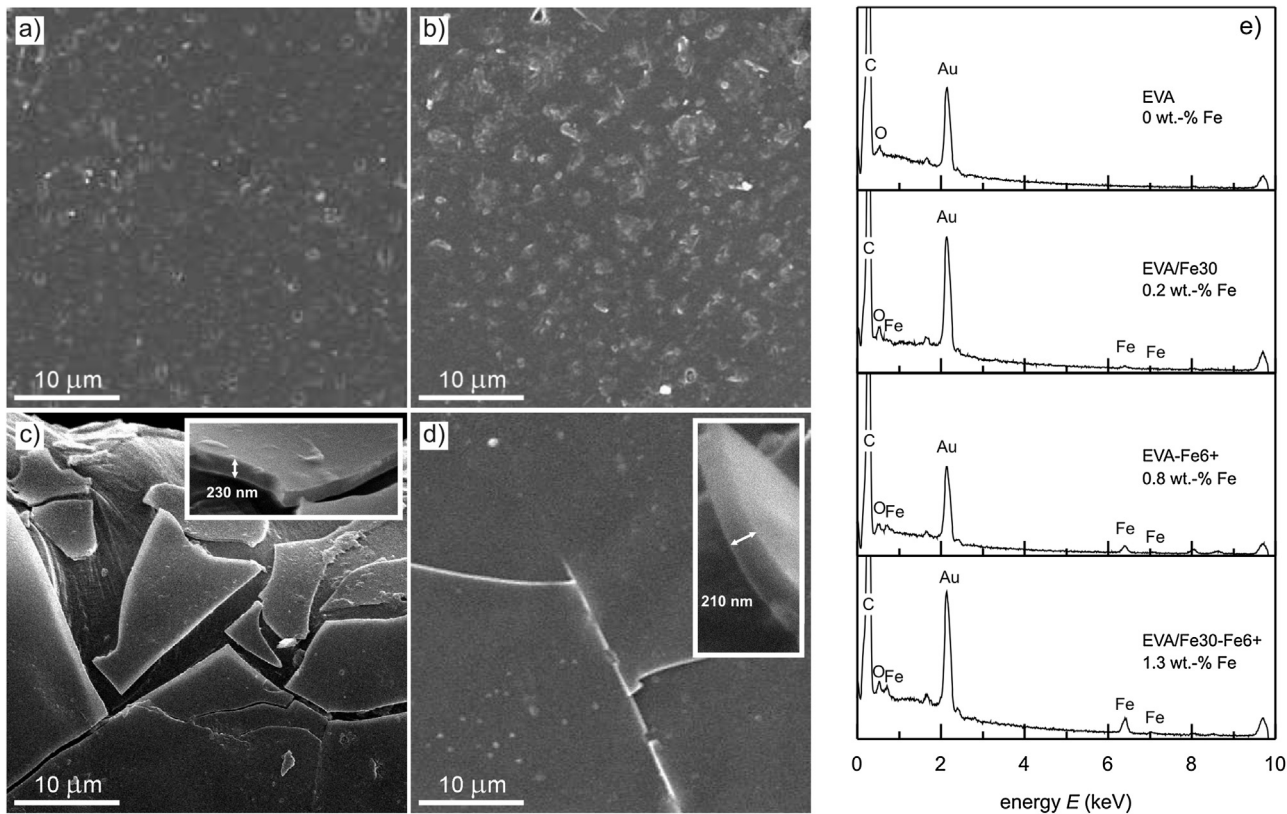


Fig. 2. SEM images of the a) EVA b) Fe30-EVA, c) Fe6+/EVA, d) Fe6+/Fe30-EVA films and their corresponding e) EDX spectra. The insets of figures c) and d) show the images of the surface layers at tilted angles (the surfaces of the films were deliberately damaged in order to determine the thickness of the layers formed by implantation with $1 \times 10^{17} \text{ cm}^{-2}$ of Fe^{6+}).

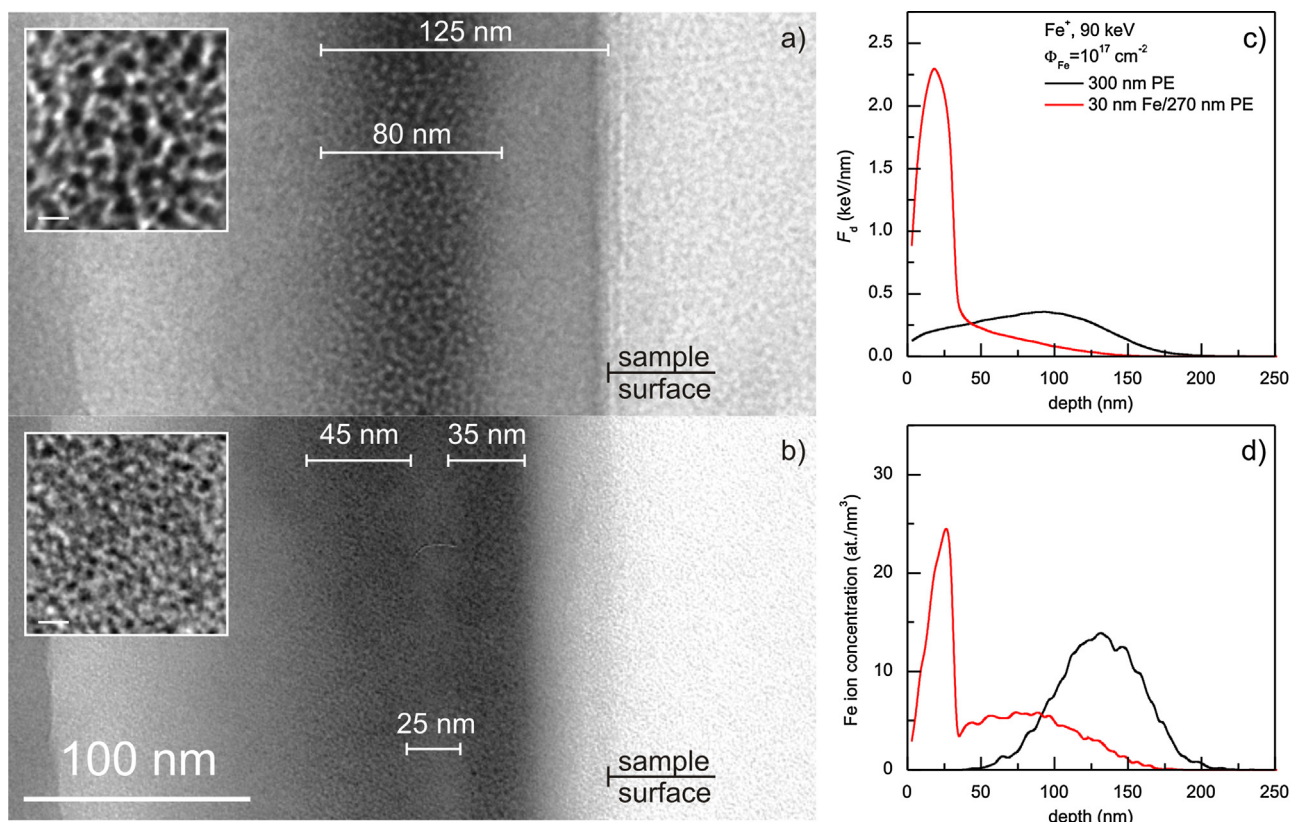


Fig. 3. TEM images of the cross sections of the a) Fe⁶⁺/EVA and b) Fe⁶⁺/Fe30-EVA films. The inset images show the particles at higher resolution (bar 5 nm). c) Beam-energy density and d) the implanted ions depth profiles for the LDPE film and LDPE film with 30 nm Fe layer estimated by the SRIM code [22]. Conditions: single charged Fe ions with fluency of 1×10^{17} cm⁻² and energy of 90 keV were used in calculations. The kinetic energy (90 keV) and fluency was the same as that of the Fe⁶⁺ ions used in the experiment. Taking into account that the concentration of the vinyl co-monomer was low (9%), LDPE was used instead of EVA because it has a similar structure and density.

The other type of substrate for implantation was obtained by evaporation of iron onto EVA sheets prepared by the method described above. A 30 nm thick polycrystalline Fe layer on EVA film was prepared by electron beam evaporation of iron of natural isotope composition. The pressure in the chamber during deposition was maintained at 1×10^{-6} mbar. The emission current was 50 mA. The deposition rate was maintained at 0.5 nm s⁻¹ and the substrates were kept at room temperature during the deposition. The substrate films with the evaporated iron were further in the text labelled as Fe30-EVA.

2.2. Implantation of Fe⁶⁺ ions into copolymer films

The implantation was carried out on the C2 channel of the facility for modification and analysis of materials with ion beams (FAMA), at the Vinča Institute [21]. The scheme of the experimental setup for the implantation is shown in Fig. 1. EVA and the Fe30-EVA films, 1 cm in width and 2 cm in length, were placed in the interaction chamber of the C2 channel. The iron ions produced by an electron cyclotron resonance ion source (M1 machine of FAMA, Fig. 1), were directed onto the EVA substrate. In the ion source, the ions are usually obtained by using a mini-oven technique, which is adequate for solid materials with low melting points (the maximum oven temperature is 900 °C). Due to the much higher melting temperature of the iron, the metal-ions-from-volatile-compounds (MIVOC) method was applied to produce the ions [19]. The multiple charged iron ion beam spectrum was extracted from the ferrocene powder Fe(C₅H₅)₂ [19], while the Fe⁶⁺ ions were selected to interact with the substrate. The irradiation doses chosen were 1×10^{15} , 5×10^{15} , 1×10^{16} , 1×10^{17} ions/cm². The beam energy and the maximum current were 90 keV and 64 μA respectively. Eight sam-

ples were irradiated simultaneously and the iron ion beam was scanned over a 20 cm² surface area (the image of the sample holder is given in the Supporting Information, Fig. S1). The maximum ion beam current that reached the samples was therefore 3.2 μA cm⁻². We used a Faraday's cup to measure the exact irradiation dose. In the case of the dose of 1×10^{17} ions/cm² the irradiation lasted for 10 h and the average ion current was 2.6 μA cm⁻². The samples implanted with Fe⁶⁺ ions are referred to in the text as Fe⁶⁺/EVA and Fe⁶⁺/Fe30-EVA.

3. Methods

TEM analysis was carried out on a Philips CM10 transmission electron microscope at an operating voltage of 100 kV. In order to obtain electron beam transparent samples, the Fe⁶⁺ ion irradiated EVA films were embedded in a resin and microtomed by using a Reichert-Jung Ultracut.

The surface morphologies of the EVA and EVA/Fe films before and after implantation of the Fe⁶⁺ ions were investigated by scanning electron microscopy (JEOL JSM 6460LV instrument). Prior to SEM investigations, the samples were coated with a thin gold layer. In order to check the composition of the samples, EDX measurements were performed by using an X-ray microanalysis unit (Oxford Instruments) attached to the SEM. The results obtained from TEM and SEM analyses were correlated with Monte Carlo scattering simulation data calculated by SRIM software [22].

Magnetization measurements were performed using a SQUID magnetometer (Quantum Design MPMS system). Zero-field-cooled (ZFC) and field-cooled (FC) curves were recorded. In the zero-field-cooled (ZFC) measurements, the sample is initially at a high temperature. After the sample is cooled down to the lowest mea-

suring temperature, a small magnetic field (300 Oe) is applied and the magnetization is measured as the temperature increases. The field-cooled (FC) experiment is similar, but the magnetic field is applied at a high temperature and the sample is cooled down under the applied magnetic field.

Hysteresis loops $M(H)$ were recorded at 5 K up to a maximum field of 10 kOe.

4. Results and discussion

EVA films and EVA films with 30 nm Fe surface layer (Fe30-EVA) were irradiated with 1×10^{15} , 5×10^{15} , 1×10^{16} , 1×10^{17} cm⁻² doses of Fe⁶⁺ ions. The implantation induces a series of complex physical and chemical processes that originate from the interaction of the ions with the polymer target [2]. The energy transfer from ions to the polymer takes place by two main mechanisms: nuclear collisions and electron excitations. At low implantation energies, the nuclear stopping dominates the interactions of iron ions with the target. In the case of highly charged ions, the transfer of energy through electronic excitations may also be taken into account [2], although these effects are less important if the metallic layer is present [23]. The mentioned processes may produce scission and/or crosslinking of the matrix chains, which consequently result in changes in the surface properties of the films. In a recent conference paper [24], we communicated that the irradiation with Fe⁶⁺ ions induced changes in the optical transparency and surface resistivity of the pure EVA films. The later properties obtained with Fe30-EVA films were similar to that of the pure EVA, and we are not going pursued this topic in the present study. It was found that the optical transparency and surface resistivity of the films decreased with increasing irradiation doses and the results are given in the Supporting information (Fig. S2 and Table S1). Due to the specific interaction of highly charged iron ions with the substrates, the EVA and Fe30-EVA films irradiated with the highest irradiation dose (1×10^{17} cm⁻²) were the only nanocomposite samples in which iron nanoparticles were large enough to produce detectable magnetic response. For this reason, the discussions below will be focussed on the morphology and the magnetic properties of these particular samples.

4.1. Morphology

Fig. 2 shows SEM images of the EVA and Fe30-EVA films as well as their counterparts irradiated with 1×10^{17} cm⁻² of Fe⁶⁺. It can be seen that the typical surface morphology of the EVA film (Fig. 2a) does not change significantly after evaporation of the 30 nm Fe layer (Fig. 2b). On the other hand, the irradiation clearly changed the surface of the films. We induced mechanical damage of the surface layers formed by irradiation in order to measure their thicknesses. The presence of the evaporated iron obviously affects the mean path of the ions within the sample. The average thickness of the surface layer in the Fe6+/EVA sample (Fig. 2c) is about 230 nm, while the average thickness of the layer in the Fe6+/Fe30-EVA sample (Fig. 2d) is about 210 nm. The EDX spectra in Fig. 1e show the main composition of the samples. The EDX spectrum of the pure EVA shows peaks of carbon and oxygen, while the spectra of the other samples exhibit also the characteristic peaks of iron. The iron content in Fe30-EVA, Fe6+/EVA and Fe6+/Fe30-EVA samples were found to be 0.2, 0.8 and 1.3 wt.%, respectively.

The TEM images of the cross-sections of the Fe6+/EVA and Fe6+/Fe30-EVA films are shown in Fig. 3a,b. Both images show the presence of a large number of spherical particles. The images with a higher resolution, presented in the insets of Fig. 3a,b, show that the particles formed by irradiation of the pure copolymer are much larger. The average diameters of the particles in the Fe6+/EVA and

Fe6+/Fe30-EVA samples are about 1.5 nm and 0.8 nm, respectively. Besides the size of the nanoparticles, the morphologies of the surface implanted layers are also different. In the Fe6+/EVA sample (Fig. 3a), the particles are grouped into a single 80 nm wide strip positioned approximately 40 nm from the surface of the films. In contrast, the image of the Fe6+/Fe30-EVA sample shows particles grouped into two strips, 45 and 35 nm in width (Fig. 3b). The space between these two main strips is not completely empty; it contains nanoparticles, but their density is much lower. The additional TEM image showing the morphology of the Fe6+/Fe30-EVA sample is given in the Supporting information (Fig. S3). As can be seen, the presence of the evaporated iron layer leads to the appearance of a distinct morphology upon irradiation, both in terms of the particle sizes and their clustering. In order to check whether this is indeed the case, we performed a series of calculations using the SRIM software [22]. In the calculation procedure, single charged Fe-ions with energy of 90 kV were assumed to interact with the pure low density polyethylene (LDPE). The LDPE was chosen because it has a similar structure as EVA and the concentration of the vinyl acetate co-monomer was relatively low (9%). The substrate with evaporated iron was also assumed to be a polymer film with a 30 nm Fe layer on top of it. The estimated energy density deposited by the ion beam (F_d) and ion concentration profiles as a function of depth are shown in Fig. 3c,d. Although single charged Fe-ions were used in the calculations, the estimated data closely resemble the results obtained by TEM and SEM analyses of the films fabricated with multiple charged ions (Figs. 2 and 3). In the case of the substrate with a 30 nm Fe layer, the estimated beam-energy density profile shows that nearly all the deposited energy is transferred to the metallic layer during irradiation (Fig. 3c). The maximum deposited energy density F_d is about 2.3 keV/nm. In contrast, the beam-energy density profile calculated for the pure polymer substrate shows that the energy is more uniformly transferred through the film to a depth of about 175 nm, with a maximum of 0.7 keV/nm at ~100 nm. The difference in the absorbed energy of the substrates reflects also in the difference of the corresponding ion concentration profiles (Fig. 3d). In the substrate with an iron layer, most of the implanted Fe⁶⁺ ions stop inside the metallic layer (Fig. 3d). The implanted Fe exhibits a sharp concentration maximum of 24 at.% at a depth of around 25 nm, and a much broader peak positioned at 90 nm. On the other hand, the ion concentration profile within the pure polymer shows a single peak with a maximum at 14 at.% positioned at a depth of about 130 nm (Fig. 3c). The half-width of the peak is close to 80 nm and the maximum incident depth is about 210 nm. The fact that the depth at which formation of the iron nanoparticles takes place (Fig. 3a,b) coincides with the depth profiles calculated by using single charge Fe ions (Fig. 3c,d), suggests that the kinetic energy of the ions (90 kV in both cases) rather than their charges determines the morphology of the nanocomposite films upon implantation. On the other hand, it seems that the charge of the ions may be responsible for the small size of the obtained particles. The average particle sizes obtained by Fe⁶⁺ implantation (1.5 nm for Fe6+/EVA and 0.8 nm for Fe6+/Fe30-EVA) are lower than that obtained by implantation of a PET polymer with single charge Fe ions at similar fluencies [13]. The other possibility is that the increase in temperature of the films upon implantation was responsible for the smaller diameter of the particles, since it was shown that a change in the viscosity of the substrate could affect the size of the particles [7]. The average Fe⁶⁺ ion current in our experiments was 2.6 $\mu\text{A cm}^{-2}$ and an increase in temperature e.g. softening of the EVA substrate could be an important factor that induced the decrease in the particles sizes. However, the softening (or temperature) may not be the only factor that determines the size of the particles. In the above mentioned study [7], Khaibullin et al. used viscous and solid state silicons as substrates and irradiated them at room temperature with singly charged Fe ions up to doses of 10^{17} cm⁻² (ion current

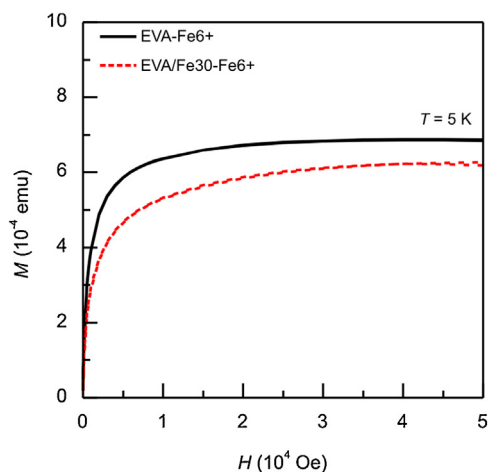


Fig. 4. Field dependence of magnetization of a) Fe6+/EVA and b) Fe6+/Fe30-EVA nanocomposite films at 5 K.

was $4 \mu\text{A cm}^{-2}$). In the uncured (viscous) silicon, they obtained iron particles several tens of nanometers in diameter, while in the cured silicon the particles were much larger. The viscosity of the uncured silicon is much lower than that of an EVA co-polymer (even if EVA is at an elevated temperature) and that is why we assume that, besides temperature, the charge of the ions might have been the reason for the significantly smaller sizes of the particles obtained in the present study. As will be seen, the Fe6+/EVA and Fe6+/Fe30-EVA films exhibit magnetic behaviour which is typical for nanocomposites with well-isolated nanoparticles.

4.2. Magnetic properties

The magnetization curves of the Fe6+/EVA and Fe6+/Fe30-EVA samples as a function of applied field are shown in Fig. 4. It can be seen that the saturation magnetization (at 5 kOe) of the Fe6+/EVA film is larger than that of Fe6+/Fe30-EVA, despite the higher iron concentration in the later sample. The fact that implantation of the pure films induces the formation of slightly bigger iron particles is probably responsible for this behaviour. The ZFC and FC results in Fig. 5 are in line with this conclusion. The specific magnetization of the Fe6+/EVA sample is more than two times higher than that of Fe6+/Fe30-EVA. On the other hand, both samples contain quite small iron nanoparticles (0.8 and 1.5 nm according to TEM) and this is also reflected in the ZFC and FC behaviour (Fig. 5). The temperature of magnetic irreversibility T_s (at which ZFC and FC curves start to split) of the Fe6+/Fe30-EVA sample is slightly shifted towards lower temperature with respect to that of the Fe6+/EVA sample (from 13.2 to 11.3 K). Due to the small size of the particles, it was difficult to precisely determine the peak temperature in the ZFC curves. As can be seen in the insets of Fig. 5, the blocking temperature of both samples is below 5 K. It should be mentioned that the results obtained by implantation of single charge ions at $4 \mu\text{A cm}^{-2}$ into polyethyleneterephthalate (PET) [11] were slightly different from those shown in Fig. 5. The fluency of $5 \times 10^{16} \text{ cm}^{-2}$ of single charged ions was sufficient to produce a visible peak in the ZFC curve at ~ 30 K. The specific magnetization of 0.3 emu g^{-1} obtained for this sample [11] is close to that obtained for our Fe6+/EVA nanocomposite film (Fig. 5). At a fluency of $1 \times 10^{17} \text{ cm}^{-2}$, the temperature of magnetic irreversibility T_s of PET implanted samples was shifted to ~ 150 K, indicating that the magnetic dipolar coupling between the particles becomes significant [11].

Although the SRIM calculations suggest that nuclear collisions dominate the energy deposition in both types of substrates, it seems that the combined effects of the increasing temperature and/or

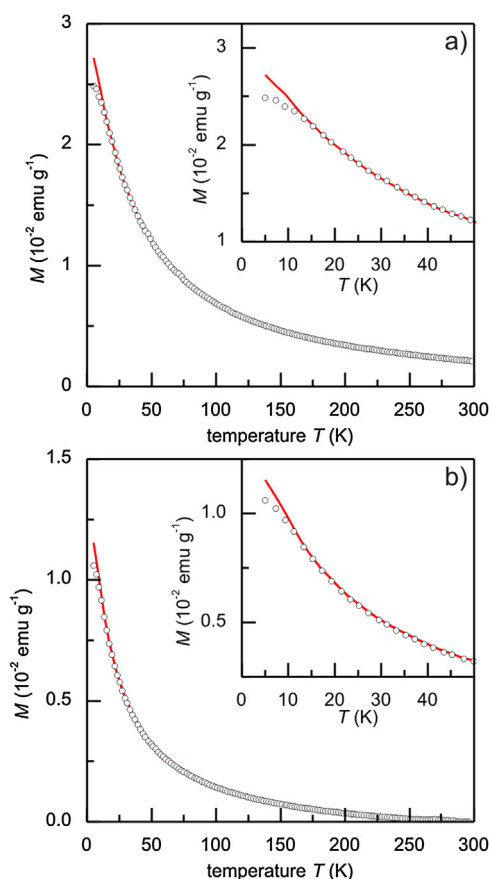


Fig. 5. Temperature dependence of ZFC (open symbols) and FC (solid lines) magnetizations of a) Fe6+/EVA and b) Fe6+/Fe30-EVA nanocomposite films. The insets show the same curves in the range from 0 to 50 K. The applied magnetic field was 300 Oe.

increasing ion charge strongly influence the size distribution of the particles formed upon irradiation. For this reason, the observed magnetic behaviour of the Fe6+/EVA and Fe6+/Fe30-EVA films will be different from that of single charge ions implanted PET films at similar ion fluencies. The implantation with highly charged ions under the conditions suggested here enables the fabrication of isolated nanoparticles (with negligible magnetic dipolar coupling), even when the amount of iron in the matrix increases. This can be of practical importance for the fabrication of the nanocomposites with desired magnetic properties.

Fig. 6 shows the magnetization–demagnetization curves of the Fe6+/EVA and Fe6+/Fe30-EVA films at 5 K. The results suggest typical superparamagnetic behaviour of the implanted particles. Nevertheless, as can be seen in the inset of Fig. 6, a small hysteresis is still present at low fields (from -500 to 500 Oe). This means that the magnetic moments of a certain number of nanoparticles (probably bigger ones) are blocked at 5 K and that a small coercive force is necessary to align them with the external field.

5. Conclusions

The morphology and magnetic properties of iron-polymer nanocomposites fabricated by ion implantation strongly depends on the charge of the iron ions employed. The implantation of Fe^{6+} ions into an EVA matrix induces the formation of spherical particles positioned about 50 nm beneath the surface of the film. A TEM image of the cross section of the film revealed that the average diameter of the particles is about 1.5 nm and that they were clustered into a single 80 nm wide strip. The particles exhibited

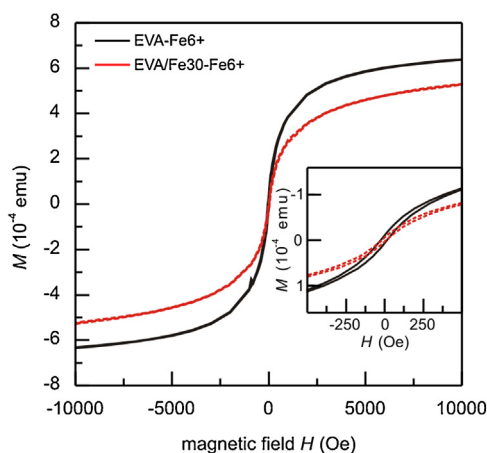


Fig. 6. Magnetization-demagnetization curves of Fe⁶⁺/EVA and Fe⁶⁺/Fe₃₀-EVA films at 5 K. The inset shows that a small hysteresis can be observed at low fields (in the range from -500 to 500 Oe).

a typical superparamagnetic behaviour with blocking temperature at around 5 K. The ZFC and FC curves of the nanocomposite films showed negligible magnetic dipolar coupling of the particles, although the ion fluency was quite high ($1 \times 10^{17} \text{ cm}^{-2}$). The results also showed that the morphology of the nanocomposite would change if iron was evaporated on the surface of the EVA films prior to the implantation with Fe⁶⁺ ions. In this case, smaller particles were obtained (~ 0.8 nm in diameter) and they were clustered into two strips separated by a 25 nm wide layer in which the density of the particles was lower. Due to the smaller size of the particles, this nanocomposite film also showed lower specific magnetization than the pure EVA implanted film, despite the slightly higher iron weight content. Depending on the particular application and desired magnetic dipolar coupling, our findings suggest that the implantation of highly charged ions under conditions used in the present study may enable specific tuning of the magnetic properties of the nanocomposite.

Acknowledgements

This work was supported in part by the Ministry of Education, Science and Technological Development, Republic of Serbia (Project Nos. 172056, III45020 and III45018). The authors wish to thank Dr. Jovan Blanuša for the useful discussions regarding the magnetic properties of the nanocomposite films.

Appendix A. Supplementary data

Supplementary data associated with this article can be found, in the online version, at <http://dx.doi.org/10.1016/j.apsusc.2016.04.020>.

References

- [1] V.N. Popok, Polymer films with ion-synthesized cobalt and iron nanoparticles: conductance and magnetism, *Rev. Adv. Mater. Sci.* 30 (2014) 1–12.
- [2] V.N. Popok, Ion implantation of polymers: formation of nanoparticulate materials, *Rev. Adv. Mater. Sci.* 30 (2012) 1–26.
- [3] A.L. Stepanov, R.I. Khaibullin, Optics of metal nanoparticles fabricated in organic matrix by ion implantation, *Rev. Adv. Mater. Sci.* 7 (2004) 108–125.
- [4] V.N. Popok, M. Hanif, A. Mackova, R. Miksova, Structure and plasmonic properties of thin PMMA layers with ion-synthesized Ag nanoparticles, *J. Polym. Sci. B: Polym. Phys.* 53 (2015) 664–672.
- [5] V. Resta, G. Quarta, I. Farella, L. Maruccio, A. Cola, L. Calcagnile, Comparative study of metal and non-metal ion implantation in polymers: optical and electrical properties, *Nucl. Instrum. Methods Phys. Res. B* 331 (2014) 168–171.
- [6] Yu. A. Bumai, V.S. Volobuev, V.F. Valeev, N.I. Dolgikh, M.G. Lukashevich, R.I. Khaibullin, V.I. Nuzhdin, V.B. Odzhaev, Optical characteristics of composites obtained by ion implantation of silver ions in polyethylene terephthalate, *J. Appl. Spectrosc.* 79 (2012) 773–779.
- [7] R.I. Khaibullin, Y.N. Osin, A.L. Stepanov, I.B. Khaibullin, Synthesis of metal/polymer composite films by implantation of Fe and Ag ions in viscous and solid state silicone substrates, *Nucl. Instrum. Methods Phys. Res. B* 148 (1999) 1023–1028.
- [8] M.C. Salvadori, F.S. Teixeira, L.G. Sgubin, M. Cattani, I.G. Brown, Surface modification by metal ion implantation forming metallic nanoparticles in an insulating matrix, *Appl. Surf. Sci.* 310 (2014) 158–163.
- [9] G. Maggioni, A. Vomiero, S. Carturan, C. Scian, G. Mattei, M. Bazzan, C. de Julián Fernández, P. Mazzoldi, A. Quaranta, G. Della Mea, Structure and optical properties of Au-polyimide nanocomposite films prepared by ion implantation, *Appl. Phys. Lett.* 85 (2004) 5712–5715.
- [10] V.N. Popok, V.I. Nuzhdin, V.F. Valeev, A.L. Stepanov, Copper nanoparticles synthesized in polymers by ion implantation: surface morphology and optical properties of the nanocomposites, *J. Mater. Res.* 30 (2015) 86–92.
- [11] M.G. Lukashevich, X. Batlle, A. Labarta, V.N. Popok, R.I. Khaibullin, V.B. Odzhaev, Modification of magnetic properties of polyethyleneterephthalate by iron ion implantation, *Nucl. Instrum. Methods Phys. Res. B* 257 (2007) 589–592.
- [12] M.G. Lukashevich, V.N. Popok, V.S. Volobuev, A.A. Melnikov, R.I. Khaibullin, V.V. Bazarov, A. Wieck, V.B. Odzhaev, Magneto-resistive effect in PET films with iron nanoparticles synthesized by ion implantation, *Open Appl. Phys. J.* 3 (2010) 1–5.
- [13] C. Okay, B.Z. Rameev, R.I. Khaibullin, M. Okutan, F. Yildiz, V.N. Popok, B. Aktas, Ferromagnetic resonance study of iron implanted PET foils, *Phys. Stat. Solidi A* 203 (2006) 1525–1532.
- [14] V. Yu Petukhov, N.R. Khabibullina, M.I. Ibragimova, A.A. Bukharaev, D.A. Biziaev, E.P. Zheglov, G.G. Gumarov, R. Müller, Magnetic properties of thin metal-polymer films prepared by high-dose ion-beam implantation of iron and cobalt ions into polyethylene terephthalate, *Appl. Magn. Reson.* 32 (2007) 345–361.
- [15] P. Sachdev, M. Banerjee, G.S. Mukherjee, Magnetic and microstructural studies on PVA/Co nanocomposite prepared by ion beam sputtering technique, *Def. Sci. J.* 64 (2014) 290–294.
- [16] M.E. Bannister, H. Hijazi, H.M. Meyer III, V. Cianciolo, F.W. Meyer, Surface-conductivity enhancement of PMMA by keV-energy implantation, *Nucl. Instrum. Methods Phys. Res. B* 339 (2014) 75–84.
- [17] E. Tavenner, P. Meredith, B. Wood, M. Curry, R. Giedd, Tailored conductivity in ion implanted polyetheretherketone, *Synth. Met.* 145 (2004) 183–190.
- [18] A. Mackova, P. Malinsky, R. Miksova, H. Pupikova, R.I. Khaibullin, P. Slepicka, A. Gombitová, L. Kovacik, V. Svorcik, J. Matousek, Characterization of PEEK: PET and PI implanted with Mn ions and sub-sequentially annealed, *Nucl. Instrum. Methods Phys. Res. B* 325 (2014) 89–96.
- [19] I. Draganić, T. Nedejković, J. Jovović, M. Šiljegović, A. Dobrosavljević, Multiply charged ions from solid substances with the mVINIS Ion Source, *J. Phys.: Conf. Ser.* 58 (2007) 427–430.
- [20] S. Dhar, P. Schaaf, N. Bibić, E. Hooker, M. Milosavljević, K.P. Lieb, Ion-beam mixing in Fe/Si bilayers by singly and highly charged ions: evolution of phases, spike mechanism and possible effects of the ion-charge state, *Appl. Phys. A* 76 (2003) 773–780.
- [21] A. Dobrosavljević, M. Milosavljević, N. Bibić, A.A. Efremov, The L3A facility at the Vinča Institute: surface modification of materials: by heavy ion beams from an electron cyclotron resonance ion source, *Rev. Sci. Instrum.* 71 (2000) 786–788.
- [22] J.F. Ziegler, M.D. Ziegler, J.P. Biersack, SRIM—The stopping and range of ions in matter, *Nucl. Instrum. Methods Phys. Res. B* 268 (2010) 1818–1823.
- [23] N. Stolterfoht, J.H. Bremer, R. Díez Muiño, Formation and cascading decay of hollow Ar atoms at a Si surface, *Int. J. Mass Spectrom.* 192 (1999) 425–436.
- [24] D.K. Božanić, I. Draganić, J. Pajović, R. Dojčilović, N. Bibić, V. Djoković, Fabrication of polymer nanocomposites by implantation with multiple charged iron ions, in: 27th Summer School and International Symposium on the Physics of Ionized Gases (SPIG 2014) Belgrade, Serbia, August 26–29, 2014, Book of contributed papers, 2016, pp. 202–205.



Formation of Self-Organized Mn₃O₄ Nanoinclusions in LaMnO₃ Films

Alberto Pomar^{1*}, Zorica Konstantinović², Núria Bagués^{1,3}, Jaume Roqueta³, Laura López-Mir¹, Lluís Balcells¹, Carlos Frontera¹, Narcís Mestres¹, Araceli Gutiérrez-Llorente⁴, Maja Šćepanović², Nenad Lazarević², Zoran V. Popović², Felip Sandiumenge¹, Benjamín Martínez¹ and José Santiso³

¹ Instituto de Ciencia de Materiales de Barcelona-Consejo Superior de Investigaciones Científicas, Bellaterra, Spain, ² Center for Solid State Physics and New Materials, Institute of Physics Belgrade, University of Belgrade, Belgrade, Serbia, ³ Catalan Institute of Nanoscience and Nanotechnology, Consejo Superior de Investigaciones Científicas and The Barcelona Institute of Science and Technology, Bellaterra, Spain, ⁴ ESCET, Universidad Rey Juan Carlos, Madrid, Spain

OPEN ACCESS

Edited by:

Marin Alexe,
University of Warwick, UK

Reviewed by:

Beatriz Noheda,
University of Groningen, Netherlands
Saeedeh Farokhipoor,
University of Cambridge, UK

*Correspondence:

Alberto Pomar
apomar@icmab.es

Specialty section:

This article was submitted to
Condensed Matter Physics,
a section of the journal
Frontiers in Physics

Received: 15 June 2016

Accepted: 30 August 2016

Published: 20 September 2016

Citation:

Pomar A, Konstantinović Z, Bagués N, Roqueta J, López-Mir L, Balcells L, Frontera C, Mestres N, Gutiérrez-Llorente A, Šćepanović M, Lazarević N, Popović ZV, Sandiumenge F, Martínez B and Santiso J (2016) Formation of Self-Organized Mn₃O₄ Nanoinclusions in LaMnO₃ Films. *Front. Phys.* 4:41. doi: 10.3389/fphy.2016.00041

We present a single-step route to generate ordered nanocomposite thin films of secondary phase inclusions (Mn₃O₄) in a pristine perovskite matrix (LaMnO₃) by taking advantage of the complex phase diagram of manganese oxides. We observed that in samples grown under vacuum growth conditions from a single LaMnO₃ stoichiometric target by Pulsed Laser Deposition, the most favorable mechanism to accommodate Mn²⁺ cations is the spontaneous segregation of self-assembled wedge-like Mn₃O₄ ferrimagnetic inclusions inside a LaMnO₃ matrix that still preserves its orthorhombic structure and its antiferromagnetic bulk-like behavior. A detailed analysis on the formation of the self-assembled nanocomposite films evidences that Mn₃O₄ inclusions exhibit an epitaxial relationship with the surrounding matrix that it may be explained in terms of a distorted cubic spinel with slight (~9°) c-axis tilting. Furthermore, a Ruddlesden-Popper La₂MnO₄ phase, helping to the stoichiometry balance, has been identified close to the interface with the substrate. We show that ferrimagnetic Mn₃O₄ columns influence the magnetic and transport properties of the nanocomposite by increasing its coercive field and by creating local areas with enhanced conductivity in the vicinity of the inclusions.

Keywords: self-organization, nanocomposite, LaMnO₃, oxide thin films, strain effects

INTRODUCTION

The large choice in chemical elements in either A- and B-site of the perovskite structure allows tailoring many parameters including lattice constants, electronic band structures, magnetic interactions, and more. In particular, manganese based oxides display a huge range of properties from total spin polarization and colossal magnetoresistance to multiferroicity, with potential use from active electrodes in electronic devices to sensors and magnetic memories. Furthermore, nanostructured thin films widen their application range as their final functional properties are determined by the very active role of interfaces and surfaces which may be efficiently modified by strain relaxation mechanisms [1–4]. Specially in the case of undoped LaMnO₃ (LMO), the appearance of ferromagnetism in heterostructures of LaMnO₃/SrTiO₃ [5] and LaMnO₃/SrMnO₃ [6], or the observation of exchange bias in LaMnO₃/LaNiO₃ superlattices [7] evidence the importance of interfacial phenomena. In addition to standard heterointerfaces in layered structures, new strategies have been developed to increase the surface to volume ratio and to enhance interfacial effects. In this sense, vertically heteroepitaxial nanocomposites (VHN) provide

a vertical contact area between two immiscible compounds much larger than substrate to films. Additionally, lateral strain may be tuned to large film thicknesses [8].

Spontaneous organization of vertical heteroepitaxial nanocomposite thin films has enabled the discovery of new physical phenomena at the nanoscale and their possible use in magnetoelectric devices. For instance, large adjustable low-field magnetoresistance is observed in vertically aligned La_{0.7}Ca_{0.3}MnO₃ [9] or La_{0.7}Sr_{0.3}MnO₃ (LSMO) based nanocomposites [10, 11]. A good example of this is the system LSMO:Mn₃O₄ that has been often proposed as potential nanocomposite due to the chemical compatibility of Mn₃O₄ with the whole manganite perovskite family [12]. Indeed, if the composition ratio [La+Sr]/[Mn] < 1, a spinodal decomposition mechanism in chemical solution deposited films may lead to the spontaneous formation of LSMO:Mn₃O₄ VHNs [13]. The so-generated vertical lattice strain is found to be related to the different domain and grain boundary structures and directly impact their ferromagnetic properties [11]. In the particular case of the parent compound, i.e., undoped LaMnO₃, manganese segregation is expected to occur when La deficiency leads to a non-stoichiometric ratio of La/Mn < 0.9 [14]. There, the appearance of randomly distributed segregates of manganese oxides such as Mn₃O₄ or MnO has been reported in bulk samples [15, 16] and thin films [17]. It is important, from a fundamental point of view, to understand the formation of manganese oxide segregates, as it is a characteristic secondary phase in several REMnO₃ (RE = Rare Earth) thin films and heterostructures, thus modifying their structural quality and functional properties [18–20]. Furthermore, manganese oxides are extremely attractive for potential applications due to their electrochemical, optical, or catalytic properties [21–24]. In spite of their abundance in nature reproducible properties of manganese oxides require the fabrication of uniform structures and a large effort is devoted to produce MnO_x nanostructures (for recent Reviews see, for example, [23, 24] and references therein). In the present study, we report on the spontaneous formation of regular vertically aligned nanocolumns composed of manganese oxide embedded in antiferromagnetic LaMnO₃ matrix grown by pulsed laser deposition (PLD) on (001)-oriented single crystal perovskite substrates of LaAlO₃ (LAO) and SrTiO₃ (STO). The formation mechanisms of the manganese oxide secondary phase and their influence on functional properties of manganite thin films are discussed in detail.

MATERIALS AND METHODS

LaMnO₃ and Mn₃O₄

The primary phase i.e., the matrix in the studied films is LaMnO₃ (LMO) which in its stoichiometric bulk state is an antiferromagnetic insulator with T_N ~140 K [25, 26]. The crystal structure of the bulk LMO is described by an orthorhombic Pbnm space group with cell parameters a = 5.533 Å, b = 5.727 Å, and c = 7.668 Å at room temperature [26]. Achieving the right LaMnO₃ stoichiometry in thin films leading to an antiferromagnetic (AF) ground state remains challenging regardless of the growth technique and it requires a fine control

of growth conditions [27]. In particular, AF behavior is only obtained in films prepared at low oxygen pressures while the right stoichiometry is maintained. In fact, deviations from [La]/[Mn] = 1 stoichiometry in LMO thin films may easily change Mn oxidation state leading to ferromagnetic behavior [28, 29]. The secondary phase in films is the manganese oxide MnO_x which could present mixed Mn oxidation states (Mn²⁺, Mn³⁺, or even Mn⁴⁺). In general, manganese may easily alter its valence forming different oxide stoichiometries in response to the environmental conditions. Under thermodynamic equilibrium, bulk oxide stoichiometries are directly determined by oxygen partial pressure and temperature. In the vacuum conditions used in the present work either MnO, Mn₃O₄, or Mn₂O₃ may be formed depending on the residual oxygen partial pressure in the chamber [17]. At the growth temperature of 850°C, Mn²⁺O should be thermodynamically favored if P(O₂) < 2 × 10⁻⁴ mTorr while Mn³⁺O₃ is only expected for oxygen pressures close to atmospheric conditions (α-Mn₂O₃ being the usual polymorph phase while γ-Mn₂O₃ has been observed in nanometric form [30]). At intermediate pressures, the mixed valence manganese oxide Mn₃O₄ (or Mn²⁺Mn³⁺O₄ in spinel notation) is expected to be the dominant phase [31]. The different oxides are quite difficult to distinguish and share several characteristic features. Manganese oxides as Mn₃O₄, or γ-Mn₂O₃ are ferrimagnetic with transition temperature, T_c, around 40 K while MnO and α-Mn₂O₃ exhibit antiferromagnetic ordering below 118 and 80 K, respectively [30, 32, 33]. Regarding their crystal structure, MnO is a cubic rocksalt with a = 4.45 Å [34], α-Mn₂O₃ is cubic bixbyite (a = 9.42 Å) while Mn₃O₄ and γ-Mn₂O₃ exhibit spinel-like structures. Mn₃O₄ is hausmannite mineral with distorted spinel structure with manganese ions placed on two non-equivalent tetrahedral (Mn²⁺) and octahedral (Mn³⁺) sites. The structure is well described by tetragonal I₄/amd space group with cell parameters of a = 5.76 Å and c = 9.47 Å [35, 36]. A very similar spinel structure is reported for γ-Mn₂O₃ with a = 5.79 Å and c = 9.40 Å [30]. As each of these oxides have cubic or tetragonal symmetry they can epitaxially grow on cubic perovskite substrates under suitable conditions. Furthermore, biaxial strain (either compressive or tensile) may modify not only their equilibrium phase diagram but it also may lead to the appearance of other crystal structures as, for example, the high pressure Mn₃O₄ cubic phase [37–39]. This epitaxial stabilization reported on MgO substrates was not observed for Mn₃O₄ films grown on STO or LAO due to the large compressive mismatch of (a_{Mn3O4}/√2-a_{STO})/a_{STO} = -4% and (a_{Mn3O4}/√2-a_{LAO})/a_{LAO} = -7% [40]. However, in VHNs where lateral strain imposed by the surrounding oxide matrix may add a supplementary gain to the free energy balance, the formation of Mn₃O₄ cubic phase has been recently reported [13, 41].

Experimental Methods

Thin films of LaMnO₃ with self-assembled manganese oxide nanocolumns have been prepared from stoichiometric LaMnO₃ ceramic targets by PLD with a KrF excimer laser. A spontaneous assembly of manganese oxide nanocolumns has been observed at 850°C under vacuum conditions (background pressure of <5 × 10⁻⁴ mTorr). The laser fluency was kept below <1 J/cm²

with 10 Hz pulse repetition rate. The films were grown on top of SrTiO₃ (100) and LaAlO₃ (100) substrates and their thickness are kept between 30 and 100 nm as determined by X-ray reflectometry.

The structural characterization was carried out by X-ray diffraction using a four-angle diffractometer with a Cu-K_α radiation source (X'Pert Pro MRD-Panalytical). All the structural drawings and schemes were produced by using VESTA program [42].

The detailed microstructure and the chemical composition was investigated by Transmission Electron Microscopy (TEM) observations of cross section specimens of LMO/STO on a FEI Tecnai G² F20 S-TWIN HR(S)TEM operated at 200 kV. Cross section specimens were prepared by conventional cutting, gluing and grinding procedures followed by an Ar-ion milling step down to electron transparency by Precision Ion Polishing System (PIPS™)—Gatan. High annular dark field (HAADF) images, energy dispersive X-ray spectroscopy (EDS) profiles and electron energy loss spectroscopy (EELS) spectrum—images (SI) were obtained to identify the composition of the nanopillars. EELS-SI of cross-section samples was also carried out in DualEELS mode with a Titan3™ G2 60-300 operating at 300 kV, equipped with a Dual-EELS spectrometer. The principal components analysis (PCA) provided by Lucas et al. [43] for Digital Micrograph was used to remove the random noise. The power law was used before energy peak to remove the background and then data was deconvolved using the Fourier Log method. The La/Mn ratio was obtained from EDS of areas in the matrix tilting the sample out-of-zone axis in order to minimize the electron channeling. High resolution TEM images obtained from selected regions in the micrograph (the matrix, the nanopillar, and the interface between them) were used to identify the matrix orientation and the manganese oxide phase of the inclusions using the Eje-Z software [44].

The surface morphology was studied by Scanning Electron Microscopy (SEM) using a QUANTA FEI 200 FEG-ESEM microscope. Measurements of the local electrical conductivity were performed by Conducting-Atomic Force Microscopy (c-AFM) using a MFP-3D Asylum and ORCA module. A conductive tip with PtIr coating was used as a top electrode and the voltage was applied directly to the sample. A constant nominal force of 3 N/m was used in tapping mode. The topography and current maps were acquired simultaneously.

The magnetic properties were measured in a commercial SQUID magnetometer (Quantum Design). The magnetic field was applied parallel to the substrate in all measurements. The substrate diamagnetic contribution is evaluated from the field dependence of the magnetization at room temperature and systematically subtracted from the measurements.

Raman scattering measurements were performed using a TriVista 557 Raman system equipped with a nitrogen-cooled CCD detector, in backscattering micro-Raman configuration. The 532 nm line of the Verdi G laser was used as an excitation source. A microscope objective with 100 magnification was used for focusing the laser beam. All measurements were carried out at low laser power, in order to minimize local heating of the sample. Raman scattering measurements at temperatures lower

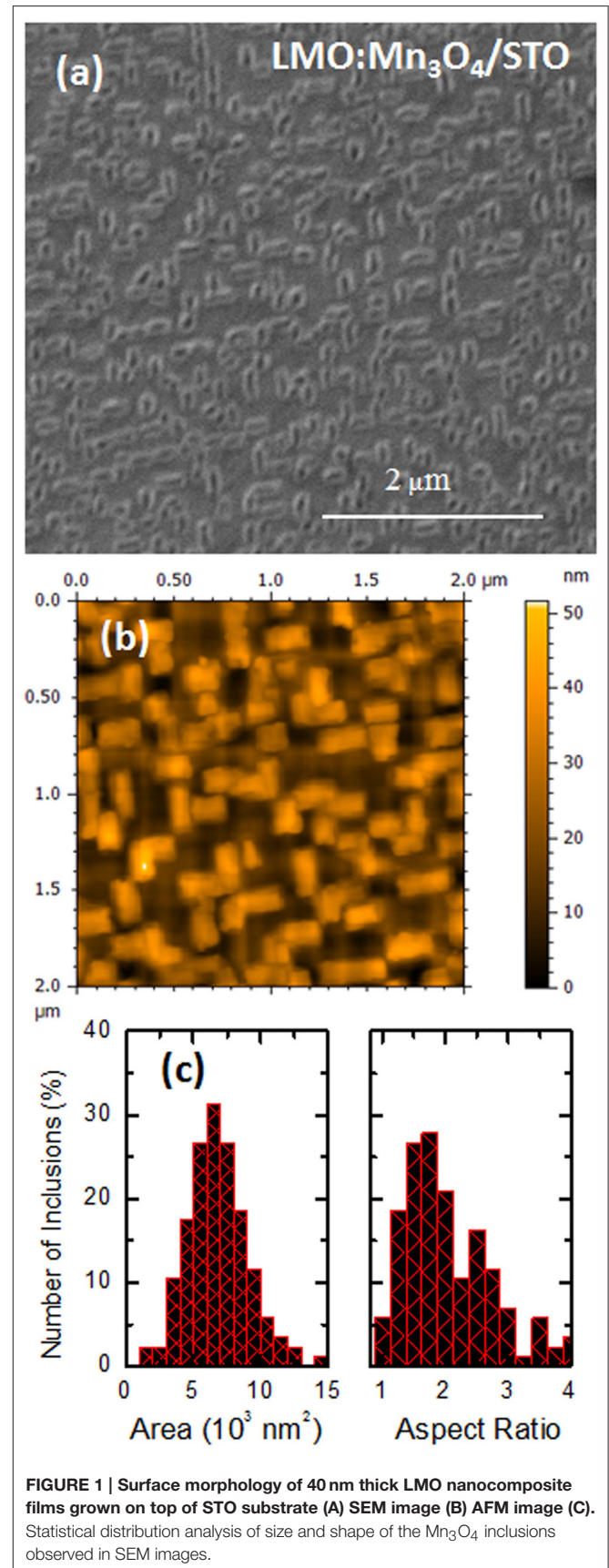


FIGURE 1 | Surface morphology of 40 nm thick LMO nanocomposite films grown on top of STO substrate (A) SEM image (B) AFM image (C). Statistical distribution analysis of size and shape of the Mn₃O₄ inclusions observed in SEM images.

than room temperature were performed in the back-scattering geometry in a cryostat system using 488-nm line of an Ar⁺ laser, Jobin–Yvon U1000 double monochromator, and photomultiplier as detector.

The experimental results presented in this work were obtained on the exact same samples, either on LAO or STO substrates with the only exception of temperature dependent Raman measurements where, to enhance signal to background ratio, a thicker sample grown on LAO (~100 nm) was used.

RESULTS AND DISCUSSION

Films grown in vacuum conditions exhibit a clear ordered nanocomposite surface, as evidenced by SEM images either on STO or LAO substrates (see **Figures 1A, 2A**, respectively). It is observed that the inclusions of the secondary phase (manganese oxide) are uniformly distributed in the LMO matrix (primary phase) with typical rectangular-based dimensions of 40 × 150 nm (on STO substrate) and 40 × 90 nm (on LAO substrate). It is worth reminding here that this spontaneous regular formation of manganese oxide in LMO thin films has been obtained by laser ablation of single target and it is linked to the low oxidation conditions during the PLD process. Films grown at higher oxygen pressures exhibit flat surfaces with no sign of phase segregation [27]. More information about the arrangement of the secondary phase may be obtained from atomic force microscopy images as the shown in **Figure 1B** (on STO) and **Figure 2B** (on LAO). While the manganite LMO phase appears to be very flat with low roughness (rms < 0.5 nm), MnO_x nanopillars appear as large inclusions exceeding the surface of the matrix by several nm. From this preliminary characterization we may estimate that secondary phase occupies around 10–15% of the total surface, as determined by quantifying black areas (different chemical composition) in the SEM images. An interesting observation is that MnO_x inclusions are mainly oriented with their rectangular sides aligned with the main axes of the substrates. Statistical analysis of the inclusions is presented in the histograms of **Figures 1C** and **2C**. We may see that size and aspect ratio is enhanced in the case of films grown on STO substrates. This suggests that the different mismatch with substrate plays a role in the statistical size distribution of the segregates.

As mentioned above, epitaxial growth of orthorhombic stoichiometric LMO films has been studied by several groups in the past to elucidate the controversial appearance of ferromagnetic behavior. Either strain or oxygen content has been claimed to be at the origin of this anomalous magnetic behavior [28, 29, 45–49]. In LMO bulk state, oxygen off-stoichiometry (in fact, cation vacancy) is accommodated by modifying the Mn–O octahedral environment mainly resulting in a strong change in the orthorhombic lattice parameters that also influences the cooperative Jahn–Teller effect and, as a result, the magnetic ordering. Quite recently we have shown that a careful epitaxial analysis is required to fully understand the growth of LMO films under different oxygen conditions [27]. For this reason, we have performed reciprocal 2θ–φ area scans at grazing incidence around 220 and 004 orthorhombic in-plane reflections (corresponding to 200 reflections in

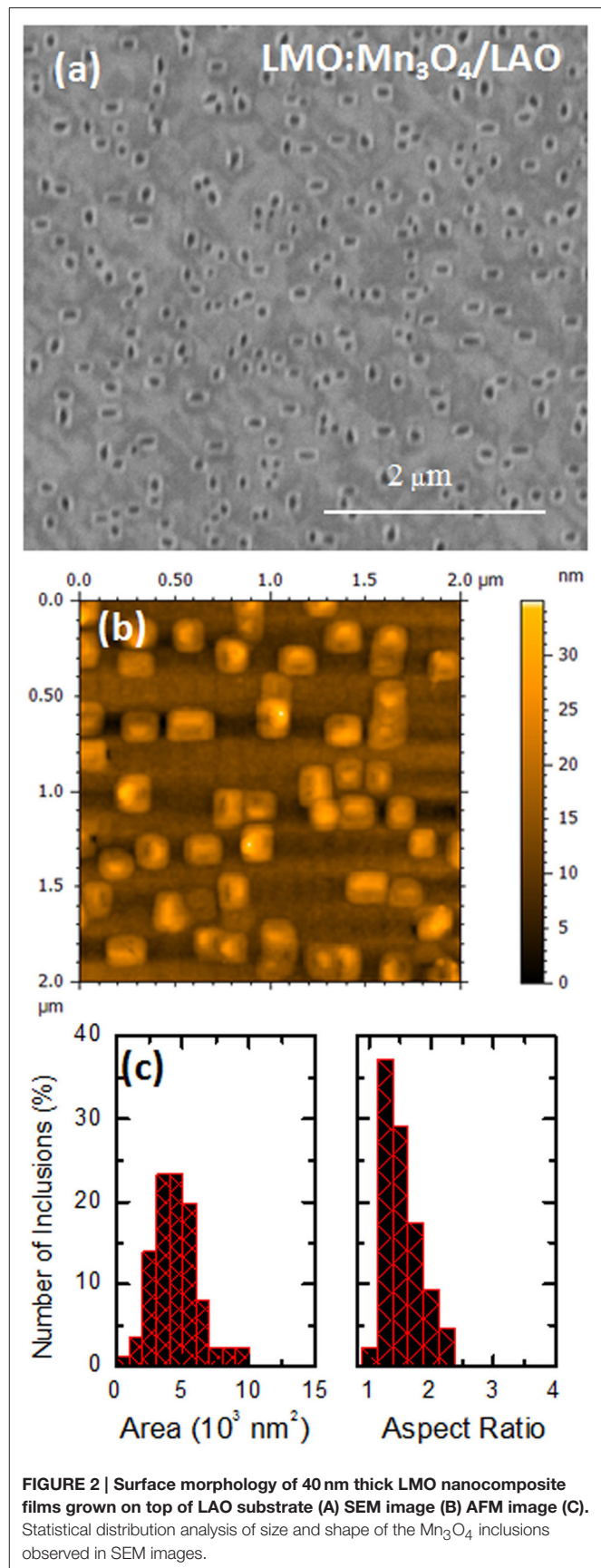
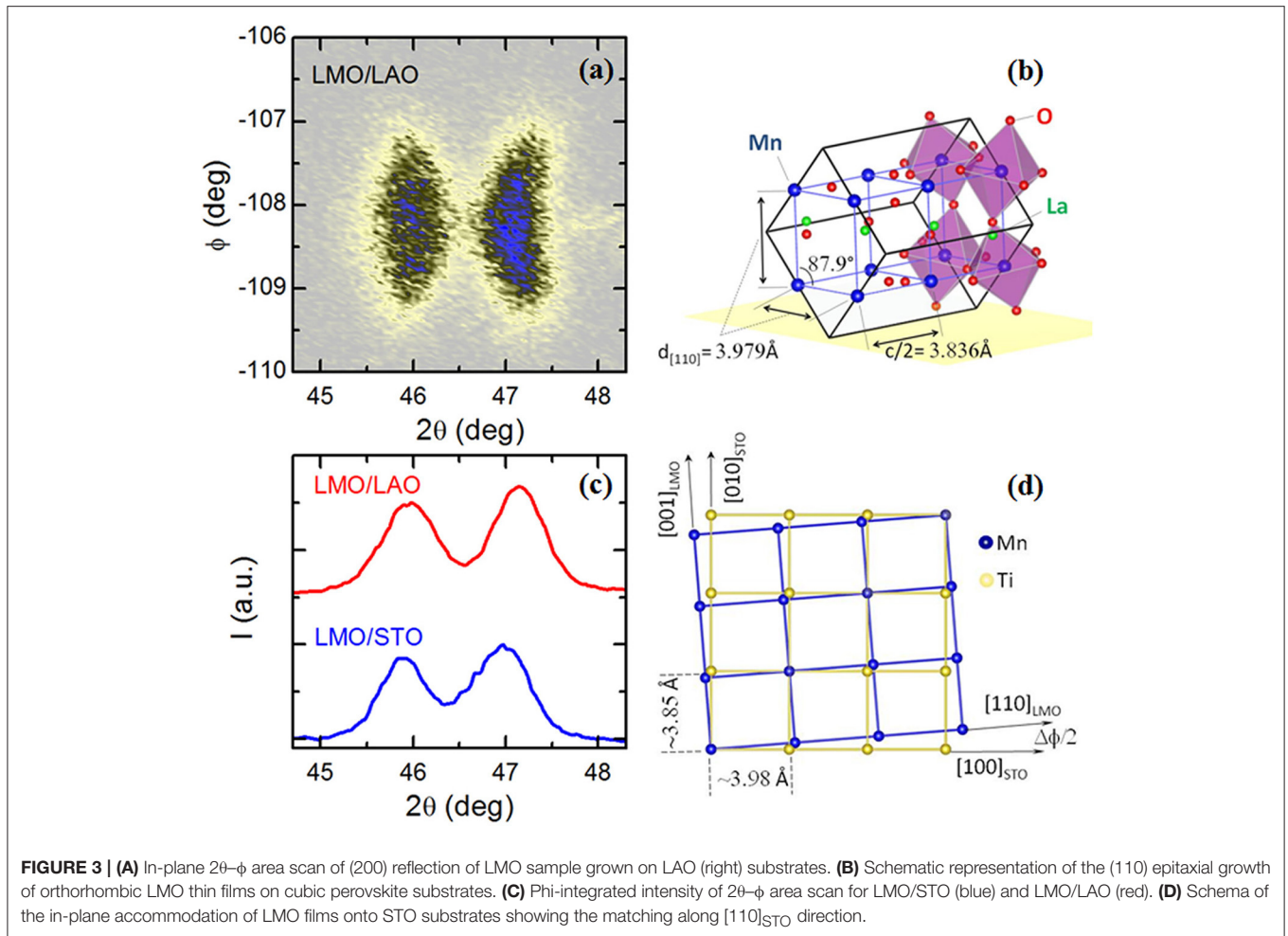


FIGURE 2 | Surface morphology of 40 nm thick LMO nanocomposite films grown on top of LAO substrate **(A)** SEM image **(B)** AFM image **(C)**. Statistical distribution analysis of size and shape of the Mn₃O₄ inclusions observed in SEM images.



pseudocubic notation). **Figure 3A** shows a typical area scan for LMO sample grown on LAO. Similar results were obtained previously for films grown on STO [27]. We observe the presence of two peaks occurring at different 2θ angles that are the clear signature of twinned domains with two in-plane lattice parameters. To understand this result, we need to consider that growth temperature ($T_g = 1123$ K) is well above Jahn-Teller transition of LMO ($T_{JT} = 750$ K) and, although still exhibiting Pbnm crystallographic structure, all orthorhombic LMO matching distances are nearly equal ($a_{\text{LMO}798\text{K}}/\sqrt{2} = 3.9468$ Å, $b_{\text{LMO}798\text{K}}/\sqrt{2} = 3.9478$ Å, $c_{\text{LMO}798\text{K}} = 3.9448$ Å) [50]. Thus, LMO structure is metrically cubic and a cube-on-cube epitaxial relationship with substrate is expected. During cooling, cooperative Jahn-Teller transition takes place in LMO and its MnO₆ octahedral framework is extremely distorted (Mn-O bond distances being 1.903, 1.957, and 2.184 Å). To accommodate this structural distortion to the underlying substrate lattice, film may adopt either (110) or (001) orientation. In such situation, it is useful to consider the area mismatch in the basal plane, i.e., $\varepsilon_{\text{area}}(110) = (d_{[110]f}^2 - a_s^2)/a_s^2$ for (110)-orientation and $\varepsilon_{\text{area}}(001) = (d_{[110]f}c_f/2 - a_s^2)/a_s^2$ for (001) orientation, where f and s indicate film and substrate, respectively, and $d_{[110]} =$

$(a^2 + b^2)^{1/2}/2$. We may see that $\varepsilon_{\text{area}}[110]_{\text{STO}} = -0.1\%$ and $\varepsilon_{\text{area}}[001]_{\text{STO}} = -3.7\%$ for STO and $\varepsilon_{\text{area}}[110]_{\text{LAO}} = -5.9\%$ and $\varepsilon_{\text{area}}[001]_{\text{LAO}} = -9.3\%$ for LAO. In both cases, (110) orientation shows clearly a better matching which very likely favors this orientation. In this case, when LMO c -axis is contained in the plane of the substrate, we have two different in-plane Mn-Mn matching distances, $d_{[110]_{\text{LMO}}} = 3.982$ Å and $d_{[001]_{\text{LMO}}} = c_{\text{LMO}}/2 = 3.834$ Å (see schema in **Figure 3B**) leading to twinned domains and the two peaks in **Figure 3A**. A reliable quantitative analysis of the in-plane cell parameters has been performed by integrating the intensity of the respective area scans along the azimuthal angle ϕ and fitting the corresponding peaks (see **Figure 3C**). We have obtained values of 3.952 and 3.875 Å (on STO) and 3.947 and 3.875 Å (on LAO) for $d_{[110]_{\text{LMO}}}$ and $d_{[001]_{\text{LMO}}}$, respectively. The resulting effective strains are approximately -1% compressive and 1% tensile for STO and -4 and -2% compressive for LAO substrate. These values of residual strain and in-plane lattice parameters indicate that the LMO thin films grown under vacuum conditions are almost in a relaxed state. In the case of the films grown on STO, such relaxed state may be understood if we calculate the corresponding diagonal basal distances of STO, $d_{[110]_{\text{STO}}} = 5.523$ Å and film, $d_{\text{LMO}} = 5.534$ Å which show a mismatch of 0.3%. This suggests

that LMO tends to accommodate to the underlying substrate along STO[110] direction, i.e., in-plane LMO *c*-axis is slightly rotated with respect to substrate principal axes (see scheme in **Figure 3D**) which is characteristic of the formation of LMO twined domains being the twin boundary plane aligned with the [110]STO direction. The formation of these twin domains takes place during the cooling down process below the Jahn–Teller transition temperature. From standard θ - 2θ x-ray diffraction measurements we have also determined the pseudocubic LMO out-of-plane cell parameter, obtaining 3.985 Å for LMO on STO and a larger value of 4.006 Å for LMO on LAO. In both cases, our estimation of pseudocubic unit cell volume leads to ~ 61 Å³, close to the expected bulk value for orthorhombic stoichiometric LMO [26]. The relative orientations of film and substrate were also observed by X-ray diffraction reciprocal space maps, as depicted in **Figure 4A**. The map shows the area around the main symmetrical 002 reflection of LaAlO₃ substrate. The position of the main film peak close to the substrate peak is compatible with 220 LMO, which corresponds to c_{\parallel} -oriented domains. The observation of 221 LMO reflection indicates the formation of orthorhombic *Pbnm* LMO (which corresponds to half order $2\ 0\ \frac{1}{2}$ reflection in cubic primitive notation). The fact that half order reflection lies along Q_x direction supports the c_{\parallel} -orientation of the LMO. The two separate reflections at lower Q_z values are consistent with 004 reflections from Mn₃O₄ spinel with their *c*-axis tilted 9° at both sides of the vertical direction. The corresponding pole figure of this 004 Mn₃O₄ reflection is depicted in **Figure 4B** showing the presence of four reflections at $\chi \sim 9^\circ$ separated by $\phi = 90^\circ$. This indicates the textured orientation of Mn₃O₄ inclusions within the LMO matrix.

Further confirmation that partially relaxed LMO films still preserve orthorhombic symmetry has been obtained by studying the Raman response. **Figure 5A** shows the Raman spectra of LMO nanostructured films at room temperature. In both spectra the same peaks are observed. Those found at frequencies of 257, 244, and 481 cm⁻¹ are associated to A_g symmetry whereas those at 308 and 611 cm⁻¹ correspond to Raman frequency of B_{2g} symmetry. All of them are fully

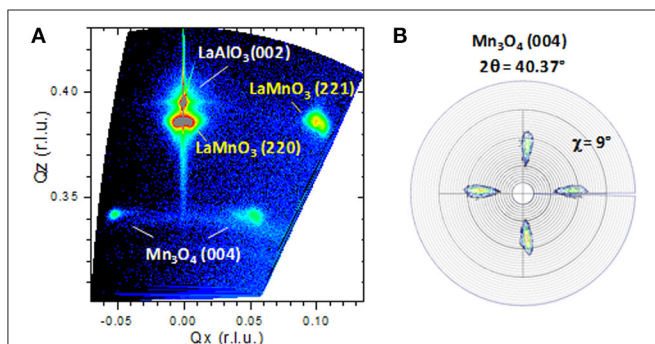


FIGURE 4 | (A) X-ray diffraction reciprocal space map around the 220 LaMnO₃ and 002 LaAlO₃ main reflections showing the presence of 221 half order reflection of c_{\parallel} -LaMnO₃, and the presence of 9°-tilted c_{\parallel} Mn₃O₄ domains. **(B)** Pole figure of the 004 Mn₃O₄ reflection showing the four-fold symmetry of the Mn₃O₄ inclusions.

compatible with those of orthorhombic LaMnO₃ reported for stoichiometric single crystals [51]. Temperature dependence of Raman response for LMO samples grown on LAO substrates is presented in **Figure 5B**. The most pronounced features in the Raman spectra of LMO/LAO sample in the range of 450–660 cm⁻¹ correspond to the E_g Raman mode of LAO substrate and to the modes of A_g and B_{2g} symmetry of orthorhombic LMO structure. Note that with lowering of the temperature, B_{2g} Raman mode shows characteristic softening in the antiferromagnetic phase [52], as shown in the right inset of **Figure 5B**. Besides, a low-intensity peak at about 640 cm⁻¹, better discerned in the Raman spectra collected at low temperatures (**Figure 5B**, left inset), can be attributed to the stretching vibration of Mn–O bond in the MnO₆ unit of manganese oxide, possibly nanocrystalline Mn₃O₄. Namely, due to phonon confinement effect, with decreasing mean crystallite size the A_{1g} Raman mode in nanostructured Mn₃O₄ gradually redshifts compared to its position in bulk

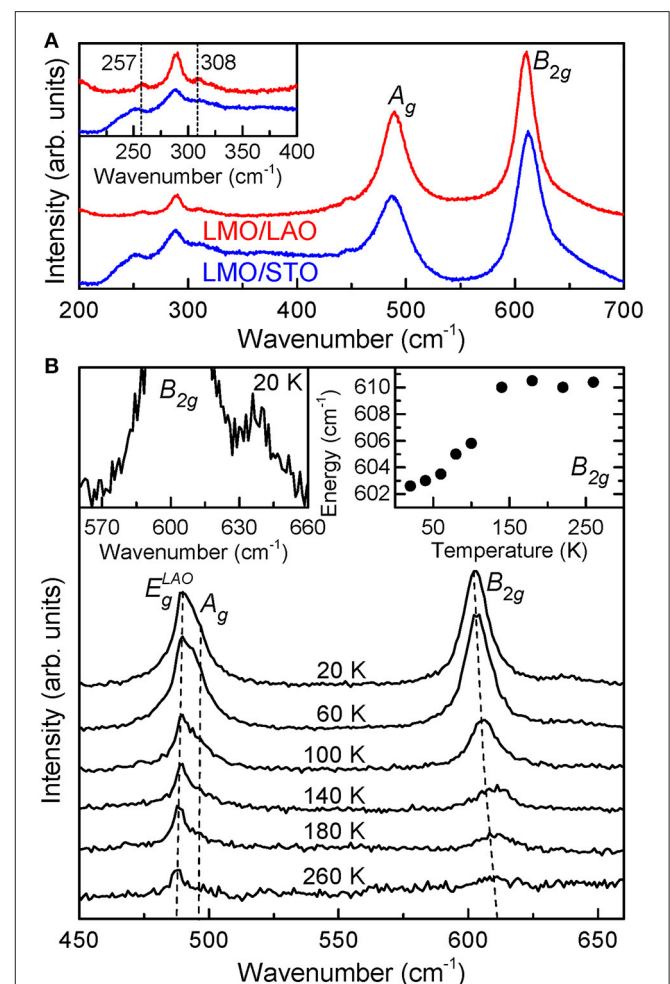


FIGURE 5 | (A) Raman shift at room temperature from corresponding samples of LMO samples grown on STO (blue) and LAO (red) substrates. **(B)** Raman spectra of LMO/LAO sample at low temperatures. Right inset: Temperature dependence of B_{2g} wavenumber. Left inset: Enlarged part of Raman spectrum measured at 20 K.

crystal ($\sim 656\text{ cm}^{-1}$) [53]. In the case of $\gamma\text{-Mn}_2\text{O}_3$, the main Raman feature is reported to appear at 628 cm^{-1} and, thus, it cannot explain our results of **Figure 5B** [54]. So, the appearance of the Raman mode at $\sim 640\text{ cm}^{-1}$ could be related to the presence of Mn_3O_4 nanocrystallites with mean size of about 30 nm.

The microstructural analysis on the formation of the MnO_x secondary phase ordered nanostructures, their correlation with substrate/film interface and the relaxation of strain was studied in detail by cross-section TEM (**Figure 6**). The TEM images reveal a wedge-like shape of the nanopillars. Surprisingly, MnO_x columns do not reach the interface with the substrate. However, there

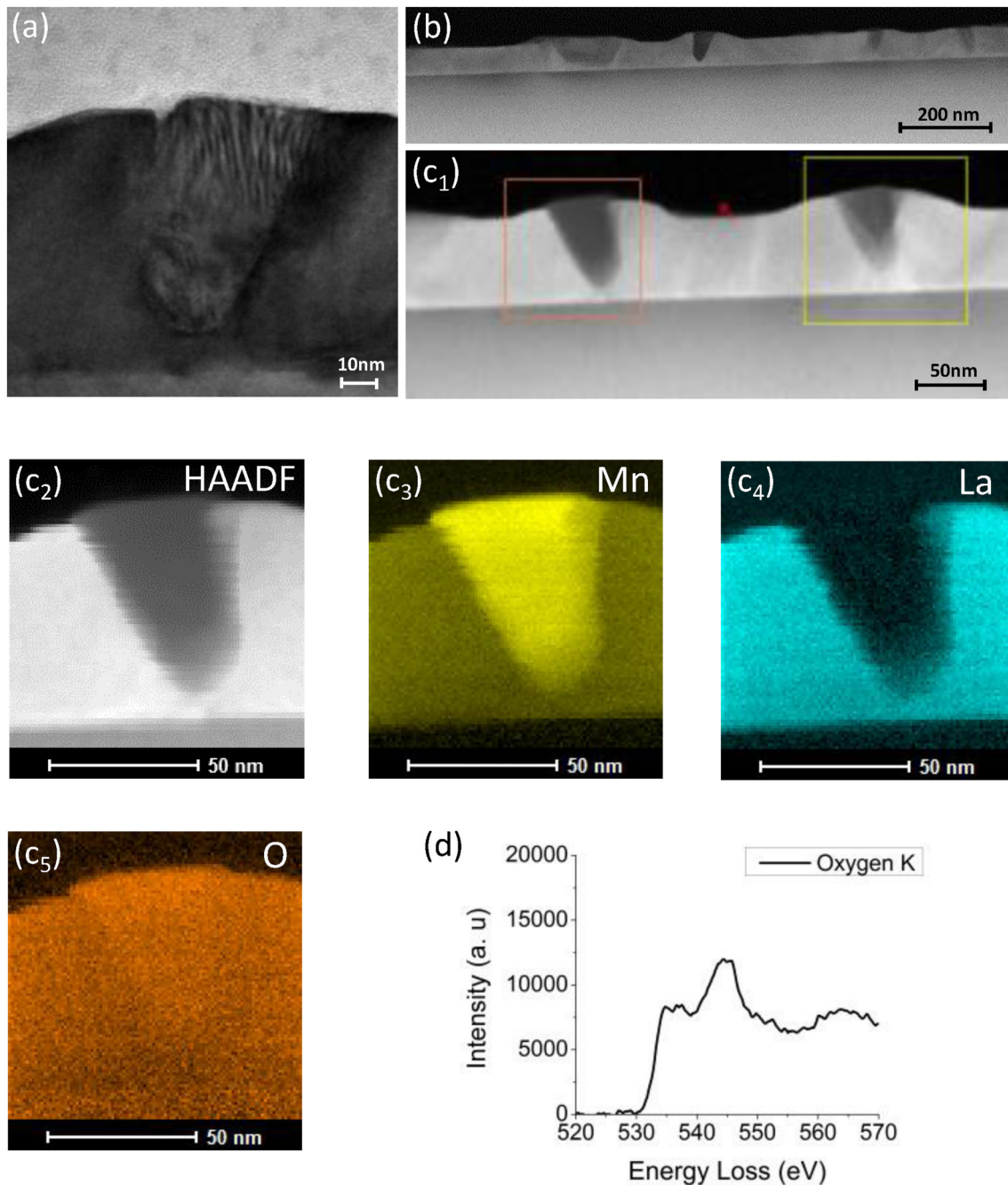


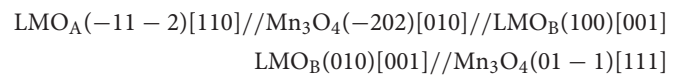
FIGURE 6 | TEM images of 40 nm LMO thick film grown on STO (A) TEM image around a MnO_x inclusion (B) HAADF image of the film (C) EELS mapping: (c1) HAADF image where orange square indicate the zone of the mapping and yellow square is drift correction reference, (c2) Z-contrast image used as a reference for the maps: (c3) manganese energy windows, (c4) lanthanum energy windows, and (c5) oxygen energy window. (D) Oxygen K edge EELS corresponding to MnO_x nanocolumn obtained from EELS-SI in DualEELS mode.

is a thin LMO matrix layer of around 5 nm (**Figure 6**). Taking into account the huge lattice mismatch between manganese oxide and substrate, it looks energetically unfavorable to nucleate directly on top of the substrate and, instead, a thin LMO layer could act as an efficient buffer layer for drastically decreasing the strain. HAADF images (Z-contrast images) presented in **Figure 6C** show a different contrast between matrix (bright contrast) and nanopillar (dark contrast) indicating different cation composition. Specifically, the chemical analysis, EDS profiles and EELS maps, reveals that the dark zones in HAADF image correspond to a pure manganese oxide whereas the bright zone corresponds to LMO matrix with ratio La/Mn~1. It is noticeable the absence of La inside the inclusions. The analyses of HRTEM images of these nanopillars indicate that manganese oxide has a spinel crystal structure (compatible with Mn₃O₄) with interplanar distances of 5.2 Å in-plane and of 9.2 Å out-of-plane. Further confirmation that nanoinclusions may be associated to Mn₃O₄ phase was obtained by studying the oxygen coordination by EELS. **Figure 6D** shows the oxygen K edge EELS spectrum obtained at the nanoinclusions. By comparing this result with the EELS spectrum series of the manganese oxides reported in literature, the best agreement is found for the Mn₃O₄ phase [55, 56].

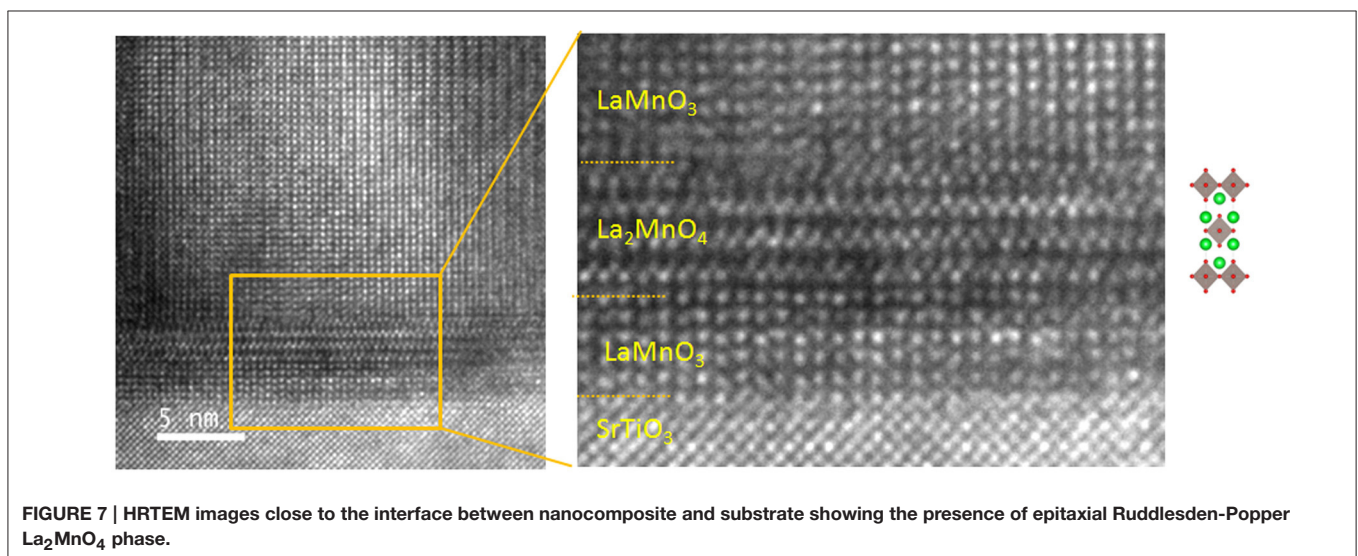
With respect to the perovskite substrate, all precipitates exhibit a similar crystallographic orientation that may be understood in terms of a distorted cubic spinel. Epitaxy may be defined as (001)-oriented cube-on-diagonal (i.e., in-plane rotation of 45°) but with a slight c-axis tilting of 9°, in agreement with the above x-ray diffraction results. HRTEM images (**Figure 6**) also show that interfaces between LMO and Mn₃O₄ inclusions are not flat, making difficult to define any contact plane. We should note that zig-zag interfaces between Mn₃O₄ films and manganese perovskite films (in that case La_{0.7}Sr_{0.3}MnO₃) have been previously reported [57], suggesting a tendency in this system to avoid flat interfaces. Nevertheless, statistical analysis shows a tendency to form angles of 35 and 10° with the vertical at both sides of the inclusion. These angles are independent of the surrounding LMO orientation. This suggests

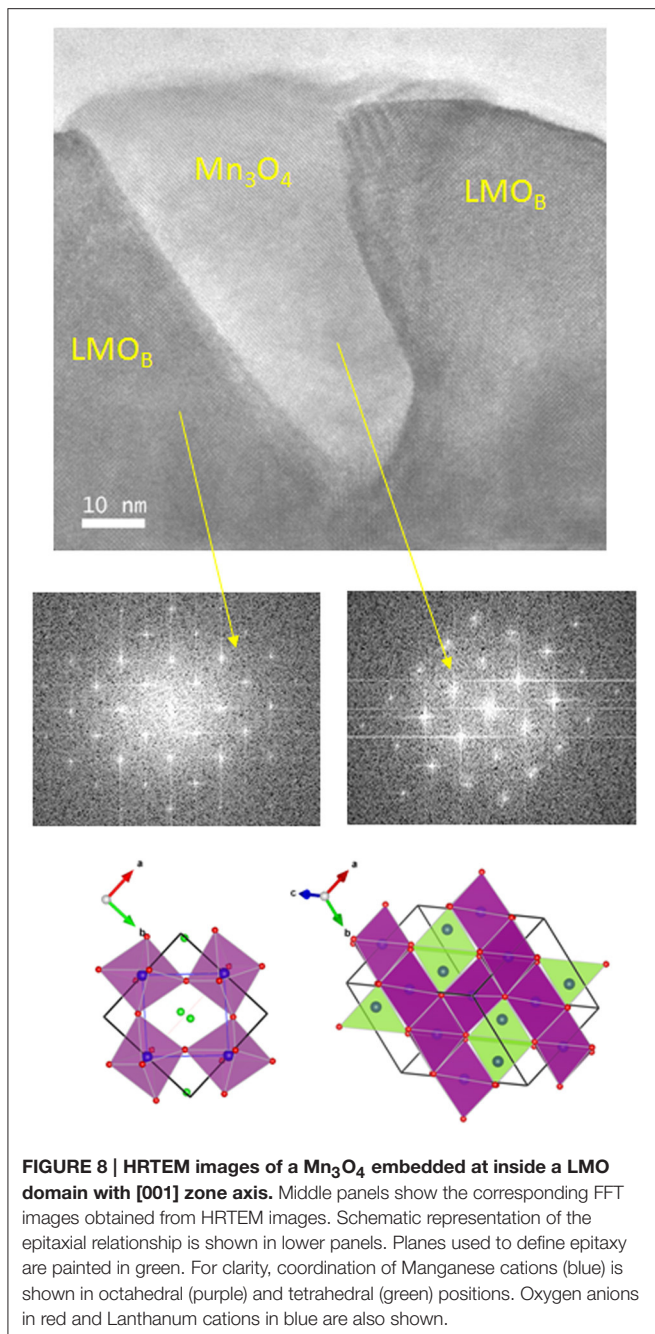
that shape of the inclusions is completely determined during nucleation and growth at the high temperature stage, regardless of their relative orientation with the twinned LMO domains formed during cooling. The other relevant feature identified by HRTEM images and spectroscopy (EDS and EELS) analysis is the presence of an epitaxial (001)-oriented layer of a La-rich secondary phase. This layer is not directly at the interface with the substrate but embedded in the LMO matrix (see **Figure 7**). This secondary phase, of around 2–4 nm thick, has interplanar distances of 3.94 Å in-plane and 13.5 Å out-of-plane and may correspond to the rarely observed Ruddlesden-Popper La₂MnO₄ phase [14].

The presence of twin domains in LMO has been also confirmed by cross-section analyses as two different orientations of LMO were identified, i.e., if zone axis is [001]_{LMO} (noted as LMO_B) or [110]_{LMO} (noted as LMO_A). As the Mn₃O₄ inclusions are significantly elongated, especially for LMO grown on STO (aspect ratio ~1.7) it is interesting to determine the relative orientation of their long side with respect to the LMO matrix axis. Surprisingly, we have only observed Mn₃O₄ inclusions with their long side aligned with [001]_{LMO} (see **Figure 8**) or at the interface between [001]_{LMO} or [110]_{LMO} domains (see **Figure 9**). We have not identified inclusions with long axis fully embedded in [110]_{LMO} domains. The epitaxial orientation of the precipitates was determined by analyzing electron diffraction FFT images (middle panels in **Figures 8, 9**) and by taking hausmannite I₄/amd crystal structure for Mn₃O₄. Although not strictly parallel (disorientations angle between planes are ~1.5–2°) the most accurate description for the corresponding epitaxial relationships are the following:



The lower panels in **Figures 8, 9** are schematized representations of both epitaxial relationships where, for clarity, the defining planes are painted in green.





Chemical phase segregation is a complex problem that involves not only thermodynamic stability of the different phases but also kinetic considerations. In general, segregation occurs when the energy cost associated with the creation of new interface and contact area is overcome by the gain in free energy by nucleating a stable secondary phase. Furthermore, in epitaxial thin films, strain associated with the mismatch between lattice parameters of film phases and substrate play an important role and segregates with selected composition may occur to minimize the overall elastic energy of the film. Previous investigations have demonstrated that such mechanism may explain the

occurrence of a three phase oxide manganese nanocomposite similar to our present case [58–60]. In those works, stoichiometry unbalance caused by the spontaneous outcropping of La-Sr-O islands during the growth of La_{1-x}Sr_xMnO₃ (LSMO) films is compensated by the appearance of a Sr₃Mn₂O₇ Ruddlesden-Popper phase. The main difference in our present study is that LMO films are almost relaxed while formation of La-Sr-O islands helped to maintain LSMO fully strained state. Thus, in LMO films, the energy gain associated with reducing the overall elastic energy of the nanocomposite should be less important than the thermodynamic tendency to form Mn²⁺ ions. It is worth noting that outcropping of secondary phase islands toward the surface of the film is governed by misfit relaxation mechanisms and the resulting topological distribution depends on film thickness and kinetic effects [59]. As a consequence, secondary phases well embedded in the matrix or outcropped toward the surface could just reflect different evolution stages of a similar segregation mechanism.

We have mentioned above that phase diagram of manganese oxides indicates a strong tendency of manganese to adopt an oxidation state of Mn²⁺ in the vacuum conditions (residual oxygen) used to grow the LMO films. The crystal radius of Mn²⁺ in octahedral coordination is 0.97 Å and, attending to the cation radius and the Goldschmidt tolerance factor for perovskites, it could be feasible for Mn to occupy the La site (La³⁺ radius being 1.172 Å) in the LMO perovskite up to the solubility ratio [14]. This mechanism has been reported for La-deficient thin films [61, 62] but, in stoichiometric films should lead to the formation of La-based oxides as La₂O₃ [14] not present in our films. Furthermore, TEM and Raman measurements suggest that LMO matrix preserves [La]/[Mn] ~ 1. Thus, in the present case, the main mechanism to accommodate Mn²⁺ ions is to form Mn₃O₄ segregates (i.e., Mn²⁺[Mn³⁺]₂O₄) and the creation of a La-rich phase as the observed La₂MnO₄ phase helps to compensate the stoichiometry unbalance. It is very likely that Mn₃O₄ particles are formed on LMO films during growth process. At that stage, cube-on-cube nucleation of the Mn₃O₄ spinel on the metrically cubic LMO is plausible. The crystallite Mn₃O₄ shape may now be seen as a reminiscence or truncated form of the typical octahedral crystal shape of spinels where {111} surfaces (forming an angle of ~35° with the vertical) have the lowest surface energy. It is not difficult now to argue that during cooling, when LMO Jahn-Teller transition takes place, Mn₃O₄ accommodates to the surrounding LMO twins by distorting its own structure. The two epitaxial relationships of hausmannite Mn₃O₄ with LMO at room temperature could be just the result of the loss of cubic symmetry, probably linked to distortions originated itself by the Mn³⁺ ion in the octahedral positions of Mn₃O₄. Thus, to fully understand this mechanism, it could be very interesting then to obtain structural information of these nanocomposites at high temperature, namely above T_{JT}.

Temperature dependence at 0.5 T (A) and magnetic field dependence at 10 K

The temperature and the magnetic field dependence of the in-plane magnetization were used to study the effects of the secondary phase on the magnetic properties (Figure 10). The temperature dependence of magnetization (in a magnetic field

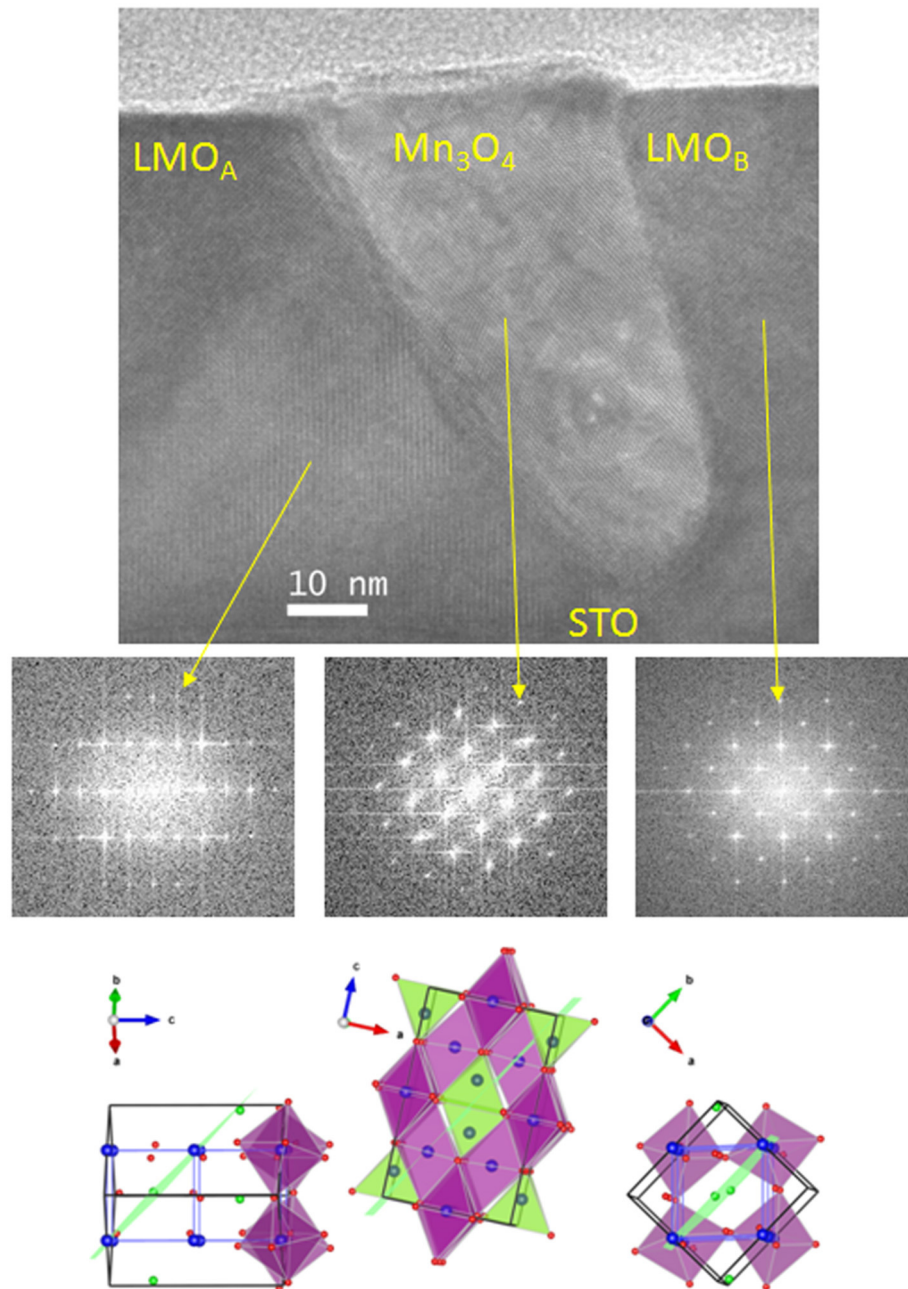
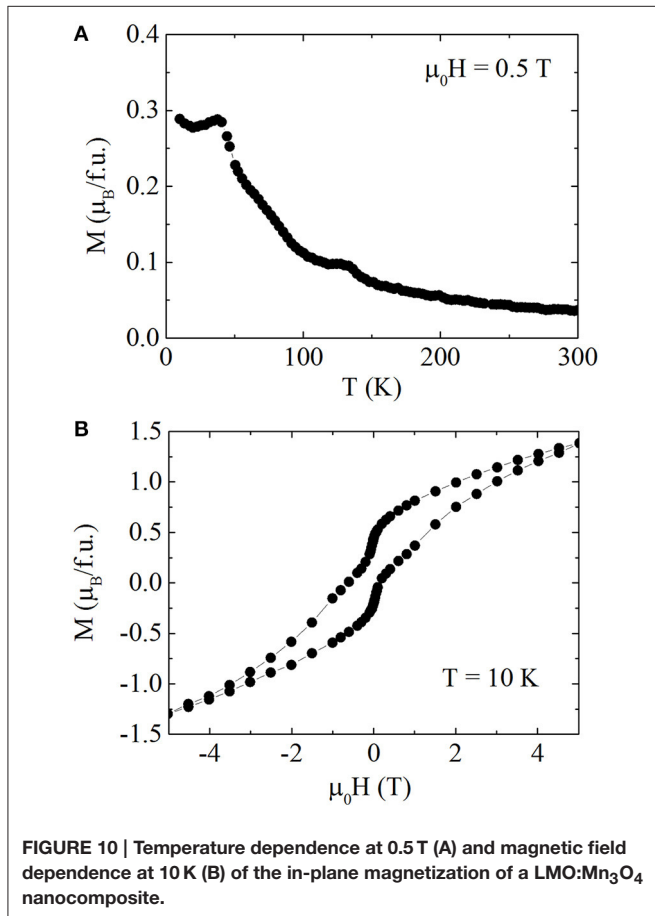


FIGURE 9 | HRTEM images of a Mn_3O_4 embedded at the interface between LMO domains with $[001]$ or $[110]$ zone axis. Middle panels show the corresponding FFT images obtained from HRTEM images. Schematic representation of the epitaxial relationship is shown in lower panels. Planes used to define epitaxy are painted in green. For clarity, coordination of manganese cations (blue) is shown in octahedral (purple) and tetrahedral (green) positions. Oxygen anions in red and Lanthanum cations in blue are also shown.

of 0.1 T) revealed two transitions, the first one is the expected antiferromagnetic transition of LMO at ~ 140 K and the second one is the ferrimagnetic transition of manganese oxide secondary phase at around ~ 40 K (**Figure 10A**). It is known that LMO thin films may exhibit a broad range of magnetic behaviors, from antiferromagnetic to strongly ferromagnetic, depending on the preparation conditions [27]. In our case, films are prepared

in vacuum conditions leading to a residual moment below $0.3 \mu_B/\text{f.u.}$ at 10 K which approaches the bulk value reported in the literature [63]. This residual magnetization is usually associated to a canted antiferromagnetic structure (magnetic moments pointing along b-axis but at a small angle out of ab-plane). The hysteresis loop at 10 K (**Figure 10B**) exhibits typical features observed in loops of thin films composed of soft magnet

with small H_c and hard magnet with larger H_c [12]. However, pure antiferromagnetic LMO thin films shows almost closed hysteresis loop with a very small coercive field H_c that is usually associated to the existence of uncompensated spins at interfaces. On the other hand, manganese oxide with spinel structure is a hard ferrimagnetic with large values of $\mu_0 H_c \sim 0.35$ T [64], whose presence in LMO matrix enlarges loop shape in our system comparing with pure undoped manganite compound.

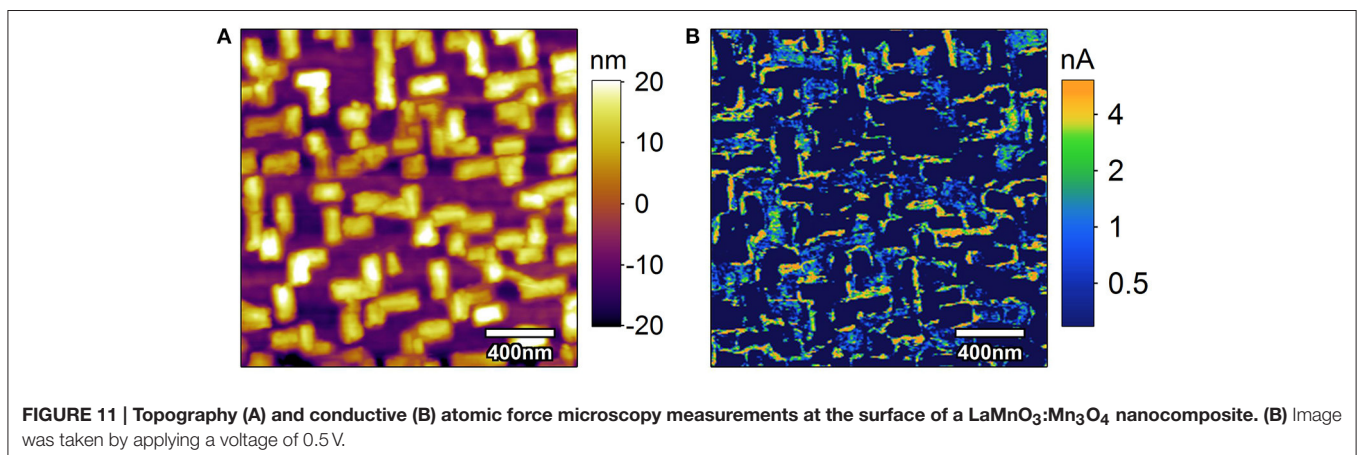


The presence of disordered phase boundaries between LMO and Mn₃O₄ and the larger vertical strain could additionally increase the pinning effects and coercivity in thin films [11].

Effects of secondary phase are revealed also by the local transport measurements shown in **Figure 11**. Characterization is performed by conductive AFM (cAFM) which senses the current flowing from a metallic probe to Pt electrodes deposited on top of the sample. The Mn₃O₄ secondary phase is highly insulating. However, we observe large spatial differences of the current distribution within the LMO matrix. The overall LMO primary phase in regions between inclusions shows some conduction of the order of few nA for an applied voltage of 0.5 V. Particularly, we observe that conduction is enhanced at the interface region of LMO in close proximity to the inclusions (up to a factor of 10 in these experimental conditions). Moreover, it seems that we observe that not all the four sides of each inclusion are equally conductive. This fact could be supported by TEM cross section images in **Figures 6–9**, showing that nanostructures exhibit a quite asymmetrical shape and thus, conduction could be differently affected at both sides of the inclusion. The driving force for the enhanced conductivity at these interfaces is far from being understood. Several mechanisms are known to increase electrical conductivity of LMO films as, for example, cationic vacancies or oxygen diffusion. Also, the effect on electrical conductivity of local strain fields is quite relevant in oxide thin films and it cannot be disregarded to explain the results in **Figure 11**. However, a deeper study of the transport mechanisms is beyond the scope of this manuscript.

CONCLUSIONS

In conclusion, we report the formation of self-organized Mn₃O₄ nanocolumns in Pulsed Laser Deposited LaMnO₃ films. We show that under vacuum growth conditions there is a strong tendency to form Mn²⁺ cations leading to the segregation of wedge-like Mn₃O₄ inclusions aligned with the main axis of the substrate. Formation mechanism at high temperatures (850°C) may be understood by considering that Mn₃O₄ nucleate directly



on the nearly cubic LMO matrix. The final epitaxial relationship is determined by the subsequent Jahn-Teller transition that takes place during cooling creating LMO domains and twins and it may be defined as a distorted cubic spinel with *c*-axis slightly tilted from the direction perpendicular to the film plane. Partial accommodation of off-stoichiometry and residual strain may be achieved by the creation of an epitaxial La-rich Ruddlesden-Popper La₂MnO₄ phase close to the interface with the substrate. The magnetic and transport properties of the nanocomposite are strongly modified by the presence of the inclusions. In particular, an enhanced coercivity together with an increase of local conductivity close to the insulating inclusions has been observed. Our results demonstrate an easy single-step route for the preparation of nanocomposite thin films with tuned functional properties consisting of self-assembled ordered nanostructures embedded in a matrix that still preserves its structural characteristics.

AUTHORS CONTRIBUTIONS

AP, ZK, and JS led the research, data interpretation and manuscript preparation. NL, MS, and ZP were responsible for Raman results. NB, FS, and JS were responsible for

microstructural analysis. LL, LB, AP, ZK, NM, CF, and BM contributed to the initial structural characterization and to the magnetic and *c*-AFM measurements. JR, AG, AP, and JS were responsible for sample preparation. AP was responsible for preparing the final version of the manuscript that includes the inputs and comments of all the authors.

ACKNOWLEDGMENTS

Financial support from the Spanish Ministry of Economy and Competitiveness, through the “Severo Ochoa” Program for Centres of Excellence in R&D (SEV-2015-0496 and SEV 2013-0295), Projects MAT2011-29081 and MAT2015-71664-R and Ministry of Education and Science of Serbia (Grant—III45018) is acknowledged. This work has received funding from the European Union’s Horizon 2020 research and innovation programme under the Marie Skłodowska-Curie grant agreement No. 645658 (DAFNEOX Project). AP thanks hospitality from Senzor-INFIZ d.o.o. where the first draft of this manuscript was written. NB thanks the Spanish MINECO for financial support through the FPI program. We thank R.E.A. Williams and D.W. McComb (CEMAS, The Ohio State University) for assistance and support in Dual-EELS experiments.

REFERENCES

- Choi WS, Kwon JH, Jeon H, Hamann-Borrero JE, Radi A, Macke S, et al. Strain-induced spin states in atomically ordered cobaltites. *Nano Lett.* (2012) **12**:4966–70. doi: 10.1021/nl302562f
- Vaz CAF. Electric field control of magnetism in multiferroic heterostructures. *J Phys Condens Matter* (2012) **24**:333201. doi: 10.1088/0953-8984/24/33/333201
- Pomar A, Santiso J, Sandiumenge F, Roqueta J, Bozzo B, Frontera C, et al. Growth kinetics engineered magnetoresistance response in La_{2/3}Sr_{1/3}MnO₃ thin films. *Appl Phys Lett.* (2014) **104**:152406. doi: 10.1063/1.4871984
- Sandiumenge F, Bagués N, Santiso J, Paradinas M, Pomar A, Konstantinovic Z, et al. Misfit dislocation guided topographic and conduction patterning in complex oxide epitaxial thin films. *Adv Mater Interfaces* (2016) **3**:1600106. doi: 10.1002/admi.201600106
- García-Barriocanal J, Bruno FY, Rivera-Calzada A, Sefrioui Z, Nemes NM, García-Hernández M, et al. “Charge leakage” at LaMnO₃/SrTiO₃ interfaces. *Adv Mater.* (2010) **22**:627–32. doi: 10.1002/adma.200902263
- Bhattacharya A, May SJ, te Velthuis SGE, Warusawithana M, Zhai X, Jiang B, et al. Metal-insulator transition and its relation to magnetic structure in (LaMnO₃)_{2n}/(SrMnO₃)_n superlattices. *Phys Rev Lett.* (2008) **100**:257203. doi: 10.1103/PhysRevLett.100.257203
- Gibert M, Zubko P, Scherwitzl R, Íñiguez J, Triscone JM. Exchange bias in LaNiO₃-LaMnO₃ superlattices. *Nat Mater.* (2012) **11**:195–8. doi: 10.1038/nmat3224
- MacManus-Driscoll JL. Self-assembled heteroepitaxial oxide nanocomposite thin film structures: designing interface-induced functionality in electronic materials. *Adv Funct Mater.* (2010) **20**:2035–45. doi: 10.1002/adfm.201000373
- Moshnyaga V, Damaschke B, Shapoval O, Belenchuk A, Faupel J, Lebedev OI, et al. Structural phase transition at the percolation threshold in epitaxial (La_{0.7}Ca_{0.3}MnO₃)_{1-x}:(MgO)_x nanocomposite films. *Nat Mater.* (2003) **2**:247–52. doi: 10.1038/nmat859
- Aiping C, Zhenxing B, Harshad H, Xinghang Z, Qing S, Li C, et al. Microstructure, magnetic, and low-field magnetotransport properties of self-assembled (La_{0.7}Sr_{0.3}MnO₃)_{0.5}:(CeO₂)_{0.5} vertically aligned nanocomposite thin films. *Nanotechnology* (2011) **22**:315712. doi: 10.1088/0957-4484/22/31/315712
- Chen A, Bi Z, Tsai CF, Lee J, Su Q, Zhang X, et al. Tunable low-field magnetoresistance in (La_{0.7}Sr_{0.3}MnO₃)_{0.5}:(ZnO)_{0.5} self-assembled vertically aligned nanocomposite thin films. *Adv Funct Mater.* (2011) **21**:2423–9. doi: 10.1002/adfm.201002746
- Mukherjee D, Bingham N, Hordagoda M, Phan MH, Srikanth H, Witanachchi S, et al. Influence of microstructure and interfacial strain on the magnetic properties of epitaxial Mn₃O₄/La_{0.7}Sr_{0.3}MnO₃ layered-composite thin films. *J Appl Phys.* (2012a) **112**:083910. doi: 10.1063/1.4759237
- Jian H, Zhang Z, Wang Y, Tang X, Yang J, Hu L, et al. Preparation of La_{0.7}Sr_{0.3}Mn_{1+x}O_y (1 < x < 4) thin films by chemical solution deposition: dual epitaxy and possible spinodal growth. *J Alloys Compd.* (2013) **561**:95–100. doi: 10.1016/j.jallcom.2013.02.004
- Grundy AN, Chen M, Hallstedt B, Gauckler LJ. Assessment of the La-Mn-O system. *J Phase Equilib Diff.* (2005) **26**:131–51. doi: 10.1007/s11669-005-0132-2
- Joy PA, Sankar CR, Date SK. The limiting value of x in the ferromagnetic compositions La_{1-x}MnO₃. *J Phys Condens Matter* (2002) **14**:L663. doi: 10.1088/0953-8984/14/39/104
- Dezanneau G, Audier M, Vincent H, Meneghini C, Djurado E. Structural characterization of La_{1-x}MnO_{3±δ} by x-ray diffraction and x-ray absorption spectroscopy. *Phys Rev B* (2004) **69**:11. doi: 10.1103/PhysRevB.69.014412
- Bosak A, Dubourdieu C, Audier M, Sénateur JP, Pierre J. Compositional effects on the structure and magnetotransport properties of lacunar La_{1-x}MnO_{3-δ} films (x>0) grown by MOCVD. *Appl Phys A* (2004) **79**:1979–84. doi: 10.1007/s00339-003-2179-4
- Jehanathan N, Lebedev O, Gelard I, Dubourdieu C, Van Tendeloo G. Structure and defect characterization of multiferroic ReMnO₃ films and multilayers by TEM. *Nanotechnology* (2010) **21**:075705. doi: 10.1088/0957-4484/21/7/075705
- Gelard I, Jehanathan N, Roussel H, Gariglio S, Lebedev OI, Van Tendeloo G, et al. Off-stoichiometry effects on the crystalline and defect structure of hexagonal manganite REMnO₃ films (RE = V, Er, Dy). *Chem Mater.* (2011) **23**:1232–8. doi: 10.1021/cm1029358
- Wunderlich R, Chliotte C, Bridoux G, Maity T, Kocabiyyik O, Setzer A, et al. Structural, magnetic and electric properties of HoMnO₃ films on SrTiO₃(001).

- J Magn Magn Mater.* (2012) **324**:460–5. doi: 10.1016/j.jmmm.2011.08.021
21. Tian ZR, Tong W, Wang JY, Duan NG, Krishnan VV, Suib SL. Manganese oxide mesoporous structures: mixed-valent semiconducting catalysts. *Science* (1997) **276**:926–30. doi: 10.1126/science.276.5314.926
 22. Zhang L, Zhou Q, Liu Z, Hou X, Li Y, Lv Y. Novel Mn₃O₄ micro-octahedra: promising cataluminescence sensing material for acetone. *Chem Mater.* (2009) **21**:5066–71. doi: 10.1021/cm901369u
 23. Najafpour MM, Holynska M, Salimi S. Applications of the “nano to bulk” Mn oxides: Mn oxide as a Swiss army knife. *Coord Chem Rev.* (2015) **285**:65–75. doi: 10.1016/j.ccr.2014.11.001
 24. Najafpour MM, Renger G, Holynska M, Moghaddam AN, Aro EM, Carpentier R, et al. Manganese compounds as water-oxidizing catalysts: from the natural water-oxidizing complex to nanosized manganese oxide structures. *Chem Rev.* (2016) **116**:2886–936. doi: 10.1021/acs.chemrev.5b00340
 25. Huang Q, Santoro, A, Lynn JW, Erwin RW, Borchers JA, Peng JL, et al. Structure and magnetic order in undoped lanthanum manganite. *Phys Rev B* (1997) **55**:14987–99. doi: 10.1103/PhysRevB.55.14987
 26. Ritter C, Ibarra MR, De Teresa JM, Algarabel PA, Marquina C, Blasco J, et al. Influence of oxygen content on the structural, magnetotransport, and magnetic properties of LaMnO_{3+δ}. *Phys Rev B* (1997) **56**:8902–11. doi: 10.1103/PhysRevB.56.8902
 27. Roqueta J, Pomar A, Balcells L, Frontera C, Valencia S, Abrudan R, et al. Strain-engineered ferromagnetism in LaMnO₃ thin films. *Cryst Growth Des.* (2015) **15**:5332–7. doi: 10.1021/acs.cgd.5b00884
 28. Marton Z, Seo SSA, Egami T, Lee HN. Growth control of stoichiometry in LaMnO₃ epitaxial thin films by pulsed laser deposition. *J Cryst Growth* (2010) **312**:2923–7. doi: 10.1016/j.jcrysgro.2010.07.013
 29. Marozau I, Das PT, Dobeli M, Storey JG, Uribe-Laverde MA, Das S, et al. Influence of La and Mn vacancies on the electronic and magnetic properties of LaMnO₃ thin films grown by pulsed laser deposition. *Phys Rev B* (2014) **89**:174422. doi: 10.1103/PhysRevB.89.174422
 30. Kim SH, Choi BJ, Lee GH, Oh SJ, Kim B, Choi HC, et al. Ferrimagnetism in γ -manganese sesquioxide (γ -Mn₂O₃) nanoparticles. *J Korean Phys Soc.* (2005) **46**:941. doi: 10.3938/jkps.46.491
 31. Fritsch S, Navrotsky A. Thermodynamic properties of manganese oxides. *J Am Ceram Soc.* (1996) **79**:1761–8. doi: 10.1111/j.1151-2916.1996.tb07993.x
 32. Grant RW, Geller S, Cape JA, Espinosa GP. Magnetic and crystallographic transitions in α -Mn₂O₃-Fe₂O₃ system. *Phys Rev.* (1968) **175**:686. doi: 10.1103/PhysRev.175.686
 33. Boucher B, Buhl R, Perrin M. Magnetic structure of Mn₃O₄ by neutron diffraction. *J Appl Phys.* (1971) **42**:1615–7. doi: 10.1063/1.1660364
 34. Radler MJ, Cohen JB, Sykora GP, Mason T, Ellis DE, Faber J. The defect structures of Mn_{1-x}O. *J Phys Chem Solids* (1992) **53**:141–54. doi: 10.1016/0022-3697(92)90022-6
 35. Aminoff G. On the crystal structure of hausmannite (MnMn₂O₄). *Z Kristallogr.* (1926) **64**:475–90.
 36. Baron V, Gutzmer J, Rundlof H, Tellgren R. The influence of iron substitution on the magnetic properties of hausmannite, Mn²⁺(Fe,Mn)₂³⁺O₄. *Am Mineral.* (1998) **83**:786–93. doi: 10.2138/am-1998-7-810
 37. Ross CR, Rubie DC., Paris E. Rietveld refinement of the high-pressure polymorph of Mn₃O₄. *Am Mineral.* (1990) **75**:1249–52.
 38. Gorbenko OY, Samoilenkov SV, Graboy IE, Kaul AR. Epitaxial stabilization of oxides in thin films. *Chem Mater.* (2002b) **14**:4026–43. doi: 10.1021/cm021111v
 39. Kaul AR, Gorbenko OY, Graboy IE, Samoilenkov SV. Epitaxial stabilization of oxide phases in thin film growth. In: Guilloux-Viry M, Perrin A, editors. *Cryst Growth Thin Solid Films*. Trivandrum: Research SignPost (2002), 265–94.
 40. Gorbenko OY, Graboy IE, Amelichev VA, Bosak AA, Kaul AR, Guttler B, et al. The structure and properties of Mn₃O₄ thin films grown by MOCVD. *Solid State Commun.* (2002a) **124**:15–20. doi: 10.1016/S0038-1098(02)00470-2
 41. Bi Z, Weal E, Luo H, Chen A, MacManus-Driscoll JL, Jia Q, et al. Microstructural and magnetic properties of (La_{0.7}Sr_{0.3}MnO₃)_{0.7}:(Mn₃O₄)_{0.3} nanocomposite thin films. *J Appl Phys.* (2011) **109**:054302. doi: 10.1063/1.3552594
 42. Momma K, Izumi F. VESTA 3 for three-dimensional visualization of crystal, volumetric and morphology data. *J Appl Crystallogr.* (2011) **44**:1272–6. doi: 10.1107/S0021889811038970
 43. Lucas G, Burdet P, Cantoni M, Hebert C. Multivariate statistical analysis as a tool for the segmentation of 3D spectral data. *Micron* (2013) **52**:53:49–56. doi: 10.1016/j.micron.2013.08.005
 44. Bernal S, Botana FJ, Calvino JJ, Lopez-Cartes C, Perez-Omil JA, Rodriguez-Izquierdo JM. The interpretation of HREM images of supported metal catalysts using image simulation: profile view images. *Ultramicroscopy* (1998) **72**:135–64. doi: 10.1016/S0304-3991(98)00009-6
 45. Aruta C, Angeloni M, Balestrino G, Boggio NG, Medaglia PG, Tebano A, et al. Preparation and characterization of LaMnO₃ thin films grown by pulsed laser deposition. *J Appl Phys.* (2006) **100**:023910. doi: 10.1063/1.2217983
 46. Choi WS, Marton Z, Jang SY, Moon SJ, Jeon BC, Shin JH, et al. Effects of oxygen-reducing atmosphere annealing on LaMnO₃ epitaxial thin films. *J Phys D Appl Phys.* (2009) **42**:165401. doi: 10.1088/0022-3727/42/16/165401
 47. Orgiani P, Aruta C, Ciancio R, Galdi A, Maritato L. Enhanced transport properties in La_xMnO_{3-δ} thin films epitaxially grown on SrTiO₃ substrates: the profound impact of the oxygen content. *Appl Phys Lett.* (2009) **95**:013510. doi: 10.1063/1.3168649
 48. Kim HS, Christen HM. Controlling the magnetic properties of LaMnO₃ thin films on SrTiO₃(100) by deposition in a O₂/Ar gas mixture. *J Phys Condens Matter* (2010) **22**:146007. doi: 10.1088/0953-8984/22/14/146007
 49. Choi WS, Jeong DW, Jang SY, Marton Z, Seo SSA, Lee HN, et al. LaMnO₃ thin films grown by using pulsed laser deposition and their simple recovery to a stoichiometric phase by annealing. *J Korean Phys Soc.* (2011) **58**:569–74. doi: 10.3938/jkps.58.569
 50. Rodriguez-Carvajal J, Hennion M, Moussa F, Moudden AH, Pinsard L, Revcolevschi A. Neutron-diffraction study of the Jahn-Teller transition in stoichiometric LaMnO₃. *Phys Rev B*(1998) **57**:R3189–92. doi: 10.1103/PhysRevB.57.R3189
 51. Iliiev MN, Abrashev MV, Lee HG, Popov VN, Sun YY, Thomsen C, et al. Raman spectroscopy of orthorhombic perovskitelike YMnO₃ and LaMnO₃. *Phys Rev B* (1998) **57**:2872–7. doi: 10.1103/PhysRevB.57.2872
 52. Iliiev MN, Abrashev MV. Raman phonons and Raman Jahn-Teller bands in perovskite-like manganites. *J Raman Spectrosc.* (2001) **32**:805–11. doi: 10.1002/jrs.770
 53. Zuo J, Xu CY, Liu YP, Qian YT. Crystallite size effects on the Raman spectra of Mn₃O₄. *Nanostruct Mater.* (1998) **10**:1331–5. doi: 10.1016/S0965-9773(99)00002-1
 54. Julien CM, Massot M, Poinssignon C. Lattice vibrations of manganese oxides. Part I. *Periodic structures. Spectrochim Acta Part A Mol Biomol Spectrosc.* (2004) **60**:689–700. doi: 10.1016/S1386-1425(03)00279-8
 55. Kurata H, Colliex C. Electron-energy-loss core-edge structures in manganese oxides. *Phys Rev B* (1993) **48**:2102–8. doi: 10.1103/PhysRevB.48.2102
 56. Tan HY, Verbeeck J, Abakumov A, Van Tendeloo G. Oxidation state and chemical shift investigation in transition metal oxides by EELS. *Ultramicroscopy* (2012) **116**:24–33. doi: 10.1016/j.ultramic.2012.03.002
 57. Mukherjee D, Bingham N, Phan MH, Srikanth H, Mukherjee P, Witanachchi S. Zig-zag interface and strain-influenced ferromagnetism in epitaxial Mn₃O₄/La_{0.7}Sr_{0.3}MnO₃ thin films grown on SrTiO₃ (100) substrates. *J Appl Phys.* (2012b) **111**:3. doi: 10.1063/1.3680531
 58. Moreno C, Abellan P, Hassini A, Ruyter A, Perez del Pino A, Sandiumenge F, et al. Spontaneous outcropping of self-assembled insulating nanodots in solution-derived metallic ferromagnetic La_{0.7}Sr_{0.3}MnO₃ films. *Adv Funct Mater.* (2009) **19**:2139–46. doi: 10.1002/adfm.200900095
 59. Abellan P, Moreno C, Sandiumenge F, Obradors X, Casanove MJ. Misfit relaxation of La_{0.7}Sr_{0.3}MnO₃ thin films by a nanodot segregation mechanism. *Appl Phys Lett.* (2011) **98**:041903. doi: 10.1063/1.3549182
 60. Moreno C, Abellan P, Sandiumenge F, Casanove MJ, Obradors X. Nanocomposite lanthanum strontium manganite thin films formed by using a chemical solution deposition. *Appl Phys Lett.* (2012) **100**:023103. doi: 10.1063/1.3675461

61. Orgiani P, Galdi A, Aruta C, Cataudella V, De Filippis G, Perroni CA, et al. Multiple double-exchange mechanism by Mn^{2+} doping in manganite compounds. *Phys Rev B* (2010) **82**:205122. doi: 10.1103/PhysRevB.82.205122
62. Orgiani P, Aruta C, Ciancio R, Galdi A, Maritato L. Synthesis and properties of highly metallic orbital-ordered A-site manganites. *J Nanopart Res.* (2013) **15**:1655. doi: 10.1007/s11051-013-1655-9
63. Topfer J, Goodenough JB. $\text{LaMnO}_{3+\delta}$ revisited. *J Solid State Chem.* (1997) **130**:117–28.
64. Guo LW, Peng DL, Makino H, Inaba K, Ko HJ, Sumiyama K, et al. Structural and magnetic properties of Mn_3O_4 films grown on $\text{MgO}(0\ 0\ 1)$ substrates by plasma-assisted MBE. *J Magn Magn Mater.* (2000) **213**:321–5. doi: 10.1016/S0304-8853(00)00008-1

Conflict of Interest Statement: The authors declare that the research was conducted in the absence of any commercial or financial relationships that could be construed as a potential conflict of interest.

Copyright © 2016 Pomar, Konstantinović, Bagués, Roqueta, López-Mir, Balcells, Frontera, Mestres, Gutiérrez-Llorente, Šćepanović, Lazarević, Popović, Sandiumenge, Martínez and Santiso. This is an open-access article distributed under the terms of the Creative Commons Attribution License (CC BY). The use, distribution or reproduction in other forums is permitted, provided the original author(s) or licensor are credited and that the original publication in this journal is cited, in accordance with accepted academic practice. No use, distribution or reproduction is permitted which does not comply with these terms.

Transport properties of $\text{La}_{2/3}\text{Sr}_{1/3}\text{MnO}_3/\text{LaAlO}_3/\text{Pt}$ tunnel junctions

R. Galceran, Ll. Balcells, A. Pomar, Z. Konstantinović, F. Sandiumenge, and B. Martínez
Instituto de Ciencia de Materiales de Barcelona - CSIC, Campus UAB, Bellaterra 08193, Spain

(Received 12 December 2014; accepted 27 February 2015; published online 12 March 2015)

Magnetotransport properties of $\text{La}_{2/3}\text{Sr}_{1/3}\text{MnO}_3/\text{LaAlO}_3/\text{Pt}$ tunnel junctions have been thoroughly analyzed, as a function of temperature and magnetic field, to test the suitability of LaAlO_3 for insulating barriers and spin injection processes. The insulating behavior of LaAlO_3 maintained down to 1–2 nm (corresponding to 4–5 unit cells) renders this material useful as tunnel barrier. The temperature dependence of the junction resistance, $R(T)$, down to 200 K confirms direct tunneling as the dominant conduction channel. The barrier parameters of the junctions, ϕ_0 and s , are estimated using Simmons' model in the intermediate voltage range. The energy of the barrier was estimated to be $\phi_0 \sim 0.4$ eV at room temperature. The dependence of $R(T)$ and ϕ_0 on the magnetic field shows an anisotropic tunneling magnetoresistance of $\sim 4\%$ at low T when changing the direction of the magnetization with respect to the current flow. © 2015 AIP Publishing LLC.
[\[http://dx.doi.org/10.1063/1.4914412\]](http://dx.doi.org/10.1063/1.4914412)

INTRODUCTION

The ever increasing demand for massive information storage and high speed management of the information has boosted the search for new nonvolatile memory devices in the last decade. Magnetic random access memories (MRAM) based on magnetic tunneling junctions (MTJ) have been proposed as one of the most solid candidates because they combine alternatives based on new materials and/or new architectures.¹ However, in spite of the intense work already done, some technical challenges, such as the uniformity of the magnetic properties of the electrodes, the insulating barrier uniformity or the thermal stability, are still not fully resolved.² Among the different attempts made to surpass these challenges, the increase in the magnitude of the tunneling magnetoresistance (TMR) response by using half-metallic materials as electrodes has been profusely investigated.^{3–6} Nevertheless, only in the cases of optimized junctions based on manganite electrodes, such as $\text{La}_{2/3}\text{A}_{1/3}\text{MnO}_3$ ($\text{A} = \text{Sr}, \text{Ca}$), TMR values of several hundred percent have been reported so far^{7–10} but, unfortunately those TMR values become vanishing small well below room temperature.^{7,8,11,12} Among manganites, $\text{La}_{2/3}\text{Sr}_{1/3}\text{MnO}_3$ (LSMO), with the highest Curie temperature ($T_C \sim 370$ K) of this family of materials, is the most interesting one for the implementation of devices. For this reason, the interface between LSMO and various insulating materials has been studied.^{13–15} Since tunneling current depends mainly on two factors, i.e., the electronic structure of the barrier, as illustrated by recent results on MgO-based MTJs,¹⁶ and the electronic properties of the electrode/barrier interfaces,¹⁷ many efforts have been devoted to study the properties of these interfaces.^{15,18–20} However, this is not an easy task to do because interfaces are buried below several nanometers of material of the upper electrode, thus requiring the use of interface-selective probing techniques. High-resolution transmission electron microscopy (HRTEM) jointly with electron energy loss spectroscopy (EELS) has been used to investigate manganite-oxide interfaces^{21–23} aimed to determine not only

the chemical composition of the interface areas but also the effect of the neighboring atoms on their electronic structure. On the other hand, surface, element-, and magnetic sensitive x-ray spectroscopy techniques have also been used to clarify the microscopic origin of the depression of the magnetotransport properties at the interfaces.^{20,21,24,25} While these techniques may offer a profound and accurate vision of the different physical and chemical aspects of the electrode/insulating barrier interface, they either require a complex sample preparation or are expensive and not of easy access. To overcome these challenges, direct transport measurements across the interfaces may offer a very interesting alternative especially suitable for tunneling barrier characterization aimed at technological applications.

In this work, we board the characterization of LaAlO_3 (LAO) insulating barriers and their behavior as a function of temperature and applied magnetic field with the aim to clarify the potential of this material as a tunnel barrier for efficient spin injection. For this purpose, magnetotransport properties across the LSMO/LAO/Pt heterostructure will be studied. LAO is a high- k dielectric with a broad band gap and a band offset with Si of about 1.8 eV, which renders it one of the ideal materials for spin injection into semiconductors.²⁶ However, for obtaining efficient spin injection, it is of major relevance to distinguish between electrical spin injection and impurity-driven effects in the tunnel barrier. On the other hand, LAO has a perovskite structure; thus, it is structurally compatible with many other functional oxides, such as manganites, ferroelectrics, and superconductors. In addition, LAO capping has demonstrated to be less harmful for the magnetic and electronic properties of LSMO than other oxides, such as SrTiO_3 or MgO.^{13,19,20} It has also been shown that the temperature dependence of spin polarization of LSMO with LAO capping resembles that of the magnetization $M(T)$, but with lower critical temperature.¹⁵

The conduction across the LAO layer exhibits typical parabolic I-V curves expected for a tunneling process. However, the temperature dependence of the LSMO/LAO/Pt

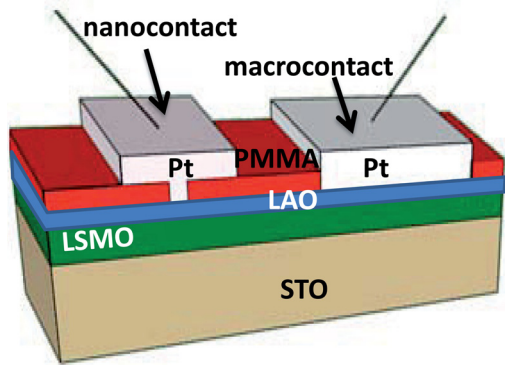


FIG. 1. Sketch of the experimental setup used for measuring the transport properties of the LSMO/LAO/Pt tunnel junctions.

heterostructure suggests that different parallel conduction channels other than ideal spin-dependent tunneling may be present. The analysis of I - V curves using the Simmons model allows us to estimate the barrier energy that results $\varphi_0 \sim 0.4$ eV at room temperature, and to study its dependence on temperature and magnetic field.

RESULTS AND DISCUSSION

LSMO/LAO bilayers have been prepared by using RF-magnetron sputtering on top of (001)-oriented SrTiO₃ substrates treated before deposition to select a unique atomic termination likely to be TiO₂.²⁷ LSMO epitaxial thin film of about 40 nm thick has been prepared at a deposition temperature $T_D = 900$ °C and a pressure of 250 mTorr (20% O₂), and then annealed for 1 h at the same temperature and an oxygen pressure of 350 Torr. A LAO layer of about 1.5 nm was deposited on top of the LSMO film at $T_D = 800$ °C and a pressure of 250 mTorr (20% O₂). For the fabrication of the junctions, samples were covered with a layer of polymethyl methacrylate (PMMA) resist (~ 200 nm thick) by spin coating, and electron beam lithography was used to define a series of square holes of areas ranging from 0.01 to 100 μm^2 in the PMMA resist (see Fig. 1). After developing, a photo-sensitized oxidation process (UVO) cleanse, in which the contaminant molecules of photo resists, resins, human skin

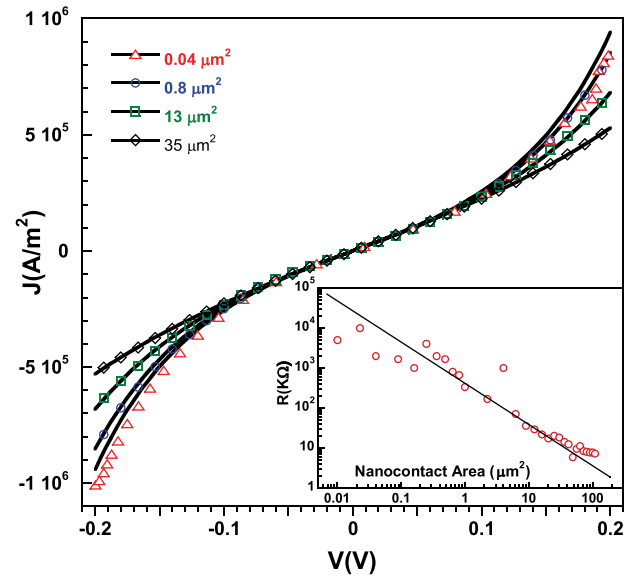


FIG. 3. I - V curves corresponding to LSMO/LAO/Pt tunnel junctions with different areas. Inset: Resistance of the LSMO/LAO/Pt junction as a function of the area.

oils, etc., are excited and/or dissociated by the absorption of short-wavelength UV radiation, was made to ensure a clean LAO surface inside the holes. Without removing the resist, Pt was deposited by evaporation through a shadow mask defining metallic macrocontacts, of about $350 \times 350 \mu\text{m}^2$, precisely on top of the openings of PMMA resist defined by lithography. I - V curves were measured using a two-point configuration, between a large area Pt macrocontact and nanocontacts with different areas, using an external Keithley power supply in a commercial physical properties measurement system (PPMS) by Quantum Design. Measurements were taken as a function of temperature and magnetic field.

The samples are highly crystalline with a STO(001)/LSMO(001)/LAO(001) epitaxial relationship and sharp clean interfaces, as can be seen in Figure 2. Transmission electron microscopy (TEM) images evidence that samples are of excellent nanostructural quality with sharp LSMO/LAO interfaces (see Fig. 2(a)). The surface roughness of LSMO/LAO bilayers, measured by using atomic force microscopy (AFM),

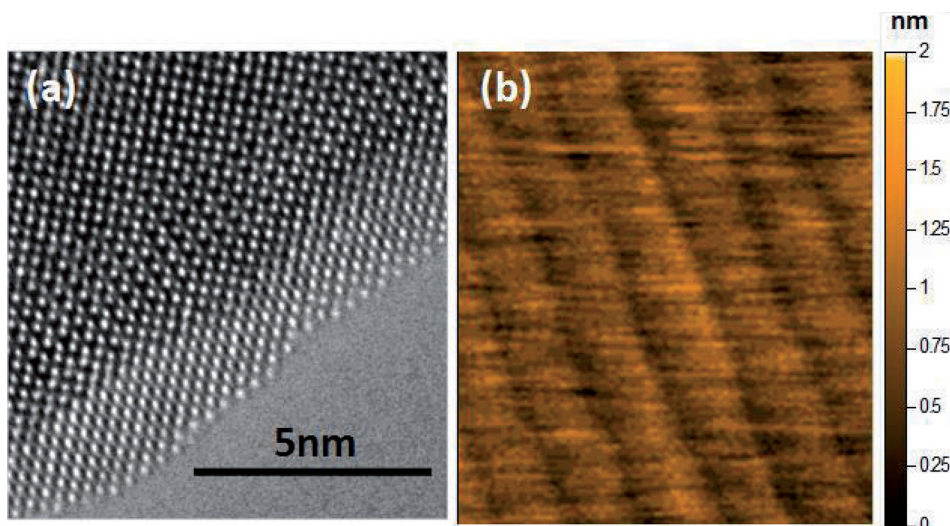


FIG. 2. (a) HRTEM picture of the LSMO/LAO interface. (b) AFM picture of the surface of LSMO/LAO bilayers. LAO layer wets the surface of LSMO completely, exhibiting at the surface a terrace-steps morphology mimicking that of the LSMO surface beneath.

turns out to be very small (root mean square (rms) deviation ~ 0.2 nm), and steps of about 0.4 nm, corresponding to one unit cell, are clearly visible (see Figure 2(b)). LAO layer wets the surface of LSMO completely, exhibiting at the surface terrace-steps morphology mimicking that of the LSMO surface beneath originated from the single termination of the STO substrate. TEM images corroborate that the thickness of the LAO layer is of about 1.5 nm in good agreement with the estimation from growth rate.

I-V curves exhibit the typical features of a tunneling conduction process. Some of them, corresponding to nanocontacts with different areas, are shown in Fig. 3. In the

ohmic region, resistance must be inversely proportional to the nanocontact area. However, as shown in the inset of Fig. 3, this is not fulfilled neither for very small nor for very large area contacts. The former is because for very small contacts, contact areas are ill-defined, while in the latter case, it is because of the non-negligible contribution of the experimental setup to the measured resistance (two contacts, contact resistance contribution $\sim 2\text{--}3$ k Ω). For that reason, in principle, we will take into consideration nanocontacts with areas within the range of $0.2\text{--}40$ μm^2 only.

I-V curves have been analyzed in the intermediate voltage regime by using the Simmons model given by the equation²⁸

$$J = \left(\frac{e}{2\pi\hbar s^2} \right) \left\{ \begin{array}{l} \left(\varphi_0 - \frac{1}{2} eV \right) \exp \left[- (2m)^{1/2} \frac{4\pi s}{\hbar} \left(\varphi_0 - \frac{1}{2} eV \right)^{1/2} \right] - \\ \left(\varphi_0 + \frac{1}{2} eV \right) \exp \left[- (2m)^{1/2} \frac{4\pi s}{\hbar} \left(\varphi_0 + \frac{1}{2} eV \right)^{1/2} \right] \end{array} \right\}, \quad (1)$$

where J is the density of current obtained by dividing the intensities by the area of the different nanocontacts, e and m are the electron charge and mass, respectively, \hbar is Planck's constant, s the effective barrier thickness, φ_0 the energy of the barrier, and V the applied voltage. Some examples of these fits are shown in Fig. 3, while the different values of φ_0 and s corresponding to nanocontacts with different areas are depicted in Fig. 4(a). Assuming a uniform and defects free LAO layer, the obtained φ_0 and s values should be independent of the nanocontact area. However, the figure makes evident that both parameters change when large area nanocontacts are considered. This fact indicates that, as mentioned above, for large area nanocontacts, the non-negligible contribution of the experimental setup resistance to the measured resistance masks the intrinsic properties of the insulating LAO barrier. For that reason, we will limit our study to nanocontacts with area smaller than 5 μm^2 only. Barrier thickness values determined by using Eq. (1) are around $s \approx 2.5$ nm, therefore our analysis yields values for the effective insulating barrier thickness, s , larger by $\Delta s \sim 1$ nm than those corresponding to the nominal thickness determined by growth rate and TEM. This enhancement of the effective barrier thickness has been previously observed in these systems and it is usually attributed to interfacial effects in the LSMO topmost layers.^{18–20} Interfacial effects may be of extrinsic origin, due to a minute amount of secondary phases formed at the interface, or intrinsic, due to the structural disruption and inversion symmetry breaking at the LSMO interface that promote the appearance of an insulating antiferromagnetic slab at the topmost LSMO layers of about 1–2 unit cells. Previous experimental results indicate that intrinsic effects are dominant in LSMO/LAO interfaces.^{19,20} On the other hand, the values obtained for the barrier height, φ_0 , are around 0.4 eV, significantly smaller than the value of the corresponding Schottky barrier between LSMO and

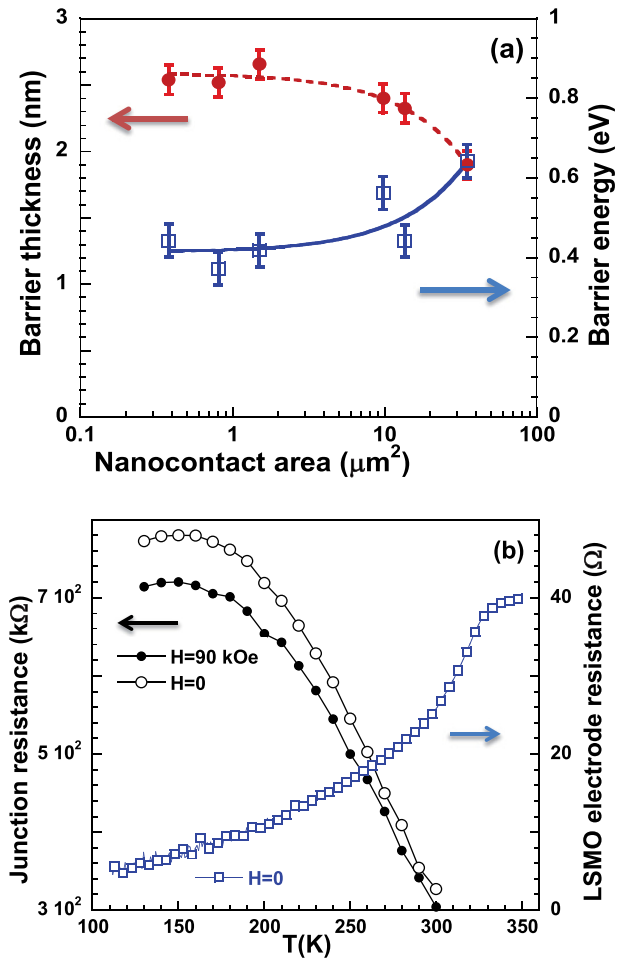


FIG. 4. (a) Barrier thickness and barrier energy for LSMO/LAO/Pt tunnel junctions of different areas obtained from I-V curves by using the Simmons model in intermediate voltage regime. (b) Junction resistance as a function of temperature. The resistance of the LSMO electrode is also shown for comparison.

LAO. The upper limit of the barrier height between LSMO and LAO, i.e., in the Schottky limit, is given by $\phi_0 = W_{\text{LSMO}} - \phi_{\text{LAO}} \sim 2.4$ eV, being W_{LSMO} the work function of LSMO ($W_{\text{LSMO}} \sim 4.9$ eV)²⁹ and ϕ_{LAO} the electron affinity of LAO ($\phi_{\text{LAO}} \sim 2.5$ eV).³⁰ However, this value could be significantly reduced due to the presence of impurities or defects in the LAO barrier and image charge effects.³⁰ Fitting I-V curves by using the Brinkman model³¹ gives similar values for ϕ_0 and S with a small asymmetry parameter, thus indicating I-V curves are substantially symmetric as can be appreciated in Fig. 3. Due to the slimness of the LAO barrier and the procedure to prepare it, the existence of microstructural defects and randomly distributed pinholes through the barrier cannot be fully excluded *a priori*. Thus, different parallel conduction channels other than ideal spin-dependent tunneling may be present in the samples, particularly in those with larger area nanocontacts. In these circumstances, the temperature dependence of the zero bias resistance of the heterojunction, $R(T)$, would be a reliable indicator of the quality of the barrier and the role of the tunneling conduction process. The temperature dependence of the LSMO/LAO/Pt junction resistance at the ohmic region measured through a nanocontact of $\sim 0.8 \mu\text{m}^2$ is shown in Fig. 4(b). The $R(T)$ curve of the LSMO electrode is also plotted for comparison. Both exhibit a clear distinct behavior, thus ensuring that the measured resistance corresponds to the LSMO/LAO junction. The $R(T)$ curve of the junction exhibits an increase in the resistance on lowering temperature compatible with direct tunneling transport according to the criteria given in Ref. 32 down to about 200 K. Noteworthy, $R(T)$ develops a peak with the maximum at about $T = 160$ K, which seems to be a common feature of junctions having manganite electrodes.^{9,33–35} The particular dependence of the $R(T)$ curves in junctions having manganite electrodes has not been clarified yet and it has been usually related to the degradation of the magnetotransport properties at the manganite/insulating barrier interfaces. The presence of an interfacial layer of underdoped manganite with reduced ordering temperature, due to oxygen off-stoichiometry, has been proposed.^{35,36} However, the absence of the expected upward shift in temperature of the $R(T)$ peak under the application of a 90 kOe magnetic field, as should occur in double exchange mediated manganites in which magnetic field promotes enhancement of ferromagnetic correlations, strongly suggest that the peak may well have a different origin (see Fig. 4(b)).

Next, the temperature and magnetic field dependencies of the tunneling conduction process were analyzed. For this purpose, I-V curves were measured at different temperatures and fields (see Fig. 5(a)) and then fitted by using Eq. (1) in the low voltage regime (± 0.2 V). The magnetic field was applied perpendicular to the sample surface, therefore parallel to the current. The results are depicted in Fig. 5(b). In principle, barrier height, ϕ_0 , and barrier thickness, S , should be almost temperature-independent. However, a progressive increase in ϕ_0 is detected when lowering temperature concomitant with a smooth reduction of S , of about a unit cell. Regarding this temperature dependence, it is worth mentioning here that the values of ϕ_0 and S depicted in Fig. 5(b) have been determined by using Eq. (1) that does not include

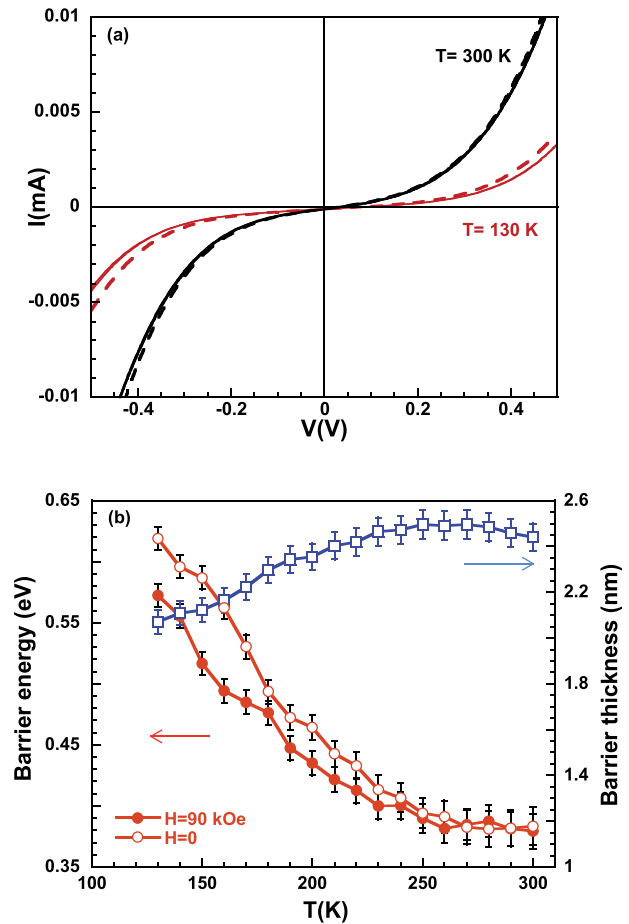


FIG. 5. (a) I-V curves at different temperatures as indicated. Solid lines correspond to curves measured at zero applied magnetic field, while dashed curves have been measured with a magnetic field of 90 kOe applied parallel to the current direction. (b) Dependence of the barrier energy and barrier thickness on temperature and magnetic field.

temperature effects. As shown by Simmons,³⁶ the thermal component of the tunneling current is proportional to T^2 and this contribution, which is not taken into account in Eq. (1), is reflected in our results as a decrease in ϕ_0 when increasing temperature. In fact, as shown in Fig. 6, the observed variation of ϕ_0 is clearly proportional to $1/T^2$. Other additional mechanisms, such as temperature dependence of the dielectric constant of LAO, the thermal expansion of the barrier volume or the increase in the thermal activation across de barrier, may also affect the tunneling conductance, but in our case, their effects are very much smaller than the thermal broadening of the Fermi-Dirac statistics.

On the other hand, the variation of the barrier thickness may also have different contributions. First, thermal expansion of the barrier thickness when increasing temperature was considered. However, a rough approximation gives $\Delta S/S \approx 0.002$, clearly smaller than the observed $\Delta S \approx 0.5$ nm on increasing T from 130 K to room temperature. Other possible sources to explain the change of S are related to interfacial effects in the LSMO topmost layers. However, in the case of LAO/LSMO interface intrinsic effects, structural disruption and inversion symmetry breaking at the LSMO interface, are dominant, thus not likely to be temperature dependent. Nevertheless, some thermal induced disorder by the interface

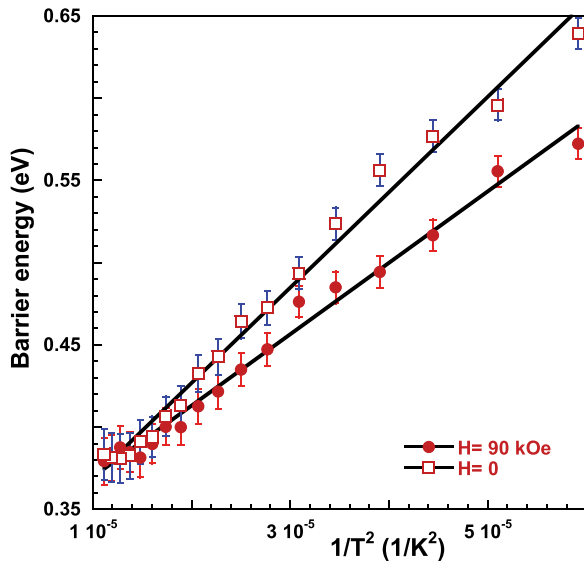


FIG. 6. Plot of the barrier energy as a function of $1/T^2$ for two different magnetic fields.

cannot be fully disregarded. It is worth to comment here that similar variation of the estimation of the barrier width with temperature has been previously reported for standard planar tunneling junctions.³⁷

With respect to the effect of the applied magnetic field, it is worth mentioning that no effect of the magnetic field should be expected “*a priori*” because only one of the electrodes is magnetic (LSMO). Nevertheless, the temperature dependence of the LSMO/LAO/Pt junction resistance exhibits a clear negative magnetoresistance that amounts about 4% at $T = 120$ K when a magnetic field of $H = 90$ kOe is applied perpendicular to the sample surface, i.e., parallel to the current (see Fig. 4(b)). A similar behavior is also observed in the barrier height that also exhibits a reduction as a function of magnetic field of the same amount (see Fig. 5(b)). To account for this unexpected magnetic field dependence, tunneling anisotropic magnetoresistance (TAMR) should be taken into consideration. It was recently shown that magnetoresistance in magnetic tunneling junctions may also depend on the orientation of the magnetization with respect to the crystallographic axis or the direction of the current flow.^{38,39} This effect is the so-called TAMR and it can exist even in tunneling junction with only one magnetic electrode.^{40,41} The origin of TAMR is the interference between Bychkov-Rashba and Dresselhaus spin-orbit couplings, which appears at junctions’ interfaces and in the tunneling region. The geometry of the present LSMO/LAO/Pt stack corresponds to the so-called out-of-plane TAMR with a single magnetic electrode.⁴¹ It is important to comment here that, due to shape anisotropy, magnetization lies on the film plane. Therefore, in these circumstances, TAMR reflects the change in the tunneling magnetoresistance when the magnetization is rotated from parallel to the plane of the junction ($H = 0$) to perpendicular to it ($H = 90$ kOe), i.e., parallel to the current direction. The change of the tunneling magnetoresistance is due to the different orientations of the magnetization with respect to the direction of the current flow and reflects the dependence of the tunneling density of states on the direction of the

magnetization of the magnetic electrode with respect to the direction of the current. A negative TAMR of about 4% at 120 K is observed. A similar value is obtained assuming that the change in the barrier height as a function of magnetic field reflects the change of the tunneling current due to the variation of the resistance of the LSMO electrode. Similar TAMR values have been reported for other single magnetic electrode tunneling junctions although at a much lower temperature.^{41,42} Nevertheless, our results also suggest that TAMR is vanishing small at room temperature which would restrict potential technological applications.

In summary, we have studied the properties of LAO thin films aimed at spintronic applications. For that purpose, we have fabricated and characterized tunneling junction with different areas from LSMO/LAO/Pt heterostructures. The magnetotransport properties of LSMO/LAO/Pt tunneling junction, as a function of temperature and magnetic field, have been thoroughly analyzed. The results obtained demonstrate that LAO barriers maintain their insulating properties down to 1–2 nm, i.e., 4–5 unit cells, thus being an appropriate material for tunnel barrier and for efficient spin injection. The temperature dependence of the junction resistance, $R(T)$, down to about 200 K makes evident that direct tunneling transport is the dominant conduction channel. In turn, this would indicate that insulating LAO barriers are of excellent microstructural quality with no pinholes or other microstructural defects, in contrast to other results previously reported. In the low temperature regime ($T \leq 190$ K), $R(T)$ develops a dome, as in the case of other tunneling junctions with manganite electrodes, whose origin is not well understood yet. Our results strongly suggest that the previously reported scenario of an interfacial layer of underdoped manganite with reduced ordering temperature is very unlikely. On the other hand, the parameters of the LAO barrier, ϕ_0 and S , have been estimated from I-V curves by using the Simmons model in the intermediate voltage regime. Values of ϕ_0 (≈ 0.4 eV at room temperature) are significantly smaller than the value of the corresponding Schottky barrier between LSMO and LAO. This reduction may be explained taking into consideration image charge effects and the presence of impurities or defects in the LAO barrier. The dependence of $R(T)$ and the barrier energy on the applied magnetic field indicates the existence of tunneling anisotropic magnetoresistance due to the change of the orientation of the magnetization with respect to the direction of the current flow.

ACKNOWLEDGMENTS

We acknowledge financial support from the Spanish MINECO (MAT2012-33207 and MAT2011-29081-C02-02) and FEDER program. R.G. thanks the Spanish MINECO for the financial support through the FPI program. We acknowledge Professor M.-J. Casanove for her contribution to the electron microscopy study of the LSMO/LAO junctions.

¹R. P. Cowburn, *Mater. Today* **6**, 32 (2003).

²E. Y. Tsymlal, O. N. Mryasov, and P. R. LeClair, *J. Phys.: Condens. Matter* **15**, R109–R142 (2003).

- ³A. Gupta, X. W. Li, and G. Xiao, *Appl. Phys. Lett.* **78**, 1894 (2001).
- ⁴T. Leo, C. Kaiser, H. Yang, S. S. Parkin, M. Sperlich, G. Guntherodt, and D. J. Smith, *Appl. Phys. Lett.* **91**, 252506 (2007).
- ⁵P. Seneor, A. Fert, J. L. Maurice, F. Montaigne, F. Petroff, and A. Vaures, *Appl. Phys. Lett.* **74**, 4017 (1999).
- ⁶G. Hu and Y. Suzuki, *Phys. Rev. Lett.* **89**, 276601 (2002).
- ⁷M. Bowen, M. Bibes, A. Barthélémy, J. P. Contour, A. Anane, Y. Lemaître, and A. Fert, *Appl. Phys. Lett.* **82**, 233 (2003).
- ⁸M. H. Jo, N. D. Mathur, N. K. Todd, and M. G. Blamire, *Phys. Rev. B* **61**, R14905 (2000).
- ⁹Y. Ishii, H. Yamada, H. Sato, H. Akoh, Y. Ogawa, M. Kawasaki, and Y. Tokura, *Appl. Phys. Lett.* **89**, 042509 (2006).
- ¹⁰E. T. Wertz and Q. Li, *Appl. Phys. Lett.* **90**, 142506 (2007).
- ¹¹J. O'Donnell, A. E. Andrus, S. Oh, E. V. Colla, and J. N. Eckstein, *Appl. Phys. Lett.* **76**, 1914 (2000).
- ¹²J. S. Noh, T. K. Nath, C. B. Eom, J. Z. Sun, W. Tian, and X. Q. Pan, *Appl. Phys. Lett.* **79**, 233 (2001).
- ¹³H. Yamada, Y. Ogawa, Y. Ishii, H. Sato, M. Kawasaki, H. Akoh, and Y. Tokura, *Science* **305**, 646 (2004).
- ¹⁴H. Yamada, M. Kawasaki, Y. Ogawa, and Y. Tokura, *Appl. Phys. Lett.* **81**, 4793 (2002).
- ¹⁵V. Garcia, M. Bibes, A. Barthélémy, M. Bowen, E. Jacquet, J. P. Contour, and A. Fert, *Phys. Rev. B* **69**, 052403 (2004).
- ¹⁶S. S. P. Parkin, C. Kaiser, A. Panchula, P. M. Rice, B. Hughes, M. Samant, and S.-H. Yang, *Nature Mater.* **3**, 862 (2004).
- ¹⁷P. LeClair, H. J. M. Swagten, J. T. Kohlhepp, R. J. M. van de Veerdonk, and W. J. M. de Jonge, *Phys. Rev. Lett.* **84**, 2933 (2000).
- ¹⁸Ll. Balcells, Ll. Abad, H. Rojas, A. Perez del Pino, S. Estrade, J. Arbiol, F. Peiro, and B. Martínez, *Small* **4**, 365 (2008).
- ¹⁹S. Valencia, Z. Konstantinovic, D. Schmitz, A. Gaupp, Ll. Balcells, and B. Martínez, *Phys. Rev. B* **84**, 024413 (2011).
- ²⁰S. Valencia, L. Peña, Z. Konstantinovic, Ll. Balcells, R. Galceran, D. Schmitz, F. Sandiumenge, M. Casanove, and B. Martínez, *J. Phys.: Condens. Matter* **26**, 166001 (2014).
- ²¹J. L. Maurice, D. Imhoff, J. P. Contour, and C. Colliex, *Philos. Mag.* **86**, 2127 (2006).
- ²²T. Riedl, T. Gemming, K. Dörr, M. Luysberg, and K. Wetzig, *Microsc. Microanal.* **15**, 213 (2009).
- ²³L. Samet, D. Imhoff, J. L. Maurice, J. P. Contour, A. Gloter, T. Manoubi, A. Fert, and C. Colliex, *Eur. Phys. J. B* **34**, 179 (2003).
- ²⁴C. Aruta, G. Ghiringhelli, V. Bisogni, L. Braicovich, N. B. Brookes, A. Tebano, and G. Balestrino, *Phys. Rev. B* **80**, 014431 (2009).
- ²⁵S. Valencia, A. Gaupp, W. Gudat, Ll. Abad, Ll. Balcells, A. Cavallaro, B. Martínez, and F. J. Palomares, *Phys. Rev. B* **73**, 104402 (2006); S. Valencia, A. Gaupp, W. Gudat, Ll. Abad, Ll. Balcells, and B. Martínez, *ibid.* **75**, 184431 (2007).
- ²⁶V. Garcia, M. Bibes, J. L. Maurice, E. Jacquet, K. Bouzehouane, J. P. Contour, and A. Barthélémy, *Appl. Phys. Lett.* **87**, 212501 (2005).
- ²⁷T. Nakamura, H. Inada, and M. Iiyama, *Appl. Surf. Sci.* **130–132**, 576 (1998).
- ²⁸J. G. Simmons, *J. Appl. Phys.* **34**, 1793 (1963).
- ²⁹D. W. Reagor, S. Y. Lee, Y. Li, and Q. X. Jia, *J. Appl. Phys.* **95**, 7971 (2004).
- ³⁰P. W. Peacock and J. Robertson, *J. Appl. Phys.* **92**, 4712–4721 (2002).
- ³¹W. F. Brinkman, R. C. Dynes, and J. M. Rowell, *J. Appl. Phys.* **41**, 1915 (1970).
- ³²B. J. Jonsson-Akerman, R. Escudero, C. Leighton, S. Kim, and I. K. Schuller, *Appl. Phys. Lett.* **77**, 1870 (2000).
- ³³J. Z. Sun, K. P. Roche, and S. S. P. Parkin, *Phys. Rev. B* **61**, 11244 (2000); J. Z. Sun, D. W. Abraham, K. P. Roche, and S. S. P. Parkin, *Appl. Phys. Lett.* **73**, 1008 (1998).
- ³⁴M. Viret, M. Drouet, J. Nassar, J. P. Contour, C. Fermon, and A. Fert, *Europhys. Lett.* **39**, 545 (1997).
- ³⁵J. Z. Sun, L. Krusin-Elbaum, P. R. Ducombe, A. Gupta, and R. B. Laibowitz, *Appl. Phys. Lett.* **70**, 1769 (1997).
- ³⁶J. G. Simmons, *J. Appl. Phys.* **35**, 2655 (1964).
- ³⁷K. Gloos, R. S. Poikolainen, and J. P. Pekola, *Appl. Phys. Lett.* **77**, 2915 (2000).
- ³⁸M. Tanaka and Y. Higo, *Phys. Rev. Lett.* **87**, 026602 (2001).
- ³⁹L. Brey, C. Tejedor, and J. Fernandez-Rosier, *Appl. Phys. Lett.* **85**, 1996 (2004).
- ⁴⁰J. Moser, A. Matos-Abiague, D. Schuh, W. Wegscheider, J. Fabian, and D. Weiss, *Phys. Rev. Lett.* **99**, 056601 (2007).
- ⁴¹A. Matos-Abiague and J. Fabian, *Phys. Rev. B* **79**, 155303 (2009).
- ⁴²B. G. Park, J. Wunderlich, D. A. Williams, S. J. Joo, K. Y. Jung, K. H. Shin, K. Olejnik, A. B. Shick, and T. Jungwirth, *Phys. Rev. Lett.* **100**, 087204 (2008).

Enhanced conduction and ferromagnetic order at (100)-type twin walls in $\text{La}_{0.7}\text{Sr}_{0.3}\text{MnO}_3$ thin films

Lluís Balcells,¹ Markos Paradinas,¹ Núria Baguès,^{1,2} Neus Domingo,² Roberto Moreno,² Regina Galceran,¹ Michael Walls,³ José Santiso,² Zorica Konstantinovic,¹ Alberto Pomar,¹ Marie-Jo Casanove,⁴ Carmen Ocal,¹ Benjamín Martínez,¹ and Felip Sandiumenge^{1,*}

¹*Institut de Ciència de Materials de Barcelona, ICMAB-CSIC, Campus de la Universitat Autònoma de Barcelona, 08193 Bellaterra, Catalonia, Spain*

²*Centre for Nanoscience and Nanotechnology, CIN2 (CSIC-ICN), Campus de la Universitat Autònoma de Barcelona, 08193 Bellaterra, Catalonia, Spain*

³*Laboratoire de Physique des Solides, Bureau 242-2ème étage Est-Bâtiment 510–Rue André, Rivière, 91400 Orsay, France*

⁴*CNRS, CEMES, Université de Toulouse UPS, 29 Rue J. Marvig, Toulouse 31055, France*

(Received 23 January 2015; revised manuscript received 27 May 2015; published 7 August 2015)

There is increasing evidence supporting the strong potential of twin walls in ferroic materials as distinct, spatially tunable, functional elements in future electronic devices. Here, we report an increase of about one order of magnitude in conductivity and more robust magnetic interactions at (100)-type twin walls in $\text{La}_{0.7}\text{Sr}_{0.3}\text{MnO}_3$ thin films. The nature and microscopic origin of such distinctive behavior is investigated by combining conductive, magnetic, and force modulation scanning force microscopies with transmission electron microscopy techniques. Our analyses indicate that the observed behavior is due to a severe compressive strained state within an ~ 1 nm slab of material centered at the twin walls, promoting stronger Mn $3d$ –O $2p$ orbital overlapping leading to a broader bandwidth and enhanced magnetic interactions.

DOI: [10.1103/PhysRevB.92.075111](https://doi.org/10.1103/PhysRevB.92.075111)

PACS number(s): 77.80.Dj, 61.72.Mm, 73.63.–b, 75.47.Lx

I. INTRODUCTION

Domain walls in ferroic complex oxides are stirring up a lot of interest in nanoscience and nanotechnology owing to their intrinsically distinctive functional behavior relative to that exhibited by the host material [1,2]. Domain walls constitute a class of natural, spatially ordered, and tunable homointerfaces where, similar to complex oxide epitaxial heterointerfaces [3,4], symmetry breaking and stress promote emergent phenomena with new physics and functionalities at the nanoscale. Owing to the subtle interplay between charge, spin, orbital, and lattice degrees of freedom characterizing transition metal oxides [5], homointerface induced phenomena does not appear restricted to any particular type of ferroic order. Thus, for instance, ferroelectric domain walls in multiferroic materials with simultaneous ferroelectric and magnetic order, such as BiFeO_3 , YMnO_3 or TbMnO_3 , have been reported to exhibit variable levels of electrical conductance [6–8], or ferromagnetism [9], respectively, while an $\sim 10^9$ times increase in conductivity has been observed at strongly charged 90° head-to-head walls in the canonical ferroelectric BaTiO_3 [10]. On the other hand, twin walls (TWs) in nonferroelectric ferroelastics have been shown to exhibit ferroelectric polarization (SrTiO_3 [11]), two-dimensional superconductivity (WO_{3-x} [12]), or ferrielectricity (CaTiO_3 [13]), and computer simulations on undoped manganites (bulk insulating state with antiferromagnetic ordering) also predict an enhancement in conductance at TWs [14].

Ferroelastic TWs are defined to satisfy the compatibility between two orientations of the spontaneous strain on the contact plane which generally coincides with a prominent crystallographic plane [15], yet they are associated to large strain gradients perpendicular to it [16]. In strongly correlated electron oxides such distortions affect electrical and magnetic

functionalities in an intricate way. As ABO_3 octahedral frameworks can deform by octahedral tilting (i.e., B–O–B bond angle distortion) and octahedral B–O bond length distortion simultaneously, the cornerstone in the interpretation of TW phenomena is the disentanglement of the strain state underpinning the coupling mechanism. To this end, various approaches based on aberration-corrected high resolution transmission electron microscopy have been reported [6,9,13,17,18]. In particular, experimental studies on the influence of chemical pressure in doped bulk materials [19,20] and theoretical investigations on thin films (see Ref. [21] and references therein) converge in identifying the competing effect of $\langle \text{Mn-O-Mn} \rangle$ bond angle and Mn–O bond length on the degree of orbital overlapping as the leading structural mechanism governing the bandwidth of these materials.

Among strongly correlated electron oxides, doped manganese perovskites exhibit a variety of phenomena, such as metal-insulator transition, half-metallic character, and cooperative orbital ordering [22]. However, despite their fascinating hetero-interfacial behavior (see, e.g., Ref. [23]), TWs in this materials remain unexplored. In this paper we focus on the TWs properties of the ferroelastic half-metallic $\text{La}_{0.7}\text{Sr}_{0.3}\text{MnO}_3$ (LSMO) room temperature ferromagnet, demonstrating that the electrical conductivity and ferromagnetic interactions at the surface of epitaxial thin films are substantially enhanced along the trace of (100) and (010) TWs perpendicular to the substrate. Using a combination of scanning probe and electron microscopies we are able to correlate this behavior with a strongly compressive state occurring at the TW which promotes stronger Mn $3d$ –O $2p$ orbital overlapping leading to a broader bandwidth and enhanced magnetic interactions.

II. EXPERIMENT

LSMO thin films with thicknesses $t \sim 40$ – 100 nm were grown on (001)-oriented, TiO_2 terminated SrTiO_3 (STO)

*Corresponding author: felip@icmab.es

substrates by rf magnetron sputtering, as described in Ref. [24]. The topography of as-grown films consists of atomically flat terraces with a roughness below 0.3 \AA bounded by unit cell ($\sim 4 \text{ \AA}$) height steps. Among the $\{100\}$ and $\{110\}$ TWs allowed in the $m3m \rightarrow 3m$ ferroelastic transition [15], only those with (100) and (010) orientations, perpendicular to the substrate, are present in these films [25,26]. The lateral twin size increases as $t^{1/2}$ [26]. The TDs remain fully in-plane strained by the substrate in the explored thickness range [25]. In-plane electrical resistivity and magnetization measurements of these samples are reported elsewhere [25].

Local electrical conductivity measurements were carried out using conducting scanning force microscopy (C-SFM) using a commercial head and software from Nanotec under an N_2 environment ($\text{RH} \approx 2\%$) to diminish any possible humidity effect. We used Si tips mounted on cantilevers with $k = 0.5 \text{ N/m}$ (Veeco) for friction force measurements (FFM) and commercial conductive CrPt coated Si tips mounted on cantilevers with $k = 40 \text{ N/m}$ (Budgetsensors). In at least one series of measurements the same tip was conserved for all experiments. To check tip-sample conditions, the adhesion force was systematically determined from force versus distance curves prior to and after each conductivity experiment. Current images were acquired in a noninvasive manner (the absence of sample indentation was always checked) by using the contact operation mode at the lowest possible applied load needed. The conducting tip (first electrode) was placed in direct contact with the sample, under controlled load, i.e., by using a normal force feedback, and the current was measured between tip and sample. Simultaneous topographic images $z(x,y)$ and current maps $I(x,y)$ were obtained over a given region at a fixed voltage. The current-voltage (I - V) characteristics of the contact were obtained as a function of the bias voltage applied between tip and sample at chosen specific single points on the surface (i.e., the lateral scan of the tip is disabled). In this mode, direct comparison between I - V characteristics at different locations on the $I(x,y)$ map is therefore possible. Both, forwards and backwards, current-voltage (I - V) characteristics of the contact were always measured starting from negative tip voltages. In our setup, the sample was always grounded and the voltage was applied to the tip. Because of the insulating character of the substrates used (SrTiO_3) the direct electric contact to ground is established through a metallic clamp (counterelectrode) firmly attached to the surface of the film at the sample border (millimeters apart from the tip-surface contact). An external I - V converter (Stanford Research Systems) was used to provide access to a wide range of compliance currents (1 pA to 1 mA). Whereas for topographic images the color code is the commonly used, bright for high and dark for low, for the current maps it depends on the voltage sign. Thus higher currents appear darker in C-SFM images taken at negative V_{tip} values, while brighter for positive V_{tip} .

The spatially resolved mechanical response of the surface of the films was analyzed by Force Modulation Microscopy (FMM, Asylum Research). FMM is a SFM-based mode where the tip in direct contact with the surface is forced to vibrate at a high frequency (contact resonance frequency typically of several 100's of KHz) in order to evaluate the mechanical response of the material [27–29]. Any variation in the contact

resonance frequency is related to the local sample stiffness, i.e., a positive shift in frequency corresponds to stiffer mechanical properties. The topography was collected in contact mode and an ac voltage was applied to the piezoelectric actuator at the cantilever in order to induce this vibrational motion. The contact resonance frequency was tracked by a dual ac resonance tracking system. The topography of the films did not change during the measurement, meaning that they were performed in the elastic regime.

The spatially resolved magnetic behavior of the films was investigated by magnetic force microscopy (MFM). Images were taken with Nanosensors MFM tips, showing a nominal magnetic moment of $3 \times 10^{-14} \text{ emu}$. Phase contrast images are obtained at different tip distances from the film surface (h), while adjusting the amplitude ratio ($A_{\text{MFM}}/A_{\text{sp}}$) of MFM imaging (A_{MFM}) vs topography imaging set point (A_{sp}). In this way, we obtained MFM images over different long range force areas and lateral spatial resolutions.

The local atomic and chemical structure of the TWs was studied by aberration-corrected high-resolution transmission electron microscopy techniques. Samples for TEM observation were prepared by conventional cutting-gluing-grinding procedures, followed by Ar milling down to perforation at a small incidence angle. Annular dark field images and electron energy-loss spectroscopy (EELS) spectrum-images (SI) of cross-section samples were acquired using a Nion Ultrastem 200 scanning transmission electron microscope (STEM) operating at 100 kV. The probe convergence angle was 35 mrad. The data shown here used a 50 mrad EELS collection angle (smaller angles did not significantly improve visible detail in the spectra, while greatly reducing signal). Data were denoised using principal components analysis (PCA) as provided in the Hyperspy suite [30]. To avoid the possibility of any small shift or signal shape change being lost through an excessive noise removal, the first three components appearing to contain only noise were left in the PCA reconstruction (i.e., three more components than would normally be retained in this analysis). The Mn edges in the spectra were then modeled also using Hyperspy over the energy-loss range 600–680 eV. The components in the model were an AE^{-r} type power law background, two Gaussian peaks centered on the L_2 and L_3 peak energies and continuum L_2 and L_3 edges as calculated via the Hartee-Slater method [31]. Atomic resolution phase contrast images were obtained in planar view orientation using a Hitachi HF3300 electron microscope working at 300 kV and equipped with a CFEG and an imaging aberration corrector CEOS aplanator.

III. RESULTS AND DISCUSSION

Figure 1(a) shows a typical orientation-contrast scanning electron micrograph (OC-SEM) image of the film used for nanoscale conductivity measurements, which clearly indicates a long range ordered pattern of TDs in the films. The different contrast levels reflect the various degrees of misorientation between different domains; see Ref. [26]. As shown in Fig. 1(b), the sample surface topography consists of flat terraces separated by unit cell height steps (see inset). In spite of the extremely flat surface morphology, the simultaneously acquired current map shown in Fig. 1(c) reveals a considerable

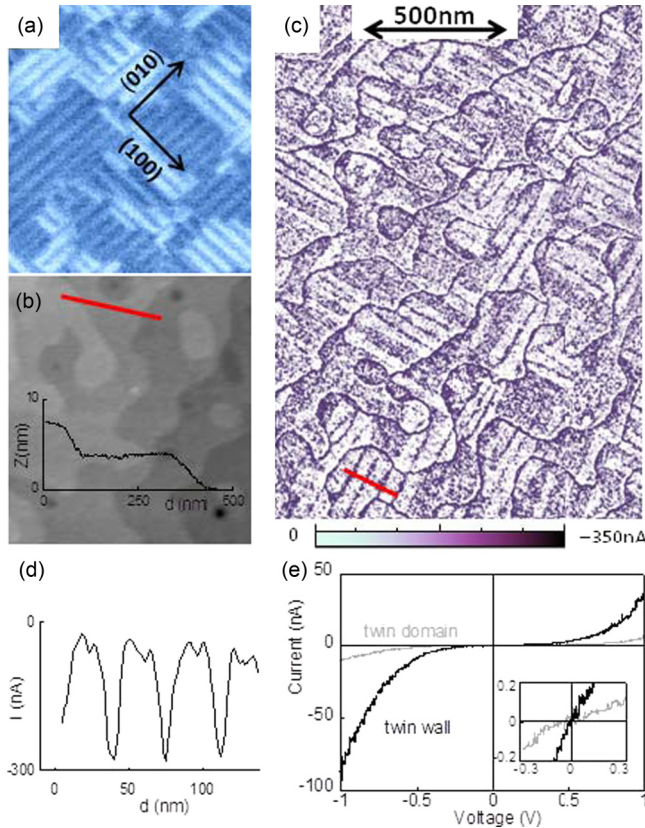


FIG. 1. (Color online) (a) OC-SEM image exhibiting the twin pattern, (b) SFM topographic image (profile along the red line shown as inset), and (c) current map acquired at $V = -1.4$ V, of a 40 nm thick LSMO film. Note that negative (dark) current values are measured for $V_{tip} < 0$. (a), (b), and (c) are presented with the same scale as indicated in (c). In (c), enhanced current running along the [100] and [010] directions corresponds to the TW locations. (d) Averaged current profile along the red line in (c). (e) I - V characteristics obtained at the TWs (black) and on the TD (gray). Each I - V corresponds to the average of five different measurements on the same position. In spite of the low current detected at low voltages both I - V curves present a linear behavior around $V = 0$. Inset is a zoom at the linear regime.

intensity along lines running along (010) and (100) directions which are superimposed to a quite uniform current background [Figs. 1(c) and 1(d)]. The separation between conducting lines coincides with the lateral size of the TDs shown in Fig. 1(a) and forms domains of perpendicular orientations that perfectly mimic the twin pattern. Thus we correlate the position of the conducting lines with the position of TWs. As can be clearly seen, the meandering lines in current correspond to the step ledges and are due to extended tip-surface contact at them and therefore are not at the focus of the present study. However, as C-SFM measurements can be affected by local variations of the elastic response of the film surface leading to variations in tip-surface contact area, we probed the local mechanical response of the films by FMM. A clear positive shift of the contact resonance frequency was detected along the TWs, indicating that they are harder than the TDs (see Supplemental Material [32]). This observation rules out any contribution of surface elasticity to the observed enhancement

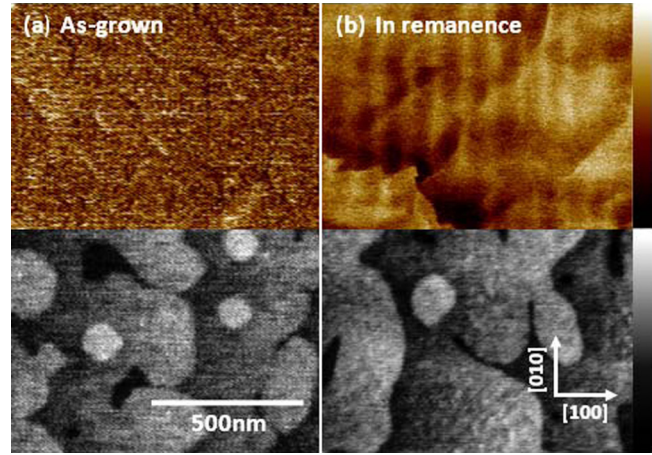


FIG. 2. (Color online) MFM images of an as-grown 100 nm thick LSMO film (a) and in the remanent state (b). Bottom images show the corresponding topographic images. In (b) the TWs appear brighter indicating a stronger tip-sample interaction. Color scale bars correspond to a full range of 2.5° and 1.2 nm for MFM and topographic images, respectively.

in conductivity. Characteristic I - V curves obtained from one TW (black line) and an adjacent TD (gray line) are shown in Fig. 1(e). The voltage range was limited to ± 1.4 V to minimize undesired structural or chemical perturbations derived from the resistive switching effect observed in LSMO films [33]. The I - V response is linear at low voltages [see inset in Fig. 1(e)] as expected for tunneling conducting systems.

Similar to C-SFM, MFM images also bring out the presence of an ordered linear pattern matching the underlying arrangement of TWs, superimposed to an homogeneous darker background, as shown in Fig. 2. An analysis of the MFM contrast as a function of the tip-surface distance, h , is presented in Fig. 3. Figure 3(a) is a topographic image of the area analyzed in (b) through (d). Note that, as the tip-surface distance, h , is reduced from (b) to (d), the concomitant reduction in oscillation amplitude to avoid the short range topography interactions noticeably improves the lateral resolution of the images but deteriorates the signal to noise ratio. For higher distances, h , the tip magnetic moment mainly interacts with the stray fields of long-range ferromagnetically ordered magnetic moments present in the bulk of the sample, resulting in the low magnetic phase contrast over blurry areas as observed in Fig. 3(b). Superimposed to this interaction background, we can observe a series of lines running parallel to the [100] and [010] directions, that we attribute to the signal coming out from the TWs. At the working tip-sample distances shown in (b) and (c), the tip stray magnetic field is too weak to perturb the intrinsic magnetic order at the TWs. When the tip-surface distance is further reduced the TWs appear brighter than the TDs owing to a stronger attractive tip-sample interaction; at these distances, the tip stray magnetic fields are strong enough to overcome the coercive magnetic field of the TW and align the magnetic moments during the scan. From this analysis, the magnetic configuration of the films can be described as composed by two ferromagnetic materials, one corresponding to the TDs and a second one with larger ferromagnetic moment corresponding to the TWs.

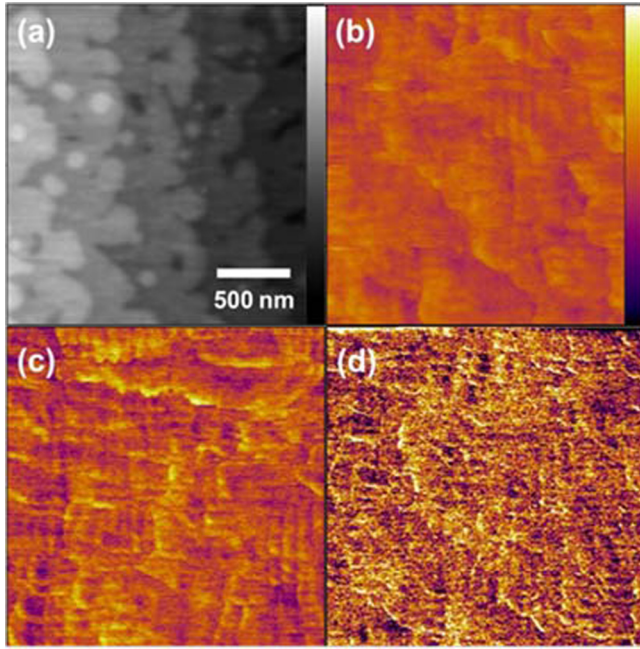


FIG. 3. (Color online) (a) Topography image over an area of $2 \text{ mm} \times 2 \text{ mm}$ of the surface of a LSMO thin film. The color scale bar corresponds to a full range of 3 nm . (b) to (d) show the MFM phase contrast over the same area as in (a) under different conditions: (d) $h = 15 \text{ nm}$ and $A_{\text{MFM}}/A_{\text{sp}} = 0.9$, (c) $h = -11 \text{ nm}$ and $A_{\text{MFM}}/A_{\text{sp}} = 0.5$, and (d) $h = -22 \text{ nm}$ and $A_{\text{MFM}}/A_{\text{sp}} = 0.12$. The color scale bar for all MFM images is shown in (d) and corresponds to a full range scale of 2.5° . In (b) and (c) the tip coercive field is smaller than the coercive field of the TWs, which accordingly appear darker than the TDs. In (d) the tip coercive field becomes larger than the coercive of the TWs, causing a contrast reversal (TWs appear brighter than the TDs).

In order to understand the microscopic origin of the distinctive behavior of the TWs, we investigated their local structure and chemistry by combining different transmission electron microscopy techniques. Figure 4(a) is a cross section high-resolution high-angle annular dark-field (HAADF) image obtained around a TW. This is an incoherent image [34]; the influence of strains is negligible and the brightness of each atomic column is proportional to the atomic number, Z . Therefore, brighter and bigger dots correspond to the La/Sr sublattice, while columns of alternating Mn and O atoms are hardly visible. Careful inspection of the image does not reveal any distinctive feature associated to the position of the twin-plane separating the two adjacent TDs. Hence we conclude that cationic order is not significantly altered at the TW. Moreover, analysis of EEL spectra corresponding to the Mn- $L_{3/2}$ edges acquired within selected regions containing the TW and away from it did not reveal any signature of variations in the oxidation state of the Mn cations (see Supplemental Material [32]).

The strain state of the TW has been investigated by HRTEM. Since we are interested in the strain distribution along the trace of the TWs on the surface of the films, observations were performed in planar-view configuration; see Fig. 4(b). As in the HAADF image, direct inspection of the image shown in the right panel, only allows to recognize the TW

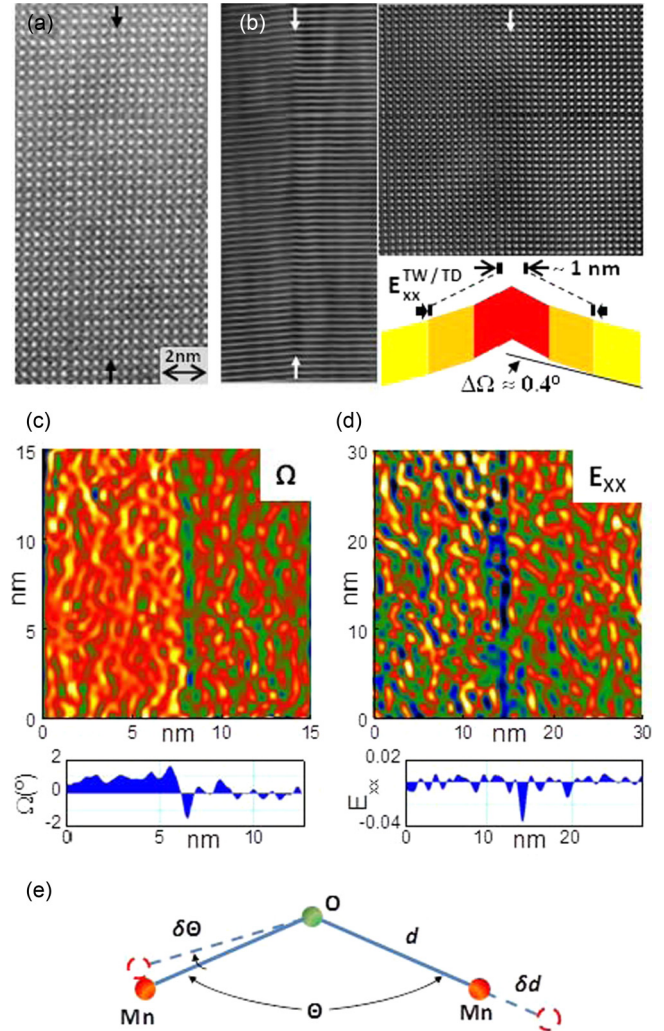


FIG. 4. (Color online) (a) Cross section HAADF image of a (100)-TW (indicated with vertical arrows) viewed along the [010] axis, of a 40 nm thick LSMO film. The position of the TW is only recognized by the tilt of the (001) planes by twin angle Ω . The contrast of atomic columns (proportional to their atomic number, Z) is not altered at the TW. (b) Right panel: planar view HRTEM image of a (100)-TW (indicated with vertical arrows) viewed along the [001] axis, of a 40 nm thick film. Left panel: same image but laterally compressed to emphasize the increase of Ω in the TW. Inset is a schematic drawing illustrating the distortion of the structure in the TW according to the GPA analysis presented below. (c) and (d) show the corresponding Ω and $E_{xx}^{\text{TW/TD}}$ maps, along with their averaged profiles, as obtained by GPA analysis. $E_{xx}^{\text{TW/TD}}$ is the strain component perpendicular to the TW, relative to the TD. (e) Distortion mechanisms of the octahedral framework: octahedral tilting distorts the (Mn-O-Mn) bond angle by $\delta\Theta$ and distortion of the MnO_6 octahedra results in the elastic stretching or compression (δd) of the Mn-O bond.

through the tilt of the (001) or (100) planes, respectively, which corresponds to the twin angle, $\Omega = 2(\alpha_{\text{pc}} - 90^\circ) \sim 0.8^\circ$, where α_{pc} is the pseudocubic interaxial angle. However, the laterally compressed image depicted in the left panel clearly reveals an increase of Ω seen as a cusp along the trace of the (100) planes. This effect is quantified in the Ω map shown in Fig. 4(c), computed from geometrical

phase analysis (GPA) [35]. This map clearly features a discontinuous ridge corresponding to an increase in Ω up to $\sim 1.5^\circ$ within an ~ 1 nm thick region centered at the TW. The corresponding map of the strain component perpendicular to the TW, also reveals an ~ 1 nm thick region centered at the TW [see Fig. 4(d)] submitted to a severe compressive strain relative to the TD of $E_{xx}^{\text{TW/TD}} = -3.5\%$, otherwise consistent with the increased hardness observed by FMM. The strain state of the TW deduced from this analysis is schematically depicted in Fig. 4(b); its consequences on the distortion of the octahedral framework are illustrated in Fig. 4(e). The twinned film thus can be viewed as a self-organized nanostructure consisting of 1 nm thick sheets of strongly compressed LSMO embedded in matrix of tensilely strained LSMO. In our GPA analysis $E_{xx}^{\text{TW/TD}}$ is defined relative to the TD, which is fully in-plane strained by the STO substrate [25] (misfit $\delta \sim 0.6$); therefore, the effective compression relative to the bulk LSMO phase is of $\sim -2.9\%$.

The distortion of the octahedral framework building ABO_3 perovskites is conveniently described by a combination of rigid BO_6 octahedral rotations about the *pseudocubic* unit cell axes, α (or equivalently $\langle \text{Mn-O-Mn} \rangle$ bond angle distortions, $\delta\Theta$) and elastic stretching/compression of the B-O bonds, δd , as shown in Fig. 4(e). In order to disentangle the strain state of the TW, here we take advantage of the link between Ω and the rigid octahedral tilts about the *pseudocubic* unit cell axes, α , as derived from geometrical formalisms reported for rhombohedral perovskites [36]:

$$\alpha = \sin^{-1} \sqrt{3 \cos \alpha_{\text{pc}} / (1 - 2 \cos \alpha_{\text{pc}})} / \sqrt[3]{3}, \quad (1)$$

where $\alpha_{\text{pc}} = (\Omega + \pi)/2$. The octahedral tilt inside the TW derived from this approximation is thus $\alpha_{\text{TW}} = 7.55^\circ$, larger than the bulk value, $\alpha = 5.2^\circ$ (as calculated from $\langle \text{Mn-O-Mn} \rangle = 165.24^\circ$ [37]). Using Eq. (1), the amount of strain accommodated by rigid octahedral tilts is only $\Delta a/a_{\text{TD}} = \cos^2 \Delta \alpha - 1 = -0.0014$. Therefore, most of the compression is mediated by a severe distortion of the Mn-O bonds of $\sim -2.7\%$.

The influence of strain on the bandwidth, W , of ABO_3 perovskite compounds is mediated through the relative modifications induced in the $\langle \text{Mn-O-Mn} \rangle$ bond angle and the Mn-O bond length, which control the overlap integrals between the Mn $3d$ and the O $2p$ orbitals [see Fig. 4(e)]. This double dependence is described by the empirical formula [19],

$$W \propto \frac{\cos \varphi}{d_{\text{Mn-O}}^{3.5}}, \quad (2)$$

$$\varphi = \frac{1}{2}(\pi - \langle \text{Mn-O-Mn} \rangle) = \frac{2\alpha}{\sqrt{2}}, \quad (3)$$

where φ is the ‘‘tilt’’ angle. In the bulk LSMO structure, $\langle \text{Mn-O-Mn} \rangle = 165.24^\circ$ ($\varphi = 7.38^\circ$, $\alpha = 5.2^\circ$) and $d_{\text{Mn-O}} = 1.964 \text{ \AA}$ [37]. Thus combining Eqs. (2) and (3)

one obtains $\frac{\cos \varphi}{d_{\text{Mn-O}}^{3.5}} = 0.0934$. In the TW, the calculated value $\alpha_{\text{TW}} = 7.5^\circ$ corresponds to $\varphi_{\text{TW}} = 10.68^\circ$ (the $\langle \text{Mn-O-Mn} \rangle$ bond angle is decreased down to 158.64°). The distortion of the octahedral framework in the TW is thus described by $\delta\Theta/\Theta = -0.040$ and $\delta d/d = -0.027$, yielding $\frac{\cos \varphi}{d_{\text{Mn-O}}^{3.5}} = 0.1019$. Therefore, despite the stronger angular distortion, the balance between $\delta\Theta/\Theta$ and $\delta d/d$ results in a broadening of the bandwidth inside the TW, thus explaining the observed enhancement in conductivity. It is worth mentioning that even smaller variations of the $\frac{\cos \varphi}{d_{\text{Mn-O}}^{3.5}}$ ratio, induced in bulk manganites by cationic substitutions at the A site, cause huge variations in T_C of about 200 K [20]. This behavior is fully consistent with theoretical work showing that compressive strains in half-doped manganite epitaxial films promote an increase of T_C [21], in agreement with experimental observations at other doping levels such as for instance in $\text{La}_{0.8}\text{Ba}_{0.2}\text{MnO}_3$ [38]. With this in mind, the observed room temperature enhancement of the magnetic moment in the TWs can be explained as an apparent effect resulting from the strengthening of the magnetic interactions and, therefore, an increase in T_C .

IV. CONCLUSION

We have used a combination of electron microscopy, EELS, C-SFM, and MFM and modeling of the strained state of (100)-TWs in LSMO thin films that converge in signaling an enhancement of the electric conductivity and the strengthening of the magnetic interactions at TWs associated with a severe compression of the TW material. Notably, we find that the TWs are not affected by any significant chemical modification, and therefore the causes of their distinctive functional behavior are governed by geometrical effects that propitiate bandwidth broadening.

ACKNOWLEDGMENTS

We thank Julien Nicolai for assistance with the I2TEM electron microscope in Toulouse (France). This research was sponsored by the Spanish MINECO (Grants No. MAT2011-29081-C02, No. MAT2012-33207, and No. MAT2013-47869-C4-1-P) projects. We also acknowledge financial aid from the Generalitat de Catalunya (2014 SGR 501). N.B. and F.S. also acknowledge funding from the European Union Seventh Framework Programme under Grant Agreement No. 312483-ESTEEM2 (Integrated Infrastructure Initiative I3) for providing access to aberration corrected electron microscopes at CEMES (Toulouse) and LPS (Orsay). R.G. and N.B. thank the Spanish MINECO for financial support through the FPI program. F.S. acknowledges support from the Labex (Excellence Laboratory) NEXT through a visiting scientist fellowship at CEMES (Toulouse, France).

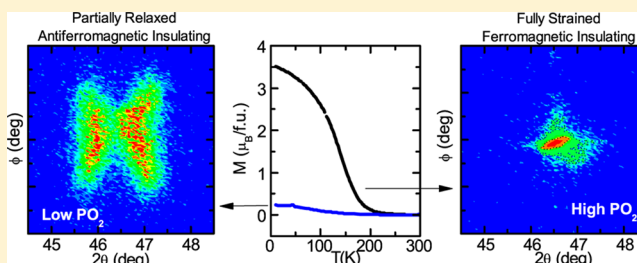
[1] G. Catalan, J. Seidel, R. Ramesh, and J. F. Scott, *Rev. Mod. Phys.* **84**, 119 (2012).

[2] J. Seidel, G. Singh-Bhalla, Q. He, S.-Y. Yang, Y.-H. Chu, and R. Ramesh, *Phase Transit.* **86**, 53 (2013).

- [3] P. Zubko, S. Gariglio, M. Gabay, Ph. Ghosez, and J. J.-M. Triscone, *Annu. Rev. Condens. Matter Phys.* **2**, 141 (2011).
- [4] H. Y. Hwang, Y. Iwasa, M. Kawasaki, B. Keimer, N. Nagaosa, and Y. Tokura, *Nat. Mater.* **11**, 103 (2012).
- [5] Y. Tokura, *Phys. Today* **56**, 50 (2003).
- [6] J. Seidel, L. W. Martin, Q. He, Q. Zhan, Y.-H. Chu, A. Rother, M. E. Hawkrige, P. Maksymovych, P. Yu, M. Gajek, N. Balke, S. V. Kalinin, S. Gemming, F. Wang, G. Catalan, J. F. Scott, N. A. Spaldin, J. Orenstein, and R. Ramesh, *Nat. Mater.* **8**, 229 (2009).
- [7] S. Farokhipoor and B. Noheda, *Phys. Rev. Lett.* **107**, 127601 (2011).
- [8] T. Choi, Y. Horibe, H. T. Yi, Y. J. Choi, W. Wu, and S.-W. Cheong, *Nat. Mater.* **9**, 253 (2010).
- [9] S. Farokhipoor, C. Magén, S. Venkatesan, J. Íñiguez, C. J. M. Daumont, D. Rubí, E. Snoeck, M. Mostovoy, C. de Graaf, A. Müller, M. Döblinger, C. Scheu, and B. Noheda, *Nature (London)* **515**, 379 (2014).
- [10] T. Sluka, A. K. Tagantsev, P. Bednyakov, and N. Setter, *Nat. Commun.* **4**, 1808 (2013).
- [11] P. Zubko, G. Catalan, A. Buckley, P. R. L. Welche, and J. F. Scott, *Phys. Rev. Lett.* **99**, 167601 (2007).
- [12] A. Aird and E. K. H. Salje, *J. Phys.: Condens. Matter* **10**, L377 (1998).
- [13] S. Van Aert, S. Turner, R. Delville, D. Schryvers, G. Van Tendeloo, and E. K. H. Salje, *Adv. Mater.* **24**, 523 (2012).
- [14] J. Salafranca, R. Yu, and E. Dagotto, *Phys. Rev. B* **81**, 245122 (2010).
- [15] J. Sapiel, *Phys. Rev.* **12**, 5128 (1975).
- [16] C. W. Haas and W. F. Jaep, *Phys. Lett. A* **49**, 77 (1974).
- [17] A. Borisevich, O. S. Ovchinnikov, H. J. Chang, M. P. Oxley, P. Yu, J. Seidel, E. A. Eliseev, A. N. Morozovska, R. Ramesh, S. J. Pennycook, and S. V. Kalinin, *ACS Nano* **4**, 6071 (2010).
- [18] C. L. Jia, S.-B. Mi, K. Urbam, I. Vrejoiu, M. Alexe, and D. Hesse, *Nat. Mater.* **7**, 57 (2008).
- [19] M. Medarde, J. Mesot, P. Lacorre, S. Rosenkranz, P. Fischer, and K. Gobrecht, *Phys. Rev. B* **52**, 9248 (1995).
- [20] P. G. Radaelli, G. Iannone, M. Marezio, H. Y. Hwang, S.-W. Cheong, J. D. Jorgensen, and D. N. Argyriou, *Phys. Rev. B* **56**, 8265 (1997).
- [21] A. Mukherjee, W. S. Cole, P. Woodward, M. Randeria, and N. Trivedi, *Phys. Rev. Lett.* **110**, 157201 (2013).
- [22] A. Urushibara, Y. Moritomo, T. Arima, A. Asamitsu, G. Kido, and Y. Tokura, *Phys. Rev. B* **51**, 14103 (1995).
- [23] N. M. Nemes, M. J. Calderón, J. I. Beltrán, F. Y. Bruno, F. García-Barriocanal, Z. Sefrioui, C. León, M. García-Hernández, M. C. Muñoz, L. Brey, and J. Santamaría, *Adv. Mater.* **26**, 7516 (2014).
- [24] Z. Konstantinovic, J. Santiso, D. Colson, A. Forget, Ll. Balcells, and B. Martínez, *J. Appl. Phys.* **105**, 063919 (2009).
- [25] F. Sandiumenge, J. Santiso, Ll. Balcells, Z. Konstantinovic, J. Roqueta, A. Pomar, J. P. Espinós, and B. Martínez, *Phys. Rev. Lett.* **110**, 107206 (2013).
- [26] J. Santiso, Ll. Balcells, Z. Konstantinovic, J. Roqueta, P. Ferrer, A. Pomar, B. Martinez, and F. Sandiumenge, *CrystEngComm* **15**, 3908 (2013).
- [27] K. Yamanaka and S. Nakano, *Appl. Phys. A* **66**, S313 (1998).
- [28] U. Rabe, E. Kester and W. Arnold, *Surf. Interface Anal.* **27**, 386 (1999).
- [29] A. Gannepalli, D. G. Yablon, A. H. Tsou and R. Proksch, *Nanotechnology* **22**, 355705 (2011).
- [30] F. de la Peña, M.-H. Berger, J.-F. Hochepeid, F. Dynys, O. Stephan, and M. Walls, *Ultramicroscopy* **111**, 169 (2011).
- [31] P. Rez, *Ultramicroscopy* **28**, 16 (1989).
- [32] See Supplemental Material at <http://link.aps.org/supplemental/10.1103/PhysRevB.92.075111> for results on FMM and EELS.
- [33] L. Peña, L. Garzón, R. Galceran, A. Pomar, B. Bozzo, Z. Konstantinovic, F. Sandiumenge, Ll. Balcells, C. Ocal, and B. Martínez, *J. Phys.: Condens. Matter* **26**, 395010 (2014).
- [34] S. J. Pennycook and D. E. Jesson, *Phys. Rev. Lett.* **64**, 938 (1990).
- [35] M. J. Hÿtch, *Microsc. Microanal. Microstruct.* **8**, 41 (1997).
- [36] H. D. Megaw and C. N. W. Darlington, *Acta Crystallogr. A* **31**, 161 (1975).
- [37] J. F. Mitchell, D. N. Argyriou, C. D. Potter, D. G. Hinks, J. D. Jorgensen, and S. D. Bader, *Phys. Rev. B* **54**, 6172 (1996).
- [38] H. Chou, M.-H. Tsai, F. P. Yuan, S. K. Hsu, C. B. Wu, J. Y. Lin, C. I. Tsai, and Y.-H. Tang, *Appl. Phys. Lett.* **89**, 082511 (2006).

Strain-Engineered Ferromagnetism in LaMnO₃ Thin FilmsJaume Roqueta,[†] Alberto Pomar,^{*,‡} Lluís Balcells,[‡] Carlos Frontera,[‡] Sergio Valencia,^{||} Radu Abrudan,^{||,⊥} Bernat Bozzo,[‡] Zorica Konstantinović,^{‡,§} José Santiso,[†] and Benjamín Martínez[‡][†]Institut Català de Nanociència i Nanotecnologia, ICN2 (CSIC-ICN), Campus de la UAB, 08193 Bellaterra, Spain[‡]Instituto de Ciencia de Materiales de Barcelona-CSIC, Campus de la UAB, 08193 Bellaterra, Spain[§]Center for Solid State Physics and New Materials, Institute of Physics Belgrade, University of Belgrade, Pregrevica 118, 11080 Belgrade, Serbia^{||}Helmholtz-Zentrum-Berlin für Materialien und Energie, Albert-Einstein Strasse 15, D-12489 Berlin, Germany[⊥]Institut für Experimentalphysik/Festkörperphysik, Ruhr-Universität Bochum, 44780 Bochum, Germany

ABSTRACT: A systematic study of the growth process of LaMnO₃ (LMO) thin films, by pulsed laser deposition, on top of SrTiO₃ substrates under different oxygen partial pressures (P_{O_2}) is reported. It is found that the accommodation of the orthorhombic LMO phase onto the cubic STO structure, i.e., the amount of structural strain, is controlled by the background oxygen pressure. We demonstrate that magnetic behavior can be continuously tuned from robust ferromagnetic (FM) ordering to an antiferromagnet. These results strongly point to a strain-induced selective orbital occupancy as the origin of the observed FM behavior, in agreement with recent theoretical calculations.



■ INTRODUCTION

The LaMnO₃ (LMO) perovskite compound has gained renewed interest for being an essential building block in some heterostructures showing emerging phenomena as, for instance, unexpected exchange bias in LaMnO₃/LaNiO₃ multilayers¹ or evidence of ferromagnetism (FM) at the interface of LaMnO₃/SrTiO₃^{2,3} or LaMnO₃/SrMnO₃⁴ heterostructures. Irrespective of the growth conditions used in those works, LMO layers were reported to exhibit robust FM behavior in contrast to the antiferromagnetic (AF) character of the ground state of the stoichiometric LMO bulk material, where Mn³⁺ magnetic moments are arranged in an A-type AF ordering.^{5–7} This unexpected FM character has been often detected in LMO films, and in spite of several attempts to explain it, its origin is still unclear. First, it is known that LMO perovskite structure cannot accommodate oxygen excess at interstitial positions, and thus, it must be accommodated by the creation of La and/or Mn vacancies.⁵ In this scenario, to compensate for the charge unbalance, a Mn^{3+/4+} mixed valence state is invoked, and therefore, the observed ferromagnetism is simply explained by a double-exchange mechanism with the concomitant tendency to metallic behavior, similar to doped manganites.^{8–10} However, this explanation is in contradiction with some experimental results evidencing a FM-insulating (I) behavior that should be excluded in a canonical double-exchange model.^{11–14} To solve this puzzling situation, several extrinsic origins have been proposed to account for the observed FM behavior. Most of them are based on a nonstoichiometric La:Mn relationship^{8,12,14} and a multiple-double-exchange mechanism by the creation of Mn²⁺ ions.^{15,16}

On the other hand, strain effects due to the film/substrate mismatching have also been invoked in some cases. As shown by theoretical studies, strain may lead to different patterns of octahedral distortions, either by Jahn–Teller distortions or by oxygen octahedral rotations, thus promoting selective magnetic/orbital arrangements.^{17–21} Therefore, because magnetic and orbital ordering in LMO is directly correlated to the particular arrangement and configuration of the MnO₆ octahedral framework, it is clear that strain may strongly affect its magnetotransport properties.^{6,22} This possibility has raised new interest because strain-induced FM has already been reported in other manganese thin films. Quite recent first-principle calculations suggest that, in fact, FM-I could be an intrinsic ground state in these manganese oxides under some given values of biaxial strain.²³ In this scenario, the change in the magnetic order (AF/FM) would be explained as being due to the occurrence of a novel $d_{3z^2-r^2}/d_{x^2-y^2}$ alternated orbital ordering that is stabilized in the distorted MnO₆ octahedra of the strained LMO monoclinic cell.

In this work, we report on the magnetic, transport, and structural properties of LMO thin films grown on SrTiO₃ (STO) substrates. The influence of oxygen partial pressure (P_{O_2}) during the growth process on the accommodation of the orthorhombic LMO phase onto the cubic STO structure is thoroughly analyzed. Our results demonstrate that magnetic

Received: June 24, 2015

Revised: August 29, 2015

Published: September 16, 2015

behavior can be continuously tuned from a robust FM to an AF depending on the amount of structural strain that accumulates in the structure. Our findings will be analyzed in terms of recent theoretical calculations suggesting different orbital orderings in LMO as a function of biaxial strain.

EXPERIMENTAL DETAILS

LaMnO₃ thin films have been grown on top of (100)STO single-crystalline substrates by pulsed laser deposition (PLD) at substrate temperatures between 700 and 900 °C and under a wide range of background oxygen partial pressures (from 200 to 5×10^{-3} mTorr). Laser fluence was kept constant at 0.8 J/cm². The number of pulses was adjusted to obtain film thicknesses in the range of 35–45 nm. The thickness of the films was determined by X-ray reflectometry and by contact profilometry. Systematic X-ray diffraction characterization was conducted in a four-angle diffractometer with a Cu K α radiation source (X'Pert MRD-Panalytical) and a Bruker D8 Advance GADDS system. The phase purity and structural quality of the films were confirmed by standard $\theta - 2\theta$ diffraction measurements. The strain of the films was carefully studied by performing reciprocal space maps around some selected LMO Bragg peaks. The relative concentration of La and Mn cations in the deposited films was studied by wavelength dispersive spectrometer (WDS) microprobe analysis. X-ray absorption spectroscopy (XAS) at the Mn L_{2/3} edge was measured at BESSY II in total electron yield (TEY) configuration. Magnetic properties were measured in a commercial SQUID magnetometer (Quantum Design). Field-cooled temperature-dependent magnetization measurements and magnetic hysteresis loops were performed up to applied magnetic fields of 70 kOe between 10 and 250 K. The magnetic field was applied parallel to the substrate plane. The diamagnetic contribution of the STO substrate was accurately subtracted by measuring magnetization loops at 300 K and assuming a temperature-independent susceptibility.

RESULTS AND DISCUSSION

Magnetic and transport properties of LMO thin films as a function of P_{O_2} during the growth process are shown in Figure 1. The evolution of the temperature-dependent magnetization (measured at 5 kOe) is plotted in Figure 1a, while $M(H)$ curves at 5 K are plotted in Figure 1b. It is evident from the figures that films grown at the lowest available pressure ($P_{O_2} \sim 5 \times 10^{-3}$ mTorr) show a negligible magnetization from 300 to 140 K. At this temperature, there is a slight cusp in the $M(T)$ curve, and then, magnetization increases up to a value of 0.25 $\mu_B/f.u.$. This dependence is consistent with the canted AF behavior usually reported for bulk stoichiometric LMO material with a T_N of ~ 140 K and a residual moment of 0.16 $\mu_B/f.u.$ at 10 K.²⁴ In our case, the $M(T)$ dependence below 100 K suggests the existence of an antiferromagnet where some uncompensated moments are responsible for the slightly higher residual magnetization. Hysteresis loops also reflect the change in the magnetic properties for the different samples. It is evident from Figure 1b that coercivity diminishes as magnetization increases. Moreover, $M(H)$ loops for samples grown below $P_{O_2} = 0.1$ mTorr could correspond to an AF material in a background of unbalanced magnetic moments. As P_{O_2} is increased during deposition, the magnetization of films progressively increases. At the highest available P_{O_2} , i.e., $P_{O_2} \sim 200$ mTorr, LMO films show a robust ferromagnetic behavior with a T_C of ~ 200 K and an $M_s(10\text{ K})$ of $\sim 3.6 \mu_B/f.u.$ (as determined from M vs H curves). This result is to be compared either with a value of 4 $\mu_B/f.u.$ expected for Mn³⁺ ions or with a 40% content of Mn⁴⁺ in a double-exchange scenario. Possible variations on the Mn oxidation state between different samples have been evaluated

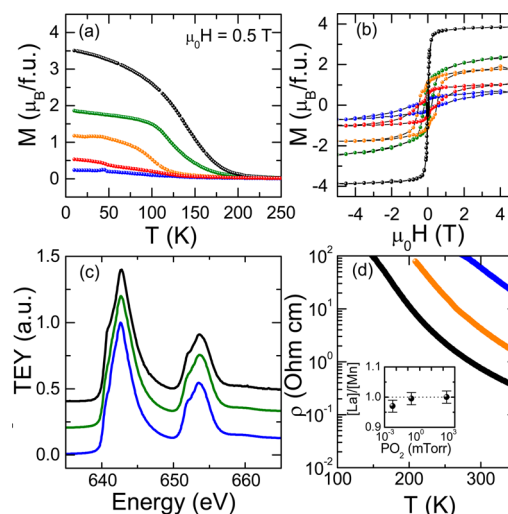


Figure 1. Magnetic and electronic properties of LMO thin films grown at different oxygen pressures (P_{O_2}) of 200 mTorr (black), 40 mTorr (green), 0.2 mTorr (orange), 0.04 mTorr (red), and 5×10^{-3} mTorr (blue). (a) Temperature dependence of magnetization measured at 0.5 T. (b) Hysteresis loops at 10 K. The diamagnetic contribution of the substrate has been removed. (c) Manganese L-edge XAS spectra measured by TEY for three different LMO samples showing that no significant change in the Mn³⁺:Mn⁴⁺ ratio is observed. (d) Temperature dependence of the electrical resistivity. The inset of panel d shows the La:Mn ratio as measured by WDS.

by means of XAS experiments. It has been previously reported that as the Mn valence is increased, the Mn L₃ edge peak shifts toward higher energies (almost 1.5–2 eV in the case of Mn³⁺ to Mn⁴⁺) and the ratio of L₃ (~ 642.5 eV) to L₂ (~ 653.5 eV) intensity decreases.^{25,26} Figure 1c shows the TEY spectra around the L_{2/3} edge for three different films prepared under different P_{O_2} partial pressures. Neither an energy shift in the peak position nor an overall change of the spectral shape on the P_{O_2} partial pressures can be detected. This result clearly indicates that the Mn³⁺:Mn⁴⁺ ratio remains unchanged through the whole series of samples. The small shoulder observed around 640 eV in the sample grown at 200 mTorr may be attributed to the presence of Mn²⁺ formed at the surface of the film after exposure to air as previously reported for manganite films.²⁷ The temperature dependence of the electrical resistivity of the LMO thin films is depicted in Figure 1d. All the measured samples exhibit insulating behavior with no sign of metallic-insulating transition within our accessible range of resistances. The electronic transport properties of LMO films may be affected by the presence of La/Mn vacancies. It is usually observed that La vacancies promote metallic behavior by a double-exchange mechanism, while doping induced by Mn vacancies is thought to lead to insulating behavior.^{10,11,13,14} To exclude this scenario, it is crucial to ensure a stoichiometric 1:1 La:Mn relationship in all the films. WDS results, shown in the inset of Figure 1d, indicate that this is the case, except for a small La deficiency detected in samples grown at the lowest P_{O_2} . For these samples grown at the lowest P_{O_2} , WDS results indicate a La:Mn ratio of ~ 0.97 , thus suggesting that the generation of La vacancies is the mechanism for accommodating oxygen vacancies during the growth process in a reducing atmosphere. Therefore, for samples grown at the lowest P_{O_2} , assuming no change in the Mn oxidation state, charge

equilibrium would lead to a film composition of $\text{La}_{0.97}\text{MnO}_{3+\delta}$ clearly in the AF-I region of the phase diagram. In all the other samples, even at high oxygen pressures, a La:Mn ratio is 1 and the arguments made above cannot be invoked to explain the observed transport properties.

As mentioned in the Introduction, the electronic properties of LMO samples may also be affected by structural strain. In this regard, it is worth mentioning that epitaxial accommodation of the highly distorted orthorhombic LMO structure onto cubic STO substrates is not trivial. We recall that at thin film growth temperatures ($T = 850^\circ\text{C}$), stoichiometric bulk LMO crystallizes in a $Pbnm$ orthorhombic structure with pseudocubic parameters $a/\sqrt{2} \sim b/\sqrt{2} \sim c/2 = 0.3932\text{ nm}$.²⁸ At 750 K, a cooperative Jahn–Teller transition takes place, and even though the structure is still described by an orthorhombic $Pbnm$ space group, MnO_6 octahedra are highly distorted and cell parameters change to $a = 0.5533\text{ nm}$, $b = 0.5727\text{ nm}$, and $c = 0.7668\text{ nm}$ (at 300 K).⁶ As a result, two different Mn–Mn matching distances are found, 0.3982 nm in the a – b plane and 0.3834 nm along the c -axis, resulting in approximately -2% compressive and $+2\%$ tensile mismatching, respectively. In an oxygen rich atmosphere, La and/or Mn vacancies may be created to accommodate oxygen off-stoichiometry, although, for the sake of clarity, the $\text{LaMnO}_{3+\delta}$ notation is commonly used in the literature. $Pbnm$ symmetry is maintained, and lattice parameters vary then as a function of this oxygen excess up to values of $a = 0.5507\text{ nm}$, $b = 0.5495\text{ nm}$, and $c = 0.7766\text{ nm}$ for $\delta = 0.07$.⁷ In this case, Mn–Mn distances are 0.3890 nm in plane and 0.3883 nm out of plane. Here, strain induced by STO substrate ($a_{\text{STO}} = 0.3905\text{ nm}$) is tensile in a parallel or perpendicular configuration and lower than 0.6%. At higher values of δ , the phase is no longer described by the $Pbnm$ space group, and instead, a rhombohedral $R3c$ structure is found.^{5–7} Because of the closely competing epitaxial relationships, it is important to first determine if LMO grows with its c -axis parallel or perpendicular to the plane of the substrate as schematically indicated in panels a and b of Figure 2. To distinguish between these two possible crystallographic orientations, we have performed a series of ϕ scans around integer and half-integer reflections. These half-integer Bragg peaks are associated with the rotations of oxygen octahedra, and their occurrence (or absence) is used to determine the orientation of the LMO orthorhombic c -axis relative to the substrate.^{29,30} In particular, assuming h , k , l Miller indexes following the reciprocal space axes Q_x , Q_y , and Q_z of a primitive cubic cell, when the c -axis is contained in the plane of the substrate reflections of the type $h/2$, k , l (with $h = \text{odd}$) appear while h , k , $l/2$ with $l = \text{odd}$ are present only if the LMO c -axis is out of plane. Reflections of the type $h/2$, $k/2$, $l/2$ with all indexes h , k , l being odd are allowed for both orientations. In panels c and d of Figure 2, we have plotted a two-dimensional projection of the reciprocal space map (in units of STO cell) with $Q_{\text{ip}} = \sqrt{(Q_x^2 + Q_y^2)}$ being the in-plane component (referred to substrate) and the Q_z component of momentum being perpendicular to the substrate. For both samples, reflections with integer h , k , l are masked by those of the STO substrate, while reflections of the type $h/2$, k , l are observed and those of the type h , k , $l/2$ absent. This result is consistent with orthorhombic LMO with the c -axis in plane following both $[100]$ and $[010]$ directions of the STO substrate (Figure 2a). Note that this epitaxial relationship has important implications for the analysis of the expected magnetic behavior of the films as a – b planes are lying perpendicular to the

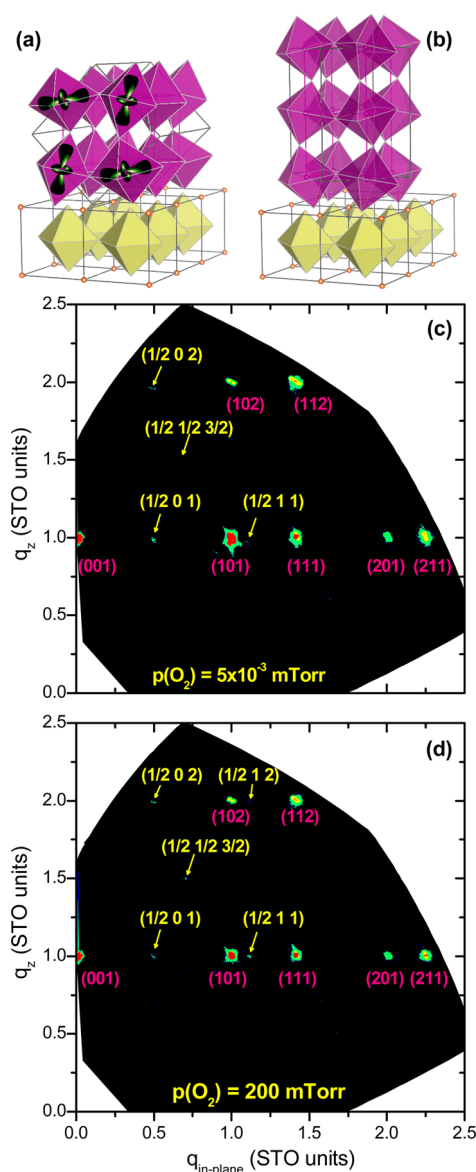


Figure 2. Schematic representation of the possible crystallographic orientation of LMO thin films, with an orthorhombic c -axis in the plane of the substrate (a) or perpendicular to it (b). Schema of the expected orbital ordering leading to the antiferromagnetic state shown in panel a. (c and d) Two-dimensional projections of the reciprocal space map for the samples grown at the lowest (5×10^{-3} mTorr) and highest (200 mTorr) oxygen pressures, respectively. For the sake of clarity, STO substrate units are used by taking $a_{\text{STO}} = 0.3905\text{ nm}$. Reflections are labeled in yellow, showing that only half-integer reflections of the kind $h/2$, k , l are observed, compatible with crystallographic orientation in panel a. Integer LMO reflections are masked by those of the STO substrate (labeled in violet).

substrate and the expected staggered orbital ordering leading to the AF state will be arranged in an out-of-plane manner as schematically shown in Figure 2a.

As LMO thin film reflections are difficult to resolve from those of substrate, resolution of usual reciprocal space maps (for example, using a 114 reflection) is not enough to elucidate the in-plane strain state of the LMO thin films. For this, we have performed high-resolution reciprocal space maps around h , k , 0 reflections with grazing incidence. In this experimental configuration, low X-ray penetration minimizes the substrate

signal and information about the LMO thin film can be accurately obtained. Panels a and b of Figure 3 show reciprocal

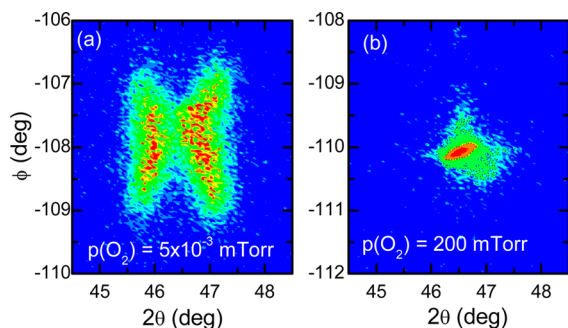


Figure 3. In-plane reciprocal space maps around 200 reflections of samples grown at (a) the lowest (5×10^{-3} mTorr) and (b) highest (200 mTorr) oxygen pressures.

space maps around 200 reflections for the same samples as in Figure 2. We see (Figure 3a) that the sample grown under low P_{O_2} presents a microstructure with well-defined twinned domains corresponding to two different in-plane cell parameters of 0.3946 and 0.3866 nm. Comparing those values with the expected bulk values (0.3982 and 0.3834 nm, respectively), we may conclude that the film is partially relaxed. The cross shape of the in-plane map is consistent with the formation of (110) twin planes inducing a slight in-plane rotation of the domains, which produces the spread in the ϕ angle shown in the map. On the other hand, for films grown under oxidizing atmospheres, only one clear peak is observed and in-plane parameters match those of the underlying substrate $a_{STO} = 0.3905$ nm (Figure 3b). In this case, LMO films are fully strained. Films grown at intermediate oxygen pressures exhibit different degrees of strain. A way to monitor this continuous evolution of the microstructural strain state of the films has been possible by studying the equivalent out-of-plane pseudocubic lattice parameter. The out-of-plane values obtained by fitting the $\theta - 2\theta$ (002 LMO + 002 STO) high-resolution XRD profiles are plotted in Figure 4a as a function of

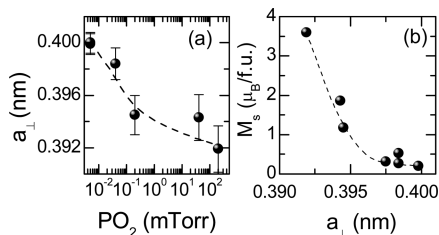


Figure 4. (a) Variation of the out-of-plane lattice parameter (referred to the pseudocubic lattice) of LMO thin films as a function of oxygen pressure. (b) Dependence of saturation magnetization on the out-of-plane lattice parameter.

oxygen partial pressure during deposition. Error bars, determined from the standard deviation of the least-squares fit, increase as the LMO peak position approaches that of the underlying substrate. We may observe that out-of-plane parameter ranges from values as high as 0.400 nm when LMO is grown under reducing conditions to 0.392 nm, i.e., close to the STO lattice parameter in the highest- P_{O_2} atmosphere. This structural evolution is concomitant to the

variation of the functional properties presented above, and indeed, there is a close relationship between saturation magnetization and out-of-plane parameter as shown in Figure 4b. In light of these findings, a plausible scenario emerges to account for the spread of experimental results reported for LMO thin films. At reducing atmospheres, LMO thin films are partially relaxed, with their structure close to that of the stoichiometric bulk compound. Cooperative Jahn–Teller distortions lead to the stabilization of a staggered $d_{3x^2-r^2}/d_{3y^2-r^2}$ ordering resulting in an A-type AF-I state. However, magnetic moments are supposed to be aligned along the orthorhombic b -axis that, in twinned films, is pointing out of the substrate at four possible directions forming a 45° angle with the direction perpendicular to the film substrate. As a consequence, it is difficult to observe a clean and net AF response. This twinned structure, leading to antiferromagnetic domain walls, could account also for the residual magnetic moment observed in the AF phase. In films deposited at progressively higher P_{O_2} values, the extent of film substrate mismatch is reduced, allowing a coherent epitaxial growth of fully strained films. In this situation, strain modifies the usual Jahn–Teller distortion picture and different orbital orderings are possible. In our case, an FM-I phase is stabilized, which is compatible with recent theoretical proposals suggesting a three-dimensional $d_{3z^2-r^2}/d_{x^2-y^2}$ orbital ordering.²³ Note that, in both cases, the expected orbital arrangements lead to a mixing of occupied out-of-plane and in-plane orbitals (see Figure 2). Thus, the usual synchrotron techniques for studying orbital occupancy as, for example, X-ray linear dichroism (XLD) are not longer straightforward to apply. Furthermore, the presence of twinned microstructures would make it almost impossible to reach any solid conclusion about selective orbital occupancy from XLD measurements. Nevertheless, our results showed that the possible orbital and magnetic arrangements and the role of cooperative Jahn–Teller distortions in the parent compound $LaMnO_3$ and other reported FMI phases as, for example, low-doped $La_{1-x}Sr_xMnO_3$ deserve further attention.^{31,32}

CONCLUSIONS

In summary, we have carefully studied the epitaxial growth process of $LaMnO_3$ thin films on STO substrates, demonstrating that the accommodation of the LMO orthorhombic structure on the STO cubic structure is a complex process that can be properly controlled by modifying the nominal oxygen pressure during the growth process. This structural accommodation implies a substantial modification of the amount of structural strain in the LMO film that, in turns, has subtle effects on the final magnetic and electronic properties of the films. Our results show that films with bulklike AF-I properties are obtained only when they are grown under reducing atmospheres that lead to partially relaxed structures. In contrast, when film growth takes place under oxidizing conditions, fully strained films exhibiting FM-I behavior are obtained. Other scenarios, such as La or Mn vacancies, leading to a variation of the Mn oxidation state have been excluded in the base of WDS and XAS measurements. Although further spectroscopic research may be necessary to gain a complete picture of the magnetic and orbital arrangements while still disregarding doping effects, our results strongly point to a strain-induced selective orbital occupancy

as the origin of the observed FM behavior in agreement with recent theoretical calculations.

AUTHOR INFORMATION

Corresponding Author

*E-mail: apomar@icmab.es. Telephone: + 34-93-580-18-53. Fax: +34-93-580-57-29.

Notes

The authors declare no competing financial interest.

ACKNOWLEDGMENTS

We acknowledge financial support from the Spanish MINECO (MAT2011-29081 and MAT2012-33207), CONSOLIDER (CSD2007-00041), and FEDER program. We thank P. García for his kind assistance during X-ray experiments. ICN2 acknowledges support from the Severo Ochoa Program (MINECO, Grant SEV 2013-0295). Z.K. is grateful for the support from the Ministry of Education, Science, and Technological Development of the Republic of Serbia through Project III45018. This work has received funding from the European Union's Horizon 2020 research and innovation programme under the Marie Skłodowska-Curie grant agreement No. 645658.

REFERENCES

- (1) Gibert, M.; Zubko, P.; Scherwitzl, R.; Iniguez, J.; Triscone, J. M. Exchange bias in LaNiO₃-LaMnO₃ superlattices. *Nat. Mater.* **2012**, *11*, 195–198.
- (2) Garcia-Barriocanal, J.; Bruno, F. Y.; Rivera-Calzada, A.; Sefrioui, Z.; Nemes, N. M.; Garcia-Hernandez, M.; Rubio-Zuazo, J.; Castro, G. R.; Varela, M.; Pennycook, S. J.; Leon, C.; Santamaria, J. "Charge Leakage" at LaMnO₃/SrTiO₃ Interfaces. *Adv. Mater.* **2010**, *22*, 627–632.
- (3) Garcia-Barriocanal, J.; Cezar, J. C.; Bruno, F. Y.; Thakur, P.; Brookes, N. B.; Uthfeld, C.; Rivera-Calzada, A.; Giblin, S. R.; Taylor, J. W.; Duffy, J. A.; Dugdale, S. B.; Nakamura, T.; Kodama, K.; Leon, C.; Okamoto, S.; Santamaria, J. Spin and orbital Ti magnetism at LaMnO₃/SrTiO₃ interfaces. *Nat. Commun.* **2010**, *1*, 82.
- (4) Bhattacharya, A.; May, S. J.; te Velthuis, S. G. E.; Warusawithana, M.; Zhai, X.; Jiang, B.; Zuo, J. M.; Fitzsimmons, M. R.; Bader, S. D.; Eckstein, J. N. Metal-insulator transition and its relation to magnetic structure in (LaMnO₃)_{2n}/(SrMnO₃)_n superlattices. *Phys. Rev. Lett.* **2008**, *100*, 257203.
- (5) Topfer, J.; Goodenough, J. B. LaMnO_{3+delta} revisited. *J. Solid State Chem.* **1997**, *130*, 117–128.
- (6) Huang, Q.; Santoro, A.; Lynn, J. W.; Erwin, R. W.; Borchers, J. A.; Peng, J. L.; Greene, R. L. Structure and magnetic order in undoped lanthanum Manganite. *Phys. Rev. B: Condens. Matter Mater. Phys.* **1997**, *55*, 14987–14999.
- (7) Ritter, C.; Ibarra, M. R.; DeTeresa, J. M.; Algarabel, P. A.; Marquina, C.; Blasco, J.; Garcia, J.; Oseroff, S.; Cheong, S. W. Influence of oxygen content on the structural, magnetotransport, and magnetic properties of LaMnO_{3+delta}. *Phys. Rev. B: Condens. Matter Mater. Phys.* **1997**, *56*, 8902–8911.
- (8) Aruta, C.; Angeloni, M.; Balestrino, G.; Boggio, N. G.; Medaglia, P. G.; Tebano, A.; Davidson, B.; Baldini, M.; Di Castro, D.; Postorino, P.; Dore, P.; Sidorenko, A.; Allodi, G.; De Renzi, R. Preparation and characterization of LaMnO₃ thin films grown by pulsed laser deposition. *J. Appl. Phys.* **2006**, *100*, 023910.
- (9) Orgiani, P.; Aruta, C.; Ciancio, R.; Galdi, A.; Maritato, L. Enhanced transport properties in La_xMnO_{3-delta} thin films epitaxially grown on SrTiO₃ substrates: The profound impact of the oxygen content. *Appl. Phys. Lett.* **2009**, *95*, 013510.
- (10) Kim, H. S.; Christen, H. M. Controlling the magnetic properties of LaMnO₃ thin films on SrTiO₃(100) by deposition in a O₂/Ar gas mixture. *J. Phys.: Condens. Matter* **2010**, *22*, 146007.
- (11) Choi, W. S.; Marton, Z.; Jang, S. Y.; Moon, S. J.; Jeon, B. C.; Shin, J. H.; Seo, S. S. A.; Noh, T. W.; Myung-Whun, K.; Lee, H. N.; Lee, Y. S. Effects of oxygen-reducing atmosphere annealing on LaMnO₃ epitaxial thin films. *J. Phys. D: Appl. Phys.* **2009**, *42*, 165401.
- (12) Marton, Z.; A. Seo, S. S.; Egami, T.; Lee, H. N. Growth control of stoichiometry in LaMnO₃ epitaxial thin films by pulsed laser deposition. *J. Cryst. Growth* **2010**, *312*, 2923–2927.
- (13) Choi, W. S.; Jeong, D. W.; Jang, S. Y.; Marton, Z.; Seo, S. S. A.; Lee, H. N.; Lee, Y. S. LaMnO₃ Thin Films Grown by Using Pulsed Laser Deposition and Their Simple Recovery to a Stoichiometric Phase by Annealing. *J. Korean Phys. Soc.* **2011**, *58*, 569–574.
- (14) Marozau, I.; Das, P. T.; Dobei, M.; Storey, J. G.; Uribe-Laverde, M. A.; Das, S.; Wang, C. N.; Rossle, M.; Bernhard, C. Influence of La and Mn vacancies on the electronic and magnetic properties of LaMnO₃ thin films grown by pulsed laser deposition. *Phys. Rev. B: Condens. Matter Mater. Phys.* **2014**, *89*, 174422.
- (15) Orgiani, P.; Galdi, A.; Aruta, C.; Cataudella, V.; De Filippis, G.; Perroni, C. A.; Marigliano Ramaglia, V. M.; Ciancio, R.; Brookes, N. B.; Moretti Sala, M.; Ghiringhelli, G.; Maritato, L. Multiple double-exchange mechanism by Mn²⁺ doping in Manganite compounds. *Phys. Rev. B: Condens. Matter Mater. Phys.* **2010**, *82*, 205122.
- (16) Galdi, A.; Aruta, C.; Orgiani, P.; Brookes, N. B.; Ghiringhelli, G.; Moretti Sala, M.; Mangalam, R. V. K.; Prellier, W.; Luders, U.; Maritato, L. Magnetic properties and orbital anisotropy driven by Mn²⁺ in nonstoichiometric La_xMnO_{3-delta} thin films. *Phys. Rev. B: Condens. Matter Mater. Phys.* **2011**, *83*, 064418.
- (17) Ahn, K. H.; Millis, A. J. Effects of in-plane strain on magnetism in LaMnO₃ thin films. *Int. J. Mod. Phys. B* **2002**, *16*, 3281–3284.
- (18) Nanda, B. R. K.; Satpathy, S. Effects of strain on orbital ordering and magnetism at perovskite oxide interfaces: LaMnO₃(3)/SrMnO₃(3). *Phys. Rev. B: Condens. Matter Mater. Phys.* **2008**, *78*, 054427.
- (19) Nanda, B. R. K.; Satpathy, S. Magnetic and orbital order in LaMnO₃ under uniaxial strain: A model study. *Phys. Rev. B: Condens. Matter Mater. Phys.* **2010**, *81*, 064418.
- (20) Nanda, B. R. K.; Satpathy, S. Density functional studies of LaMnO₃ under uniaxial strain. *J. Magn. Magn. Mater.* **2010**, *322*, 3653–3657.
- (21) Lee, J. H.; Delaney, K. T.; Bousquet, E.; Spaldin, N. A.; Rabe, K. M. Strong coupling of Jahn-Teller distortion to oxygen-octahedron rotation and functional properties in epitaxially strained orthorhombic LaMnO₃. *Phys. Rev. B: Condens. Matter Mater. Phys.* **2013**, *88*, 174426.
- (22) Solov'ev, I.; Hamada, N.; Terakura, K. Crucial role of the lattice distortion in the magnetism of LaMnO₃. *Phys. Rev. Lett.* **1996**, *76*, 4825–4828.
- (23) Hou, Y. S.; Xiang, H. J.; Gong, X. G. Intrinsic insulating ferromagnetism in manganese oxide thin films. *Phys. Rev. B: Condens. Matter Mater. Phys.* **2014**, *89*, 064415.
- (24) Skumryev, V.; Ott, F.; Coey, J. M. D.; Anane, A.; Renard, J. P.; Pinsard-Gaudart, L.; Revcolevschi, A. Weak ferromagnetism in LaMnO₃. *Eur. Phys. J. B* **1999**, *11*, 401–406.
- (25) Cramer, S. P.; Degroot, F. M. F.; Ma, Y.; Chen, C. T.; Sette, F.; Kipke, C. A.; Eichhorn, D. M.; Chan, M. K.; Armstrong, W. H.; Libby, E.; Christou, G.; Brooker, S.; McKee, V.; Mullins, O. C.; Fuggle, J. C. Ligand-field strengths and oxidation states from manganese L-edge spectroscopy. *J. Am. Chem. Soc.* **1991**, *113*, 7937–7940.
- (26) Qiao, R. M.; Chin, T.; Harris, S. J.; Yan, S. S.; Yang, W. L. Spectroscopic fingerprints of valence and spin states in manganese oxides and fluorides. *Curr. Appl. Phys.* **2013**, *13*, 544–548.
- (27) Valencia, S.; Gaupp, A.; Gudat, W.; Abad, L.; Balcells, L.; Cavallaro, A.; Martinez, B.; Palomares, F. J. Mn valence instability in La_{2/3}Ca_{1/3}MnO₃ thin films. *Phys. Rev. B: Condens. Matter Mater. Phys.* **2006**, *73*, 7104402.
- (28) Chatterji, T.; Fauth, F.; Ouladdiaf, B.; Mandal, P.; Ghosh, B. Volume collapse in LaMnO₃ caused by an orbital order-disorder transition. *Phys. Rev. B: Condens. Matter Mater. Phys.* **2003**, *68*, 052406.
- (29) Johnson-Wilke, R. L.; Marincel, D.; Zhu, S.; Warusawithana, M. P.; Hatt, A.; Sayre, J.; Delaney, K. T.; Engel-Herbert, R.; Schlepütz, C. M.; Kim, J. W.; Gopalan, V.; Spaldin, N. A.; Schlom, D. G.; Ryan, P. J.; Trolrier-McKinstry, S. Quantification of octahedral rotations in strained

LaAlO₃ films via synchrotron x-ray diffraction. *Phys. Rev. B: Condens. Matter Mater. Phys.* **2013**, *88*, 174101.

(30) May, S. J.; Kim, J. W.; Rondinelli, J. M.; Karapetrova, E.; Spaldin, N. A.; Bhattacharya, A.; Ryan, P. J. Quantifying octahedral rotations in strained perovskite oxide films. *Phys. Rev. B: Condens. Matter Mater. Phys.* **2010**, *82*, 014110.

(31) Geck, J.; Wochner, P.; Kiele, S.; Klingeler, R.; Reutler, P.; Revcolevschi, A.; Büchner, B. Orbital Polaron Lattice Formation in Lightly Doped La_{1-x}Sr_xMnO₃. *Phys. Rev. Lett.* **2005**, *95*, 236401.

(32) Golenishchev-Kutuzov, A. V.; Golenishchev-Kutuzov, V. A.; Kalimullin, R. I.; Semennikov, A. V. Ordered states of Jahn-Teller distorted MnO₆ octahedra in weakly doped lanthanum-strontium manganites. *Phys. Solid State* **2015**, *57*, 1633–1638.

■ NOTE ADDED AFTER ASAP PUBLICATION

This paper was published ASAP on September 24, 2015, with an error to an author's surname. The corrected version was reposted on September 29, 2015.

Intrinsic antiferromagnetic/insulating phase at manganite surfaces and interfaces

S Valencia^{1,4}, L Peña², Z Konstantinovic², LI Balcells², R Galceran²,
D Schmitz¹, F Sandiumenge², M Casanove³ and B Martínez²

¹ Helmholtz-Zentrum-Berlin, Albert-Einstein-Str. 15, 12489 Berlin, Germany

² Institut de Ciència de Materials de Barcelona-CSIC, Campus de la UAB, 08193 Bellaterra, Spain

³ Centre d'Elaboration de Matériaux et d'Etudes Structurales (CNRS-CEMES),
BP 94347, 29 rue Jeanne Maarving, 31055 Toulouse, France

E-mail: ben.martinez@icmab.es

Received 10 December 2013, revised 4 February 2014

Accepted for publication 6 February 2014

Published 1 April 2014

Abstract

In this work we investigate interfacial effects in bilayer systems integrated by $\text{La}_{2/3}\text{Sr}_{1/3}\text{MnO}_3$ (LSMO) thin films and different capping layers by means of surface-sensitive synchrotron radiation techniques and transport measurements. Our data reveal a complex scenario with a capping-dependent variation of the Mn oxidation state by the interface. However, irrespective of the capping material, an antiferromagnetic/insulating phase is also detected at the interface, which is likely to originate from a preferential occupancy of Mn 3d $3z^2-r^2$ e_g orbitals. This phase, which extends approximately to two unit cells, is also observed in uncapped LSMO reference samples, thus pointing to an intrinsic interfacial phase separation phenomenon, probably promoted by the structural disruption and inversion symmetry breaking at the LSMO free surface/interface. These experimental observations strongly suggest that the structural disruption, with its intrinsic inversion symmetry breaking at the LSMO interfaces, plays a major role in the observed depressed magnetotransport properties in manganite-based magnetic tunneling junctions and explains the origin of the so-called dead layer.

Keywords: complex oxides, manganites, interfacial effects, thin films

(Some figures may appear in colour only in the online journal)

1. Introduction

Complex oxides have emerged as one of the most interesting classes of materials due to their remarkable variety of properties which are of strong theoretical and technological interest, including superconductivity, ferromagnetism, ferroelectricity, etc. Transition metal (TM) oxides are especially relevant since they present large electronic correlations leading to strong competition between various degrees of freedom [1]. The physical properties of TM oxides are determined by d electrons and the way they are distributed between the five-fold degenerate 3d orbitals. Hence, control of 3d-orbital occupancy is expected to allow the engineering of new functionalities [2–4]. The strong electronic correlations in these materials induce a local entanglement of the charge, spin and orbital degrees of freedom, which enables different options, such as structural

distortions and crystal chemistry, to control 3d-orbital occupancy. These features offer the possibility of an active tuning of physical (electronic and magnetic) and chemical (catalytic reactivity, wettability, etc) properties. From this perspective TM oxide heterostructures offer a unique arena for engineering new functionalities since charge, spin and orbital degrees of freedom meet at interfaces and are strongly affected by electronic processes such as charge transfer, hybridization and exchange interactions. In recent years, there has been intense activity in this field and several new phenomena and novel states of matter have been reported [2, 5–7].

Among complex oxides, manganites, with their very robust perovskite structure, offer a plethora of possibilities, from both a fundamental and an applied physics point of view. Manganites are complex systems exhibiting a broad range of physical phenomena, including large spin polarization and colossal magnetoresistance [8]. These properties make them very appealing for

⁴ Author to whom any correspondence should be addressed.

the development of novel concepts for the implementation of oxide-based spintronic devices. Especially relevant is the case of $\text{La}_{0.67}\text{Sr}_{0.33}\text{MnO}_3$ (LSMO) which exhibits the highest magnetic transition temperature ($T_C \sim 370\text{K}$) of this family of compounds [9], and therefore could be implemented in magnetic tunneling devices that work at room temperature. However, state-of-the-art LSMO-based junctions show vanishingly small tunneling magnetoresistance (TMR) values above 280 K [10]. This is usually attributed to the existence of a so-called dead layer, a few unit cells wide, at the interface between the manganite and the tunnel barrier, whose origin is not yet well understood. TMR is a spin-dependent process and, as such, depends critically on the conducting and magnetic properties of the few atomic layers next to the insulating barrier. When two dissimilar oxides are placed together, such as the case of manganite/tunnel barriers in all oxide magnetic tunneling junctions (MTJs), electronic and structural reconstruction at the interface, controlled primarily by elastic strain and electrostatic boundary conditions, may substantially modify 3d-orbital filling, breaking the e_g -orbital degeneracy, thus drastically modifying the magnetic and transport properties.

The study of interfacial effects is difficult because in LSMO/tunnel barrier structures interfaces are buried several nm below the top electrode. Consequently, most approaches have consisted of investigating the film/substrate bottom interface in ultra-thin films. In these cases it is expected that the structural strain imposed by the substrate will play a dominant role. The substrate constrains the in-plane film cell parameters and imposes its in-plane symmetry operations on the film. The latter, being much weaker than the former, will affect the first few cells close to the film/substrate interface and relax [11,12]. In fact, it has been shown both theoretically [13] and experimentally [14–16] that tensile stress favors the x^2-y^2 orbital occupancy and thus CE-type antiferromagnetic (AF) ordering while compressive strain favors $3z^2-r^2$ occupancy leading to a C-type AF ordering. However, x-ray linear dichroism (XLD) investigations in manganite ultra-thin films show that, irrespective of the biaxial strain conditions, the interfacial Mn atoms show a preferential occupancy of the Mn 3d $3z^2-r^2$ e_g orbitals [15–17]. The reason for this strain-independent selective orbital occupancy is not yet clearly established.

In this work we address the origin of the so-called dead layer appearing by the interface in the manganite/tunnel barrier MTJ. We characterize the magnetic and transport properties at the interface between LSMO and different capping layers (CLs) of interest for spintronic applications (SrTiO_3 , LaAlO_3 (LAO), NdGaO_3 (NGO), MgO and Au), representative of the manganite/tunnel barrier interface in MTJ. In order to isolate the electronic structure at the interface, we performed a systematic series of experiments on heterostructures with different CLs, taking advantage of the element specificity and shallow probing depth of x-ray absorption spectroscopy (XAS), x-ray magnetic circular dichroism (XMCD) and XLD in the total electron yield (TEY) mode.

Our data reveals the presence of about 1 nm thick AF/insulating layer at the LSMO/CL interface, which is independent of the capping material and very similar to that found at the free surface of the LSMO thin films. Our results indicate that the structural

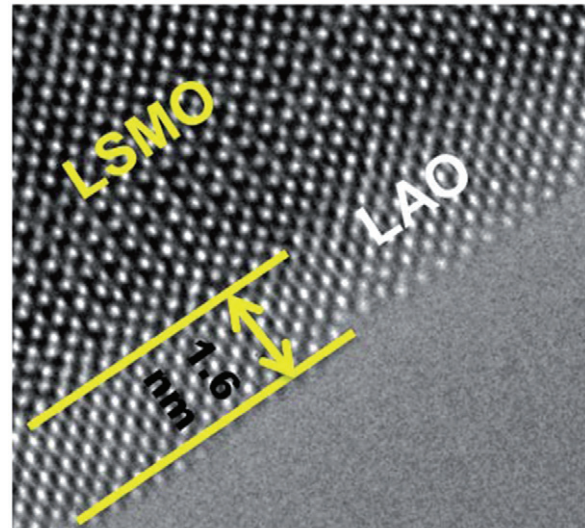


Figure 1. HRTEM picture of the LSMO/LAO interface

disruption, with its intrinsic inversion symmetry breaking at the interfaces, lay at the origin of the so-called dead layer.

2. Results and discussion

LSMO samples used in this work were prepared by radio frequency (RF) magnetron sputtering on top of the (001)-oriented SrTiO_3 (STO) substrates. Prior to deposition STO substrates were cleaned in an ultrasonic bath with Milli-Q water and annealed at 1000°C in air for 2 h to obtain a typical morphology of terraces and step with unit cell height ($\approx 0.4\text{ nm}$), thus selecting a mostly unique atomic termination, likely to be TiO_2 . The thickness of the samples ($\sim 40\text{ nm}$) was determined by using grazing incident x-ray reflectometry. The thickness of the CLs ($t_c \sim 1.6 \pm 0.2\text{ nm}$) was determined by controlling the evaporation time after a careful calibration of the growth rate for each of the different materials used. It was also checked ‘*a posteriori*’ by using high-resolution transmission electron microscopy (HRTEM), obtaining good agreement with the nominal values (see figure 1). Further details regarding sample preparation can be found in [18]. Reciprocal space mapping was performed using a Bruker D8 GADDS system equipped with a 2D Hi-Star x-ray detector to determine the degree of strain on the films. LSMO films are in-plane fully strained [19], which according to previous results will favor the preferential occupancy of x^2-y^2 orbitals [13–16]. Samples exhibit ferromagnetic (FM) transition temperatures slightly below that of the bulk material with values of the saturation magnetization close to that of the bulk. A complete magnetic characterization of the samples can be found in [19].

The synchrotron radiation experiments were performed at the electron storage ring of the Helmholtz-Zentrum Berlin (BESSY) by using the 70 kOe high-field end station located at the UE46-PGM1 beamline. The experiments were done at low temperature ($T=10\text{ K}$), thus well within the FM phase of the LSMO thin films ($T_C \approx 350\text{ K}$). XAS and XMCD spectra at the Mn $L_{3,2}$ -edge were obtained at various fields ranging from 0 to 6 T applied perpendicular to the sample surface with the

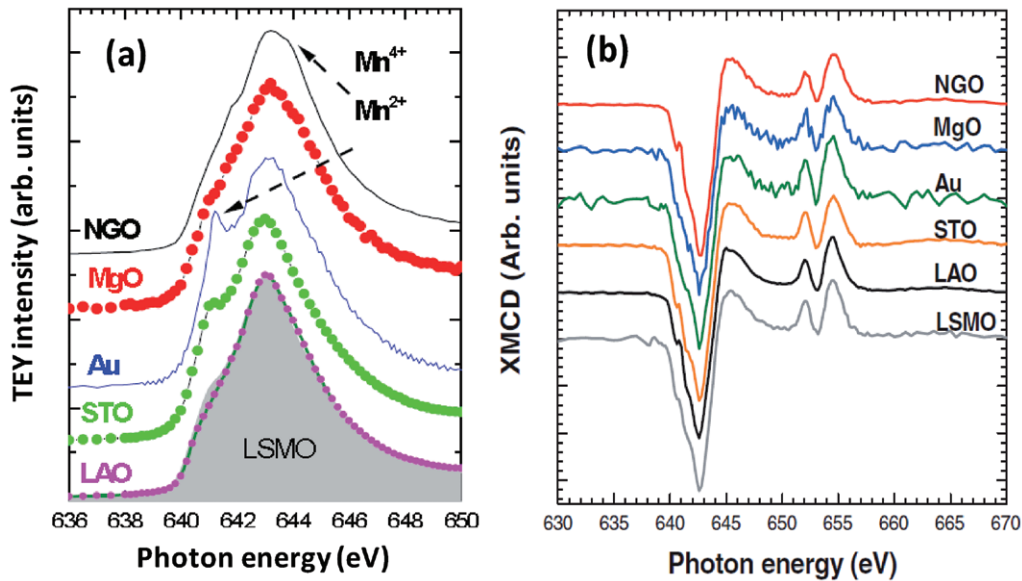


Figure 2. (a) Mn L_3 -edge absorption spectra for LSMO/CL bilayers obtained at $H = 0$ T and $T = 10$ K. Spectra are vertically shifted in order to allow better comparison. The reference spectrum corresponding to an LSMO uncapped film is shown in gray. (b) XMCD spectra corresponding to LSMO films with different CLs. Spectra are vertically shifted in order to allow better comparison.

incoming circularly polarized radiation impinging the sample at normal incidence with respect to its surface plane. XMCD spectra were obtained by reversing the polarization of the incoming circularly polarized light. The XLD experiments were done using incoming horizontal linearly polarized radiation at the Mn $L_{3,2}$ -edges and measuring spectra at two different angles of incidence, i.e. 90° (normal incidence) and 30° in order to gain sensitivity to in-plane x^2-y^2 and out-of-plane $3z^2-r^2$ oriented e_g Mn 3d orbitals, respectively. TEY detection mode was used in all cases. The escaping depth of the secondary photoelectrons (2–5 nm) guarantees that the measured spectra are mainly determined by the Mn atoms close to the interfacial region.

XAS results, obtained by averaging spectra measured with left and right incoming circularly polarized light are shown in figure 2(a), together with the reference spectrum corresponding to an uncapped LSMO film. Due to their similarities, the latter will be taken as representative of bulk LSMO [20]. It is evident from the figure that NGO and MgO capping promotes the appearance of increased intensity at the high-energy side of the L_3 peak (643–645 eV) with respect to the reference spectrum. Spectral shifts towards higher energy values are also observed, thus indicating an increase of the oxidation state of the Mn ions, i.e. an increase in the Mn^{4+} content at the interface. A comparison with the reference sample allows us to estimate that the increase in the Mn^{4+} content at the interface amounts to ~ 15 – 18% in both cases. In contrast, STO and Au capping promotes an increase of the L_3 peak intensity at the low-energy side (641.2 eV), together with a spectral shift (~ 0.1 eV) towards lower energy values. The spectral energy shift and the size of the spectral feature at 641.2 eV observed for the case of LSMO films allows for the exclusion of Mn^{4+} and Mn^{3+} contributions [21] and points to the presence of Mn^{2+} by the interface [20]. According to the procedures described in [20] the amount of Mn^{2+} is estimated to be $\sim 6\%$ for STO capping and $\sim 14\%$ for Au capping. Of particular interest is the LAO capping which

exhibits almost bulk-like spectrum with only minute differences at the low-energy side of the L_3 peak, indicating a tiny increase of Mn^{3+} /reduction of Mn^{4+} (~ 1 – 2% [21]).

The magnetic properties of the interface have been studied by using XMCD and XLD. XMCD is experimentally obtained as the difference between two absorption spectra measured with opposite helicities ($\mu+$ and $\mu-$) at normal incidence and with the films magnetically saturated out-of-plane by using a magnetic field of 3 T. A non-zero difference is the signature of FM phases. The results for different interfaces are compiled in figure 2(b). An exact determination of the interface Mn magnetization by using the so-called sum rules [22, 23] is not possible due to the large error associated with the determination of the spin contribution to the magnetic moment of Mn [24]. However, a relative comparison between the magnetic moment ($m_{\text{spin}} + m_{\text{orb}}$) per Mn atom for the different interfaces can be performed by normalizing their values to that obtained for the reference uncapped sample. It is found that, compared to the uncapped film, all CLs, except LAO, promote depressed magnetic moments at the LSMO/CL interface, in agreement with the departure from the Mn^{3+}/Mn^{4+} valence balance corresponding to the $2/3$ – $1/3$ nominal composition previously shown. The behavior observed in the case of LAO capping has been explained in terms of the different effect of electron-hole doped schemes at the LSMO interfacial layers [6, 19]. As shown in [6], hole doping by the interface, as in the case of the LSMO/LAO interface, seems to be less detrimental for the FM ordering at the uppermost LSMO layers than electron doping. The close similarity of all the XMCD spectra with that of the uncapped LSMO allows for the exclusion of any other FM phase, a part from the one expected to correspond to the $2/3$ – $1/3$ nominal composition. It is therefore clear that the reduction of magnetic properties at the LSMO/CL interface must arise from the local presence of non-magnetic (NM) and/or AF phases. To explore this possibility we employed XLD.

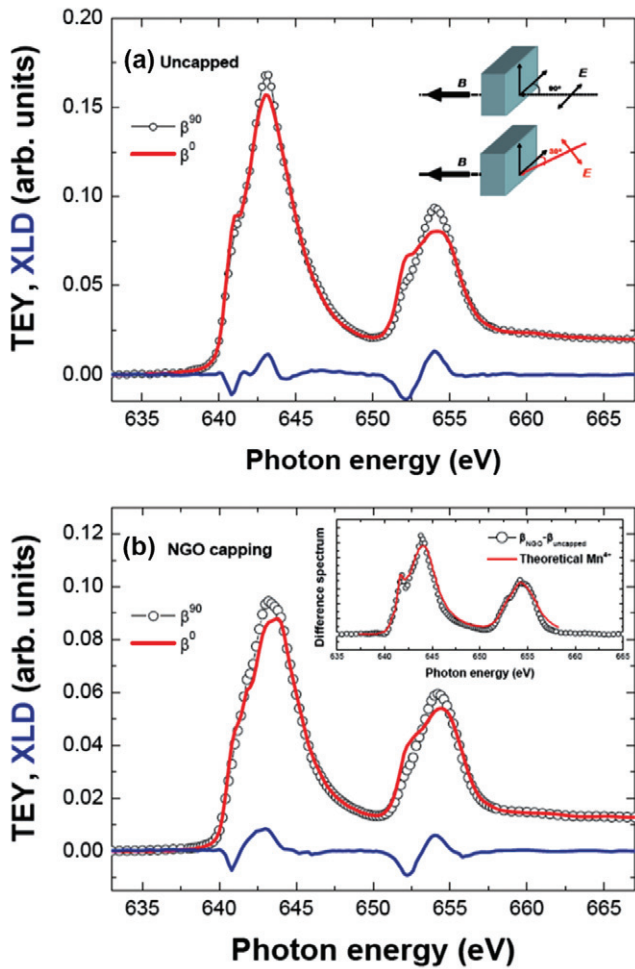


Figure 3. (a), (b) Mn $L_{3,2}$ -edge XAS spectra corresponding to the uncapped and NGO-capped LSMO samples, respectively. The electric field vector of the incoming linearly polarized radiation was set parallel (β^{90}) and almost perpendicular (β^{30}) to the surface of the sample. Both sets of data allowed calculation of the β^0 spectrum (see text). A magnetic field of 20kOe was applied parallel to the beam propagation direction saturating the sample magnetization (inset 1(a)) to remove the FM contribution to the XLD ($\beta^{90}-\beta^0$) signal (blue line). Inset 1(b): the $\beta^{NGO}-\beta^{uncapped}$ difference agrees with the expected shape for Mn^{4+} after proper scaling (open dots) (see [21]). $\beta^{uncapped}$ is characterized by a bulk-like mixed valence Mn^{3+}/Mn^{4+} spectral shape.

A magnetic field of 20kOe was applied along the beam propagation direction, saturating the sample magnetization in order to eliminate the FM contribution to the XLD spectra, thus leaving only AF and anisotropic orbital occupancy contributions. Two spectra were obtained at $\theta=90^\circ$ (β^{90}) and at $\theta=30^\circ$ (β^{30}) in order to gain sensitivity to in-plane x^2-y^2 and out-of-plane $3z^2-r^2$ oriented e_g Mn 3d orbitals, respectively. The XLD spectrum, (defined as $XLD = \beta^{90}-\beta^0$, being $\beta^0 = 4/3(\beta^{30}-1/4\beta^{90})$ [25]) corresponding to the uncapped LSMO sample is depicted in figure 3(a). Comparison with previously reported temperature-dependent XLD spectra [17] allows us to identify the presence of an AF phase whose magnetic axis is aligned perpendicularly to the sample's plane. Note that the experimental conditions guarantee that the XLD signal arises only from AF and anisotropic orbital occupancy contributions. The XLD

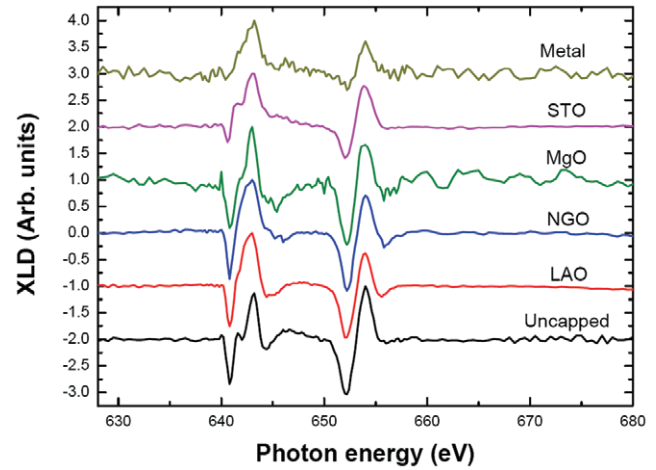


Figure 4. XLD spectra obtained at Mn $L_{3,2}$ -edge for the various LSMO/CL bilayers included in this study. The XLD has been normalized to its maximum value and an offset has been artificially applied for better comparison.

curve for the LSMO surface is identical to that reported by Aruta *et al* [17] (see figure 4(b) in [17]) as indicative of a C-type AF phase which originates from a preferential Mn 3d $3z^2-r^2$ e_g orbital occupancy, indicating that at the topmost LSMO layers close to the free surface, the e_g orbital degeneracy is broken. Similarly, recent results reported in [16] indicate that irrespective of the strained state of the samples, a preferential 3d $3z^2-r^2$ e_g orbital occupancy occurs at free surfaces. Our data go a step further and reveal that, irrespective of the CL material, a breaking of the e_g orbital degeneracy takes place at the LSMO/CL interface. The XLD spectra for the different CLs are shown in figure 4. The closeness in their spectral shape indicates that the AF phase observed in the uncapped film is also present at the interface of LSMO with different CLs, irrespective of the capping material. Moreover, a quantitative analysis of the XLD spectra demonstrates that this similarity extends not only to the spectral shape, but also to its amplitude. The amplitude, defined as $100|I_{XLD}|/I_{XAS}$, where $I_{|XLD|}$ stands for the integrated intensity of the $|XLD|$ spectrum and I_{XAS} corresponds to that of the absorption spectrum β , is similar for all samples. Comparison with the results obtained by XAS and XMCD show that the XLD amplitude is neither correlated to the NM phase content (table 1) nor to the interface magnetization reduction deduced from XMCD data. However, the XLD amplitude does exhibit a clear correlation with the DE-FM phase with the nominal Mn^{3+}/Mn^{4+} valence balance (figure 5), thus indicating the intrinsic character of this interfacial layer.

These results therefore reveal a complex scenario at the manganite's surface and interfaces in which FM, NM and AF phases coexist. Both NM and AF phases depress interfacial magnetotransport properties. The NM phase is characterized by the existence of Mn^{2+} or by an excess of Mn^{4+} atoms and is sensitive to the absence/presence and nature of the CL. On the other hand, the AF phase seems to be bound to the amount of the 2/3–1/3 DE-FM LSMO phase at the surface/interface. This fact, in addition to the surface sensitivity of the TEY detection technique, suggests that the AF phase extends homogeneously at the interface, i.e. it is indeed an interfacial layer.

Table 1. Values of the barrier thickness, t , and the barrier height, ϕ_0 , for the different CLs obtained from equation (1) in the low bias voltage regime. Δt corresponds to the difference between t and the thickness of the CL (~ 1.6 nm). NM corresponds to the fraction of phase with Mn oxidation state differing from the nominal $\text{Mn}^{3+/4+}$ mixed valence state. The relatively low value of Δt in the case of MgO deserves further investigation and might be related to the active role of the MgO barrier and its spin filtering effect. It is also worth mentioning here that for MgO capping $J(V)$ curves are slightly asymmetric and the fittings from equation (1) are worse than in the other cases. This might also affect the evaluation of Δt for MgO capping.

Capping layer	ϕ_0 (eV)	t (nm)	$\Delta t \sim t - t_c$ (nm)	NM (%)
LAO	0.45	2.6	1	$\sim 0\%$
STO	0.32	3	1.4	6%
NGO	0.41	3.6	2	15–18%
MgO	0.38	2.5	1	15–18%

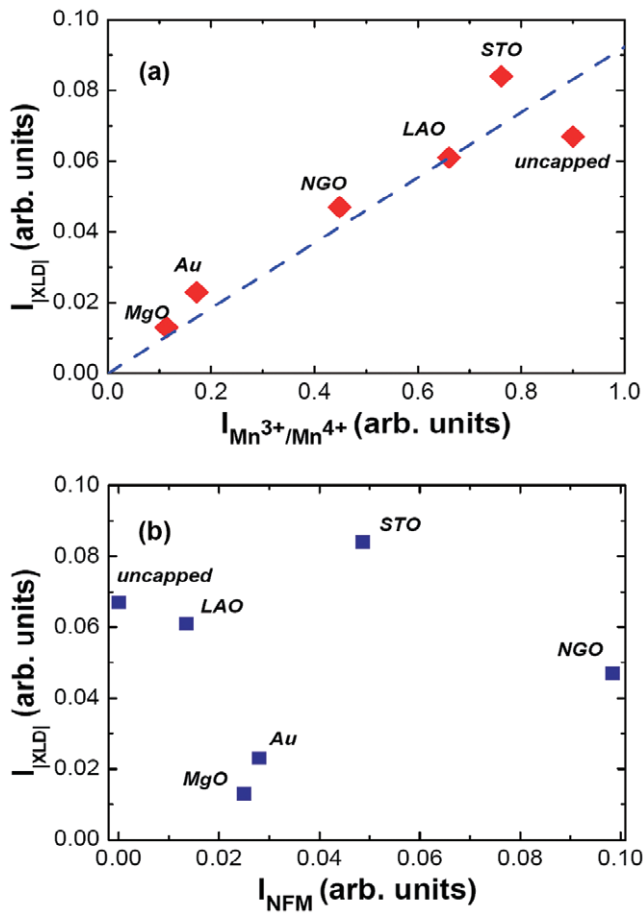


Figure 5. Comparison between the integrated intensity of [XLD], i.e. I_{XLDI} versus the integrated intensity of the raw XAS (no normalization) originating from a nominal $2/3-1/3$ mixed valence $\text{Mn}^{3+/4+}$ state, i.e. $I_{\text{Mn}^{3+}/\text{Mn}^{4+}}$ (a) and from the Mn^{2+} and Mn^{4+} impurities (b). The intensity corresponding to the NM has been calculated by using the NM (%) values of table 1. A clear linear correlation is observed only between I_{XLDI} and $I_{\text{Mn}^{3+}/\text{Mn}^{4+}}$.

To further characterize this AF phase we have investigated the transport properties across the interface for the samples capped with LAO, STO, NGO and MgO by means of an atomic force microscope (AFM) system, working in

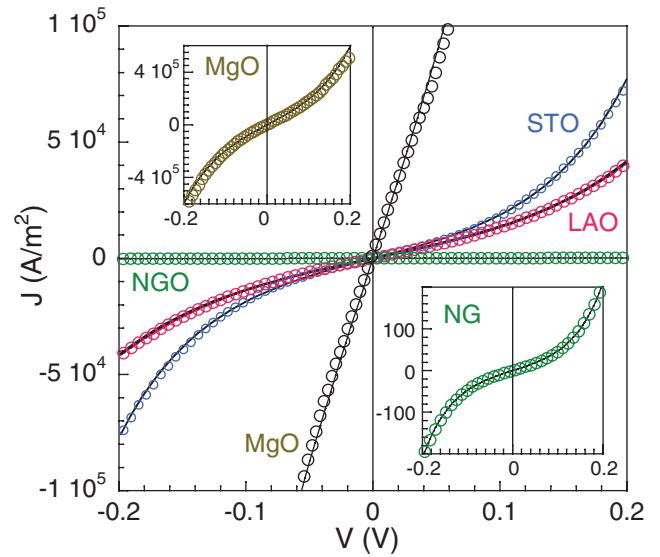


Figure 6. Dependence of the current density as a function of the voltage bias, $J(V)$, across the LSMO/CL interface for different CLs. The continuous line corresponds to the fitting from equation (1) in the text. Insets: details of the $J(V)$ curve for the LSMO/MgO (upper) and LSMO/NGO (lower) systems.

the current sensing (CS) mode (see [26] for details). As expected, $I(V)$ characteristic curves across the LSMO/CL interfaces exhibit the typical features of a tunneling conduction process (see figure 6). The effective thickness of the insulating barrier layer has been estimated from a quantitative analysis of the $I-V$ characteristic curves by using the Simmons model in the intermediate voltage range given by the equation [27]

$$J = \left(\frac{e}{2\pi\hbar t^2} \right) \left\{ \left(\phi_0 - \frac{eV}{2} \right) \exp \left[- (2m)^{1/2} \frac{4\pi t}{h} \left(\phi_0 - \frac{eV}{2} \right)^{1/2} \right] - \left(\phi_0 + \frac{eV}{2} \right) \exp \left[- (2m)^{1/2} \frac{4\pi t}{h} \left(\phi_0 + \frac{eV}{2} \right)^{1/2} \right] \right\} \quad (1)$$

ϕ_0 being the barrier height and t the effective insulating barrier thickness. Some examples of these fits are shown in figure 6. The obtained values for ϕ_0 and t are summarized in table 1. The values obtained for ϕ_0 are in good agreement with those previously reported [27–30]. Our analysis yields values for the effective insulating barrier thickness, t , larger by $\Delta t \sim 1-2$ nm than those corresponding to the nominal thickness of the CL (see figure 1). This indicates that the effective insulating barrier thickness has been increased by interfacial effects in the LSMO topmost layers. In principle, there are two possible sources for explaining this extra insulating layer at the interface, i.e. the NM and the AF phases. Comparison of the values obtained for Δt with the amount of secondary NM phases detected with XAS (see table 1) for the different interfaces yields an almost perfect linear correlation ($r^2=0.99$) between Δt and the amount of NM phase. However the intercept for NM= 0% turns out to be non-zero

(~1 nm). This can be understood by assuming that in all cases there is an extra ~1 nm thick interfacial insulating layer, i.e. independent of the amount of NM phase. We argue that this ~1 nm insulating layer is related to the AF layer, whose existence at the LSMO surface/interfaces has been highlighted by XLD measurements and whose presence turned out to be independent of the capping material. Indeed this idea is corroborated by the results obtained for the LSMO/LAO interface in which no NM phase has been detected, but a $\Delta t = 1$ nm is still observed. These results therefore allow us to assign an effective thickness of approximately 2 ML (~1 nm) for the C-type AF-insulating phase present at the LSMO surface and LSMO/CL interfaces.

The origin of this C-AF insulating phase is controversial. The main forces at work by the interface can be grouped in (i) structural strain [31], (ii) electronic reconstruction [32], and (iii) structural disruption with inversion symmetry breaking at the interface [1, 11, 33]. In what follows, we will analyze each of these contributions in order to clarify their relevance in determining the e_g orbitals occupancy at the interfacial region, and therefore their magnetic and electronic properties.

- (i) Structural strain is very important since the substrate constrains the films in-plane cell parameters. Indeed our samples are in-plane fully strained ($a_{\text{Film}} = a_{\text{Subst}} \sim 0.3905$ nm) with a slightly reduced out-of-plane cell parameter c (~0.3870(3) nm). This elongation of the in-plane cell parameters would favor the preferential occupancy of the x^2-y^2 orbitals due to the combined effect of the anisotropic change of the cell parameters, and therefore of the hopping amplitudes leading to a CE-type AF phase [11, 13, 14]. However our XLD data, corresponding mainly to the LSMO/CL interfacial region, exhibit clear features indicative of a $3z^2-r^2$ preferential orbital occupancy promoting a C-type AF ordering irrespective of the CL material and the structural strain. In fact, recent results reported in [16] clearly demonstrate that, irrespective of the strained state of LSMO thin films, a preferential occupancy of the Mn 3d $3z^2-r^2$ e_g orbitals takes place at LSMO free surfaces. Consequently it is clear that strain alone cannot explain the observed preferential occupancy of the $3z^2-r^2$ orbitals neither at substrate/LSMO nor at LSMO/surface of LSMO/CL interfaces.
- (ii) The electronic structure of the LSMO film and the CLs interact at the interface and possible delocalization effects should be taken into consideration. For instance, in the case of LSMO/STO interfaces it is expected that the e_g manganese orbitals delocalize to some extent into the Ti 3d empty states. This scenario is particularly favored in the case of the 3d $3z^2-r^2$ orbitals of the Mn and Ti atoms. This delocalization energy tends to favor a Jahn–Teller distortion increasing the occupancy of the $3z^2-r^2$ orbitals of the Mn and therefore the C-AF phase [11]. Although the expected preferential occupancy in that case agrees with our experimental finding, interfacial electronic effects can also be ruled out based on our

experimental results. First, the amplitude of the XLD signal is similar in both capped and uncapped LSMO films pointing to a minor (if any) effect of the capping on the appearance of the C-AF phase. Second, the effect is observed for different CL materials such as, STO; with neutral SrO or TiO₂ layers, NGO; with charge unbalanced NdO or GaO₂ layers or LAO; where the above mentioned hole-doping mechanism does not apply [34]. In addition it is also observed in the case of CL materials with no perovskite structure, such as MgO, or even a metallic capping as for Au.

- (iii) Finally, it has to be considered that the interface introduces a structural disruption that implies inversion symmetry breaking, which may strongly modify the electronic properties of the LSMO interfacial layers. In this sense, the evident effect of the interface is distorting the cubic symmetry around the Mn ions. This distortion is accommodated by a combination of uniform deformations and staggered rotations of the metal-oxide octahedra, which influence the orbital occupancy [6]. The distortion of the cubic symmetry around the Mn ions by the interface implies changes of the local crystal field and the oxygen mediated covalent bonding between metal ions. These changes may trigger specific spin–orbital reconstructions and selective orbital occupancy with the concomitant change of the magnetic and electronic properties. In fact, in the extreme case of manganite free surfaces it has been theoretically predicted that the charge state of the Mn ions is strongly modified leading to charge localization and the preferential occupancy of the $3z^2-r^2$ orbital within the 2 ML closest to the surface [35], i.e. the formation of a thin C-type AF phase at the surface. Our experimental results obtained in the uncapped LSMO film clearly confirm these theoretical predictions. We observe the existence of an AF phase at the LSMO surface by XLD and also in the LSMO/CL interfaces. In addition, transport measurements in the bilayers allow it to demonstrate its insulating character and estimate its thickness (~1 nm), which is also in excellent agreement with the theoretical predictions [36].

We would like to emphasize the fact that the strength of the detected C-AF phase is independent of the CL material and similar in all the cases to that of the LSMO uncapped surface. From these results we conclude that a robust C-AF phase arises at the surface of LSMO films immediately after the growth due to the structural disruption and breaking of the inversion symmetry, and once formed this AF phase is strong enough to persist after capping.

The AF/insulating layer detected here offers a clear explanation of the microscopic origin of the so-called dead layer that has often been studied in the case of manganite/substrate interfaces. The structural strain is very relevant, but scarcely investigated at the interface, which determines the magnetotransport properties in oxide-based MTJ, i.e. the interface with the insulating barrier. Moreover, it might also explain

why the improvement of the microstructural quality with atomic sharp interfaces in manganite MTJ, although leading to an increase of the temperature range where TMR can be observed, does not lead to the observation of a sizable room temperature magnetoresistance.

As we have shown, the capping of the LSMO samples leads in most cases to the appearance of NM phases. In addition, due to the structural disruption, we also detect the existence of an AF/insulating phase which should be considered as concomitant to the interface because of inversion symmetry breaking. Advances in thin film deposition techniques might have yielded almost perfect atomic sharp interfaces from a chemical and crystallographic point of view, thus reducing the presence of the NM phase. The structural disruption, however, with its intrinsic inversion symmetry breaking and the appearance of the concomitant robust C-type AF phase, is unavoidable.

These results allow us to envisage the correct strategy for the construction of manganite-based tunneling devices. Our results suggest that in order to avoid the degradation of the performances of manganite layers at the interfaces, the insulating barrier has to be chosen to avoid the structural disruption, i.e. taking advantage of the very rich phase diagram of these materials and modifying the doping rate to obtain an AF-insulating phase for the barrier. This could explain the good performance of $\text{La}_{0.67}\text{Ca}_{0.33}\text{MnO}_3/\text{La}_{0.3}\text{Sr}_{0.7}\text{MnO}_3/\text{La}_{0.67}\text{Ca}_{0.33}\text{MnO}_3$ tunneling junctions presenting TMR values vanishing only 10K below the T_C of one of the electrodes [36].

In conclusion, the combination of synchrotron radiation spectroscopic techniques with transport measurements at room temperature, both sensitive to the LSMO interface, highlights a complex scenario at the manganite thin film surfaces and interfaces in which FM, NM and AF phases coexist. Transport measurements show that the disruption of the DE-FM phase occurs only at the interface where a thin insulating layer of about 2–4 ML is present. This insulating layer is linked to the NM and AF phases. However, in addition to this, we have detected the existence of a residual 2 ML thick AF-insulating layer whose existence is concomitant to the nominal 2/3–1/3 DE-FM phase. Its origin lies on the preferential occupancy of the $3d\ z^2-r^2\ e_g$ orbitals at the interface, due to the structural disruption and inversion symmetry breaking of the crystal structure, leading to a C-AF ordering. This AF phase is robust enough to survive after capping and therefore is likely to be present in MTJ interfaces. The presence of this phase modifies the features of the tunneling barrier, severely affecting the tunneling conduction process.

Acknowledgments

We acknowledge financial support from the Spanish MINECO (MAT2012-33207), CONSOLIDER (CSD2007-00041), and FEDER program. The research leading to these results has received funding from the European Community's Seventh Framework Program (FP7/2007–2013) under Grant

agreement no 226716. ZK thanks the Spanish MEC for the financial support through the RyC program.

References

- [1] Hwang H Y, Iwasa Y, Kawasaki M, Keimer B, Nagaosa N and Tokura Y 2012 *Nature Mater.* **11** 103
- [2] Chakhalian J, Freeland J W, Habermeier H-U, Cristiani G, Khaliullin G, van Veenendaal M and Keimer B 2007 *Science* **318** 1114
- [3] Zubko P, Gariglio S, Gabay M, Ghosez P and Triscone J-M 2011 *Annu. Rev. Condens. Matter Phys.* **2** 141
- [4] Yu P, Chu Y-H and Ramesh R 2012 *Mater. Today* **15** 320
- [5] Ohtomo A, Muller D A, Grazul J L and Hwang H Y 2002 *Nature* **419** 378–80
- [6] Yamada H, Ogawa Y, Ishii Y, Sato H, Kawasaki M, Akoh H and Tokura Y 2004 *Science* **305** 646
- [7] Brinkman A, Huijben M, van Zalk M, Huijben J, Zeitler U, Maan J C, van der Wiel W G, Rijnders G, Blank D H A and Hilgenkamp H 2007 *Nature Mater.* **6** 493
- [8] Dagotto E, Hotta T and Moreo A 2001 *Phys. Rep.* **344** 1
- [9] Schiffer P, Ramirez A P, Bao W and Cheong S W 1995 *Phys. Rev. Lett.* **75** 3336
- [10] Bowen M, Bibes M, Barthélémy A, Contour J-P, Anane A, Lemaître Y and Fert A 2003 *Appl. Phys. Lett.* **82** 233
- [11] Lepetit M-B, Mercey B and Simon C 2012 *Phys. Rev. Lett.* **108** 087202
- [12] Abad LI, Laukhin V, Valencia S, Gaupp A, Gudat W, Balcells LI and Martínez B 2007 *Adv. Funct. Mater.* **17** 3918–25
- [13] Baena A, Brey L and Calderón M J 2011 *Phys. Rev. B* **83** 064424
- [14] Aruta C, Ghiringhelli G, Tebano A, Boggio N G, Brookes N B, Medaglia P G and Balestrino G 2006 *Phys. Rev. B* **73** 235121
- [15] Tebano A et al 2008 *Phys. Rev. Lett.* **100** 137401
Tebano A et al 2009 *Phys. Rev. Lett.* **103** 079902(E) (erratum)
- [16] Pesquera D, Herranz G, Barla A, Pellegrin E, Bondino F, Magnano E, Sanchez F and Fontcuberta J 2012 *Nature Commun.* **3** 1189
- [17] Aruta C, Ghiringhelli G, Bisogni V, Braicovich L, Brookes N B, Tebano A and Balestrino G 2009 *Phys. Rev. B* **80** 014431
- [18] Konstantinovic Z, Santiso J, Colson D, Forget A, Balcells LI and Martínez B 2009 *J. Appl. Phys.* **105** 063919
- [19] Valencia S, Konstantinovic Z, Schmitz D, Gaupp A, Balcells LI and Martínez B 2011 *Phys. Rev. B* **84** 024413
Valencia S, Konstantinovic Z, Gaupp A, Schmitz D, Balcells LI and Martínez B 2011 *J. Appl. Phys.* **109** 07D718
- [20] Valencia S, Gaupp A, Gudat W, Abad LI, Balcells LI, Cavallaro A, Martínez B and Palomares F J 2006 *Phys. Rev. B* **73** 104402
Valencia S, Gaupp A, Gudat W, Abad LI, Balcells LI and Martínez B 2007 *Phys. Rev. B* **75** 184431
- [21] Abbate M et al 1992 *Phys. Rev. B* **46** 4511
- [22] Thole B T, Carra P, Sette F and van der Laan G 1992 *Phys. Rev. Lett.* **68** 1943
Carra P, Thole B T, Altarelli M and Wang X D 1993 *Phys. Rev. Lett.* **70** 694
- [23] Piamonteze C, Miedema P and de Groot F M F 2009 *Phys. Rev. B* **80** 184410 and references therein
- [24] Crocombette J P, Thole B T and Jolet F 1998 *J. Phys.: Condens. Matter* **8** 4095
- [25] Huang D J et al 2004 *Phys. Rev. Lett.* **92** 087202
- [26] Balcells LI, Abad LI, Rojas H, Perez del Pino A, Estrade S, Arbiol J, Peiro F and Martínez B 2008 *Small* **4** 365
- [27] Simmons J G 1963 *J. Appl. Phys.* **34** 2581
- [28] Sun J Z, Krusin-Elbaum L, Duncombe P R, Gupta A, Laibowitz R B 1997 *Appl. Phys. Lett.* **70** 1769

- [29] Bibes M, Bowen M, Barthelemy A, Anane A, Bouzehouane K, Carretero C, Jacquet E, Contour J P and Durand O 2003 *Appl. Phys. Lett.* **82** 3269
Infante I C, Sanchez F, Laukhin V, Perez del Pino A, Fontcuberta J, Bouzehouane K, Fusil S and Barthelemy A 2006 *Appl. Phys. Lett.* **89** 172506
- [30] Yuasa S, Nagahama T, Fukushima A, Suzuki Y and Ando K 2004 *Nature Mater.* **3** 868
- [31] Fang Z, Solov'yev I V and Terakura K 2000 *Phys. Rev. Lett.* **84** 3169
- [32] Konishi Y, Fang Z, Izumi M, Manako T, Kasai M, Kuwahara H, Kawasaki M, Terakura K and Tokura Y 1999 *J. Phys. Soc. Japan* **68** 3790
- [33] Zenia H, Gehring G A, Banach G and Temmerman W M 2005 *Phys. Rev. B* **71** 024416
- [34] Yamada H, Kawasaki M, Ogawa Y and Tokura Y 2002 *Appl. Phys. Lett.* **81** 4793
- [35] Calderón M J, Brey L and Guinea F 1999 *Phys. Rev. B* **60** 6698
- [36] Sefrioui Z *et al* 2010 *Adv. Mater.* **22** 5029



Room-temperature ferromagnetism in Ni²⁺ doped TiO₂ nanocrystals synthesized from nanotubular precursors



M. Vranješ^a, Z. Konstantinović^b, A. Pomar^b, J. Kuljanin Jakovljević^a, M. Stoiljković^a, J.M. Nedeljković^a, Z. Šaponjić^{a,*}

^aUniversity of Belgrade-Vinča Institute of Nuclear Sciences, P.O. Box 522, 11001 Belgrade, Serbia

^bInstitut de Ciència de Materials de Barcelona, CSIC, Campus UAB, 08193 Bellaterra, Spain

ARTICLE INFO

Article history:

Received 25 September 2013

Received in revised form 21 November 2013

Accepted 23 November 2013

Available online 1 December 2013

Keywords:

Nanostructured materials

Oxide materials

Hydrothermal synthesis

Transmission electron microscopy/TEM

X-ray diffraction

Magnetic measurements

ABSTRACT

Hydrothermal synthetic route for synthesis of Ni²⁺ doped TiO₂ nanocrystals showing room temperature ferromagnetism, using dispersion of titania nanotubes in the presence of Ni²⁺ ions at different pHs as precursors, is reported. Morphologies of tubular precursors and Ni²⁺ doped TiO₂ nanocrystals were characterized by transmission electron microscopy. Titania nanotubes have outer diameter of about 10 nm while the length varies widely even reaching few hundred nanometers. Ni²⁺ doped TiO₂ nanoparticles synthesized at pH 3 have polygonal shape and dimension of about 20 nm. Transmission electron microscopy analysis revealed presence of mixed shapes (polygonal and rod like) in the sample of Ni²⁺ doped TiO₂ nanoparticles synthesized at pH 5. X-ray diffraction analysis of resultant powder and selected area electron diffraction pattern confirmed the anatase crystal phase of Ni²⁺ doped TiO₂ nanoparticles independently of dopant concentrations (0.09, 0.25, 0.86, 1.48 and 1.80 at%), followed by slight changes of their microstructural parameters. Reflection spectra of Ni²⁺ doped TiO₂ nanoparticles revealed their altered optical properties in comparison to undoped TiO₂ nanoparticles. Room temperature ferromagnetic ordering with saturation magnetic moment in the range of 10⁻³–5 × 10⁻² μB per Ni atom was observed for all measured films made of Ni²⁺ doped TiO₂ nanoparticles.

© 2013 Elsevier B.V. All rights reserved.

1. Introduction

The possibility for combining semiconducting with magnetic behavior in a single material recently attracted a great interest. Diluted magnetic semiconductors, in particular III–V and II–VI compounds, represent a new class of materials that could be used in the field of magneto-electronic devices and will enable progress to information processing technology. On the other hand, nano-scale diluted magnetic semiconductors are the key components of spintronic devices in which simultaneous control of charge currents and spin polarized currents will be possible [1,2]. The advantage of the use of single crystalline DMS nanoparticles in comparison to polycrystalline or bulk DMS is in lower possibility for defect formation and the agglomeration of dopants within DMS. Thermodynamic arguments revealed that the formation energy of defects increases with decreasing size of nanocrystals [3]. Various interesting physical phenomena such as spin persistent coherence, room temperature ferromagnetism and spin-polarized based photoluminescence were studied in these systems [4].

Another class of DMS materials that has been identified by theoretical considerations and proved as a good candidate for achieving room temperature ferromagnetism (Curie temperatures higher than room temperature) is based on wide band metal oxide semiconductors such as TiO₂ and ZnO doped with Co, Cu, Mn and Fe [5–11].

There is couple of different carrier-mediated mechanisms that could provide a possible explanation for the ferromagnetic ordering in these types of DMSs: exchange mechanism (direct or superexchange), carrier mediated exchange (Ruderman–Kittel–Kasuya–Yosida (RKKY) interaction or Zener carrier-mediated exchange or Zener double exchange) and bound magnetic polarons [1]. The main problem when considering ferromagnetism in oxide DMSs is whether it really derives from the doped matrices or from the dopant clusters. Even when the cluster formation is excluded, the origin of ferromagnetism in this type of semiconductors still remains a very controversial topic. The sp–d exchange mechanism between the sp itinerant carriers and the local d states of the dopant, so called a carrier-mediated mechanism, is inapplicable to explain the ferromagnetism in oxide DMSs, taking into account that the transition metal ions doped oxide films with ferromagnetic properties are often poor conductors or even insulators [12,13]. An additional way to induce ferromagnetic ordering in

* Corresponding author. Tel.: +381 11 8066428; fax: +381 11 7408607.

E-mail address: saponjic@vinca.rs (Z. Šaponjić).

these systems is based on double exchange mechanism between d states of transition metal elements. However, double exchange mechanism is excluded in cases of the low doping concentrations and single valence state of magnetic elements [2].

Recently Bahadur et al. [14] have proposed that the observed room temperature ferromagnetism in doped metal oxide originates from the spin ordering through exchange interaction between holes trapped in oxygen 2p orbital adjacent to dopant site. On the other hand, Patel and Gajbhiye [8] explained the observed ferromagnetism in Cu doped titanate in terms of the non-carrier-mediated bound magnetic polaron (BMP) model. According to this theory, when defect concentration exceeds the percolation threshold, oxygen vacancy defects overlap many dopant ions to yield BMPs, which results in ferromagnetic coupling between dopant ions. In addition to the magnetic doping effect, oxygen vacancies generated during synthesis, have been proposed to play an important role in the magnetic origin for oxide DMSs [6,7,15].

In this paper we report on synthetic procedure, structural, optical and magnetic properties of Ni²⁺ doped TiO₂ nanoparticles. The Ni²⁺ doped TiO₂ nanoparticles are synthesized by shape transformation of titania nanotubes in the presence of Ni²⁺ ions, as precursors, in extended hydrothermal treatment. Such approach in sample preparation eliminates the driving force problem that arises from the increase in the activation energy for nanocrystal nucleation in the presence of the dopant ions and consequent exclusion of the Ni²⁺ ions during nanoparticle growth. The shape transformation from nanotubes into nanoparticles in the presence of Ni²⁺ ions induces structural reorganization, while at the same time avoiding the nucleation stage and problems related to it. Morphology of the doped faceted nanocrystals was characterized by transmission electron microscopy (TEM), while the crystal structure was determined by X-ray diffraction (XRD) analysis. The percent of Ni²⁺ ions in TiO₂ nanocrystals was determined using ICP Emission Spectrometry. The magnetic properties of films made of Ni²⁺ doped TiO₂ nanoparticles were investigated using a superconducting quantum interference device (SQUID) magnetometer.

2. Experimental

All chemicals were reagent-grade from Aldrich and used as received. Titania nanotubes were synthesized according to Kasuga et al. [16], using TiO₂ powder as a precursor. The 250 mg of Degussa TiO₂ powder was dispersed in 10 ml 10 M NaOH and hydrothermally treated 24 h in a Teflon vessel (total volume 25 ml) under saturated vapor pressure of water at 150 °C. After autoclaving, the ensuing powder was washed with distilled water. Separation of powder from the washing solution, after each washing step, was done by centrifugation. The washing procedure was repeated until pH of water achieved 7. The powder was then air dried at 70 °C.

Two sets of dispersions of Ni²⁺ doped TiO₂ nanocrystals at pH 3 and pH 5 were synthesized applying hydrothermal treatment to precursor dispersions containing titania nanotubes (25 mg/10 ml) at pH 3 or pH 5, in the presence of five different concentrations of Ni(NO₃)₂ × 6H₂O in the range of 1–8%. The dispersion was stirred for 3 h followed by a hydrothermal treatment at 250 °C for 90 min. Doped nanoparticles were efficiently redispersed in water. The excess of Ni²⁺ ions was removed by dialysis against 10 times the larger volume of acidified water (pH 3) at 4 °C for 3 days. Water was changed daily. For dialysis process was used Spectra/Por Dialysis Membrane, MWCO: 3500 (Spectrum Laboratories, Inc., Rancho Dominguez, CA).

Films for magnetic characterization were prepared by drop casting of dialyzed dispersions of Ni²⁺ doped TiO₂ nanoparticles onto pre-cleaned glass substrate. The films were annealed in air for 2 min at 100 °C after each drop.

The percentage ratio of Ni²⁺ ions to Ti⁴⁺ ions in doped nanocrystals was determined using ICP Emission Spectrometer: ICAP 6000 series (Thermo Electron Corporation). Prior to the ICP measurements, the powdered sample was dispersed in 5 ml of concentrated sulfuric acid and hydrothermally treated 60 min/250 °C in Teflon vessel (Parr acid digestion bomb). The concentrations of Ni²⁺ ions in dialyzed samples of doped TiO₂ nanoparticles synthesized at pH 3 were 0.09 and 0.25 at% of the amount of Ti⁴⁺ ions. The concentrations of Ni²⁺ ions in dialyzed samples of doped TiO₂ nanoparticles synthesized at pH 5 were 0.86, 1.48 and 1.80 at% of the amount of Ti⁴⁺ ions.

The shape and size of titania nanotubes were characterized using Hitachi H-7000 FA TEM operated at 125 kV while the Ni²⁺ doped TiO₂ nanoparticles were characterized by JEOL 1210 TEM operated at 120 kV.

Reflection spectra of Ni²⁺ doped TiO₂ powders were recorded at room temperature using Thermo Scientific Evolution 600 UV/Vis spectrophotometer.

The X-ray Powder Diffraction (XRPD) patterns were obtained on a Philips PW-1050 automated diffractometer using Cu K α radiation (operated at 40 kV and 30 mA). Diffraction data for structural analysis were collected in the 2 θ range 10–80°, with scanning steps of 0.02 and exposition time of 12 s. Structure analysis was done using the KOALARIIE computing program [17], based on the Rietveld full profile refinement method [18]. Samples for XRPD measurements were prepared using standard protocol [19].

The field dependence of the magnetic moment was measured with a superconducting quantum interference device magnetometer (Quantum Design). The magnetic field was applied parallel to the film surface. The measured magnetization at 300 K was corrected for the diamagnetic background of the glass substrate (derived from high-field dependence magnetization data).

3. Results and discussion

3.1. Structural analysis

Additional hydrothermal treatment of dispersion of multiwall open-ended titania nanotubes, synthesized according to procedure reported by Kasuga et al. [16], was applied in the presence of Ni²⁺ ions at pH 3 in order to synthesize internally doped Ni²⁺:TiO₂ nanoparticles. As we showed in our previous work the existence of undercoordinated surface defect sites that terminate layers of titania nanotubes enables initial adsorption of dopant ions [20]. Also, it should be mentioned that the bigger portion of these defect sites are located in the interior/interface between the layers that constituted the scrolled nanotubes [21]. It allows synthesis of Ni²⁺ doped TiO₂ faceted nanocrystals through encapsulation of nanotube's surface-bound Ni²⁺ ions with extra layers of TiO₂ during shape transformation [20,21].

Conventional TEM images of titania nanotubes and Ni²⁺ doped TiO₂ nanoparticles are shown in Fig. 1. Reasonably uniform size distributions of nanotubes and Ni²⁺ doped TiO₂ nanoparticles synthesized at pH 3 were confirmed. The SAED patterns revealed well developed crystalline structure in Ni²⁺ doped TiO₂ nanoparticles.

Titania nanotubes have outer diameter of about 10 nm while the length varies widely even reaching few hundred nanometers. The faceted Ni²⁺ doped TiO₂ nanoparticles made from nanotubes at pH 3, have polygonal shape and dimension of about 20 nm. Selected area electron diffraction pattern (SAED) of the Ni²⁺ doped TiO₂ nanocrystals, inset Fig. 1b, indicated undisturbed anatase crystal phase of TiO₂. On the other hand, TEM image of the sample of Ni²⁺ doped TiO₂ nanoparticles synthesized at pH 5 revealed presences of the mixed shapes. Next to polygonal doped TiO₂ nanoparticles, which prevailed, also bigger anisotropic, rod like nanoparticles are easy to be observed, Fig. 1c. Highly crystalline anatase phase of this sample is proved by electron diffraction measurements, inset Fig. 1c. These findings are in agreement with our previous work showing that hydrothermal treatment of dispersions of titania nanotubes at different pH results in anatase polymorph of shaped TiO₂ nanocrystals [22]. In general, the titania phase transformation is a consequence of rearrangement of face-sharing and edge sharing TiO₆ octahedra which present basic structural unit in all titania polymorphs and also in titanates [23,24]. When either heat applied or acid added the dissolution of titania is followed by crystallization in anatase or rutile [25]. According to Wang et al. [26] the reason for transformation of nanotubes considered as titanates in nanoparticles with anatase crystal structure during additional hydrothermal treatment in acidic medium, could be the existence of structural defects on the outside walls which induce local stress followed by disorder of atomic arrangement in nanotubes. Such disorder in combination with H⁺ catalytic dehydration of tubular layered structure is accompanied by an in situ rearrangement of structural units to form anatase nanocrystals [27]. Taking into account that acidic medium implies the pH far away from isoelectric point of TiO₂,

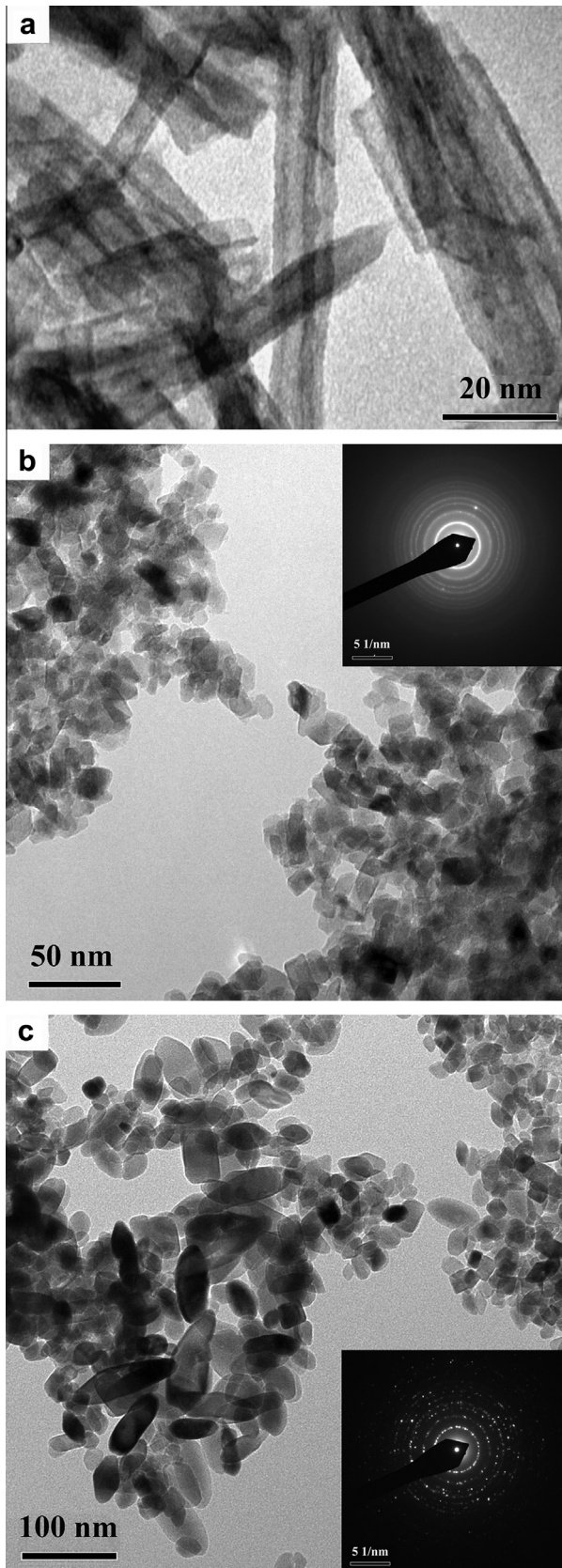


Fig. 1. TEM images of titania nanotubes (a), 0.25 at% Ni²⁺ doped TiO₂ nanoparticles synthesized at pH 3; Inset: SAED pattern (b), and 1.48 at% Ni²⁺ doped TiO₂ nanoparticles synthesized at pH 5; Inset: SAED pattern (c).

significant electrostatic forces between anatase nuclei exist and aggregation and further crystal growth are retarded [28]. The

mechanism of the tube-to-rod transformation, according to Nian and Teng [28] involve local shrinkage of the nanotubes which due to decrease of interlayer distance between the tube walls, results in production of small anatase crystallites and rupturing of the nanotubes. These processes under mild acidic condition, pH~5–6, near the isoelectric point for anatase TiO₂, is followed by oriented attachment which leads to the formation of nanorods.

Doping of TiO₂ nanomaterials with different ions could improve its optical response in the visible region. Dopant ions induce formation of localized mid-gap states which shift in dependence of atomic number of dopant. A red shift in the band gap transition or a visible light absorption, evident in metal-doped TiO₂, was attributed to the charge-transfer transition between the d electrons of the dopant and the conduction (or valence) band of TiO₂ [29,30]. In addition, the substitution of Ti ions with dopant of different valence induces formation of oxygen vacancies within TiO₂ matrix, due to charge imbalance. It was proposed that formation of oxygen vacancies and appearance of color centers also could be responsible for the red shift of the absorption edge of TiO₂ [31].

With aim to confirm the successful integration of Ni²⁺ in TiO₂ nanocrystals the optical properties of powdered samples of the 0.25 at% and 1.48 at% Ni²⁺ doped TiO₂ nanocrystals as well as bare TiO₂ nanocrystals were measured in a reflection mode, Fig. 2. Increase of absorbance of Ni²⁺ doped TiO₂ nanocrystals in the visible part of the spectra revealed that Ni atoms participate in the light-induced charge transfer processes due to the fact that incorporated Ni atoms have electronic states strongly coupled to the band structure of TiO₂ nanoparticles [32].

Dialysis, as post synthetic treatment, was applied on Ni²⁺ doped TiO₂ nanoparticles with aim to remove excess of dopant ions adsorbed on particle surface and those weakly bound to the anatase lattice in the undercoordinated surface defect sites [32]. Such approach enables that only Ni²⁺ ions doped in the core of nanoparticles, which cannot be leached by dialysis, contribute strongly to the magnetic behavior of nanoparticles [32]. The possible reason for the higher final dopant concentration in samples synthesized at pH 5 (0.86, 1.48 and 1.80 at%), could be find in their lower surface to volume ratio compared to doped nanoparticles synthesized at pH 3 (0.09 and 0.25 at%) and consequently less dopants on the surface, which are subject to postsynthetic dialysis.

Usually, it is difficult to determine the origin of ferromagnetic ordering in transition metal ions doped TiO₂ nanoparticles. To exclude the option of dopant clusters formation and thus opening possibility to assign the observed magnetism entirely to 3d element substituted in TiO₂ host, it was necessary to carry out XRD measurements.

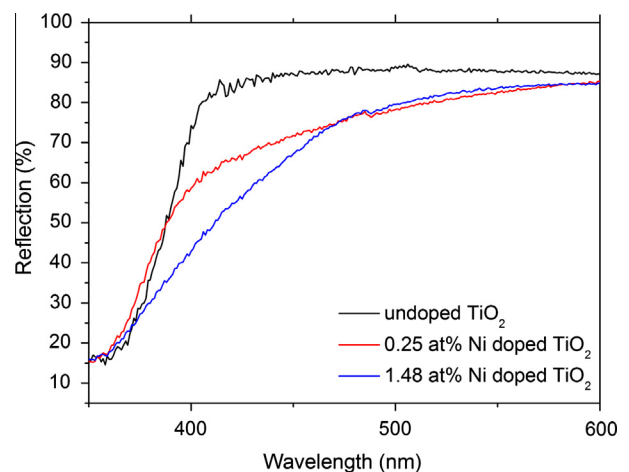


Fig. 2. Reflection spectra of powders of 0.25 and 1.48 at% Ni²⁺ doped TiO₂ nanocrystals and bare TiO₂ nanocrystals.

Rietveld refinements of the X-ray diffraction patterns of powdered samples of Ni^{2+} doped TiO_2 at different concentrations of dopant ions (0.09, 0.25, 0.86, 1.48 and 1.80 at%) and the XRD pattern of the bare TiO_2 nanoparticles are shown in Fig. 3. In the Rietveld analysis the least squares refinements method is carried out until the best fit between the calculated patterns, based on the refined structure models proposed, and the observed diffraction pattern was obtained.

Peaks appearing in XRD patterns of all investigated samples can be undoubtedly indexed as the anatase crystal form of TiO_2 . No

diffraction peaks of metallic Ti and other impurities such as metallic Ni, nickel oxides (NiO , NiO_2 , Ni_2O_3) or nickel titanate (NiTiO_3) were observed, within the detection limit of the instrument. The presence of Ni^{2+} ions has not affected the crystallization process of TiO_2 matrix taking into account that resolution and intensity ratio between the peaks preserved while the peak broadening was not observed. According to Bahadur et al., this can be expected due to strengthening of Ni–O interaction which hindered phase transformation and particles dimensions that prefer anatase crystal structure [14,33].

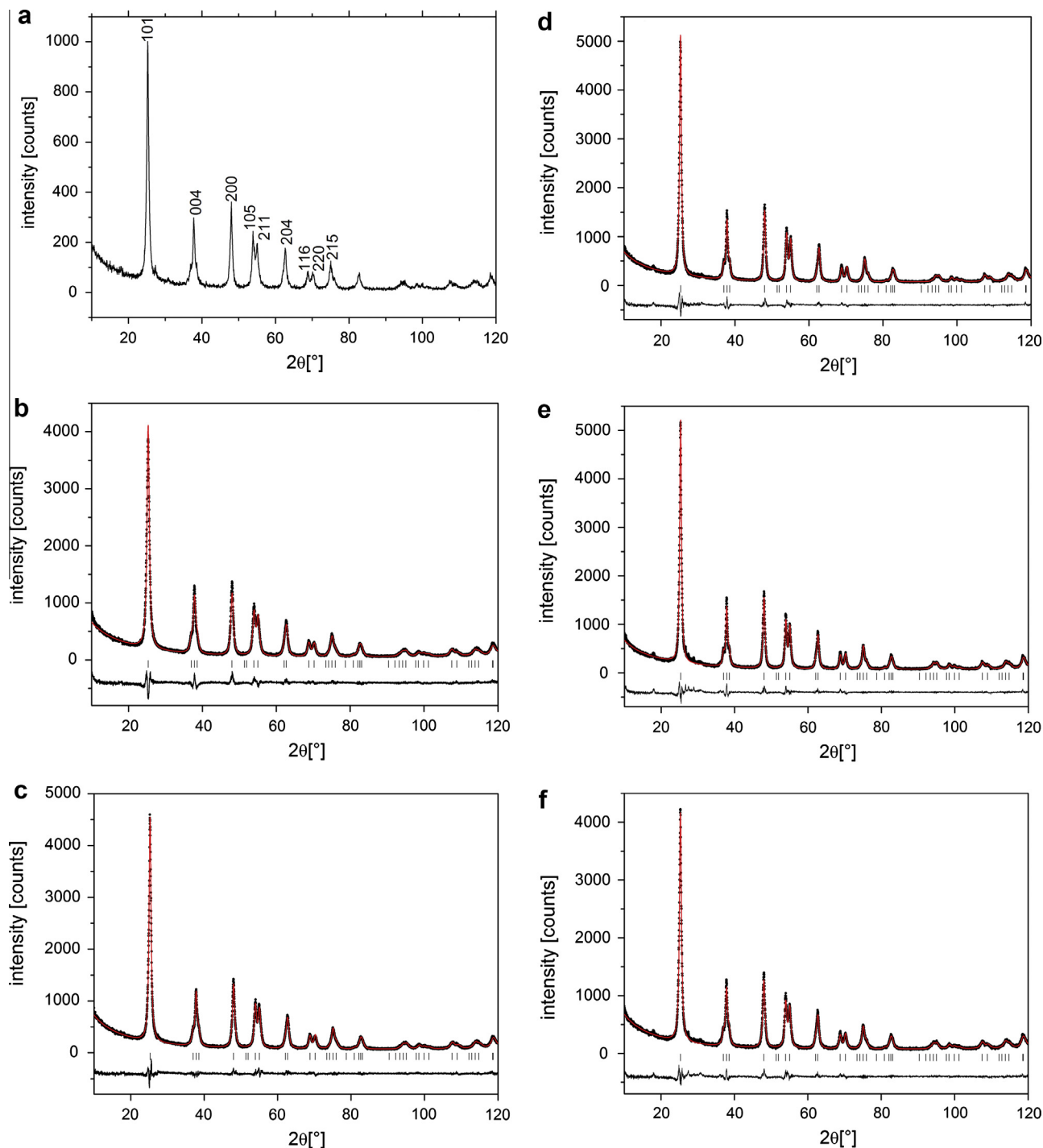
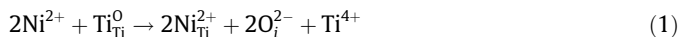


Fig. 3. X-ray powder diffraction pattern of bare TiO_2 nanoparticles (a) and Rietveld refined X-ray powder diffraction patterns of 0.09 at% (b), 0.25 at% (c), 0.86 at% (d), 1.48 at% (e) and 1.80 at% Ni^{2+} doped TiO_2 nanoparticles (f).

The XRD analysis data i.e. microstructural parameters of anatase phase in all samples are presented in Table 1. Reasonably well agreement of crystallites sizes in the range of 15–20 nm (CS values in Table 1) with dimension of nanoparticles obtained from TEM measurements was observed confirming their nanocrystalline nature.

The *a* and *c* lattice parameters in anatase TiO₂ crystal structure are 3.777 and 9.501 Å (ref. crystal table: a PDF 89-4921 *a* = 3.777; *c* = 9.501), respectively. From Fig. 3 and tabulated data, shifts towards higher values of lattice parameter *a* (Å) compared to the reference value were observed. In the same time reduction of unit cell volume of anatase crystal with increasing concentrations of doped Ni ions compared to the sample with lowest amount of Ni²⁺ (0.09 at%) was detected. The variation of the *c*-axis lattice parameter, taking into account that the radius of Ni²⁺ could be a smaller or higher than that of Ti⁴⁺ (0.745 Å) depending on the coordination, points to the possibility that Ni also substitutionally replaces Ti in the nanoparticle. It is known that the variation (decrease) of the *c*-axis lattice suggests, for example, that Ni substitutionally replaces Zn in the films since the radius of Ni²⁺ (0.69 Å) is smaller than that of Zn²⁺ (0.74 Å) [34–37].

Considering the charge imbalance between dopant (Ni²⁺) and host (Ti⁴⁺) ions the overall charge neutrality in the lattice of TiO₂ nanoparticles after incorporation of Ni²⁺ ions (two Ni²⁺ ions are required for one Ti⁴⁺) is maintained by introducing two oxygen interstitial defects according to Eq. (1):



where the O_i²⁻ is oxygen interstitial defect while the Ti_{Ti}⁰ is a titanium ion sitting on a titanium lattice site, with neutral charge.

The electrons associated with defects in oxides occupy large Bohr orbital and tend to form an impurity band which mix with the 3d states of dopant ions, allowing ferromagnetic coupling [38].

The vacancy sites formed during the doping of nanocrystals induce structure relaxation in DMSs, and consequently the magnetic properties can be enhanced compared to other systems [6,38–41].

3.2. Magnetization

The magnetization process in diluted magnetic semiconductor nanocrystals greatly depends on the 3d-metal concentration, the particle size, their aggregation density and of interfacial or grain-boundary defects [20,42,43]. Also, it is well known that ferromagnetism in 3d-metal doped metal oxide nanocrystals can be activated by the fusion of defects from the interior of nanocrystals to the interface and by the dopant ions randomization [20,44]. On the other hand, the appearance of positively charged oxygen vacancies in doped TiO₂ nanocrystals, as was mentioned earlier, also induces more charge carriers which have the role of mediator of exchange interaction between magnetic dopant atoms inducing overall enhancement of magnetic ordering [45].

The magnetic response for films made of 0.09, 0.25, 0.86, 1.48 and 1.8 at% Ni²⁺ doped TiO₂ nanoparticles as a function of magnetic field strength (*H*) was followed at room temperature. The diamagnetic contribution determined from the magnetic field dependence of magnetization at high field (for *H* > 10 kOe)

Table 1
Structural refinement of Ni²⁺ doped TiO₂ powder phase composition.

	0.09 at% Ni	0.25 at% Ni	0.86 at% Ni	1.48 at% Ni	1.80 at% Ni
<i>a</i> (Å)	3.790	3.786	3.788	3.789	3.789
<i>c</i> (Å)	9.507	9.499	9.503	9.505	9.503
CS (Å)	132	158	168	180	151
<i>V</i> (Å ³)	136.595	136.201	136.364	136.519	136.438

and room temperature was subtracted in all samples. The field dependent magnetization measured at room temperature after diamagnetic correction is shown in Fig. 4. At room temperature weak ferromagnetic behavior was observed in all samples, with coercive field of *H*_c ~ 200 Oe for the samples made of 0.09 and 0.25 at% Ni²⁺ doped TiO₂ nanoparticles synthesized at pH 3, Fig. 4a, and with coercive field of *H*_c ~ 150 Oe for the samples made of 0.86, 1.48 and 1.80 at% Ni²⁺ doped TiO₂ nanoparticles synthesized at pH 5, Fig. 4b. The presence of metallic Ni, as possibly responsible species for observed ferromagnetism, is ruled out by the applied synthetic conditions (oxidative and acidic environment) and its absence was confirmed by XRD measurements. In addition, the nickel clustering as the reason for the observed ferromagnetic hysteresis is excluded by absence of blocking temperature in zero-field-cooled measurement at 100 Oe (not shown). Moreover, it should be mentioned here that, for example, in Ni doped TiO₂ films, if the ferromagnetism is a consequence of Ni metal particles or clusters formation, *M*_s should be about 0.6 μB /Ni [46]. Finally, since the all Ni oxides and Ti–Ni oxides are not ferromagnetic, it is not hard to rule out any ferromagnetic impurity in the Ni²⁺ doped TiO₂ nanoparticles [15].

In the samples synthesized at pH 3, Fig. 4a, saturation magnetization decreases on increasing Ni contents. According to saturation magnetization values, the total number of magnetic moments in Ni²⁺ doped TiO₂ nanoparticles reduces almost twice with increasing amount of dopant ions which is in agreement with the magnetization process that depends on the 3d-metal concentration. For the set of samples where the concentrations of dopant ions were higher than 0.86 at%, Fig. 4b, saturation magnetization values are one order of magnitude lower in comparison to saturation magnetization values for samples with 0.09 and 0.25 at% of dopant ions, Fig. 4a. Such distinction could be also related to slightly different preparation conditions (pH 5) which influenced the shape and size of Ni²⁺ doped TiO₂ nanocrystals.

Three possible scenarios can be proposed for the observed loss of magnetization: (i) exchange interaction between Ni atoms within the nanoparticle, (ii) absence of ordering of Ni atoms within the anatase crystalline lattice, or (iii) absence of long-range ordering of Ni doped TiO₂ nanocrystals [32].

Since the ferromagnetic nature (saturation magnetization) decreased with increase in Ni²⁺ concentration, one may exclude the possibility that the super-exchange d–d interactions between the neighboring atoms were responsible for the observed room temperature ferromagnetism [14]. Decrease in magnetization with increase in dopant concentration should have its origin in the strength of magnetic interaction within the crystal lattice. Taking into account higher surface to volume ratio of Ni²⁺ doped TiO₂ nanocrystals synthesized at pH 3 (0.09 and 0.25 at% of dopant ions), due to uniform morphology (size and shape), it could be expected larger number of interfacial defects/oxygen vacancies in these samples in comparison to all samples synthesized at pH 5 (0.86, 1.48 and 1.80 at% Ni²⁺ doped TiO₂ nanocrystals). The presence of oxygen vacancies in Ni²⁺ doped TiO₂ nanoparticles was indicated by the observed changes in reflection spectra, Fig. 2. Since they are donor type defects, observed larger saturation magnetization could be justified by their role of mediator of exchange interaction between magnetic dopant atoms. Also, should not be forgotten presence of rod like particles in the samples synthesized at pH 5 because the shape anisotropy might be the additional reason for lower values of magnetization compared to doped nanoparticles without shape anisotropy, synthesized at pH 3 [38,47]. Assuming random orientation of rod like Ni²⁺ doped TiO₂ nanocrystals within nanocrystalline films the projection of the magnetization vectors along the field direction will be probably lower.

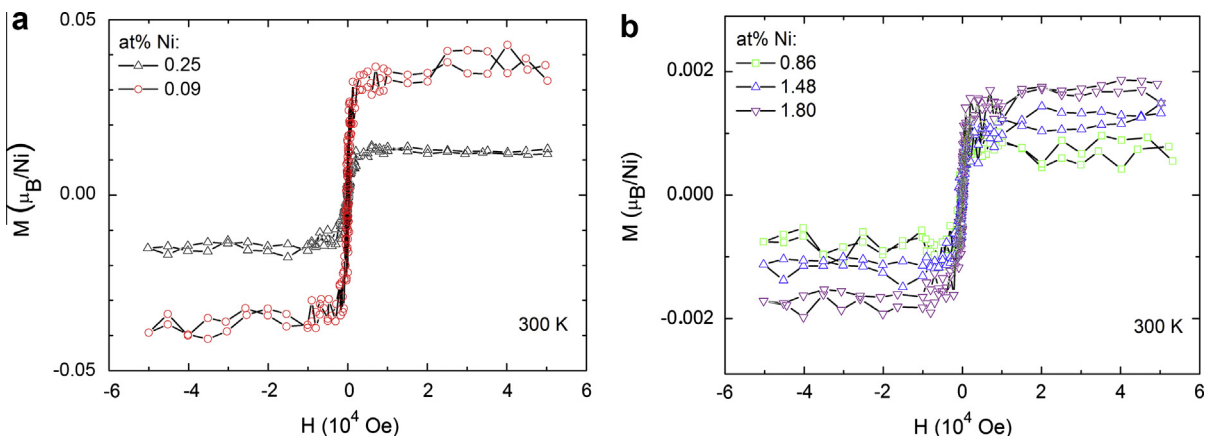


Fig. 4. Isothermal magnetizations of the films made of 0.09 and 0.25 at% Ni²⁺ doped TiO₂ nanoparticles synthesized at pH 3 (a) and 0.86, 1.48 and 1.80 at% Ni²⁺ doped TiO₂ nanocrystals synthesized at pH 5 (b).

4. Conclusions

The Ni²⁺ doped TiO₂ nanoparticles were synthesized applying hydrothermal treatment on dispersion of titania nanotubes in the presence of Ni²⁺ ions at pH 3 and pH 5. This method is a simple, reproducible and may be extended to synthesis of various transition metal ions doped anatase TiO₂ nanoparticles. XRD study demonstrates the absence of impurity phases and confirmed anatase crystal structure in all samples independently of dopant ions concentrations. TEM analysis of Ni²⁺ doped TiO₂ nanocrystals synthesized at pH 3 revealed their polygonal shape and diameter around 20 nm while in the Ni²⁺ doped TiO₂ nanocrystals synthesized at pH 5 among polygonal also anisotropic, rod like nanoparticles were observed. All samples of Ni²⁺ doped TiO₂ nanoparticles exhibit ferromagnetic behavior with almost closed loop ($H_c \sim 150$ – 200 Oe). The magnetic properties are influenced by the nickel concentrations. At low Ni doping level the saturation magnetization value decreases with the increase of at% of Ni²⁺ ions. Observed larger saturation magnetization in the doped nanocrystals synthesized at pH 3, is probably the consequence of larger number of interfacial defects/oxygen vacancies that exist in them.

Acknowledgments

The financial support for this work was provided by the Ministry of Education, Science and Technological Development of Republic of Serbia (Projects 172056 and 45020). We wish to thank the MPNS COST Action MP1106 for support. The authors are grateful to dr M. Mitrić (Vinča Institute of Nuclear Sciences, Belgrade, Serbia) for XRPD measurements and to Prof. P. Ahrenkiel (South Dakota School of Mines and Technology, Rapid City, SD, USA) for TEM image of titania nanotubes.

References

- [1] R. Janisch, P. Gopal, N.A. Spaldin, *J. Phys.: Condens. Matter* 17 (2005) 657–689.
- [2] N.A. Spaldin, *Magnetic Materials*, Cambridge University Press, 2003.
- [3] G. Dalpian, J.R. Chelikowsky, *Phys. Rev. Lett.* 96 (2006) 226802.
- [4] Das S. Sarma, *Am. Sci.* 89 (2001) 516.
- [5] N. Hong, W. Prellier, J. Sakai, A. Ruyter, *J. Appl. Phys.* 95 (2004) 7378.
- [6] J.Y. Kim, J.H. Park, B.G. Park, H.J. Noh, S.J. Oh, J.S. Yang, D.H. Kim, S.D. Bu, T.W. Noh, H.J. Lin, H.H. Hsieh, C.T. Chen, *Phys. Rev. Lett.* 90 (2003) 017401.
- [7] R. Kennedy, P. Stampe, E. Hu, P. Xion, S. von Molár, Y. Xin, *Appl. Phys. Lett.* 84 (2004) 2832.
- [8] S.K.S. Patel, N.S. Gajbhiye, *Mat. Chem. Phys.* 132 (2012) 175.
- [9] N.H. Hong, J. Sakai, W. Prellier, *J. Magn. Magn. Mater.* 281 (2004) 347.
- [10] M. Venkatesan, C.B. Fitzgerald, J.G. Lunney, J.M.D. Coey, *Phys. Rev. Lett.* 93 (2004) 177206.
- [11] L. Yan, C.K. Ong, X.S. Rao, *J. Appl. Phys.* 96 (2004) 508.
- [12] K.A. Griffin, A.B. Pakhomov, C.M. Wang, S.M. Heald, K.M. Krishnan, *Phys. Rev. Lett.* 94 (2005) 157204.
- [13] Z. Yin, N. Chen, C. Chai, F. Yang, *J. Appl. Phys.* 96 (2004) 5093.
- [14] N. Bahadur, R. Pasricha, Govind, S. Chand, R.K. Kotnala, *Mat. Chem. Phys.* 133 (2012) 471–479.
- [15] D.L. Hou, H.J. Meng, L.Y. Jia, X.J. Ye, H.J. Zhou, X.L. Li, *Phys. Lett. A* 364 (2007) 318.
- [16] T. Kasuga, M. Hiramoto, A. Hoson, T. Sekino, K. Niihara, *Adv. Mater.* 11 (1999) 1307.
- [17] R.W. Cheary, A.A.J. Coelho, *Appl. Cryst.* 25 (1992) 109–121.
- [18] H.J. Rietveld, *Appl. Cryst.* 2 (1969) 65–71.
- [19] V.K. Pecharsky, P.Y. Zavalij, *Fundamentals of Powder Diffraction and Structural Characterization of Materials*, Springer, 2005 (Chapter 3 (11) pp. 292–293).
- [20] J. Kuljanin-Jakovljević, M. Radočić, T. Radetić, Z. Konstantinović, Z.V. Šaponjić, J. Nedeljkić, *J. Phys. Chem. C* 113 (2009) 21029.
- [21] Z.V. Šaponjić, N.M. Dimitrijević, D. Tiede, A.J. Goshe, X. Zuo, L.X. Chen, A. Barnard, P. Zapol, L. Curtiss, T. Rajh, *Adv. Mater.* 17 (8) (2005) 965.
- [22] N.M. Dimitrijević, Z.V. Šaponjić, B.M. Rabatic, O. Poluektov, T. Rajh, *J. Phys. Chem. C* 111 (2007) 14597.
- [23] M. Gateshi, S. Yin, V. Ren, V. Petkov, *Chem. Mater.* 19 (2007) 2512–2518.
- [24] T. Sasaki, M. Watanabe, H. Hashizume, H. Yamada, H. Nakazawa, *J. Am. Chem. Soc.* 118 (1996) 8329–8335.
- [25] B.L. Bischoff, M.A. Anderson, *Chem. Mater.* 7 (1995) 1772–1778.
- [26] N. Wang, H. Lin, J. Li, L. Zhang, C. Lin, X. Li, *J. Am. Ceram. Soc.* 89 (2006) 3564–3566.
- [27] H.Y. Zhu, Y. Lan, X.P. Gao, S.P. Ringer, Z.F. Zheng, D.Y. Song, J.C. Zhao, *J. Am. Chem. Soc.* 127 (2005) 6730–6736.
- [28] J. Nian, H. Teng, *J. Phys. Chem. B* 110 (2006) 4193–4198.
- [29] A. Fujishima, X. Zhang, D.A. Tryk, *Surf. Sci. Rep.* 63 (2008) 515–582.
- [30] M.V. Ganduglia-Pirovano, A. Hofmann, J. Sauer, *Surf. Sci. Rep.* 62 (2007) 219–270.
- [31] N. Serpone, *J. Phys. Chem. B* 110 (2006) 24287.
- [32] Z.V. Šaponjić, N.M. Dimitrijević, O. Poluektov, L.X. Chen, E. Wasinger, U. Welp, D. Tiede, X. Zuo, T. Rajh, *J. Phys. Chem. B* 110 (2006) 25441.
- [33] T. Umebayashi, T. Yamaki, H. Itoh, K. Asai, *J. Phys. Chem. Solids* 63 (2002) 1909.
- [34] K. Karthik, S.K. Pandian, N.V. Jayatl, *Appl. Surf. Sci.* 256 (2010) 6829.
- [35] D.L. Hou, R.B. Zhao, Y.Y. Wei, C.M. Zhen, C.F. Pan, G.D. Tang, *Curr. Appl. Phys.* 10 (2010) 124–128.
- [36] Z.B. Gu, C.S. Yuan, M.H. Lu, J. Wang, D. Wu, S.T. Zhang, S.N. Zhu, Y.F. Chen, *J. Appl. Phys.* 98 (2005) 053908.
- [37] H.Y. Xu, Y.C. Liu, C.S. Xu, Y.X. Liu, C.L. Shao, *J. Phys. Chem.* 124 (2006) 074707.
- [38] M. You, T.G. Kim, Y.M. Sung, *Cryst. Growth Des.* 10 (2010) 983.
- [39] M. Venkatesan, C.B. Fitzgerald, J.M.D. Coey, *Nature* 430 (2004) 630.
- [40] S. Duhalde, M.F. Vignolo, F. Golmar, C. Chilotte, C.E. Rodriguez Torres, L.A. Errico, A.F. Cabrera, M. Renteria, F.H. Sanchez, M. Weissmann, *Phys. Rev. B* 72 (2005) 161313.
- [41] L.A. Errico, M. Renteria, M. Weissmann, *Phys. Rev. B* 72 (2005) 184425.
- [42] D.A. Schwartz, N.S. Norberg, Q.P. Nguyen, J.M. Parker, D.R. Gamelin, *J. Am. Chem. Soc.* 125 (2003) 13205.
- [43] P.V. Radovanović, D.R. Gamelin, *Phys. Rev. Lett.* 91 (2003) 157202.
- [44] K.R. Kittilstved, D.R. Gamelin, *J. Am. Chem. Soc.* 127 (2005) 5292.
- [45] T. Dietl, H. Ohno, F. Matsukura, J. Cibert, D. Ferrand, *Science* 287 (2000) 1019.
- [46] N.H. Hong, J. Sakai, W. Prellier, A. Ruyter, *J. Phys. D: Appl. Phys.* 38 (2005) 816–821.
- [47] J. Wang, Q.W. Chen, C. Zeng, B.Y. Hou, *Adv. Mater.* 16 (2004) 137.

Growth kinetics engineered magnetoresistance response in $\text{La}_{2/3}\text{Sr}_{1/3}\text{MnO}_3$ thin films

A. Pomar,¹ J. Santiso,² F. Sandiumenge,¹ J. Roqueta,² B. Bozzo,¹ C. Frontera,¹ L. Balcells,¹ B. Martínez,¹ and Z. Konstantinović¹

¹*Institut de Ciència de Materials de Barcelona–CSIC, Campus de la UAB, 08193 Bellaterra, Spain*

²*Institut Català de Nanociència i Nanotecnologia, ICN2 (CSIC, CERCA). Campus de la UAB, 08193 Bellaterra, Spain*

(Received 7 March 2014; accepted 9 April 2014; published online 16 April 2014)

A route to engineer the intrinsic colossal magnetoresistance (CMR) response in manganite thin films through an accurate control of the growth kinetics is presented. It is shown that under specific growth conditions, a particular strained state, substantially different from that of bulk-like materials and standard films, can be quenched up to film thicknesses around 60 nm. This strained state exhibits the same structural fingerprints of the interfacial dead layer in standard films and promotes surface morphology instabilities, which end up with the formation of self-organized nanopits array. At the same time, it has profound effects on the intrinsic magnetoelectronic properties of the films that exhibit an enhanced intrinsic CMR response. © 2014 AIP Publishing LLC. [<http://dx.doi.org/10.1063/1.4871984>]

From a technological point of view, optimally doped $\text{La}_{2/3}\text{Sr}_{1/3}\text{MnO}_3$ (LSMO) is the most interesting compound of the manganite perovskite family due to its Curie temperature well above room temperature that makes its fascinating physical properties suitable for practical applications.¹ However, in bulk state, LSMO only shows appreciable magnetoresistance (MR) at high fields around the transition temperature.² In recent years, there have been several attempts to improve the colossal MR (CMR) response of LSMO, mainly at low fields, to fit within the requirements for useful technological applications. LSMO, having a broad bandwidth and a quite stable ferromagnetic phase, does not present electronic phase separation, as observed in other narrow bandwidth manganite perovskites,³ which restricts the possible mechanisms for tuning the intrinsic CMR response. Nevertheless, extrinsic magnetoresistance can be properly modified by engineered grain boundaries^{4–9} in nanocomposite thin films. In these systems, extrinsic magnetoresistance, governed by spin-polarized tunneling across grain boundaries, could be significantly enhanced at low fields. In fact, MR values around 25% have been reported at low temperatures (10 K) and $H = 0.5 \text{ T}$.⁶ However, as mentioned above, enhancing the intrinsic CMR response seems to be more challenging.

An interesting approach has recently emerged by taking advantage of the strong coupling existing in these compounds between lattice, charge, orbital, and spin degrees of freedom. It is well known that the ferromagnetic/metallic state in manganite thin films can be modified by lattice perturbations through epitaxial strains.² This has been used by several groups to explore the effect of strain on the intrinsic CMR response of LSMO thin films and significant enhancements have been reported (64% at $H = 5 \text{ T}$).^{10–13} Strain-stabilized structural phase coexistence at low temperature was suggested as a possible mechanism for the observed CMR increase.¹² Similarly, analogous arguments may also be invoked to explain not only the CMR increase but also the anomalous behavior of the magnetotransport properties

of a few unit cells thick LSMO films, where competing interactions promote electronic phase separation and stabilize an insulating phase, usually referred to as dead-layer.^{14–20} This tuning of the electronic properties has been mainly explored by changing the strained state of the film through lattice mismatch with the substrate.^{10,13} The present work is devoted to explore an approach based on the effects of growth kinetics on the delicate balance between electronic and structural degrees of freedom. We will show that by properly choosing the growth conditions, films may exhibit strained states inaccessible in bulk form with enhanced CMR response.

In this paper, we study the magnetotransport properties of LSMO thin films grown under specific conditions to promote the appearance of nanostructured surface morphologies, in particular, the spontaneous formation of self-organized nanopits arrays.^{21,22} An investigation of the growth mechanism of such films²³ indicates that nanopits result from a kinetically driven surface instability encompassing the stabilization of interfacial lattice distortions²⁰ up to large film thicknesses. We will show that such films, hereafter referred to as nanostructured thin films (NTFs), present a high CMR response with values in excess of 40% at 1 T and above 90% at 9 T over a broad range of temperatures.

Epitaxial LSMO NTFs with thicknesses varying between 8 nm and 200 nm were grown by RF magnetron sputtering^{21,22,24} at 900 °C under a pure oxygen pressure of 19 Pa. Argon gas was not used during deposition process. Voltage bias of 120 V was chosen to obtain a growth rate of 1 nm min^{-1} . Since the miscut angle of the substrate plays an important role on the surface nanostructuring process, all NTFs used in this study were grown on a unique SrTiO_3 (STO) (001) substrate. The substrate was cut in several pieces, typically $1 \times 5 \text{ mm}^2$, and submitted to the standard thermal treatment to guarantee a single chemical surface TiO_2 termination.²² In addition, reference LSMO films grown under standard conditions to obtain flat surfaces with single unit cell step terraces were also prepared.²⁰ The surface morphology was investigated by atomic force microscopy (AFM)

and scanning electron microscopy (SEM). A typical image of the surface of a 17 nm thick NTF featuring self-organized nanopits is shown in the inset of Fig. 1(a). Structural properties were studied by X-ray diffraction (XRD). Measurements with synchrotron radiation were carried out at the KMC2 beamline at Helmholtz-Zentrum Berlin. Magnetotransport measurements were carried out in a standard four-probe configuration. Platinum contacts (10 nm thick) were evaporated through appropriate shadow masks. Measurements were performed in a Physical Properties Measurement System between 10 K and 400 K with perpendicular applied magnetic field up to 9 T. The main result of this work is displayed in Figs. 1(a) and 1(b), where magnetotransport properties of a 17 nm thick NTF are plotted in comparison with those of a reference flat LSMO film. From Fig. 1(a), it is observed that the NTF exhibits a much higher resistivity value (near one order of magnitude higher at room temperature) and a downward shift of the metal-to-insulator transition temperature ($T_{MI} \sim 150$ K). In the presence of magnetic fields, the resistance of the NTF is reduced over the whole range of temperatures and the maximum shifts upwards to higher temperatures giving rise to a CMR response, which achieves its maximum around the transition temperature. A huge increase of the magnetoresistance in the whole range of applied fields is detected in the NTF case, as shown in Figure 1(b), where R_H/R_0 is plotted around the corresponding T_{MI} for each sample. Both the upwards shift of the maximum of the $R(T)$ curve with magnetic field and the monotonous field dependence of the $R(H)$ curves are clearly in contrast with the typical features of grain boundary enhanced MR observed in granular materials, i.e., a sharp rise at very low fields ($H < 0.5$ T) followed by a strong change of slope in the $R(H)$ curve and no shift of the maximum of the $R(T)$ curves with field.⁴ Moreover, all microstructural studies performed in our samples did not show any signature of significant granularity, and no grain boundaries were observed around the formation of nanopits.²⁴ The results in Figure 1 and the fact that MR maximum lays around T_{MI} disregard any contribution of granularity³ and suggest an effective enhancement of the intrinsic CMR in these films.

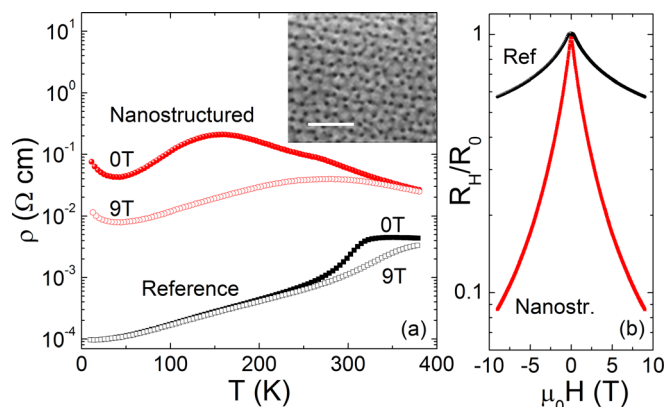


FIG. 1. (a) Temperature dependence of the electrical resistivity of a 17 nm thick LSMO nanostructured film (red circles) and a reference (flat surface) LSMO film (black squares). (b) Field dependence of resistivity of the films in (a) around their respective temperature transition. Inset in (a) shows a SEM image of the surface of the LSMO nanostructured film. Scale bar corresponds to 500 nm.

In the simplest double exchange picture of mixed-valence manganites, CMR is considered to occur when the system is close to the metal-insulator transition, and the magnetic field strongly enhances ferromagnetic correlations in the insulating phase promoting the transition to the ferromagnetic-metallic phase with the corresponding huge decrease of the resistance. Tuning of this process has been usually explored by modifying the doping rate or even by varying the optimal oxygen content, which alters the Mn^{3+}/Mn^{4+} ratio. However, according to the double exchange picture, the CMR response can also be modified by acting on some physical parameters such as Mn-O-Mn bond angle and bond distances. Fortunately, in thin films, this can be accomplished in a relatively easy manner through epitaxial strain. Epitaxial strain may modify the electronic hopping amplitude not only by changing the Mn-O-Mn bond angle and Mn-O length but also by altering the Jahn-Teller orbital splitting and thus favouring the tendency to electronic localization.^{25,26} There are several reports in the literature showing an efficient enhancement of CMR for LSMO thin films grown on substrates imposing a large epitaxial strain such as $LaAlO_3$, $DyScO_3$, or $GdScO_3$.^{10,13} Conversely, for small misfit values, as in the case of (100) STO substrates (tensile strain of $\epsilon \sim 0.6\%$), no enhancement of the CMR has been observed.¹⁰ However, elastic strain is not the only ingredient in the recipe and, indeed, insulating behaviour has been repeatedly reported for ultra thin LSMO grown on STO substrates.^{14–20} This insulating phase appears as the result of a misfit relaxation scenario where electronic distortion is the dominant mechanism over purely elastic strain or octahedral tilting mechanisms.²⁰ In NTFs, the strain relaxation mechanism is modified in such a way that the electronic distortion persists up to much larger thicknesses than in flat films. Interestingly, strain relaxation through surface instabilities leading to the formation of self-assembled nanopits seems to lock an unusual LSMO strained state with strong implications on the magnetotransport properties of the system.

As determined from X-ray measurements, similarly to flat films,²⁰ NTFs are strained with the in-plane lattice parameter matching that of the underlying STO substrate ($a = 0.3905$ nm) up to large thicknesses. In contrast, the measured c-axis parameter has been found to be unexpectedly large. For example, $c = 0.3879$ nm was measured in the 17 nm thick film, yielding an anomalously small Poisson ratio $\nu \sim 0.03$, much smaller than that obtained for flat films in the elastically strained rhombohedral state,²⁰ $\nu \sim 0.33$ ($\nu = \epsilon^+ / (\epsilon^+ - 2\epsilon^{\parallel})$, where ϵ^+ and ϵ^{\parallel} are the out-of-plane and in-plane strain components, respectively ($a_{bulk} = 0.3881$ nm (Ref. 27) is used as a reference value). Moreover, the detailed analysis of X-ray reciprocal space maps (see Figure 2(a)) shows that contrary to twinned flat films, which reveal a clear splitting associated to (100) and (010) twins,²⁰ NTFs do not exhibit a fully developed rhombohedral phase, as indicated by the large spread of the film peak intensity along both the Q_x and Q_y axes. The diamond shape of the intensity contour lines suggests an incipient stage in the development of the rhombohedral shear strain along the [100] and [010] directions.²⁸ During the growth of LSMO on STO, the electronic and structural interaction at the interface induces the formation of a Mn^{3+} enriched monoclinically distorted

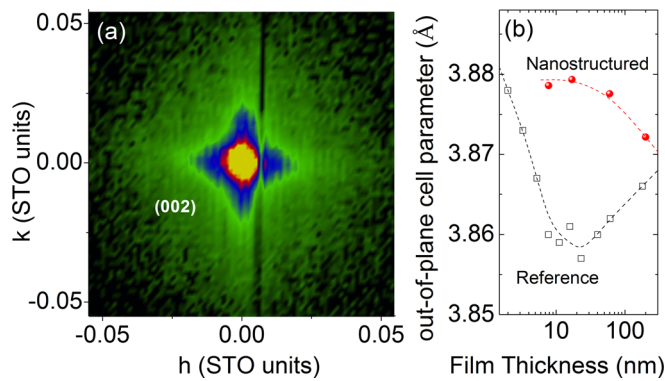


FIG. 2. (a) Reciprocal space map around the (002) reflection of a 17 nm thick nanostructured LSMO thin film. (b) Evolution with thickness of the out-of-plane cell parameter as determined from x-ray measurements for nanostructured (closed symbols) LSMO thin films. For comparison, results of reference films taken from Ref. 20 are also plotted. Lines are guides for the eyes.

~ 2.5 nm thick interfacial layer, exhibiting an anomalously large c-axis parameter and depressed magnetotransport properties.¹⁴ Therefore, it appears that the structural and magnetotransport features of NTFs resemble those characterizing the interfacial dead layer in flat films. A comparison between the thickness dependence of the c-axis parameter of flat films²⁰ and NTFs (see Fig. 2(b)) clearly shows that the anomalous high values persist in the NTFs up to much higher thicknesses. Altogether, our magnetotransport and structure results strongly point that under the present growth conditions, the same mechanism that promotes the formation of surface nanopits also hinders the full transformation of the monoclinically distorted interfacial layer to the equilibrium rhombohedral phase. The continuous intensity spread along Q_x and Q_y strongly suggests that the films retain a complex microstructure with a subtle modulation of the Mn-O-Mn path at the nanoscale that hinders the development of the double exchange ferromagnetic phase explaining the observed enhancement of CMR.

Figures 3(a) and 3(b) show the temperature dependence of the magnetoresistance defined as $MR(\%) = (\rho(T,H) - \rho(T,0)) / \rho(T,0) \times 100$, for $H = 1$ T and for $H = 9$ T, respectively. For comparison, we have also plotted the magnetoresistance of a standard 40 nm thick flat LSMO film as a solid line in both figures. Whereas in flat LSMO thin films above 10–15 nm, there is almost no appreciable influence of the thickness on their magnetotransport properties,²⁹ here we may observe that the magnetoresistance is gradually reduced as film thickness increases. Concomitantly, the maximum in MR is shifted towards higher temperatures following the same trend as the corresponding transition temperature. For a thickness of 200 nm, the magnetotransport properties are similar to those observed in standard LSMO thin films (see black lines in Fig. 1) although at $H = 9$ T there is still a significant magnetoresistance in the low temperature region. Note also that the transition temperature is well above room temperature probing that the nominal oxygen pressure is not a determinant parameter in the results here presented.

Annealing effects on the magnetotransport properties of NTFs were also performed to check the robustness of this strained state. Under annealings up to relatively high temperatures ($\sim 700^\circ\text{C}$), NTF retained their enhanced CMR

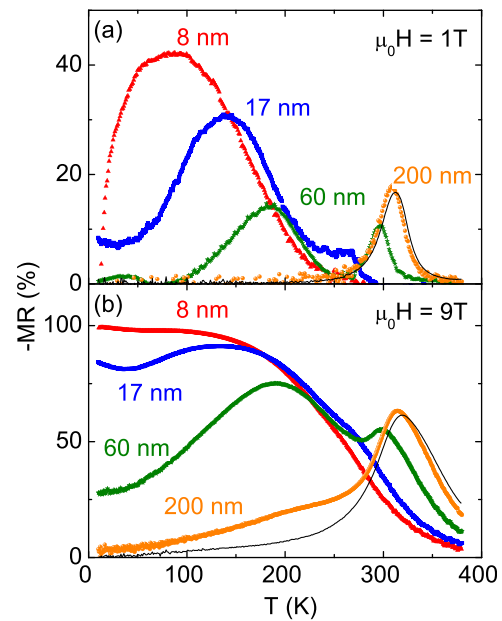


FIG. 3. Temperature dependence of the magnetoresistance for nanostructured LSMO films with different thicknesses at applied magnetic fields of (a) 1 T and (b) 9 T.

response. A significant evolution of the properties was only observed when annealings were performed at conditions approaching the growth temperature. Fig. 4(a) shows the temperature dependence of the MR at 1 T of the as-grown 17 nm thick NTF (closed red symbols) and after an annealing in oxygen atmosphere at 900°C for 1 h (open black symbols). It is observed that after annealing, the LSMO film recovers the bulk-like behaviour (compare with the black line in Fig. 3), exhibiting only a modest MR, not bigger than 15%, around the transition temperature, now shifted above 300 K. The electrical conductivity has also been improved at all temperatures (see inset in Fig. 4(a)). At the same time, annealed films tend to exhibit a flatter surface morphology.²⁴ This implies that the strained state has relaxed towards a more standard LSMO bulk-like phase. This change can be monitored as well by measuring the c-axis parameter of the as-grown and annealed films. As shown in Fig. 4(b), a reduction of the c-axis parameter is detected in the annealed film

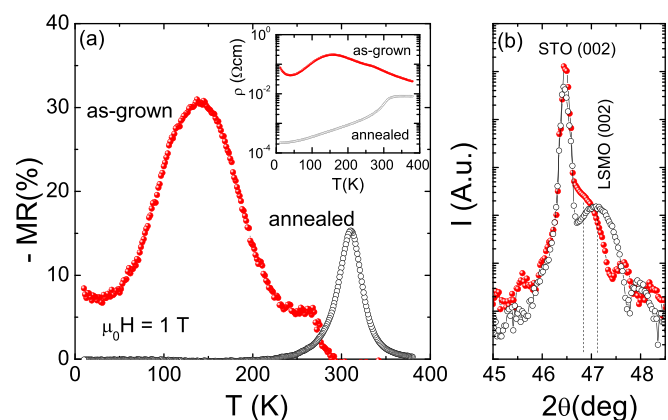


FIG. 4. (a) Magnetoresistance and electrical resistivity (inset) of a nanostructured LSMO thin film as-grown and after annealing at high temperature. (b) X-ray diffraction pattern around 002 peak of the same film in (a) reflecting the change in c-axis parameter after annealing.

($c_{\text{annealed}} \sim 0.3852$ nm and $c_{\text{as-grown}} \sim 0.3879$ nm), thus confirming that the modified strain state is responsible for the observed change of the magnetotransport properties.

In summary, we have shown experimental evidences of a route to engineer the colossal magnetoresistance response in manganite thin films through an accurate control of the growth kinetics. In this way, a balance between different competing strain relaxation mechanisms can be achieved, leading to a strained state substantially different from that of relaxed flat thin films or bulk-like materials. This strained state has a profound effect on the magnetotransport properties of the films due to a subtle modification of Mn-O-Mn bond angle and the Mn-O length and/or by altering the Jahn-Teller splitting, thus hindering the development of the double exchange ferromagnetic phase and favouring the tendency towards electronic localization. As a result, NTFs exhibit a behaviour close to that of lower doping rate compositions approaching the antiferromagnetic phase and prone to display electronic localization effects.

We acknowledge financial support from the Spanish MEC (MAT2011-29081 and MAT2012-33207), CONSOLIDER (CSD2007-00041), and FEDER program. Z.K. thanks the Spanish MINECO for the financial support through the RyC program. We thank Helmholtz-Zentrum Berlin for the allocation of neutron/synchrotron radiation beamtime. The research leading to these results has received funding from the European Community's Seventh Framework Programme (FP7/2007-2013) under Grant Agreement No. 312284.

¹A. Urushibara, Y. Moritomo, T. Arima, A. Asamitsu, G. Kido, and Y. Tokura, *Phys. Rev. B* **51**, 14103 (1995).

²Y. Tokura, *Rep. Prog. Phys.* **69**, 797 (2006).

³P. K. Siwach, H. K. Singh, and O. N. Srivastava, *J. Phys.: Condens. Matter* **20**, 273201 (2008).

⁴R. Gross, L. Alff, B. Buchner, B. H. Freitag, C. Hofener, J. Klein, Y. F. Lu, W. Mader, J. B. Philipp, M. S. R. Rao, P. Reutler, S. Ritter, S. Thienhaus, S. Uhlenbruck, and B. Wiedenhorst, *J. Magn. Magn. Mater.* **211**, 150 (2000).

⁵A. Gupta, G. Q. Gong, G. Xiao, P. R. Duncombe, P. Lecoeur, P. Trouilloud, Y. Y. Wang, V. P. Dravid, and J. Z. Sun, *Phys. Rev. B* **54**, R15629 (1996).

⁶A. P. Chen, Z. X. Bi, C. F. Tsai, J. Lee, Q. Su, X. H. Zhang, Q. X. Jia, J. L. MacManus-Driscoll, and H. Y. Wang, *Adv. Funct. Mater.* **21**, 2423 (2011).

⁷A. Chen, Z. Bi, C.-F. Tsai, L. Chen, Q. Su, X. Zhang, and H. Wang, *Cryst. Growth Des.* **11**, 5405 (2011).

⁸M. Staruch, D. Hires, A. Chen, Z. Bi, H. Wang, and M. Jain, *J. Appl. Phys.* **110**, 113913 (2011).

⁹M. Staruch, H. Gao, P.-X. Gao, and M. Jain, *Adv. Funct. Mater.* **22**, 3591 (2012).

¹⁰Y. Takamura, R. V. Chopdekar, E. Arenholz, and Y. Suzuki, *Appl. Phys. Lett.* **92**, 162504 (2008).

¹¹C. Adamo, X. Ke, H. Q. Wang, H. L. Xin, T. Heeg, M. E. Hawley, W. Zander, J. Schubert, P. Schiffer, D. A. Muller, L. Maritato, and D. G. Schlom, *Appl. Phys. Lett.* **95**, 112504 (2009).

¹²S. Mukhopadhyay, I. Das, and S. Banerjee, *J. Phys.: Condens. Matter* **21**, 026017 (2009).

¹³F. J. Wong, S. Zhu, J. M. Iwata-Harms, and Y. Suzuki, *J. Appl. Phys.* **111**, 063920 (2012).

¹⁴J. Z. Sun, D. W. Abraham, R. A. Rao, and C. B. Eom, *Appl. Phys. Lett.* **74**, 3017 (1999).

¹⁵M. Huijben, L. W. Martin, Y. H. Chu, M. B. Holcomb, P. Yu, G. Rijnders, D. H. A. Blank, and R. Ramesh, *Phys. Rev. B* **78**, 094413 (2008).

¹⁶B. Kim, D. Kwon, T. Yajima, C. Bell, Y. Hikita, B. G. Kim, and H. Y. Hwang, *Appl. Phys. Lett.* **99**, 092513 (2011).

¹⁷H. Boschker, J. Kautz, E. P. Houwman, W. Siemons, D. H. A. Blank, M. Huijben, G. Koster, A. Vaillonis, and G. Rijnders, *Phys. Rev. Lett.* **109**(5), 157207 (2012).

¹⁸C. Aruta, G. Ghiringhelli, A. Tebano, N. G. Boggio, N. B. Brookes, P. G. Medaglia, and G. Balestrino, *Phys. Rev. B* **73**, 235121 (2006).

¹⁹M.-B. Lepetit, B. Mercey, and C. Simon, *Phys. Rev. Lett.* **108**, 087202 (2012).

²⁰F. Sandiumenge, J. Santiso, L. Balcells, Z. Konstantinović, J. Roqueta, A. Pomar, J. P. Espinos, and B. Martinez, *Phys. Rev. Lett.* **110**, 107206 (2013).

²¹Z. Konstantinović, J. Santiso, L. Balcells, and B. Martinez, *Small* **5**, 265 (2009).

²²Z. Konstantinović, J. Santiso, D. Colson, A. Forget, L. I. Balcells, and B. Martinez, *J. Appl. Phys.* **105**, 063919 (2009).

²³Z. Konstantinović, J. Santiso, L. Balcells, and B. Martinez, *Nanotechnology* **21**, 465601 (2010).

²⁴Z. Konstantinović, F. Sandiumenge, J. Santiso, L. Balcells, and B. Martinez, *Nanoscale* **5**, 1001 (2013).

²⁵A. J. Millis, T. Darling, and A. Migliori, *J. Appl. Phys.* **83**, 1588 (1998).

²⁶A. Mukherjee, W. S. Cole, P. Woodward, M. Randeria, and N. Trivedi, *Phys. Rev. Lett.* **110**(15), 157201 (2013).

²⁷P. G. Radaelli, G. Iannone, M. Marezio, H. Y. Hwang, S. W. Cheong, J. D. Jorgensen, and D. N. Argyriou, *Phys. Rev. B* **56**, 8265 (1997).

²⁸J. Santiso, L. Balcells, Z. Konstantinović, J. Roqueta, P. Ferrer, A. Pomar, B. Martinez, and F. Sandiumenge, *CrystEngComm* **15**, 3908 (2013).

²⁹J. Dho, N. H. Hur, I. S. Kim, and Y. K. Park, *J. Appl. Phys.* **94**, 7670 (2003).

Macroscopic evidence of nanoscale resistive switching in $\text{La}_{2/3}\text{Sr}_{1/3}\text{MnO}_3$ micro-fabricated bridges

Luis Peña, Luis Garzón, Regina Galceran, Alberto Pomar, Bernat Bozzo, Zorica Konstantinovic, Felip Sandiumenge, Lluis Balcells, Carmen Ocal and Benjamin Martinez

Instituto de Ciencia de Materiales de Barcelona - CSIC, Campus UAB, 08193 Bellaterra, Spain

E-mail: ben.martinez@icmab.es

Received 30 June 2014, revised 6 August 2014


Accepted for publication 12 August 2014

Published 10 September 2014

Abstract

In this work we report on a combined macro, micro and nanoscale investigation where electronic transport properties through $\text{La}_{2/3}\text{Sr}_{1/3}\text{MnO}_3$ (LSMO) microfabricated bridges, in which nano-sized resistive states are induced by using a conducting scanning probe microscope (C-SPM), are analyzed. The strategy intentionally avoids the standard capacitor-like geometry, thus allowing the study of the electronic transport properties of the locally modified region, and approaches the integration of functional oxides in low dimensional devices while providing macroscopic evidence of nanoscale resistive switching (RS). The metallic and ferromagnetic LSMO is locally modified from its low resistance state (LRS) to a high resistance state (HRS) when a bias voltage is applied on its surface through the conducting tip, which acts as a mobile electrode. Starting from a metallic oxide the electroforming process is not required, thus avoiding one of the major drawbacks for the implementation of memory devices based on RS phenomena. The application of a bias voltage generates an electric field that promotes charge depletion, leading to a strong increase of the resistance, i.e. to the HRS. This effect is not only confined to the outermost surface layer, its spatial extension and final HRS condition can be modulated by the magnitude and duration of the potential applied, opening the door to the implementation of multilevel devices. In addition, the half-metallic character, i.e. total spin polarization, of LSMO might allow the implementation of memory elements and active spintronic devices in the very same material. The stability of the HRS and LRS as a function of temperature, magnetic field and compliance current is also analyzed, allowing the characterization of the nature of the switching process and the active material.

Keywords: complex oxides, resistive switching, manganites, atomic force microscopy, thin films

 Online supplementary data available from stacks.iop.org/JPhysCM/26/395010/mmedia

(Some figures may appear in colour only in the online journal)

1. Introduction

Reversible resistive switching (RS), i.e. the interchangeability of the resistive state by applying a pulse of current or voltage, is a long standing subject of active research because of its potential use for the development of two-terminal non-volatile memory devices. RS phenomena have been observed in a large

variety of materials [1–3], including metal oxide materials [4,5]. By the end of the nineties, with the explosion of research in complex oxides, transition metal oxides, such as manganites and titanates, became the epicenter of the research in this field. RS behavior can be classified taking into account the switching mechanism or the switching material [6,7]. According to the latter, complex oxide materials are classified as anion devices in

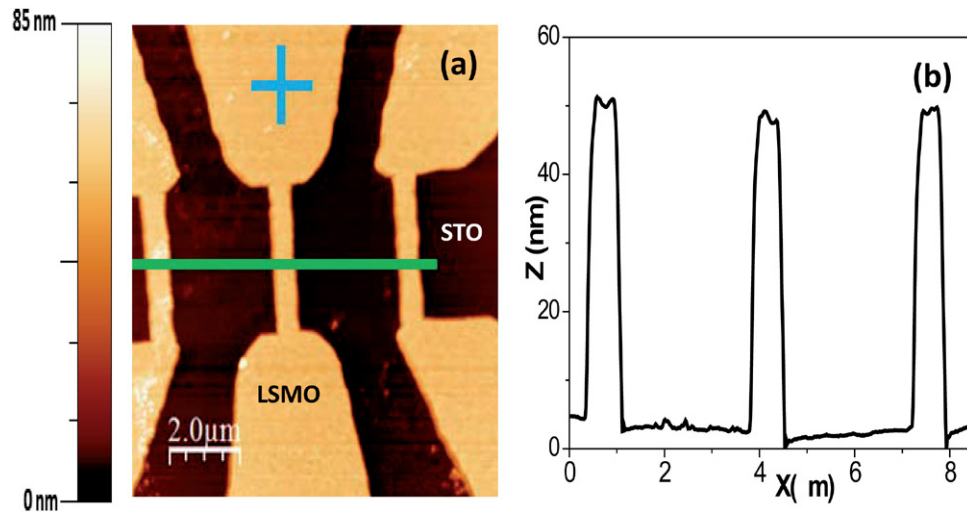


Figure 1. (a) Topographic image of a lithographed LSMO thin film ($h \sim 45$ nm). The relief profile of the microbridges (b) is measured along the green line in (a) to show that the engraving process reaches the STO substrate surface ($\Delta z \approx 45$ nm), ensuring that the LSMO bridges are electrically isolated from each other. The blue cross indicates the surface point where the local I - V curve shown in figure 2 was performed.

which RS may originate from a variety of defects (microstructural or chemical) that modify the overall electronic transport properties of the material rather than from a specific property of the electronic structure. With few exceptions, as it is the case of the metallic $\text{La}_{2/3}\text{Sr}_{1/3}\text{MnO}_3$ [8, 9], most switching materials are initially insulating and therefore an initial electroforming process is required. The research of RS in complex oxide materials have been mainly conducted in metal-insulator-metal (M-I-M) heterostructures in which the M-I interfaces appear to play a major role. Indeed, thermal redox and/or anodization near the interface between the metal electrode and the oxide has been widely considered as the driving mechanism for the change in resistance through the formation/rupture of conducting filaments in unipolar RS [10]. On the other hand, electrochemical migration of oxygen vacancies [11], charge trapping [12] or a Mott transition induced by doping on the M-I interface have been pointed as possible mechanisms in bipolar RS [13–15]. However, to clarify the true nature of the mechanism behind requires classifying the actual switching behavior of each materials' combination, which is a non-trivial task provided the variety of chemical interactions that may occur simultaneously due to the concurrence of both intense local electric fields and Joule self-heating [16,17]. In many semiconducting oxides, such as complex perovskites, the typical RS behavior found is of the bipolar type, i.e. the RS curve shows directional behavior depending on the bias polarity [11, 18]. In the particular case of manganites, RS phenomena were first described in $\text{Pr}_{0.7}\text{Ca}_{0.3}\text{MnO}_3$ compound and it was argued to be characteristic of phase-separated states [19]. Nevertheless, RS has also been observed in manganites without phase separation phenomena [20], pointing to a different origin. In fact, more recent studies suggest that RS in perovskite oxides may be originated at the metal electrode/perovskite oxide interface [5, 11, 14, 21, 22], involving redox processes triggered by the electric field and/or the temperature.

In this work we report on the electronic transport response of locally modified HRS in $\text{La}_{2/3}\text{Sr}_{1/3}\text{MnO}_3$ (LSMO) high

quality epitaxial thin films, prepared by RF sputtering on top of SrTiO_3 (STO) substrates [23,24]. The transition from the initially metallic state to the highly resistive insulating-like state is induced (writing process) by the application of a bias voltage, V_{bias} , using the conducting tip of a scanning force microscope across microbridges patterned on the LSMO thin film. The transition is bipolar, i.e. the inversion of the polarity of the applied voltage is required for the reversing (erasing) process. The chosen geometry allows us measuring the transport properties of the modified areas, by injecting current along the microbridge, to monitor the macroscopic resistance changes as well as the temperature and magnetic field dependence. Resistance versus temperature curves allow monitoring changes on the insulating to metal transition (I-M) temperature that, according to the well known phase diagram of this system, will help clarifying the nature of the mechanism responsible for the observed RS behavior in this system. In addition, the half-metallic character, i.e. total spin polarization, of LSMO will allow the implementation of memory elements and active spintronic devices in the very same material.

2. Experimental

LSMO samples of 5×5 mm² with thicknesses, h , between 15 and 50 nm were prepared by RF sputtering on top of (001)-oriented STO substrates. Prior to deposition STO substrates were cleaned in an ultrasonic bath with Milli-Q water and annealed at 1000 °C in air for 2 h to obtain a typical morphology of terraces and step with unit cell height (≈ 0.4 nm), thus selecting mostly a unique atomic termination, likely to be TiO_2 [25]. Reciprocal space mapping was performed using a Bruker D8 GADDS system equipped with a 2D Hi-Star x-ray detector to determine the degree of strain of the films. It was found that all LSMO films were in-plane fully strained [26].

Macroscopic transport measurements were performed along microbridges fabricated by using standard photolithographic

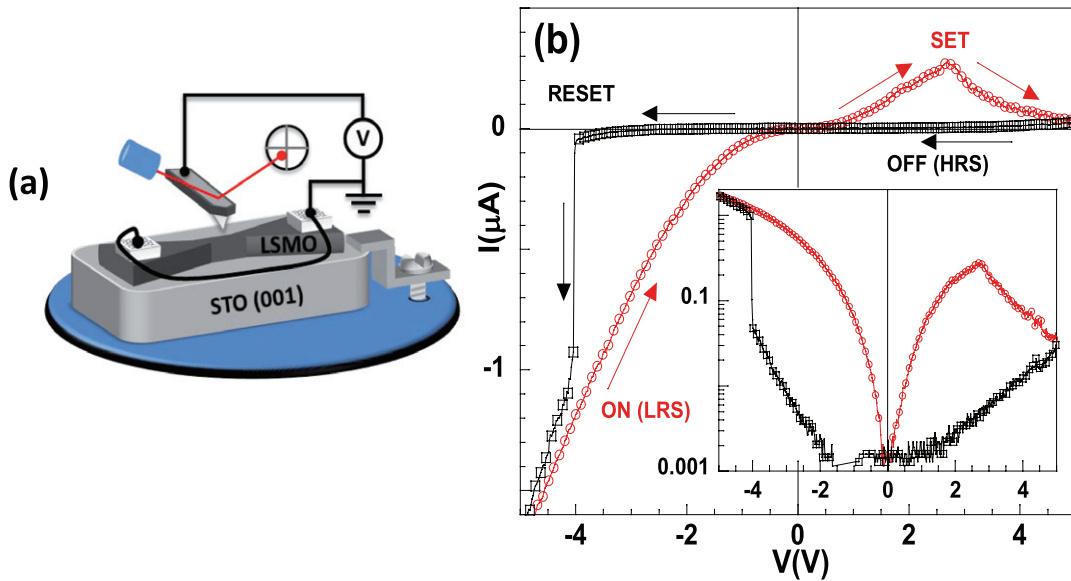


Figure 2. (a) Schematics of the experimental C-SPM set up employed for RS and local measurements. (b) Local I - V loop showing bipolar resistive switch measured on the LSMO film by placing the conducting tip at the point marked in figure 1. Inset: semilog plot of the I - V characteristic curve making evident the change of about three orders of magnitude between ON and OFF states.

techniques in a commercial physical properties measurement system (PPMS) by Quantum Design.

Scanning probe microscopy (SPM) measurements were carried out at room temperature (RT) using an instrument from Nanotec Electrónica. Moreover, Kelvin probe microscopy (KPM), a non-invasive non-contact technique that allows measuring differences in the local work function resulting from local electronic properties and is sensitive to differences in the resistive state of the surface, was also used. Data acquisition and analysis were made by using the WSxM software [27]. C-SPM and KPM measurements were conducted under humidity- ($\leq 5\%$ RH) controlled conditions obtained by a continuous N_2 flux and using silicon tips coated with a boron-doped diamond conducting film. The RS modifications were performed by applying a bias voltage by means of the conducting tip of the C-SPM working in the repulsive contact regime (applied forces 50–200 nN). To ensure no sample indentation, C-SPM was always performed under controlled constant load, i.e. by using a force feedback while measuring the current between tip and sample. The sample was always grounded and the voltage was applied to the tip. Direct electric contact to ground was established through a metallic clamp attached to the surface film at the sample border (mm apart from tip-surface contact). An external I - V converter (Stanford Research Systems) was used to access a wide range of currents (1 pA–1 mA). At selected positions, current–voltage (I - V) characteristics were measured as a function of V_{tip} .

KPM is a dynamic mode that measures the so called contact potential difference or surface potential difference (SPD) through cancelation of tip-sample electrostatic forces. Contrary to C-SPM for KPM, the conducting tip is placed far above (tens of nm) the sample surface such that they are not in direct contact but electrically connected via electronics. As a result, their Fermi levels align creating a surface potential and thus

a tip-sample electrostatic force. The method was introduced to investigate the work function of metals [28] but is nowadays applied to a wide variety of materials, including insulators [29]. In the later case, the term work function holds for the local ionization potential (IP, defined as the energy difference between the valence band maximum and the vacuum level), in close analogy to the metallic case (where the IP coincides with the work function). However, one must keep in mind that the non-conducting case is substantially more challenging.

If the work function of the KPM tip (vibrating electrode) and the sample are φ_{tip} and φ_{sample} , respectively, then the contact potential difference between the tip and the sample is $\text{SPD} = \text{SP}_{\text{sample}} = (\varphi_{\text{tip}} - \varphi_{\text{sample}})/e = \Delta\varphi_s/e$, where e is the electric charge. When the sample surface has two regions (A, B) with different electronic properties, as the virgin or RS modified LSMO of interest here, the contact potential difference between them is $\text{SPD} = \text{SP}_A - \text{SP}_B = -(\varphi_A - \varphi_B)$ independently of the material the tip is made of. Therefore, the contrast of the surface potential maps obtained by scanning the tip over the surface directly reflects the local variations of the surface work function. Note that, by definition, the higher the local SP the lower the local effective work function ($\text{SPD} = -\Delta\varphi_{AB}$). The method lacks the desired lateral resolution for measuring nanostructures but avoids problems derived from direct contact scanning.

3. Results and discussion

LSMO samples used in this study were highly homogeneous crystalline thin films (15–50 nm thick) with the STO (001)/LSMO (001) epitaxial relationship. They were ferromagnetic and metallic (FM–M) with a Curie temperature $T_C \approx 350$ K and bulk-like saturation magnetization $M_S \approx 580 \text{ emu cm}^{-3}$ at 10 K, (see online supplementary data stacks.iop.org/JPhysCM/26/395010/mmedia). Prior to local RS

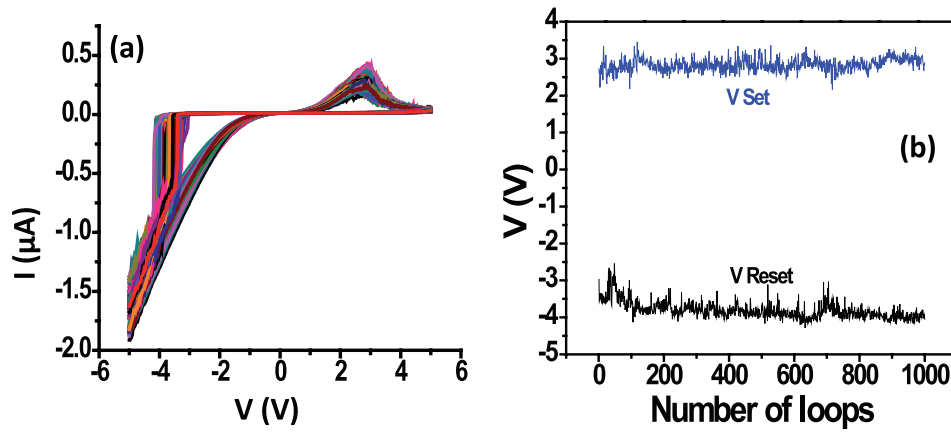


Figure 3. (a) Endurance test showing the robustness of the RS process during 1000 I - V cycles obtained at the same surface point of a 17 nm thick LSMO film. Only the 50 first loops are shown for the sake of clarity. (b) V_{Set} and V_{Reset} values measured for the whole series of I - V loops. This plot evidences that the apparent creep in (a) is in fact statistical noise.

modifications, LSMO films were patterned by using photolithographic techniques into microbridges of different width (W), length (L) and height (h). As shown in figure 1 for a patterned 45 nm thick film, topographic height across the microbridges ($W = 600$ nm) indicates that engraving reached the STO substrate, i.e. h equals the film thickness ($h = 45$ nm), and thus, LSMO microbridges are electrically isolated from each other.

As schematically shown in figure 2(a), for C-SPM measurements ground connection was established through direct electric contact using a metallic clamp (counter electrode) firmly attached to the LSMO surface and the bias voltage (V_{tip}) was applied to the conducting tip working as active top electrode. All C-SPM experiments were performed under low humidity conditions ($< 5\%$ in a N_2 flux) ruling out any important water neck influence on the process.

A typical I - V curve obtained at RT by applying a voltage cycle (-6 V \rightarrow 0 \rightarrow +6 V \rightarrow 0 \rightarrow -6 V) placing the conducting tip at a fixed location on top of a virgin (pre-switched) LSMO layer ($h = 25$ nm) is shown in figure 2(b). The curve exhibits the typical features of a bipolar counter eightwise switching process [30, 31]. Starting from the LRS (ON state) the current increases with V_{bias} until dropping at the so called reset value (V_{Reset}) and, after following a negative differential resistance region, the HRS (OFF state) is reached. Reversing the voltage sweep direction the system remains in the HRS until charge injection at the set value (V_{Set}) drives the system back to the LRS. As can be seen in the logarithmic plot (inset in figure 2(b)) the conductance ratio between states (I_{ON}/I_{OFF}) is close to three orders of magnitude in this particular case. It is worth noting that although V_{Set} depends on the film thickness and, therefore, must be determined in each case, similar I - V curves were found for the thickness range studied, irrespective of the conducting tip location on the LSMO film surface or the distance to the counter electrode.

The process is very robust and the system can be cycled back and forth between the ON and OFF states hundreds of times without substantial changes (see figure 3(a)). Figure 3(b) shows the magnitude of V_{Set} and V_{Reset} as a function of the number of I - V cycles to evidence that the apparent creep in figure 3(a) is in fact statistical noise, i.e. the switching behaviour is maintained

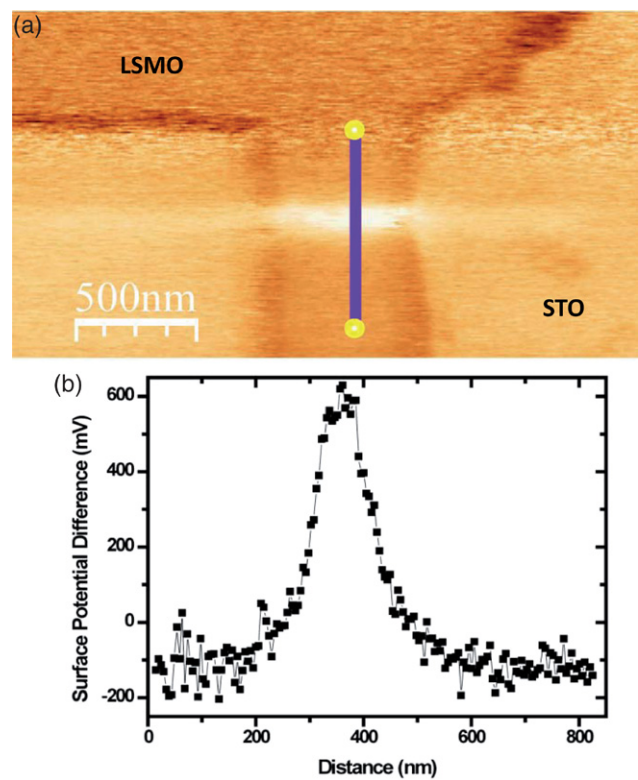


Figure 4. (a) 2D map of the SPD acquired by Kelvin probe microscopy (KPM) on a lithographed ~ 45 nm thick LSMO film. The dark contour lines coincide with the microfabricated topography (not shown) and are due to the work function discontinuity at the LSMO/STO steps. Discarding this feature, medium color corresponds to the bare STO substrate, while dark and bright colors correspond to the virgin LSMO and HRS regions, respectively. (b) The SPD profile along the microbridge crossing the HRS as marked in (a) indicates a difference in work function of ≈ 0.7 eV between the virgin and the written HRS state obtained by 3 tip scan lines at $V_w = +8$ V.

with no reduction of the reset voltage. The asymmetry of the I - V curves, with different $|V_{bias}|$ for set and reset, is commonly ascribed to the different electronic properties of the metallic electrodes in the capacitor-like geometry. However, it is also related to the mechanism acting in each case, a smooth transition

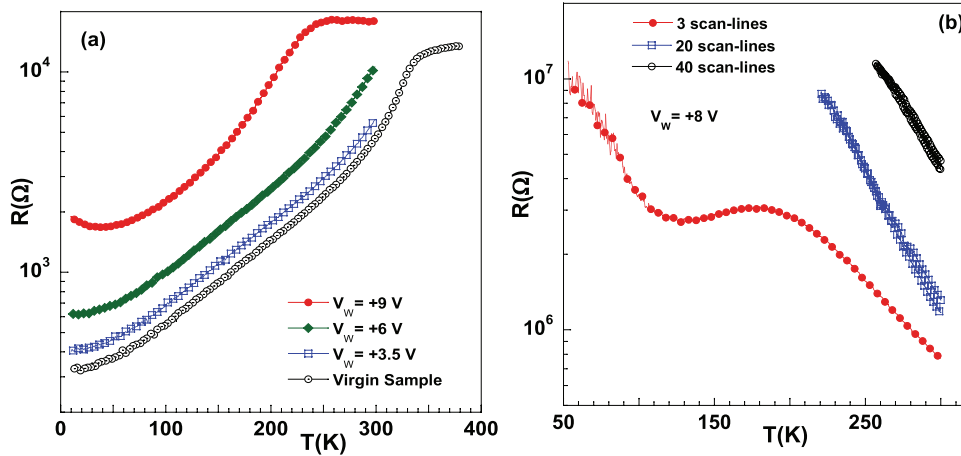


Figure 5. (a) Comparison of the temperature dependence of the resistance of a virgin LSMO film and a microbridge ($W \times L \approx 420 \text{ nm} \times 1.8 \mu\text{m}$, $h \sim 45 \text{ nm}$) as a function of the tip bias voltage of the writing process (V_w) using 3 scan-lines in all three cases. (b) Temperature dependence of the resistance of a microbridge ($W \times L \approx 1.2 \mu\text{m} \times 4.8 \mu\text{m}$, $h \sim 25 \text{ nm}$) as a function of the number of tip scan lines for the same $V_w = +8 \text{ V}$.

due to charge dragging in the reset process and a sharp change due to charge injection in the set process.

In order to explore the effect of RS on the macroscopic transport response of the microbridge device, we benefit from the scanning capability of the C-SPM to obtain 1D modifications of the LSMO surface by ‘writing’ HRS lines during tip sweeping across the microbridge at a given $V_{\text{bias}} = V_w$. The obtained HRS modifications can be observed (read) by contact mode current map imaging at a low enough V_{bias} or by using KPM. The KPM SPD signal is commonly identified with differences in the local work function resulting from local electronic properties and is sensitive to differences in the resistive state of the surface [28, 29]. The result of the writing process is illustrated in figure 4. As measured here (see experimental section), the larger surface potential signal (lower work function) on the LSMO corresponds to higher resistance values and the change of close to 700 mV in SPD indicates that the material in the written area has transitioned from the initial LRS to a HRS [8]. Since charge carriers in lightly alkaline-earth-doped manganites as $\text{La}_{2/3}\text{Sr}_{1/3}\text{MnO}_3$ are holes, the simplest way to interpret the work function lowering would be a decrease of the carrier concentration.

As shown here, in spite of the small dimensions of the tip-induced HRS areas, their influence on the whole microbridge resistance can be detected in macroscopic measurements. The nanostructured device presents the macroscopic I - V operation and temperature dependent resistance curves, $R(T)$, corresponding to the actual resistive state of the bridge. This is illustrated in figure 5 for two samples with different lithographed LSMO microbridges of dimensions $W \times L \approx 420 \text{ nm} \times 1.8 \mu\text{m}$ and $h \approx 45 \text{ nm}$ (figure 5(a)) and $W \times L \approx 1.2 \mu\text{m} \times 4.8 \mu\text{m}$ and $h \approx 25 \text{ nm}$ (figure 5(b)). The effect of V_w magnitude was first analyzed by discarding application time, i.e. for a given number of tip scan lines. In the case of the thickest microbridge the metallic-like behavior persist, with an increase of the resistance in the whole range of temperature sampled, even after using a high $V_w = +9 \text{ V}$ (figure 5(a)). For $V_w \sim +3.5 \text{ V}$, slightly above the $V_{\text{Reset}} = +2.7 \text{ V}$ determined from the local I - V curves, a tiny increase of the resistance was observed

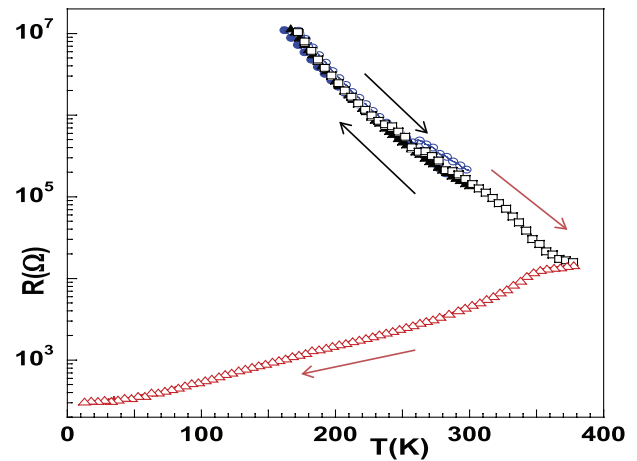


Figure 6. Temperature dependence of the resistance of a 25 nm thick microbridge after HRS writing by applying a $V_w = +8 \text{ V}$. As can be seen at the upper branch, during warming and cooling from 150–300 K (black and blue symbols) the system maintains a reversible insulating behavior (curves collapse) while cooling after reaching $T \approx 380 \text{ K}$ ($T > T_C$) (red arrows) provokes non-reversibility and the system becomes metallic, returning back to the LRS.

compared to that of the virgin sample (shown as a reference). As V_w increases the change of the resistance becomes more evident and for $V_w \sim +9 \text{ V}$ a strong decrease (of about 100 K) of the I - M transition temperature was observed. However, despite this notable change in properties, the microbridge basically maintains the same behavior than the virgin sample, i.e. the system exhibits a transition from paramagnetic (PM) to FM- M . Conversely, similar $R(T)$ experiments on the thinner microbridge reveal an insulating behavior for $V_w = +8 \text{ V}$ and same tip scan lines (figure 5(b)). In the same figure, the effect of voltage application time is also analyzed by varying the number of scan lines (3, 20 and 40 in the present case) used during the writing process.

As otherwise expected, the larger the time of voltage bias application the stronger the change of resistance in the microbridge. Moreover, a strong change of resistance is observed at

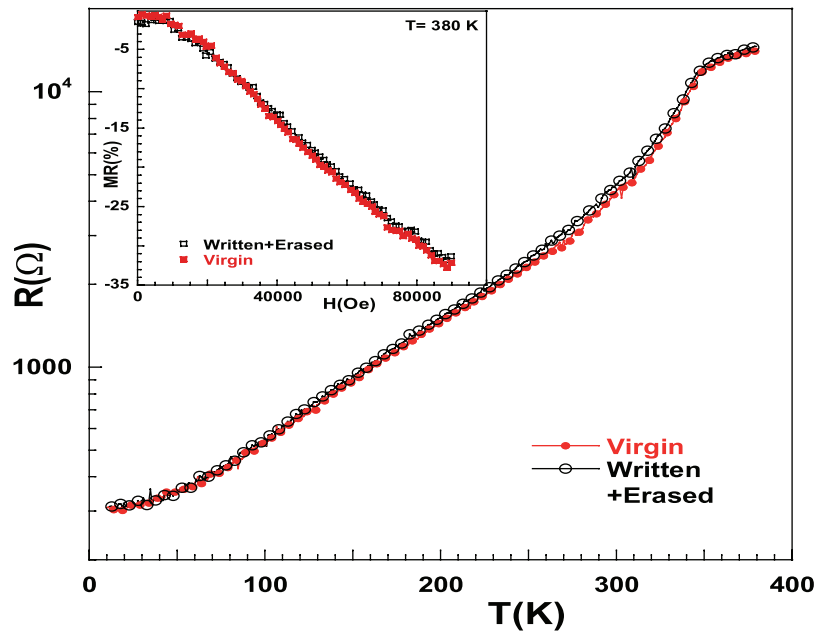


Figure 7. Temperature dependence of the resistance curves of a LSMO microbridge before (virgin) and after erasing (by reaching $T = 380\text{ K}$) a local HRS written at $V_w = +8\text{ V}$. Inset: magnetoresistance data for the same two cases. The full coincidence of resistance and magnetoresistance results for virgin and erased states demonstrate the restoration of the material state by sample annealing at high temperature.

RT while the system becomes insulating and all the features of the I - M transition disappear in the whole temperature range sampled. We conclude that the writing process has an accumulative effect promoting a progressive change on the electronic properties of the written area that proceeds more efficiently for higher V_w . These results suggest that the LSMO material in the written area has progressively changed from FM-M to FM-I with a strong decrease of T_C , and then to I with a huge increase of resistance, of about three orders of magnitude at RT, showing no traces of the PM-FM transition in the range of temperatures accessible. According to the phase diagram of LSMO the transition from FM-M to FM-I and the downward shift of T_C indicate a reduction of the charge carriers' density that may arise either from a depletion of the oxygen content or from charge accumulation/depletion in the modified area. In order to get further insight on in this issue we analyzed the stability of the FM-I phase, corresponding to the locally induced HRS, as a function of magnetic field, temperature and compliance current (CC) circulating along the microbridges.

The effect of the magnetic field on $R(T)$ curves has been explored in a LSMO microbridge ($h \approx 45\text{ nm}$) which after the HRS modification exhibited an increase of about three orders of magnitude in resistance, as compared to the virgin state, and a clear insulating-like behavior (see online supplementary data stacks.iop.org/JPhysCM/26/395010/mmedia). The application of $H = 7\text{ T}$ (significantly larger than the 3 T used in previous endurance tests) [7] induced an upwards shift of about 70 K of the PM-FM transition but the insulating character remained unaltered. For thinner microbridges ($h \approx 25\text{ nm}$), in which the increase in resistance after writing was even larger no traces of field dependence were observed for the available temperature range (see online supplementary data stacks.iop.org/JPhysCM/26/395010/mmedia). These results indicate

that the HRS regions behave as a LSMO with lower doping rate or charge carrier density than the virgin material in full agreement with the local work function KPM data (interpreted as a decrease of carrier concentration). We conclude that, remarkably, the locally induced HRS is robust enough to survive the application of magnetic fields of at least 7 T.

The effect of temperature cycling on $R(T)$ for a thin microbridge ($h = 25\text{ nm}$) after HRS writing at $V_w = +8\text{ V}$ is illustrated in figure 6. Although successive warming and cooling processes from 150 K to RT do not have any relevance on the curve, that remains basically reversible (upper branch in the figure), increasing the temperature above $T \sim 380\text{ K}$ results however in a dramatic change. Remarkably, on cooling down from 380 K the resistance strongly decreases and the FM-M state is recovered. This unquestionable fact evidences that heating the sample above 380 K promotes the transition from the HRS to the LRS recovering the low temperature FM-M state of the virgin sample. In other words, we have demonstrated that local RS can be reversed by an adequate temperature increase of the system.

At this point, it is interesting to compare the transport response of the back transformed microbridges with that of virgin LSMO (see figure 7). It is worth noting that both curves are almost coincident in the whole range of temperatures. The same coincidence is observed for the magnetoresistance in the whole range of applied fields (inset). Obviously, the exact temperature needed for the resistance reversal depends on sample thickness as well as the writing parameters (V_w and application time). It should be mentioned here that oxygen interchange with the environment is not likely responsible for the RS reported here since the samples heating up is performed inside the PPMS chamber under a He atmosphere and the C-SPM writing process

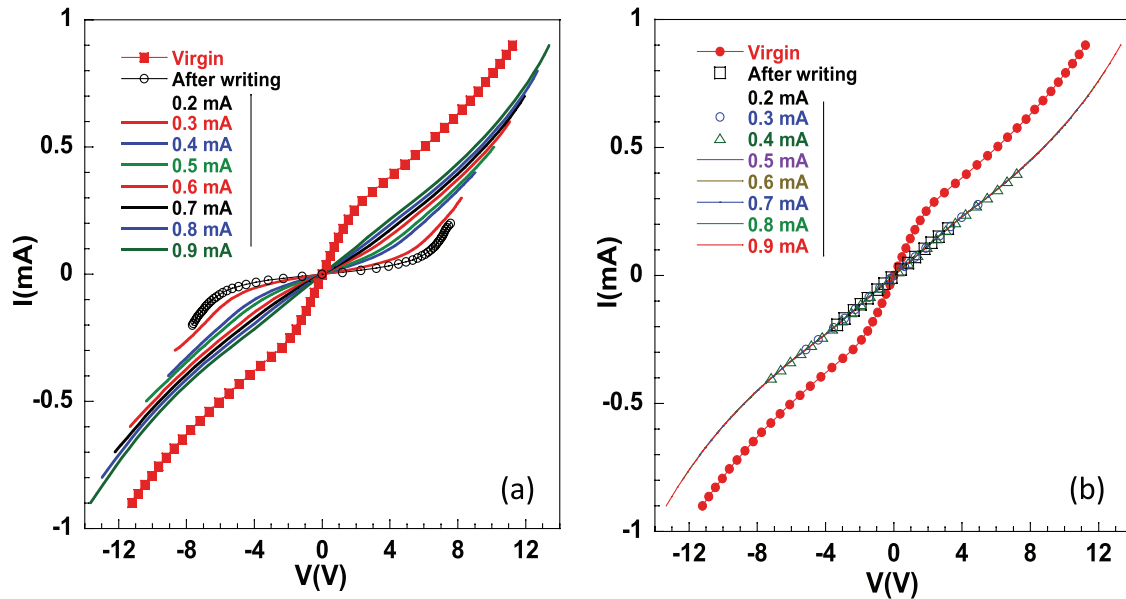


Figure 8. Effect of the circulating current on the macroscopic I - V characteristic curves along a LSMO microbridge ~ 43 nm thick after transforming to the HRS a transversal zone of the microbridge by written with 30 scan lines at a tip bias $V_w \sim +10$ V. The curve for the virgin sample corresponds to a CC of 0.9 mA and the effect of increasing or decreasing circulating current is depicted in (a) and (b) respectively. In (a) the strong increase of resistance after HRS writing with the appearance of a pseudo-gap at low voltages is evident. The capability of erasing the local HRS (back to LRS) by circulating current is demonstrated by the progressive reduction of the microbridge resistance as the current limit is raised up from 0.2–0.9 mA. As expected, this type of process, in which a local resistive state is macroscopic erased, cannot be reversed. This is illustrated in (b) where all I - V curves collapse in one, with nearly linear behavior, when the CC is decreased from a 0.9–0.2 mA.

itself is performed under clean N_2 low humidity conditions ($\leq 5\%$ RH). In this sense, it is worth mentioning here the particular properties of the mixed valence LSMO system compared with other oxides typically used for RS purposes. The magnetic and electronic properties of the LSMO system are linked to the Mn^{3+}/Mn^{4+} ratio, that is fixed for a given composition, i.e. Sr^{2+} substitution for La^{3+} . Of course, the generation of oxygen vacancies will modify this ratio and affect magnetotransport properties. However, variations of the Mn^{3+}/Mn^{4+} ratio may be locally stabilized by lattice distortions given place to local modification of the magnetotransport properties of purely electronic origin [23].

During the switching process, in particular from HRS to LRS, a CC is usually required to protect the sample from breaking down. It is known that in the parallel electrodes configuration, the effect of CC may be very important during RS processing. In order to examine the response of the tip-induced HRS with respect to this issue macroscopic I - V characteristic curves have been measured for different maximum currents injected along the microbridges through the modified nanometric HRS zones. Figure 8(a) depicts the results obtained for a microbridge ($W \times L \approx 1.5 \mu m \times 6 \mu m$, $h \approx 43$ nm) in the virgin state and after application of $V_w \sim +10$ V during 30 tip scan lines. The transport measurements were performed at RT for sequential increasing values of the maximum injected current ($\pm I_{max} = 0.2$ – 0.9 mA). The strong change in shape and the difference in magnitude between the I - V curves for the modified microbridge and the virgin case evidence the huge alteration of resistance in the modified area.

For a fixed value of the I_{max} used all I - V curves are reversible but every time I_{max} is increased, instead of a prolongation

of the previous characteristics, a new I - V curve is described. Remarkably, starting from the low conducting case (open circles in figure 8(a)) the curves approach that of the virgin sample, i.e. the resistance of the microbridge decreases with increasing I_{max} , eventually reaching the LRS. In other words, the HRS is being erased. This behavior supports the multilevel character of RS already inferred from the dependence of the HRS resistance on the magnitude and application time of V_w . Note that the transition is not completely achieved in the present study since I_{max} has been maintained below 1 mA (equivalent to $J_{max} \approx 2.3 \times 10^6$ A cm^{-2} taken into account the microbridge dimensions) to avoid damage by oxide breakdown. If the inverse procedure is followed, I_{max} is progressively decreased from the highest value ($I_{max} \sim 0.9$ mA), the I - V curves collapse in one with no further changes in the resistance (figure 8(b)). These experiments demonstrate the capability of erasing local resistive states by increasing the limit of circulating current through the microbridge. As expected, this type of process, in which a local resistive state is erased by macroscopic current circulation, cannot be reversed and the system remains in the low resistive state.

After having examined the feasibility of the resistive back transition (HRS to LRS) of nanosized written regions by macroscopic means (magnetic field, temperature and CC) we present now the macroscopic consequences of the locally induced back transition (local erase) of similar nanosized RS using the same C-SPM. For this, and as previously shown [8,9], a $V_{bias} = V_e \geq V_{Set}$ (HRS to LRS) has to be applied on the surface region previously written at a $V_w > V_{Reset}$ (LRS to HRS). For this purpose, two microbridges, as shown in

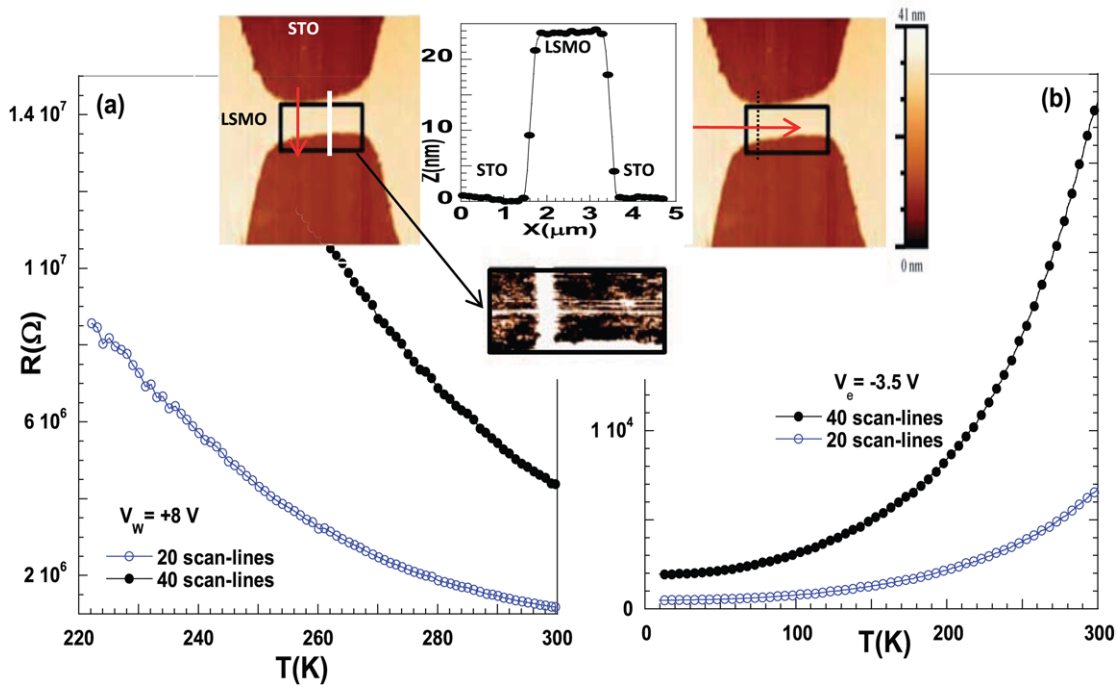


Figure 9. Demonstration of the effectiveness of the erasing process by locally applying a tip bias $V_{\text{bias}} > V_{\text{Reset}}$. Upper panels: (left) the vertical red arrow in the topographic image indicates the tip path during writing at $V_w = +8$ V, (top center) height profile performed along the white segment in the left image verifying the microbridge height (45 nm), (bottom center) current map of the indicated microbridge region showing the non-conducting character of the written HRS (white vertical region), (right) the horizontal red arrow in the topographic image indicates the tip path of the erasing process at $V_e = -3.5$ V. The color scale in the current map taken at $V < 0$ is such that higher/lower values correspond to dark/bright color. (a) Temperature dependence of the resistance curves corresponding to two LSMO microbridges ($h = 45$ nm) after HRS writing using the same $V_w = +8$ V but different number of tip scan lines (20 and 40, respectively). Note the insulating character in both cases and the decrease in resistance for increasing number of scans. (b) Temperature dependence of the resistance curves after applying a bias voltage $V_e = -3.5$ V during tip scanning. Note the restored metallic behavior in both cases.

the topographic data of figure 9, were used. After V_{Set} and V_{Reset} determination from local $I-V$ curves, each microbridge was locally written using V_w and different number of scan lines perpendicularly to the bridge length (vertical arrow in the left topographic image). At the local level, the HRS region is visualized as a non-conducting vertical region in the current C-SPM map of the figure. The $R(T)$ curves corresponding to both microbridges (figure 9(a)) indicate the influence of writing time and show the insulating character of both systems with no traces of the PM-FM transition in the accessible temperature range (restricted by the compliance limit of the experimental set-up).

In principle, restoring conduction through the microbridge would not need back transforming the complete HRS region, but just recovering electrical connection between the two conducting parts. This assertion implies verifying if the metallic behavior of the $R(T)$ is reestablished after erasing just a section of the HRS area. In order to corroborate this, several lines were scanned with the SPM tip biased at V_e along the microbridge crossing the modified region (horizontal arrow in the right topographic image of figure 9). The subsequent $R(T)$ results, depicted in figure 9(b), demonstrate the effectiveness of the local erasing process in reversing the macroscopic situation: the RT resistance drops by about two orders of magnitude and the curves recover the FM-M character confirming the success of conduction reestablishment by the partial reestablishment of the LRS.

From both the macro and the nanoscale results we can summarize that RS from LRS to HRS in thin LSMO films has a bipolar reversible behavior which is robust enough to survive magnetic fields up to at least 7 T but is reversed for temperatures above the samples' T_C . The diverse resistive states (multilevel HRS) reached for different V_w can be reversed to more conducting ones for increasing circulating currents in a non-reversible way while the transition is fully accomplished at the nanoscale by locally applying the adequate tip voltage V_e . The bipolar character of the RS process indicates that it is basically driven by electric field. On the other hand, the rectifying behavior with charge injection in the negative branch (V_{Set}) of the local $I-V$ points to the existence of a Schottky-like barrier, as suggested by several authors for RS in M-I-M heterostructures where different transition metal oxides were used as insulating barrier [11,32,33]. Moreover, in view of previous results suggesting the existence of a few unit cells (2 nm) antiferromagnetic insulating surface layer [34,35] on top of the LSMO films, due to inversion symmetry breaking, and taking into account the contact areas in C-SPM (some hundreds of nanometers), the actual geometry of these experiments is, indeed, of a M-I-M type, in which the antiferromagnetic insulating surface layer is sandwiched between the underlying metallic LSMO layer and the conducting tip, acting as bottom and top electrodes, respectively. In this context, the interfacial properties of the electrode-LSMO system play a paramount role. Enlightening results from Sawa *et al* [33] demonstrated

the appearance of RS in Ti-LSMO (M–M) structures when a thin (≥ 1 nm) $\text{Sm}_{2/3}\text{Ca}_{1/3}\text{MnO}_3$ insulating layer was introduced between the two metals. Assuming the insulating nature of the uppermost LSMO atomic layers, the application of $V_w = 5$ V will produce an electric field $E \sim V_w/d \sim 2.5 \times 10^9 \text{ V m}^{-1}$ strong enough to drive charge carriers motion in the area just below the apex of the scanning probe and, therefore, modify the carriers density (doping rate) of the LSMO electrode. Numerical simulations for 60 nm thick films show that the electric field within a few nanometers from the tip–sample contact is a factor of ~ 20 -fold larger than that in the region of the film closer to the substrate interface [36]. Therefore, it is obvious that the resistive state and, consequently, the features of the Schottky-like barrier, including charge depletion depth, depend on the magnitude of the applied electric field.

The same scenario is inferred from the transport measurements, which show that the change of resistance affects not only the outermost surface but the whole volume of material below the written area. Thus, the observed dependence with film thickness, V_w and tip scan lines is compatible with the progressive increase of the resistance derived from a gradual charge depletion (varying magnitude and/or length) within the LSMO area just below the apex of the C-SPM tip. On the other hand, this decrease of charge carriers is reflected as a progressive reduction of the FM and I–M transition temperatures of LSMO, which eventually becomes insulating.

As it is known, complex transition metal oxides are solid electrolytes where not only electronic carriers but also mobile ions or ionic defects may contribute to the current transport. Depending on the true oxide stoichiometry complex transition metal oxides are viewed as p-type or n-type semiconductors and, therefore, the I – V behavior depends on the electrode materials [16]. Charge carriers in lightly doped manganites, such as LSMO, are holes (p-type) and, for a given doping rate, the charge carriers' density can be modified by purely electronic effects or by variations of the amount of oxygen vacancies. In fact, mechanisms based on oxygen vacancy diffusion have been proposed for explaining RS phenomena in ternary oxides [37] and, in particular, in manganites [38]. The experimental results presented here suggest that, although both electronic and ionic processes may coexist, the RS behavior observed has a major electronic contribution. As previously mentioned, variations of the $\text{Mn}^{3+}/\text{Mn}^{4+}$ ratio may be locally stabilized by lattice distortions given place to local modification of the magnetotransport properties of purely electronic origin [23]. In addition, Joule heating effects should be taken into account as they promote resistance changes of LSMO microbridges for high current densities [39].

4. Conclusions

We report on the electronic transport properties of patterned $\text{La}_{2/3}\text{Sr}_{1/3}\text{MnO}_3$ (LSMO) thin films in which nanometric resistive states have been locally induced by application of electric fields using the conducting probe of a C-SPM. The transition between low resistance and high resistance states has been systematically investigated to identify the switching material

and analyze the mechanisms responsible for the reversible RS. The bipolar character of the RS indicates that the process is basically driven by electric field. In the ON state, i.e. prior to the transition, the local I – V curves are almost symmetric, but present a rectifying behaviour in the OFF state indicating the existence of a Schottky-like barrier. The clear loop suggests that the experimental configuration is, in fact, a M–I–M geometry at the submicrometric scale, with a interface switching mechanism in which the topmost unit cells of the LSMO acts as the I layer while the rest of the LSMO layer and the SPM conducting tip are the metallic electrodes. The particular geometry used in our experiments allowed, for the first time, the study of the electronic properties of the HRS and their dependence on temperature and magnetic field. These results indicate that the switching material is the LSMO electrode by itself, which is driven into an insulating state by the effect of the intense electric field generated at the apex of the biased C-SPM tip. Depending on the polarity, the local electric field attracts/repels charge carriers modifying the doping rate of the LSMO material, becoming insulating/metallic in a reversible way. Although mobile ions or ionic defects might contribute to the current transport, the present results strongly indicate that electronic effects play a paramount role in the charge depletion, due to the electric field charge carriers dragging, responsible for the RS phenomenon. Our results represent an important step forward to the implementation of oxide based memory devices and may open new avenues for device engineering and applications.

Acknowledgment

We acknowledge financial support from the Spanish MINECO (MAT2010-20020, MAT2011-29081 and MAT2012-33207), CONSOLIDER (CSD2007-00041), and FEDER program. ZK thanks the Spanish MINECO for the financial support through the RyC program.

References

- [1] Ielmini C and Lacaite A L 2011 *Mater. Today* **14** 600
- [2] Strukov D B and Kohlstedt H 2012 *MRS Bull.* **37** 108–14
- [3] Lee T and Chen Y 2012 *MRS Bull.* **37** 144–9
- [4] Joshua Yang J, Inoue I H, Mikolajick T and Hwang C S 2012 *MRS Bull.* **37** 131–7
- [5] Waser R, Dittman R, Staikov G and Szot K 2009 *Adv. Mater.* **21** 2632–63
- [6] Yang J J, Strukov D B and Stewart D R 2012 *Nat. Nanotechnol.* **8** 13–24
- [7] Jeong D S, Thomas R, Katiyar R S, Scott J F, Kohlstedt H, Petraru A and Hwang C S 2012 *Rep. Prog. Phys.* **75** 076502
- [8] Moreno C, Munuera C, Valencia S, Kronast F, Obradors X and Ocal C 2010 *Nano Lett.* **10** 3828
- [9] Moreno C, Munuera C, Obradors X and Ocal C 2012 *Beilstein J. Nanotechnol.* **3** 722–30
- [10] Min Kim K, Joon Choi B and Seong Hwang C 2007 *Appl. Phys. Lett.* **90** 242906
- [11] Baikov A, Wang Y Q, Shen B, Lorenz B, Tsui S, Sun Y Y, Xue Y Y and Chu C W 2003 *Appl. Phys. Lett.* **83** 957
- [12] Sawa A, Fujii T, Kawasaki M and Tokura Y 2004 *Appl. Phys. Lett.* **85** 4073

- [13] Rozenberg M J, Inoue I H and Sánchez M J 2004 *Phys. Rev. Lett.* **92** 178302
Rozenberg M J, Inoue I H and Sánchez M J 2006 *Appl. Phys. Lett.* **88** 033510
- [14] Fors R, Khartsev S I and Grishin A M 2005 *Phys. Rev. B* **71** 045305
- [15] Oka T and Nagaosa N 2005 *Phys. Rev. Lett.* **95** 266403
- [16] Gomez-Marlasca F, Ghenzi N, Rozenberg M J and Levy P 2011 *Appl. Phys. Lett.* **98** 042901
- [17] Jeong D S, Schroeder H, Breuer U and Waser R 2008 *J. Appl. Phys.* **104** 123716
- [18] Beck A, Bednorz J G, Gerber Ch, Rossel C and Widmer D 2000 *Appl. Phys. Lett.* **77** 139
- [19] Asamitsu A, Tomioka Y, Kuwahara H and Tokura Y 1997 *Nature* **388** 50
- [20] Yuzhelevski Y, Markovich V, Dikovskiy V, Rozenberg E, Gorodetsky G, Jung G, Shulyatev D A and Mukovskii Y M 2001 *Phys. Rev. B* **64** 224428
- [21] Fujii T, Kawasaki M, Sawa A, Kawazoe Y, Akoh H and Tokura Y 2007 *Phys. Rev. B* **75** 165101
- [22] Fors R, Khartsev S I and Grishin A M 2005 *Phys. Rev. B* **71** 045305
- [23] Sandiumenge F, Santiso J, Balcells L I, Konstantinovic Z, Roqueta J, Pomar A, Espinós J P and Martínez B 2013 *Phys. Rev. Lett.* **110** 107206
- [24] Santiso J, Balcells L I, Konstantinovic Z, Roqueta J, Ferrer P, Pomar A, Martínez B, and Sandiumenge F 2013 *Cryst. Eng. Commun.* **15** 3908
- [25] Nakamura T, Inada H and Iiyama M 1998 *Appl. Surf. Sci.* **130–2** 576
- [26] Konstantinović Z, Santiso J, Colson D, Forget A, Balcells L I and Martínez B 2009 *J. Appl. Phys.* **105** 063919
- [27] Horcas J, Fernández R, Gómez-Rodríguez J M, Colchero J, Gómez-Herrero J and Baro A M 2007 *Rev. Sci. Instrum.* **78** 013705
- [28] Nonnenmacher M O, O'Boyle M P and Wickramasinghe H K 1991 *Appl. Phys. Lett.* **58** 2921
- [29] Barth C, Foster A S, Henry C R and Shluger A L 2011 *Adv. Mater.* **23** 477
- [30] Münstermann R, Menke T, Dittmann R and Waser R 2010 *Adv. Mater.* **22** 4819
- [31] Okushi H, Matsuda A, Saito M, Kikuchi M and Hirai Y 1972 *Solid State Commun.* **11** 283
- [32] Sawa A, Yamamoto A, Yamada H, Fuji T, Kawasaki M, Matsuno J and Tokura Y 2007 *Appl. Phys. Lett.* **90** 252102
- [33] Sawa A, Fuji T, Kawasaki M and Tokura Y 2006 *Appl. Phys. Lett.* **88** 232112
- [34] Valencia S, Peña L, Konstantinovic Z, Balcells L I, Galceran R, Schmitz D, Sandiumenge F, Casanove M and Martínez B 2014 *J. Phys.: Condens. Matter* **26** 166001
- [35] Valencia S, Konstantinovic Z, Schmitz D, Gaupp A, Balcells L I and Martínez B 2011 *Phys. Rev. B* **84** 024413
- [36] Lee M H, Kim K M, Song S J, Rha S H, Seok J Y, Jung J S, Kim G H, Yoon J H and Hwang C S 2011 *Appl. Phys. A* **102** 827–34
- [37] Szot K, Speier W, Bihlmayer G and Waser R 2006 *Nat. Mater.* **5** 312–20
- [38] Nian Y B, Strozier J, Wu N J, Chen X and Ignatiev A 2007 *Phys. Rev. Lett.* **98** 146403
- [39] Balcells L I, Peña L, Galceran R, Pomar A, Bozzo B, Konstantinovic Z, Sandiumenge F and Martínez B 2013 *J. Appl. Phys.* **113** 073703